UiT The Arctic University of Norway

UNIS
The University Centre in Svalbard

Faculty of Science and Technology, Department of Geosciences

Ground Dynamics in the Norwegian Periglacial Environment Investigated by Synthetic Aperture Radar Interferometry

–

Line Rouyet

A dissertation for the degree of Philosophiae Doctor – May 2021

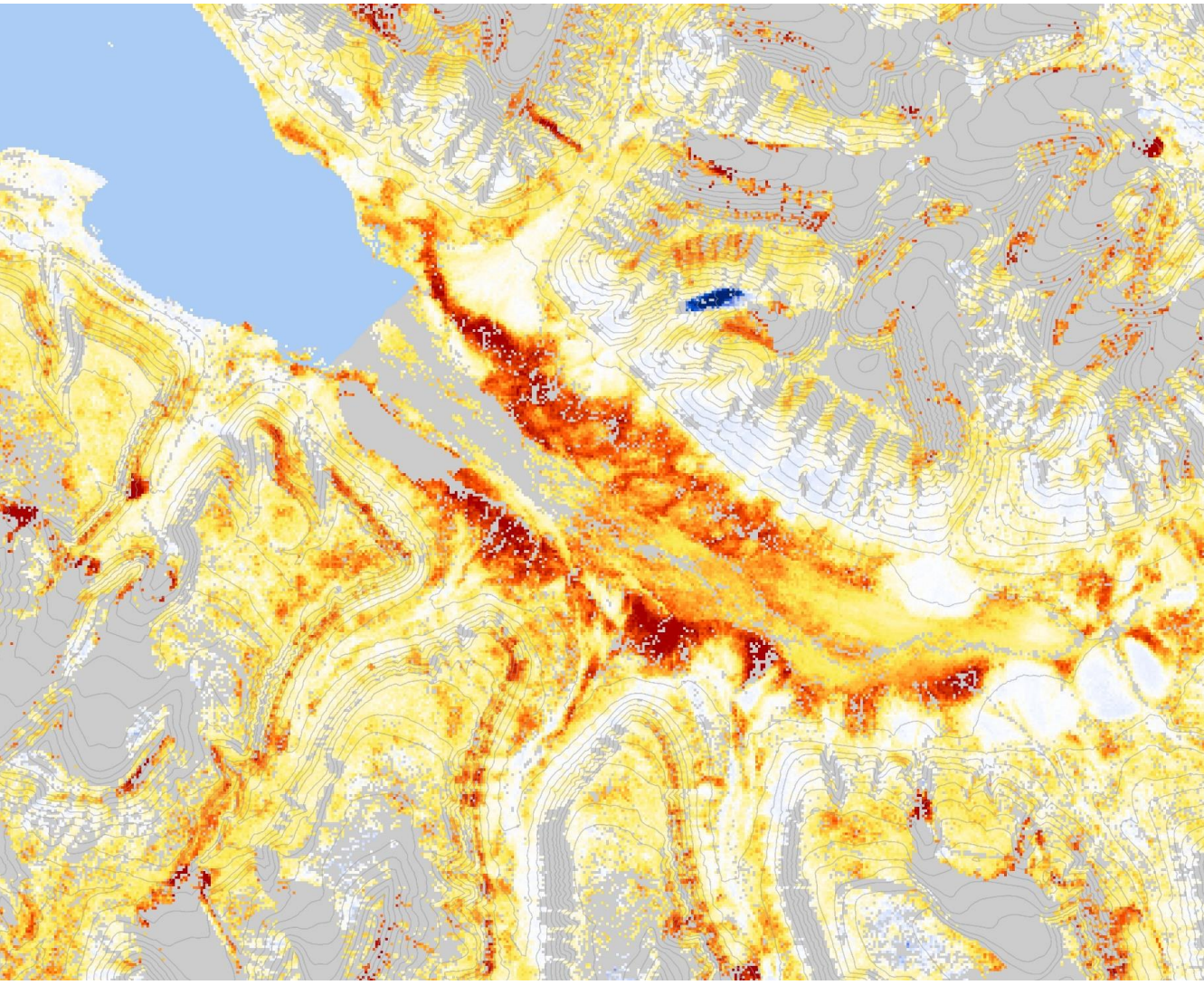

Abstract

Cold polar and mountainous periglacial environments are characterised by highly dynamic ground surfaces that move under the action of frost and gravity, and contribute to shaping the landscape. The movement rates and directions are spatially and temporally variable, depending on the involved periglacial processes and their environmental controlling factors. Spaceborne Synthetic Aperture Radar (SAR) has revolutionised the investigation of the ground surface in polar and mountainous regions, due to its ability to image large and remote areas independently of light and meteorological conditions. By comparing images taken at different times, the SAR Interferometry (InSAR) technique can remotely detect ground surface displacements at centimetre to millimetre accuracy.

This thesis exploits the InSAR technology to analyse the spatial distribution and temporal variability of the ground surface displacements in periglacial environments. The spatio-temporal displacement patterns are documented on a regional scale, allowing for the study of the kinematic signatures of various frost- and gravity-driven processes. The research takes advantage of the Copernicus Sentinel-1 SAR mission that provides open access images with unprecedented spatial coverage and at a weekly temporal resolution. Sentinel-1 InSAR is complemented with results based on the high spatial resolution TerraSAR-X images. The advantages and limitations of InSAR in the scope of periglacial research are discussed based on case studies in central and western Spitsbergen (Svalbard) and in Troms and Finnmark (Northern Norway).

In Papers I–V, we demonstrate the ability of InSAR to document the kinematic properties of the periglacial ground dynamics, characterised by displacement rates ranging from a millimetre to a metre over a season or a year. InSAR allows for investigating the displacement progression caused by the ground freeze–thaw cycles in permafrost lowlands and the gradual downslope creep of periglacial landforms in mountainous environments. InSAR observa-

tions are compared with in-situ measurements and geomorphological mapping, and coupled with statistical and physical modelling. This integration contributes to a better understanding of the factors controlling the spatio-temporal patterns of the ground movement.

This research suggests novel ways to develop dedicated InSAR products relevant for the assessment of geohazards and the systematic observation of ground dynamics in the context of climate change. The results show the value of combining satellite InSAR with complementary remote sensing techniques to document fast-moving landforms and provide decadal time series. Finally, this dissertation outlines perspectives for furthering the work in the scope of InSAR applied to periglacial research.

Plain language summary

In polar and mountainous regions, the cold climate leads to temperature fluctuations around 0 °C. The ground freezes and thaws, which causes upward and downward superficial movement due to the transition between water and ice. In inclined terrain, rocks and unconsolidated deposits tend to move downslope under the effect of gravity. These processes impact the terrain stability and can pose a hazard for population and infrastructure. Climatic, geologic and topographic factors control the variable distribution and timing of processes driven by frost and gravity, which determine the characteristics of the ground dynamics. However, the interactions between the environmental variables and the ground properties are complex and challenging to study.

The availability of extensive and frequent satellite imagery provides a valuable tool to enlarge the investigation in hard-to-access polar and mountainous regions. This thesis takes advantage of the open access images acquired by the Copernicus Sentinel-1 Synthetic Aperture Radar (SAR) satellites to analyse selected study areas in Northern Norway and Svalbard. The SAR Interferometry (InSAR) technique allows for measuring displacements at centimetre to millimetre accuracy, by comparing images taken at different times. The detected displacements are studied in relation to other datasets, such as temperature measurements and field-based maps.

The results show that InSAR is able to investigate the behaviour of moving landforms characterised by displacement rates ranging from a millimetre to a metre over a season or a year. InSAR can also be utilised to investigate the processes causing ground movement, and understand their relationship with environmental factors, such as the temperature and the ground composition. This thesis highlights the potential for future exploitation of InSAR technology to improve our understanding of the processes shaping cold-climate landscapes, for identifying hazardous landforms at the regional scale and monitoring the evolution of arctic environments under climate change.

Thesis papers

I) Rouyet, L. Lauknes, T. R., Christiansen, H. H., Strand, S. M., Larsen, Y. 2019. **Seasonal dynamics of a permafrost landscape, Adventdalen, Svalbard, investigated by InSAR**. *Remote Sensing of Environment*, *231*, 111236. https://doi.org/10.1016/j.rse.2019.111236.

II) Rouyet, L., Liu, L., Strand, S. M., Christiansen, H. H., Larsen, Y., Lauknes, T.R. **Seasonal InSAR displacements documenting the active layer freeze and thaw progression in central–western Spitsbergen, Svalbard**. Submitted to *Remote Sensing*. Dataset: https://doi.org/10.5281/zenodo.4775398.

III) Rouyet, L., Lilleøren, K., Böhme M., Vick, L., Etzelmüller, B., Delaloye, R., Larsen, Y., Lauknes, T. R., Blikra, L.H. **Regional InSAR inventory of slope movement in Northern Norway**. Under Review in *Frontiers in Earth Science: Cryospheric Sciences*. Dataset: https://doi.pangaea.de/10.1594/PANGAEA.930856.

IV) Eriksen, H. Ø., Rouyet, L., Lauknes, T. R., Berthling, I., Isaksen, K., Hindberg, H., Larsen, Y., Corner, G. D. 2018. **Recent acceleration of a rock glacier complex, Ádjet, Norway, documented by 62 years of remote sensing observations**. *Geophysical Research Letters*, *45*(16), 8314–8323. https://doi.org/10.1029/2018GL077605.

V) Rouyet, L., Karjalainen, O., Niittynen, P., Aalto, J., Luoto, M., Lauknes, T. R., Larsen, Y., Hjort, J. **Environmental controls of InSAR-based periglacial ground dynamics in a Sub-Arctic landscape**. Under Review in *Journal of Geophysical Research: Earth Surface*. Dataset: http://doi.org/10.5281/zenodo.4173256.

Supervision Committee

Prof. Dr. Anders Schomacker, UiT The Arctic University of Norway

Prof. Dr. Hanne H. Christiansen, The University Centre in Svalbard (UNIS)

Dr. Tom Rune Lauknes, NORCE Norwegian Research Centre AS

Dr. Lars Harald Blikra, Norwegian Water Resources and Energy Directorate

Funding sources

The *FrostInSAR* Ph.D. project (2017–2021) has been funded by the Space Research Programme of the Research Council of Norway (RCN) (grant 263005), with an additional support for a research visit in Finland in 2020 (overseas research grant 297519) and an Arctic Field Grant that contributed to a field campaign in Svalbard in the summer of 2018 (RiS ID 10894). Due to the Covid situation, delays and changes of work planning related to initially scheduled research visits in Hong Kong and Alaska led to a two-month project extension, supported by an additional RCN funding.

Since 2017, *FrostInSAR* had synergies with research performed in other projects led by NORCE (former Norut): the ESA Prodex *PermaSAT2* project, the Troms County Council *Fjellradar* project (grant RDA12/165), the Svalbard Miljøvernfond project on ground deformation around Longyearbyen (project 17/59), the European Space Agency (ESA) *2DInSAR* project (4000125274/18/I-NB) and the ESA *CCN2 CCI Permafrost* project on rock glacier kinematics (4000123681/18/I-NB). The project also took advantage of research developments from previous projects funded by RCN (*PermaSAR*, 2012–2014) and ESA Prodex (*PermaSAT1*, 2012–2015).

Acknowledgements

A doctoral study is like a solo musical piece with a symphonic orchestra. At the end of the concert, the soloist gets applause and receives flowers, but the whole event would not have been possible without the involvement and support of many incredible people who sometimes remain backstage.

I am deeply grateful for the complementary expertise and work of my beautifully eclectic supervision team. Thank you to Anders Schomacker for helping me to maintain a healthy bond between NORCE and UiT the Arctic University of Norway, as well as to Lars Harald Blikra for his contribution to designing my research from the very start. All my gratitude to Hanne H. Christiansen for having introduced me to the wonders of periglacial research and for her great support all along the journey. I am much obliged to Tom Rune Lauknes for having believed in me since the very beginning of my Nordic adventure and for the initiation of numerous projects that have enhanced applied InSAR in geosciences. A huge thanks also to Yngvar Larsen for his endless support these past years and for demonstrating on a daily basis that it is possible to be both a brilliant nerd and a friendly colleague.

The research presented in the thesis is the result of partnerships with great people from many different institutions. I would like to acknowledge the effort of all my co-authors. I am especially grateful to the contribution of Olli Karjalainen (The University of Oulu), as well as the long-term support of Jan Hjort (The University of Oulu) and Lin Liu (The Chinese University of Hong Kong), who helped me designing the proposal far before the project started, who followed my work all along the Ph.D. and co-authored my latest manuscripts. Thanks to Jan who made possible two great visits in Oulu in 2018 and 2020. I acknowledge the inspiring work of the whole CCI Permafrost team and the IPA Action Group on rock glacier kinematics, with a special gratitude to Tazio Strozzi (Gamma Remote Sensing AS) and Reynald Delaloye (The University of Fribourg) for great partnerships these past years. Thanks to Sarah

Strand, Ole Humlum, Fraser and Barbara Smith for an amazing field campaign in Svalbard, and to have accepted me as the french-speaking witch of the crew! Thanks also to Louise Vick (you rock Big Wild Dog!) and Henrik Sandbakken for their friendly support and advice to improve the last version of this dissertation.

I communicate all my affection to my dear colleagues at NORCE (former Norut). Thank you especially to Harald Ø. Eriksen and Markus Eckerstorfer for their work that paved the way to the FrostInSAR project. My research would not have been possible without the long-term effort of the Earth Observation and the ICT groups at NORCE, who manage the computing infrastructure and are behind the developments of the SAR processing chain. Big applause to Heidi Hindberg, Tom Grydeland, Jakob Grahn, Temegsen Yitayew, Daniel Stødle, Ståle Schwenke, Njål Borch and Ingar Arntzen. You are the bass section of the orchester, those that nobody notices when everything goes well but would make the whole piece to fall apart if missing! Thanks also to Eirik Malnes, Geir Engen and Rune Storvold for our digital beer-meetings that made my Friday evenings much more fun than expected during the lockdowns. And to all my friends in Norway, Switzerland or elsewhere: life would just not be the same without you! I express a special acknowledgement to all members of Tromsdalen Musikkorps and Tromsø Orkesterforenings Janitsjarkorps to have filled my life with music and friendship.

Last but not least, all my love to my parents, my brother and the other members of my family who taught me – all in their very unique ways – that it is possible to be eager, strong-minded and independent, and at the same time self-critical, tolerant and integrative; all elements that I believe are essential to be a valuable researcher, or maybe simply an acceptable human-being.

Line Rouyet, Tromsø, May 2021

Contents

Acronyms, abbreviations and symbols

A	Radar amplitude
ALT	Active Layer Thickness
APS	Atmospheric Phase Screen
a.s.l.	Above Sea Level
B	Spatial Baseline
B_{P}	Perpendicular Baseline
B_{T}	Temporal Baseline
d	Ground Surface Displacement
DEM	Digital Elevation Model
dGNSS	Differential Global Navigation Satellite System
DLR	Deutsches Zentrum für Luft- und Raumfahrt
DOY	Day Of Year
EM	Electromagnetic
EO	Earth Observation
FT	Front and Feature Tracking
GBM	Generalized Boosting Method
GPRI	Gamma Portable Radar Interferometer
InSAR	Synthetic Aperture Radar Interferometry
LOS	Line-Of-Sight
MAAT	Mean Annual Air Temperature
MT InSAR	Multi-Temporal InSAR
NDVI	Normalized Difference Vegetation Index
NORCE	Norwegian Research Centre AS
OT	Offset Tracking
P_{Ref}	InSAR Reference Point
PSI	Persistent Scatterer Interferometry

R	Slant Range, Sensor-To-Ground Distance
Radar	Radio Detection and Ranging
RAR	Real Aperture Radar
RG	Rock Glacier
RS	Rockslide
S1	Sentinel-1
SAR	Synthetic Aperture Radar
SBAS	Small Baseline Subset
SCD	Snow Cover Duration
TRI	Terrestrial Radar Interferometry
TSX	TerraSAR-X
TWI	Topographic Wetness Index
t_{x}	Image Acquisition at Time x
UiT	The Arctic University of Norway
UNIS	The University Centre in Svalbard
x	Azimuth, Cross-Range Distance
yr	Year
z	Elevation Above a Reference Plane
1D	One-Dimensional
2D	Two-Dimensional
λ	Radar Wavelength
θ	Incidence Angle
ϕ	Radar Phase

Cardinal directions: N (North), S (South), E (East), W (West)

Units of length: mm (millimetre), cm (centimetre), dm (decimetre), m (metre)

Chapter 1

Introduction

1.1 Motivation and objectives

Periglacial landscapes in cold polar and mountainous regions are characterised by seasonal or perennially frozen ground (permafrost) (French, 2007). These environments are highly dynamic and encompass a wide range of processes driven by frost action that cause ground movement and shape the landscape. Seasonal ground freezing and thawing cause heave and subsidence due to water-to-ice phase change (Rempel, 2007; Bonnaventure & Lamoureux, 2013). On slopes, the additional impact of the gravity induces variable mass wasting processes depending on the ground composition (Matsuoka, 2001; Haeberli et al., 2006). At local to global scales, a nested set of climatic, geomorphic, hydrological and biological variables influences these processes and controls the spatial distribution and temporal behaviour of the ground movement. Changing environmental conditions modify the ground thermal regime and the periglacial processes (Aalto et al., 2017; Biskaborn et al., 2019; Etzelmüller et al., 2020). In permafrost landscapes, climate warming causes deepening of the seasonally thawing ground (active layer) that can induce

long-term subsidence due to ice melting. On slopes, increasing ground temperatures also tend to accelerate the creep rate of permafrost landforms, which may pose a hazard for infrastructure and population (Harris et al., 2009; Kääb, 2008; Hjort et al., 2018). However, the complexity of the interactions between the environmental drivers, the resulting periglacial processes, and their consequences in terms of ground dynamics make the potential future impacts challenging to assess. The Norwegian periglacial environment is ideal to study these interactions, as it offers a variety of environmental conditions. The large latitudinal, maritime–continental and altitudinal climatic gradients lead to a combination of seasonally frozen ground, mountain and lowland permafrost areas (Etzelmüller et al., 2001; Christiansen et al., 2013).

Satellite Earth Observation has revolutionised the investigation of the Earth surface, allowing for studies of environmental changes at the regional and global scales (Nitze et al., 2018; Obu et al., 2019). The use of spaceborne imaging Synthetic Aperture Radar (SAR) is especially suitable for remote sensing measurements in the Arctic due to its insensitivity to light and meteorological conditions, as well as its ability to cover large and remote areas (Duguay et al., 2005; T. Zhang et al., 2004). SAR Interferometry (InSAR) technology can measure ground surface movement at centimetre to millimetre accuracy, by comparing images taken at different times. InSAR has been exploited for decades to detect and map moving areas (Gabriel et al., 1989; Massonnet et al., 1993), but its application in periglacial environments is more recent (Z. Wang & Li, 1999; Rignot et al., 2002; Kenyi & Kaufmann, 2003; Strozzi et al., 2004; Singhroy et al., 2007; Liu et al., 2010). In Norway, several studies showed the values of ERS, RADARSAT and/or TerraSAR-X satellites to detect, map and monitor periglacial landforms (Lauknes et al., 2010a; Dehls et al., 2012; Eriksen et al., 2017a; Eckerstorfer et al., 2018; Böhme et al., 2019). At the local scale, the availability of terrestrial radar platforms has proven its value in overcoming some limitations of satellite remote sensing by providing complementary

observation geometries, as well as potentially higher spatial and temporal resolutions (Caduff et al., 2015; Eriksen et al., 2017b).

Since 2015, the Sentinel-1 SAR mission from the European Commission Copernicus Programme has been a game changer for InSAR applications in polar and mountainous regions. The open access images from Sentinel-1 have pushed forward InSAR exploitation in periglacial research thanks to an unprecedented spatial coverage and a weekly temporal resolution (Strozzi et al., 2018; X. Zhang et al., 2019; Reinosch et al., 2020; L. Wang et al., 2020; Kääb et al., 2021). However, the availability of extensive and frequent imagery does not imply that we have all of the knowledge and tools needed to comprehensively exploit remote sensing data for geoscientific applications. To fully take advantage of InSAR technology for periglacial studies, for instance in the scope of geohazard and climate research, there is a need for studies analysing the InSAR signatures in different cold environments and relating the detected ground movement to specific processes and their drivers.

In 2017, NORCE Norwegian Research Centre AS (former Norut), in partnership with UiT The Arctic University of Norway and The University Centre in Svalbard (UNIS), started the FrostInSAR Ph.D. project funded by the Research Council of Norway. The objectives of the research project were to:

- Increase the value of satellite InSAR technology to upscale the investigation of periglacial landforms;
- Take advantage of the newly available Sentinel-1 images to cover large areas in different environments characterising the Norwegian territory;
- Exploit InSAR to investigate the spatio-temporal patterns of the ground dynamics in landscapes affected by perennially or seasonally frozen ground;
- Relate remotely measured ground movement to field-documented freeze and thaw processes and their environmental controlling factors.

More specifically, the FrostInSAR Ph.D. project aimed to answer the following Research Questions (RQs) covered by the Papers I–V of this thesis:

- **RQ1**: What is the regional variability of the magnitude and direction of ground movement driven by frost action and/or gravity, both in Svalbard (Papers I and II) and in mainland Norway (Papers III and V)?
- **RQ2**: What is the temporal behaviour of various periglacial landforms, at seasonal (Papers I and II) to decadal (Paper IV) timescales?
- **RQ3**: What explain the spatio-temporal patterns of the ground movement? How does InSAR contribute to understand the interaction between periglacial processes and their drivers (Papers I–V)?
- **RQ4**: What are the advantages and limitations of InSAR for measuring ground dynamics in periglacial environments and how can we complement it with other techniques (Papers I–V)?

1.2 Thesis content

Chapter 2 introduces the fundamentals of periglacial geomorphology, focusing on the dynamics of periglacial landforms. Chapter 3 presents the basic properties of Synthetic Aperture Radar Interferometry and their implications when applied to periglacial environments. Chapter 4 introduces the five manuscripts, forming the basis of this thesis. Chapter 5 summarises the main findings and highlights the original contribution of the author. Chapter 6 concludes and discusses the potential for future work within the field of InSAR applied to periglacial research. The papers are available in appendices.

Chapter 2

Periglacial ground dynamics

This chapter introduces the major concepts forming the basis of periglacial geomorphology. Detailed presentation of the discipline is available in e.g. French & Thorn (2006), French (2007), Harris et al. (2009), Berthling & Etzelmüller (2011) and Ballantyne (2018). The focus is placed here on the main processes controlling the seasonal to decadal ground dynamics in the Norwegian periglacial environment, both in areas with and without permafrost.

2.1 The periglacial concept

In its modern usage, periglacial landscapes refer to a range of non-glacial processes and landforms in cold-climate environments (French & Thorn, 2006; French, 2007). Periglacial geomorphology is the study of the impact of freeze and thaw processes on the ground (frost action) and their role in shaping the landscape in high-latitude and/or high-altitude regions. Periglacial geomorphology focuses on glacier-free areas. However, the interaction of glacial and non-glacial processes leads to intense scientific discussions about the overlapping and distinctive characteristics of the proglacial, paraglacial and periglа-

cial concepts (Slaymaker, 2009; Berthling et al., 2013), especially when considering the long-term climatic variations and the transitional nature of the landscapes. This debate is beyond the scope of the thesis and we consider here a large range of cryo-conditioned processes (Berthling & Etzelmüller, 2011), which lead to frost- and/or gravity-driven ground movement in the present-day Norwegian landscape. Permafrost, i.e. the ground that remains at or below 0 °C for at least two consecutive years (French, 2007), is often widespread in cold-climate environments, but periglacial geomorphology also includes the study of areas with only seasonally frozen ground. This definition may seem unnecessarily broad but reflects the reality of the natural complexity of polar and mountainous landscapes.

Four general considerations are important to keep in mind when studying periglacial ground dynamics:

1. The periglacial environment is widespread in polar, subpolar and mountainous regions, and primarily controlled by latitudinal and altitudinal climatic gradients. At the global scale, the conditions controlling frost-driven processes are highly variable (Anisimov & Nelson, 1997; T. Zhang et al., 2003; Obu et al., 2019). In Norway, maritime influence and high-relief topography complexify the periglacial zonation at the local and regional scales.

2. While permafrost is a purely thermal condition, the processes shaping periglacial landscapes are influenced by a wide range of environmental factors, such as topography, ground material, water content, vegetation and snow cover (Etzelmüller et al., 2001; Genxu et al., 2012; Gisnås et al., 2014; Schuh et al., 2017; Karjalainen et al., 2019). These variables are spatially variable on short distances. They impact the thermal transfer between the atmosphere and the ground, and consequently the response of the surface in terms of movement (Riseborough et al., 2008).

3. Even in permafrost areas, the uppermost part of the ground – the active layer – thaws in summer and refreezes in winter (Shur et al., 2005), which determines the state and distribution of water. The content of water and the type of ground ice forming in the ground largely control the ground dynamics (Thomas et al., 2009).

4. Seasonally frozen ground may lead to the development of landforms with characteristics comparable to those occurring in permafrost areas (Matsuoka et al., 1997). Cold-climate landscapes have the common denominator that they are cryo-conditioned, and characterised by a thermal regime with periodic fluctuations around 0 °C, even if occurring at variable timescales (diurnal, seasonal, annual, and multi-annual) (Berthling & Etzelmüller, 2011).

Polar and mountainous regions are usually categorised according to the extent of the frozen ground. The zonation consists of four classes: the areas where permafrost is found in 90–100% (continuous), 50–90% (discontinuous), 10–50% (sporadic) and 0–10% (isolated) of the landscape (French, 2007). In total, 20–25% of the land area of the Northern Hemisphere is underlain by permafrost (Brown et al., 2002; Obu et al., 2019), while approximately 50% is affected by seasonal frost (T. Zhang et al., 2003, 2008). For the sake of simplification, the periglacial environment is often divided into two overall geographical regions: the high-latitude or polar region, and the high-altitude or mountainous/alpine region (French & Thorn, 2006). In many cases, the rationale behind this categorisation makes geomorphologically sense. The environmental conditions and periglacial processes of the extensive Siberian or Northern Canadian lowlands are clearly different from those of the mountain ranges at lower latitudes, such as the European Alps, the Himalayas or the Andes. However, in some cases, the two domains are partly overlapping. Norway is an example of this combination, and therefore a perfect study area encompassing a large range of frost-driven ground processes (Berthling & Etzelmüller, 2011).

2.2 The Norwegian periglacial diversity

The Norwegian territory is a formidable natural research laboratory for the study of the periglacial processes. Norway has a land areal of approximately 324 000 km^2 on the mainland and 61 000 km^2 in Svalbard and Jan Mayen, and its latitude ranges from approximately 57 to 81 °N. This dramatic latitudinal gradient is combined with strong East–West climatic variations due to the temperate influence of the Atlantic ocean. Both Northern Norway and Svalbard have a complex geological and glacial history that shaped the landscape (Harland, 1997; Corner, 2005; Torsvik & Cocks, 2005; Mangerud et al., 2011). The alpine topography is characterised by a high altitudinal gradient with deep narrow fjords and high mountain peaks up to approximately 1800 m a.s.l. The combination of the latitudinal, maritime–continental and altitudinal climatic gradients impacts the distribution and characteristics of the perennially and seasonally frozen ground. This thesis includes study areas in central and western Spitsbergen, Svalbard and in Troms and Finnmark County, Northern Norway (*Figure 2.1*), to represent various environmental conditions and consider a large range of periglacial landforms.

Svalbard (Papers I and II, *Figure 2.1*) is an archipelago characterised by a polar-tundra climate, with no month with an average air temperature exceeding 10 °C (Peel et al., 2007). The climate is controlled by two oceanic influences: the West and East Spitsbergen Currents, which respectively warms the western coast and cools the eastern part of the archipelago (Harland, 1997). The study areas included in this thesis are located on Spitsbergen, the main island of the archipelago. Central and western Spitsbergen have continuous permafrost with a thickness varying from approximately 100 m in valley bottoms and coastal areas to 500 m in the mountains (Humlum et al., 2003). The active layer thickness is generally in the range of 1 to 2 m, but the amount of ground ice has high spatial variability (Christiansen et al., 2010; Cable et al., 2018; Chris-

tiansen et al., 2021). The intra- and inter-annual meteorological variability, as well as the influence of local conditions (water content, ground material, snow cover, vegetation) have a strong influence on the ground thermal regime and the dynamics of periglacial landforms (Harris et al., 2011; Christiansen et al., 2013; Schuh et al., 2017). Long-term monitoring of ground temperature and active layer thickness (ALT) indicates that the permafrost is warming and ALT increasing (Boike et al., 2018; Isaksen et al., 2019; Christiansen et al., 2021). Projections for the twenty-first century suggest similar future trends following climate change scenarios (Etzelmüller et al., 2011).

Northern Norway (Papers III, IV and V, *Figure 2.1*) is characterised by a subarctic climate with long cold winters and short cool summers (Peel et al., 2007). The region, at the interface between seasonally frozen ground and isolated to discontinuous permafrost, is characterised by highly variable ground temperature, permafrost distribution and active layer thickness (Brown et al., 2002; Gisnås et al., 2017; Obu et al., 2019, 2020). The Norwegian coast is influenced by the Nordic extension of the Gulf Stream, the North Atlantic Current, which leads to a large climatic gradient between the temperate and humid coastline and the colder and drier continental interior (Eldevik et al., 2014). Due to the general orientation of the Norwegian land–sea margin, the gradient runs NW–SE across the land area and controls the permafrost distribution. The lower elevation limit of the discontinuous permafrost zone is around 1000 m a.s.l. in coastal sites and decreases to below 400 m a.s.l. towards the interior, according to field measurements and models (Gisnås et al., 2017; Christiansen et al., 2010). Permafrost temperature is relatively high, with measured values close to or just below 0 °C. Long-term ground temperature measurements indicate that the permafrost is warming and degrading (Isaksen et al., 2007; Christiansen et al., 2010) and models project that this is likely to continue in the coming decades (Farbrot et al., 2013).

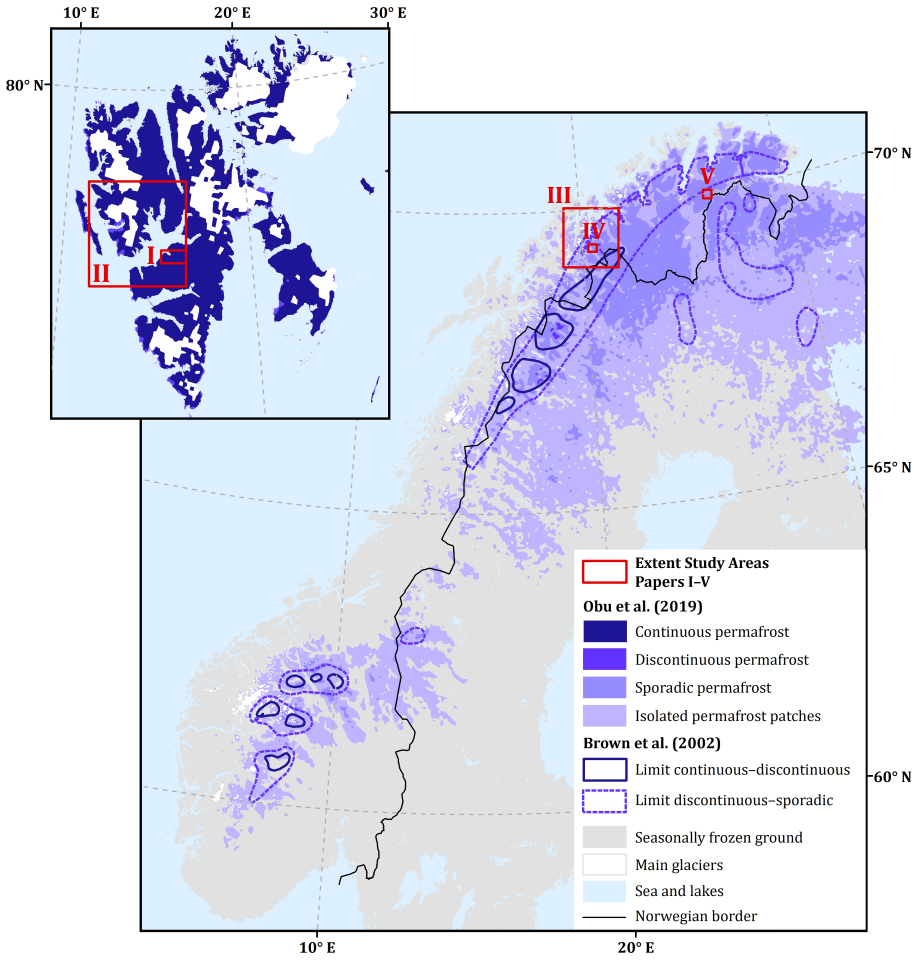

Figure 2.1: Location of the Norwegian study areas. The map of permafrost zones is based on Obu et al. (2019) and Brown et al. (2002). The two data sources show discrepancies that can be explained by the different time periods, methods and resolutions applied in the studies, but also highlight the uncertainty of the zonation. The glacier-free land in Svalbard is within the continuous permafrost zone, while mainland Norway is mostly characterised by isolated to discontinuous permafrost and seasonally frozen (permafrost-free) ground.

2.3 Periglacial landforms and ground movement

A periglacial landscape is determined by the interactions between the environmental variables influencing the system (controls), the physical processes affecting the ground (causes) and the resulting ground movement, visually expressed as landforms (effects). Climatic, topographic and geological conditions influence the distribution and temporal behaviour of periglacial processes. They control a complex net of primary and secondary environmental factors that impact the variability of the frost- and gravity-driven processes leading to ground movement and shaping distinctive landforms. The focus is placed here on changes that occur at seasonal to decadal timescales. For the sake of simplification, typical processes and landforms occurring on flat and sloping terrain are discussed separately. It is important however to realise that the interaction of multiple environmental variables can lead to an ambiguous assemblage of processes within short distances or even a combination at similar locations. The relationship between the environmental variables, the periglacial processes, the associated landforms and their movement components are summarised in *Figure 2.2*. The main landforms considered in this thesis are sketched in *Figure 2.3* and illustrated by field pictures in *Figure 2.4*.

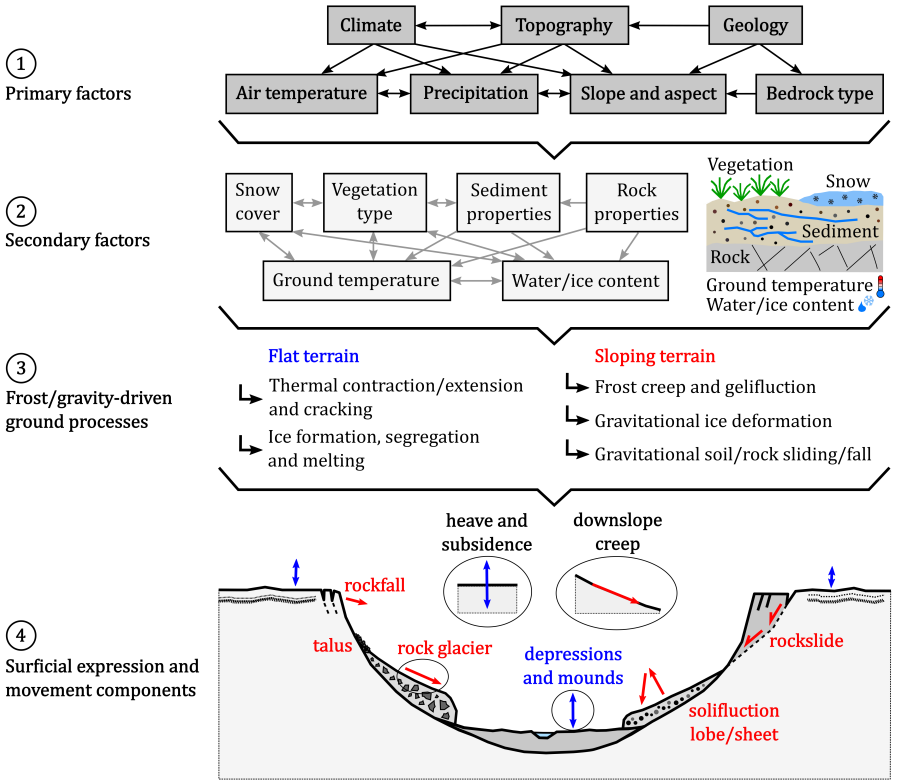

Figure 2.2: The complex net of relationships between 1) the primary climatic, topographic and geologic controlling factors; 2) the secondary environmental factors; 3) the main periglacial processes driven by the action of frost and gravity occurring in flat (blue) and sloping (red) terrain; 4) the resulting periglacial landforms and their associated movement components (arrows).

Periglacial landforms in flat terrain (Papers I, II and V)

Air temperature fluctuations below or above 0 °C transfer into the ground at variable rates and with a certain lag depending on the snow/vegetation cover and the ground properties (Riseborough et al., 2008). The progression of the freezing/thawing front into the ground can be measured using temperature data from boreholes (Paper I) or modelled based on air or surface temperature and heat flow calculations (Paper II). A simple and widely used solution to estimate the depth of freezing/thawing front is the Stefan equation (Stefan, 1891), based on the accumulated degree-days of freeze/thaw and parameters documenting the ground properties (thermal conductivity, material density, moisture content).

The seasonal variations of the ground temperature may cause ground thermal contraction and extension. In bedrock, it contributes to a fatigue of the rock mass and can lead to the development or the extension of fracture systems (Gischig et al., 2011). The purely thermal component is not negligible when considering the long-term formation of a periglacial landscape but it is the combination with hydrological effects that lead to large modifications of the ground surface in humid regions. Pure water freezes at 0 °C and expands by approximately 9% when turning into ice, either within the soil pores (in-situ freezing) or as lenses after water migration towards the freezing plane (Smith, 1985). When forming into lenses (segregation), ground ice can overcome the resistance of the overlying material, which moves the surface upwards (frost heave) (Rempel, 2007; Thomas et al., 2009). This process requires frost-susceptible ground material, i.e. a material with grain and pore sizes that can promote the water flow by capillarity and its aggregation into ice lenses. Silty sediments are typically favourable, while clay is usually too dense and gravel too coarse (Konrad & Morgenstern, 1980). In permafrost landscapes, the annual temperature cycles control the seasonal patterns of the ground displacements. Freezing of the active layer in autumn leads to ice formation that

heaves the ground surface. In spring and summer, active layer thawing causes ice melting and the ground surface consequently subsides. The annual amplitude of the cyclic displacements varies spatially depending on the ALT and its water content. It typically ranges from a few mm to several dm (Romanovsky et al., 2008; Watanabe et al., 2012).

Frost-driven processes shape distinctive landforms in flat terrain. Due to spatial variability and differential movement, frost heave and thaw subsidence can induce complex subground mixing of the soil horizons, often referred to as cryoturbation. It typically forms recognisable patterned features at the ground surface (Van Vliet-Lanoë, 1991) (*Figure 2.4, a–b*). In unconsolidated sediments, the combined effect of the thermal contradiction/extension and the ice formation contribute to shaping characteristic polygonal features called ice-wedge polygons (Christiansen, 2005). Ice segregation can also create raised landforms or frozen mounds of various sizes and geometries, such as pingos, palsas and lithalsas (Pissart, 2002). Conversely, the uneven melting of the ice forms surface depressions. In the context of climate change, ice-rich terrain affected by long-term permafrost degradation can create large topographical depressions that are referred to as thermokarst features (Kokelj & Jorgenson, 2013). For the sake of simplicity, the visual expression of differential subsidence and heave in flat terrain is here referred to as depressions and mounds.

Periglacial landforms in sloping terrain (Papers I, III, IV and V)

On periglacial slopes, the gravity is an additional driver that acts together with freeze and thaw processes. While the movement of the ground surface in flat terrain can mostly be considered as reversible due to its cyclic nature (assuming stable environmental conditions), mass wasting has a downslope component of movement that is irreversible. Depending on the ground material type, gravitational processes lead to a large diversity of landforms with distinctive movement rates, directions and temporal behaviours. Three main

landform types are studied in this thesis (*Figure 2.3, red*):

1. **Rock glaciers** (Papers I, III, IV): Rock glaciers consist of a mixture of ice, rocks and sediments. The ice-saturated mass is affected by steady-state deformation called permafrost creep (Haeberli et al., 2006). The ice can have a glacial or periglacial origin (Berthling, 2011), and the landforms are located under a rooting zone that feeds the landform with rock debris (Humlum, 2000). Rock glaciers often have a discernible lobated morphology, typically composed of a steep front, lateral margins and a ridge-and-furrow topography due to differential compressive flow (*Figure 2.4, c–d*). The annual creep rate is typically ranging from cm to m/yr, but the rock glaciers often experience strong intra-annual velocity variations with acceleration and deceleration that can exceed 50% of their annual average (Delaloye et al., 2008, 2010). The creep rate greatly depends on the topography, the characteristics of the shear horizon and the fraction of liquid water within the landform body (Ikeda et al., 2008; Cicoira et al., 2019). Rock glaciers are considered as an indicator of climate change due to increasing evidence of a relationship between their velocities and the ground temperature, influencing the ice viscosity and the liquid water content (Kääb et al., 2007). Cases of acceleration, destabilisation and even collapse of the landforms have been reported, especially in the European Alps (Delaloye et al., 2013; Bodin et al., 2017). Further permafrost degradation may lead to the progressive stabilisation of the rock glacier and the landform becomes relict when the internal ice has melted and remanent geomorphic features are not associated anymore with permafrost creep (Ikeda & Matsuoka, 2002).

2. **Solifluction lobes and sheets** (Papers I, III and V): Solifluction is a gradual process that moves fine-grained material down the slope (Matsuoka et al., 1997). Solifluction can occur both in perennially and seasonally frozen ground, and have variable characteristics depending on the depth of the

freezing/thawing front, as well as the duration and frequency of the diurnal/seasonal freeze–thaw cycles (Harris et al., 2008). It occurs on low-inclined slopes, commonly ranging from 5 to 30° (Matsuoka, 2001). Solifluction is generally classified into four categories of movement type: needle ice creep, frost creep, gelifluction and plug-like flow, mostly depending on the depth of the ice lens formation. In general, the ground movement consists of two main components: 1) diurnal or seasonal needle ice or frost creep that lifts the ground normal to the inclined surface during the freezing period and subsequently leads to a vertical settlement during the thawing periods; 2) additional downslope shear stress deformation associated to the thawing of a ground containing excess ice (Harris & Davies, 2000; Matsuoka, 2001). Solifluction includes a cyclic heave–subsidence pattern but the net annual movement is downslope. It leads to the development of lobes, when characterised by spatially differential rates, or sheets, when the movement is mostly uniform (*Figure 2.4, g–h*). The annual surface velocity is typically ranging from mm/yr to dm/yr, depending on the freeze and thaw cycles, the depth of the frost penetration, the water content and the frost-susceptibility of the ground material (Matsuoka, 2001).

3. **Rockslides** (Paper III): Unstable rock slopes are characterised by a large range of movement mechanisms, including toppling, falling or sliding (Hungr et al., 2014). For the sake of simplicity, we use the terminology rockslide here to refer to all types of large rock masses (over 100 m^3), showing signs of pre-failure deformation (e.g. backscarps, open fractures) (*Figure 2.4, e–f*). Rockslides can lead to a rock avalanche upon collapse. Rockslide research therefore has a major relevance for geohazard assessment, as a failure can directly threaten life and damage infrastructure, or secondarily generate tsunami waves in water bodies and outburst floods after river damming (Hermanns et al., 2013; Harbitz et al., 2014). Rock-

slides are not restricted to cold-climate environments and can be found in all mountainous regions. Lithological and structural properties of the rock mass are the most important internal factors pre-conditioning the rockslide geometry and dynamics (Stead & Wolter, 2015). However, permafrost and seasonal frost affect the rockslide dynamics located in periglacial environments (Blikra & Christiansen, 2014; Keuschnig et al., 2015) and a changing climate impacts their stability (Geertsema et al., 2006; Stoffel et al., 2014). Moving rock masses typically have low annual velocities (mm to dm/yr) but acceleration phases can occur in relation to external factors (e.g. rainfall, snow melting, ice formation in fractures) (Nordvik et al., 2010; Grøneng et al., 2011; Blikra & Christiansen, 2014). In complex topographies such as Norway, the variety of morphological characteristics, the multiple failure mechanisms and the interaction with other periglacial processes make the rockslide dynamics interesting to study, together with other mass wasting processes.

In addition to the three previously listed periglacial landform types, glacial features, such as debris-covered glaciers and ice-cored moraines, as well as rockfall and rock avalanche deposits (talus slopes) are also considered in Papers I and III (*Figure 2.3, blue*), to discuss the variability of the detected kinematic signatures when exploiting InSAR at the landscape scale. Other processes and landforms, such as detachment slides, mud-/debris-flows, rockfalls or debris-free glaciers, are not directly studied in this thesis but are used to discuss InSAR limitations in periglacial environments (*Figure 2.3, grey*). The spatio-temporal patterns of the ground movement associated with the landforms presented in the current section are further discussed in *Section 3.3*, when considering their consequences on InSAR measurements.

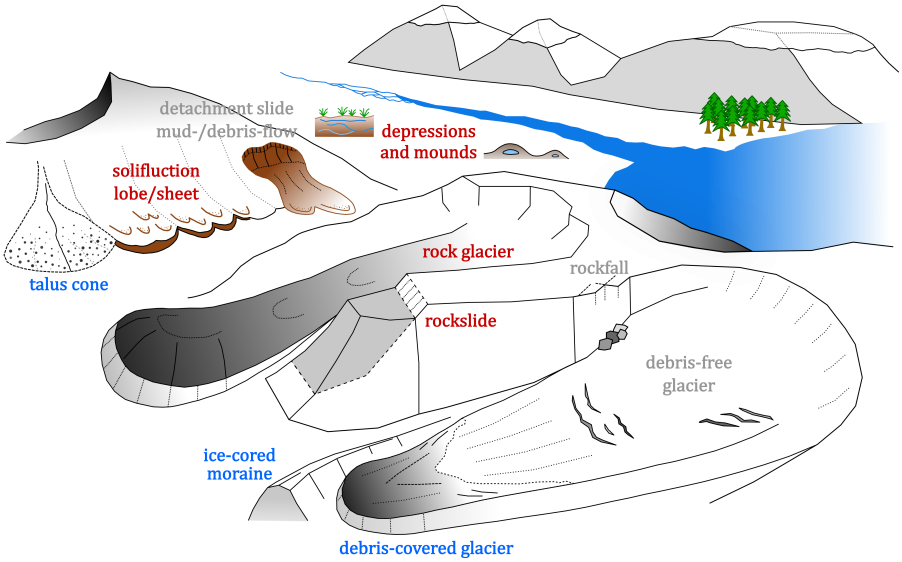

Figure 2.3: Schematic overview of a periglacial landscape and the typical landforms shaped under the action of frost and gravity. Red text corresponds to the landforms that are the main focus of the thesis. Blue text corresponds to the additional landforms that are studied in some thesis papers. Grey text corresponds to the additional landforms that are not directly studied but discussed in relation to the common InSAR limitations (*Section 3.3*).

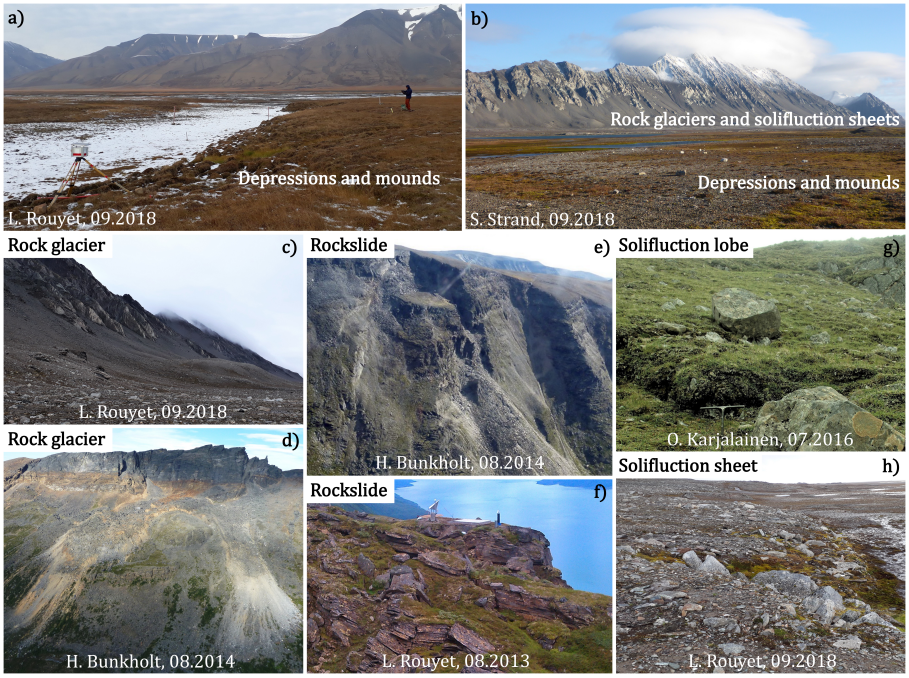

Figure 2.4: Field examples of the main landforms included in this thesis: a) sediment infilled valley bottom and mountain slopes of Adventdalen (Central Spitsbergen, Svalbard); b) raised marine beaches and mountain slopes of Kapp Linné (Western Spitsbergen, Svalbard); c) rock glacier, Kapp Linné (Western Spitsbergen, Svalbard); d) rock glacier, Ádjet (Skibotndalen, Northern Norway); e) rockslide, Gámanjunni3 (Manndalen, Northern Norway); f) rockslide, Jettan (Nordnesfjellet, Northern Norway); g) solifluction lobe, Rásttigáisa (Northern Norway); h) solifluction sheet, Kapp Linné (Western Spitsbergen, Svalbard).

Chapter 3

Synthetic Aperture Radar Interferometry

This chapter introduces the basic concepts of Synthetic Aperture Radar Interferometry (InSAR) and its application for detecting ground displacements. Detailed presentation of the method is available in e.g. Bamler & Hartl (1998), Massonnet & Feigl (1998), Rosen et al. (2000), Hanssen (2001), Woodhouse (2006), Ferretti (2014) and Caduff et al. (2015). The focus is placed here on the elements that have major significance in exploiting InSAR for the study of ground dynamics in periglacial landscapes.

3.1 Radar sensors and images

Radio detection and ranging (radar) instruments transmit electromagnetic (EM) microwave pulses and record their echoes after they have been backscattered by target objects. A radar is an active sensor that does not require sun illumination to acquire data and can therefore be used day and night. Radar systems use frequencies typically ranging from 1 to 90 GHz (wavelengths: 0.3–

30 cm). The sensors exploited in this thesis have frequencies between 5 to 30 GHz (wavelengths: 1–6 cm) (*Table 3.1*). Thanks to larger wavelengths than optical sensors, the EM waves have the ability to penetrate clouds. Radar sensors collect a complex signal that includes both an amplitude (A) and a phase (ϕ) component (*Figure 3.1, B*) (Woodhouse, 2006). The radar amplitude documents the amount of energy backscattered from the target to the antenna. The radar phase is the component that can be exploited to detect changes of the sensor-to-target distance, based on interferometry (*Section 3.2*).

Imaging radar is an application of the radar technology that exploits the motion of a sensor mounted on a terrestrial platform, an aircraft or a Earth Observation (EO) satellite to generate images of a target area. Radar images are two-dimensional (2D) arrays arranged in slant range (R, sensor-to-ground distance) and azimuth (x, cross-range distance) (*Figure 3.1, B*). The spatial resolution, i.e. the minimal distance for which a radar is able to distinguish two neighbouring objects, varies according to the sensor and is different in slant range and azimuth directions. The slant range resolution depends on the bandwidth of the transmitted pulse. The larger the bandwidth, the better the resolution. The azimuth resolution of a Real Aperture Radar (RAR) depends on the slant range and the angular beamwidth, which is proportional to the wavelength of the signal (λ) and inversely proportional to the physical length of the antenna. For a 5 cm wavelength and a distance of about 800 km (typical EO satellite orbital altitude), a metric azimuth resolution could only be reached using km-length antennas, which is obviously impossible for engineering reasons. To solve this problem, the Synthetic Aperture Radar (SAR) technology has been developed. By synthesising the effect of longer antennas using the movement of the sensor along the aircraft or satellite flying path, the azimuth resolution can be improved while still using short physical antennas (Bamler & Hartl, 1998). As a result, the azimuth resolution becomes independent to the range and reduces to approximately $L/2$, where L is the antenna

length. For terrestrial platforms located close to the target, both RAR and SAR are commonly used (Caduff et al., 2015).

The results from Paper I–V are primarily based on SAR images from Sentinel-1 (Copernicus programme) and TerraSAR-X (DLR-Airbus) satellites (*Table 3.1*). Each image covers a portion of the ground from tens to hundreds km wide, termed the scene swath. A spaceborne SAR has a side-looking geometry that leads to geometrical effects and distortions, such as shadows on steep slopes facing away from the radar (*Figure 3.1, A*). The angle between the radar beam and the surface normal is called the incidence angle (θ) (*Figure 3.1, A*) and determines the extent of these effects with respect to the angle of the imaged slope (Bamler & Hartl, 1998). The Sentinel-1 constellation and the TerraSAR-X mission operate in a sun-synchronous near-polar orbit with a revisit time of 6 days (Sentinel-1) and 11 days (TerraSAR-X). The Earth's rotation and the satellite movement lead to ascending and descending imaging geometries that provide different line-of-sight (LOS) orientations. With a right-looking sensor, a satellite crossing the equator from South to North (ascending passes) looks towards East. When crossing the equator going from North to South (descending passes), it looks towards West (*Figure 3.3*). For Paper IV, we complemented satellite SAR data with images acquired with a ground-based (terrestrial) RAR, the so-called Gamma Portable Radar Interferometer (GPRI) (Werner et al., 2008) (*Table 3.1*). GPRI provides a limited spatial coverage compared to SAR satellites and is thus designed for local-scale studies. The advantage is that the user can choose where to set up the system and thus get the most relevant observation geometry depending on the study objective (Eriksen et al., 2017a). Terrestrial radars also allow for repeated acquisitions at second to minute temporal resolution.

Table 3.1: Radar properties and effects on interferometric measurements, exemplified for the three main sensors and image modes used in the thesis. Acronyms refer to Synthetic Aperture Radar Interferometry (InSAR), Terrestrial Radar Interferometry (TRI), Interferometric Wide swath mode (IW), StripMap mode (SM) and Gamma Portable Radar Interferometer (GPRI).

Radar properties	**Effects on InSAR/TRI**	**Sentinel-1 IW**	**TerraSAR-X SM**	**GPRI**
Frequency band Radar wavelength	Detection capability (maximal velocity), coherence, atmosphere and ground penetration	C-band 5.6 cm	X-band 3.1 cm	Ku-band 1.7 cm
Highest spatial resolution (slant range x azimuth)	Detection capability (size of moving area)	$\sim$ 2–4 x 20 m	$\sim$ 1 x 3 m	$\sim$ 0.75 x 8 m *
Highest temporal resolution	Detection capability (maximal velocity)	6–12 days **	11 days	Second to minute
Observation geometry i.e. line-of-sight	Detection capability (vector orientation) and geometric effects (layover/shadow)	E–W orientation 30–45° incidence	E–W orientation 20–45° incidence	Variable, based on the chosen location and the local setting
Scene size and coverage	Operationality and study size	Thousands km^2 Global	Hundreds km^2 Regional ***	Tens km^2 Local

* At 1 km to the RAR sensor. The azimuth resolution decreases linearly with the distance. ** Both Sentinel-1 satellites have a revisit time of 12 days, providing 6 days for the constellation. *** Despite global coverage, the commercial data practically limits its use to regional applications.

3.2 Synthetic Aperture Radar Interferometry

Imaging radar interferometry is usually referred to as Synthetic Aperture Radar Interferometry (InSAR) or Terrestrial Radar Interferometry (TRI), depending on the sensor (Bamler & Hartl, 1998; Caduff et al., 2015). This thesis mostly focuses on the exploitation of satellite SAR images for regional applications. Spaceborne InSAR is therefore referred to as the primary method and used hereafter to discuss the properties of the measurements. The main principles also apply to TRI.

The radar phase

InSAR exploits the phase component of the radar images, related to the sensor-to-ground distance. Due to the sinusoidal shape of the EM wave, the distance can be expressed as a defined number of complete wave cycles with an additional fraction of a wavelength λ, corresponding to the phase (ϕ). The phase is ranging from 0 to 2π and is related to the distance (slant range R) by a linear equation (Bamler & Hartl, 1998):

$$\phi = \frac{2\pi}{\lambda} 2R = \frac{2\pi}{\lambda/2} R = \frac{4\pi}{\lambda} R \tag{3.1}$$

Where λ is the radar wavelength and R is the sensor-to-ground distance. Due to the two-way travel of the signal, the effective wavelength is $\lambda/2$.

The phase values of a single acquisition have no direct use because they consist of a superposition of echoes from multiple reflections in different parts of the pixels. However, this complex superposition is often stable in time and the phase differences between two acquisitions can therefore be exploited. By computing phase changes between acquisitions at two different times, it becomes possible to detect sensor-to-ground distance changes. The phase difference ($\Delta\phi$) can be expressed as the summation of four terms (Ferretti, 2014):

$$\Delta\phi = \underbrace{\frac{4\pi}{\lambda}\Delta R_{\mathrm{d}}}_{\Delta\phi_{\mathrm{disp}}} + \underbrace{\frac{4\pi}{\lambda}\frac{B_{\mathrm{P}}}{R\sin\theta}z}_{\Delta\phi_{\mathrm{topo}}} + \Delta\phi_{\mathrm{APS}} + \Delta\phi_{\mathrm{decorr}} \tag{3.2}$$

Where λ is the radar wavelength, z is the elevation of the target above a reference plane, B_{P} is the distance between antennas from the two acquisition times, termed the perpendicular baseline, ΔR_{d} is the sensor-to-ground distance change, R is the slant range distance, θ is the incidence angle, $\Delta\phi_{\mathrm{disp}}$ is the phase component related to the ground surface displacement projected along the radar LOS, $\Delta\phi_{\mathrm{topo}}$ is the phase component related to the topography, $\Delta\phi_{\mathrm{APS}}$ is the phase component related to the Atmospheric Phase Screen (APS) and $\Delta\phi_{\mathrm{decorr}}$ is a term encompassing other noise contributions and decorrelation sources.

To study ground displacements $\Delta\phi_{\mathrm{disp}}$, the phase contributions from the other terms of equation (3.2) have to be removed:

1. **Topographic component** $\Delta\phi_{\mathrm{topo}}$ – There is no phase contribution from topography when the sensor is at the exact same position for the two acquisitions used to calculate the phase difference. This is typically the case for a terrestrial radar, but with spaceborne SAR, small variations in the satellite orbit lead to a spatial baseline (*Figure 3.1, A*), resulting in a topographic contribution. The mitigation of this phase component can be done by using an external Digital Elevation Model (DEM) covering the area of interest (Rosen et al., 2000).

2. **Atmospheric component** $\Delta\phi_{\mathrm{APS}}$ – The spatio-temporal variability of the atmospheric refractive index causes a phase propagation delay. The so-called Atmospheric Phase Screen (APS) is mostly due to 1) turbulent mixing processes in the troposphere; 2) tropospheric stratified atmosphere related to the local topography; 3) differential interaction of the signal with free electrons in the ionosphere (Hanssen, 2001). When InSAR is based on

spaceborne SAR sensors with several days or weeks of revisit time, the atmospheric component is usually temporally uncorrelated, which provides filtering solutions through multi-temporal techniques.

3. **Decorrelation sources** $\Delta\phi_{\mathrm{decorr}}$ – A measure of the interferometric phase quality is the coherence, i.e. the complex correlation coefficient between the two SAR images (Bamler & Hartl, 1998). The coherence is affected by changes in the positions of individual scatterers within the resolution cell due to thermal, geometrical and temporal effects, referred to as decorrelation sources (Zebker & Villasenor, 1992). The thermal decorrelation is related to the sensor signal-to-noise ratio. The geometrical decorrelation depends on the difference in viewing geometry between the two acquisitions. Nowadays, this effect tends to be reduced due to the small orbital tube applied in most modern satellite missions. Temporal decorrelation occurs due to changes in the geometrical or electrical properties of the surface between the two acquisitions, e.g. caused by moving parts of the vegetation, surface water, snow or large movements. Temporal decorrelation is a major limitation of InSAR for the detection of ground displacements, especially when applied to highly dynamic natural environments. It requires important processing steps to filter out decorrelated image pairs, for instance in periods affected by snow, and to mask out pixels with low coherence, such as forested areas.

Single interferogram approach

The calculation of the phase differences for all pixels of a pair of radar images acquired at different times leads to the generation of an interferogram. Assuming that the previously listed unwanted phase components have been removed, an interferogram documents the spatial distribution of the ground surface displacements $\Delta\phi_{\mathrm{disp}}$ along the radar LOS (*Figure 3.1, A*) for a specific time interval referred to as the temporal baseline (*Figure 3.1, B*).

An initial interferogram is wrapped, highlighting a succession of patterns called fringes (*Figure 3.1, C*). The interferogram values are expressed in modulo-2π (-π to +π) corresponding to the effective wavelength $\lambda/2$. To convert the cyclic phase differences $\Delta\phi_{\mathrm{w}}$ to absolute phase differences $\Delta\phi_{\mathrm{uw}}$ and then continuous distance changes ΔR_{d}, a procedure called unwrapping is required (Goldstein et al., 1988) (*Figure 3.1, D*). The phase differences are spatially integrated, assuming that the displacement field has a spatial continuity (Chen & Zebker, 2002). The resulting unwrapped product documents one-dimensional (1D) displacements along the LOS, spatially relative to a chosen location. A reference point (P_{Ref}, *Figure 3.1, D*) is selected in an area assumed to be stable or with a known displacement rate.

The expected displacement rate in the study area determines the choice of the temporal baselines used to compute the image pair. The interferometric SAR signal becomes aliased when the displacement gradient between adjacent pixels is higher than a quarter of the wavelength ($\lambda/4$) during the selected time interval. For a wavelength of 5.6 cm, such as for Sentinel-1, the theoretical detection limit is therefore 1.4 cm in 6 days. For documenting a landform moving at a rate of 1 cm per week, only 6-day interferograms can reliably be exploited. Annual pairs can be used for a landform with a low velocity (approximately up to 1 cm/year). Longer radar wavelengths and/or shorter time intervals between the selected images increase the maximum detectable velocity, but also reduce the sensitivity to small displacement.

Multi-temporal InSAR

To robustly mitigate the unwanted phase components, especially the atmospheric effects and the temporal decorrelation sources, multi-temporal (MT) InSAR techniques were developed in recent decades. MT InSAR uses a set of connected interferograms that allows for exploiting the different statistical properties of each phase component over time and takes advantage of

the temporal redundancy of overlapping interferograms to improve the measurement accuracy. MT InSAR allows for retrieving time series, expressed as cumulative displacements relative to a specific time, typically the first acquisition of the dataset.

MT InSAR methods are usually divided into two main groups referring to the expected scattering mechanisms dominating the pixels under study:

1. Methods based on locating Persistent Scatterers (PS) are referred to as Persistent Scatterer Interferometry (PSI) (Ferretti et al., 2001). A PS is a coherent point-like target that dominates the scattering from the resolution cell. PSI uses a stack of interferograms to analyse the temporal phase evolution of individual scatterers. The PS network consists of pixels that show stable amplitude and phase statistics over long time periods, typically a corner of a human-made structure in an urban area or a rock formation in a natural environment.

2. Methods based on spatial correlation and Distributed Scattering (DS) are referred to as Stacking (Sandwell & Price, 1998) and Small Baseline Subset (SBAS) (Berardino et al., 2002). DS consists of the coherent summation of many small scatterers within a resolution cell. In DS InSAR, a complex spatial averaging procedure, termed multi-looking, is applied at the beginning of the processing chain. It decreases the spatial resolution of the results but improves the signal quality. To reduce geometric and temporal decorrelation, the interferograms are selected with spatial and temporal baselines below chosen thresholds.

In this thesis, we primarily applied DS methods (Stacking and SBAS). In Papers III and V, the initial DS datasets were also compared or complemented with PSI results made available by the InSAR Norway Ground Motion Mapping Service (Dehls et al., 2019).

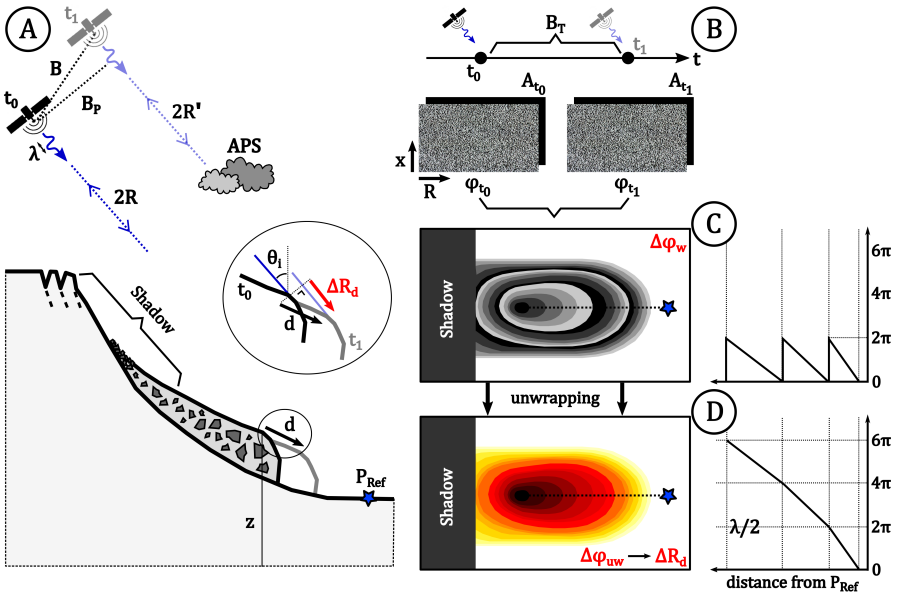

Figure 3.1: Example of SAR geometry (A) and InSAR main processing steps to measure the creep rate of a rock glacier along the radar line-of-sight (LOS) (B–D). Symbols are further explained in *Section 2.2* in relation to the equation (3.2). They refer to the image acquisition times (t_0 and t_1), the spatial baseline (B), the perpendicular baseline (B_P), the radar wavelength (λ), the atmospheric phase screen (APS), the slant range or sensor-to-ground distance (R), the azimuth or cross-range distance (x), the sensor-to-ground distance change (ΔR_d), the ground surface displacement (d), the incidence angle (θ), the elevation of the target above a reference plane (z), the reference point (P_Ref), the temporal baseline (B_T), the amplitude (A), the phase (ϕ), the wrapped phase difference ($\Delta\phi_\mathrm{w}$) and the unwrapped phase difference ($\Delta\phi_\mathrm{uw}$).

3.3 InSAR in periglacial landscapes

The theoretical properties of InSAR presented in *Section 3.1* and *Section 3.2* have several practical implications when applied to the Norwegian periglacial landscapes. Various advantages must first be underlined:

- Satellite InSAR allows for the investigation of ground dynamics in remote and hard-to-access areas, with unrivalled resolution and coverage. It allows for documenting movement with a centimetre to millimetre accuracy, valuable for the study of fine-scale frost-driven processes.

- The radar independency to sun illumination and insensitivity to cloud coverage is especially suitable for high-latitude areas with highly variable meteorological conditions, for instance due to polar nights and unstable weather.

- One typical InSAR limitation in temperate regions is the dense vegetation that causes phase decorrelation. In that respect, the small extent of the forests and the sparse vegetation characterising subarctic, arctic and mountainous environments generally provide favourable conditions.

- The diversity of currently available sensors and platforms provides a large range of detection capabilities, resolutions and geometries that allows for documenting landforms with various displacement rates, sizes and movement direction. For local studies, terrestrial platforms advantageously complement satellite InSAR by providing high temporal sampling, possibly higher spatial resolution and adjustable LOS depending on the chosen device location in respect to the target.

However, several limitations must be kept in mind when exploiting InSAR for applications in cold-climate and mountainous terrain. They are schematically summarised in *Figure 3.2* and briefly described here:

1. **Remaining atmospheric effects** (*Figure 3.2, light blue*): Atmospheric effects are considered as the main error source for most InSAR applications. Despite the processing strategies to mitigate the APS (*Section 3.2*), an uncorrected component can still affect the final results, especially when the processing includes a small stack of interferograms. Errors associated with an uncorrected atmospheric component tend to increase with the distance in respect to the reference point and thus affect large areas significantly more than local studies (Emardson et al., 2003).

2. **Moisture, snow and vegetation** (*Figure 3.2, dark blue*): Wet snow typically leads to decorrelated surfaces and reduces the possible coverage (due to perennial snow) and duration (due to the winter season) of InSAR measurements. Similarly, the ground displacement estimation on very moist surfaces is often impossible, which typically prevents the complete documentation of flooded valley bottoms during the thawing seasons (*Figure 3.2, c*), or slopes affected by wet mass wasting processes (e.g. debris-flows, mud-flows). In addition, despite the use of coherence thresholds to filter out areas affected by decorrelation, the effect of scattering mechanisms in coherent areas must be considered, as the differential propagation of the electromagnetic wave due to changing dielectric properties of the ground may lead to systematically biased phase estimates. This can occurs due to snow (Antonova et al., 2016), ground moisture (Zwieback et al., 2015) or vegetation (Zwieback & Hajnsek, 2014). With distributed scattering methods, this issue can be exacerbated when applying low multi-looking factors that tend to overestimate the coherence and thus lead to a filtering that fails to remove unreliable pixels (Bamler & Hartl, 1998).

3. **Fast-moving landforms** (*Figure 3.2, red*): Due to the centimetric wavelength of the radar sensors used in this thesis and the cyclic nature of the phase measurements, spaceborne InSAR is not adapted to very fast landforms (typically m/yr or higher). The main limitation is related to

the repeat-pass of the satellites that typically provide a weekly sampling (*Table 3.1*). If a sudden and large change of the target position occurs between two acquisitions (e.g. due to rockfall or detachment slide, *Figure 3.2, a*), a drop in the coherence is detected but InSAR may be unable to document the movement rate. Similar problems occur for gradual processes if they are too fast (e.g. glacier flow or rock glacier creep). For a 5.6 cm wavelength and a 6-day temporal baseline (Sentinel-1), the decorrelation limit is 170 cm/yr ($\lambda/2$), but aliasing between neighbouring pixels can occur when the velocity exceeds 85 cm/yr ($\lambda/4$).

4. **Shadow, layover and N–S slopes** (*Figure 3.2, grey*): The side-looking geometry of a spaceborne radar creates geometric effects and distortions in mountainous regions. Foreshortening appears on slopes facing the radar, resulting in compressed pixels on the ground. In extreme cases, pixels are affected by a so-called layover effect when the mountain top is closer to the radar than the footslope. These areas show an ambiguous mix of contributions from different locations and have to be masked out during the processing. On the other side of the mountain, shadow occurs in the area not being illuminated by the radar (*Figure 3.1, A*). In addition, the view angle with respect to the orientation of the imaged surface and the expected direction of the true displacement vector can have severe implications on the detection capability. Radar sensors are blind to any movement orthogonal to the LOS. Based on SAR satellites with E–W LOS, a N–S horizontal movement remains mostly undetected. For landforms combining a N–S horizontal and a vertical component, some movement is detected but the rate is underestimated.

Both advantages and limitations have practical consequences in the way InSAR can be exploited for periglacial applications. In the following, the spatial and temporal implications of the measurements are discussed separately.

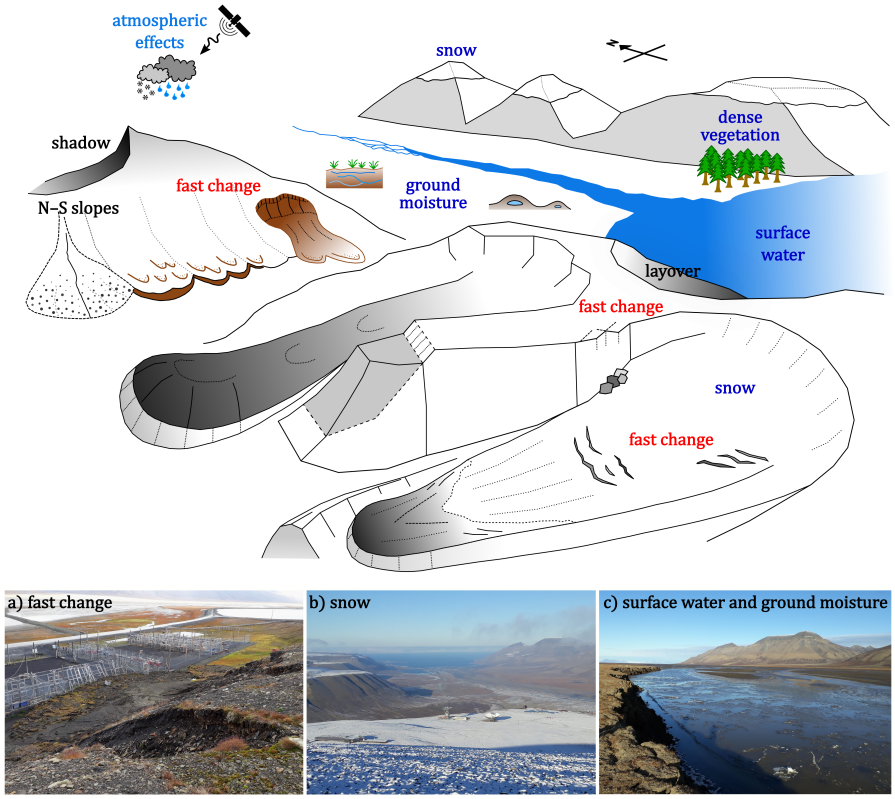

Figure 3.2: Schematic overview of a periglacial landscape (similar to *Figure 2.3*), with focus on the main limitations that reduce the InSAR coverage or the reliability of the measurements. Light blue text illustrates the remaining uncorrected atmospheric effects. Dark blue text illustrates the main sources of decorrelation and phase bias. Red text shows areas affected by fast change that may lead to decorrelation or phase aliasing. Black text shows areas affected by shadow, layover and movement underestimation, due to the side-looking geometry of satellite SAR and line-of-sight (LOS) measurements. Field pictures from central Spitsbergen, Svalbard: a) 2017 detachment slide in Longyearbyen; b) snow-covered Breinosa mountain top and view over the snow-free valley bottom in September 2019; c) flooded Adventdalen bottom in September 2019.

Spatial implications of InSAR measurements

The final outputs of an InSAR processing line are typically presented as displacement maps over the area of interest. They document averaged velocities or specific displacement values between two defined acquisition times. Especially in a highly dynamic environment, it is important to stress that all values are spatially relative to the reference point. In areas where in-situ measurements are often not available or not directly comparable to remotely sensed information, an area assumed to be stable is often chosen. The selection can be challenging as several superficial processes may affect the ground stability even in areas without any clear visual signs of movement. If the chosen location is actually moving, all results are affected by a systematic shift of displacement rates.

Without any further transformation, the 1D measurements correspond to an increase or decrease of distance along the LOS. Any displacement orthogonal to the LOS remains undetectable. However, the overlap of datasets acquired with different view angles allows for covering both East- and West-facing slopes (Paper III). By combining satellite and/or terrestrial radar geometries with complementary observation views, it becomes possible to partially or fully reconstruct the true vector (Eriksen et al., 2017a, 2017b). Two-dimensional (2D) information can be retrieved and the horizontal and vertical components decomposed to document the movement direction of different landform types (Papers I and v) (*Figure 3.3*). Alternatively, theoretical knowledge can be used to estimate the results along a relevant direction assumed to represent the true vector when focusing on one specific process, e.g. vertically for thaw subsidence and frost heave (Paper II) or downslope for creeping landforms (Paper IV).

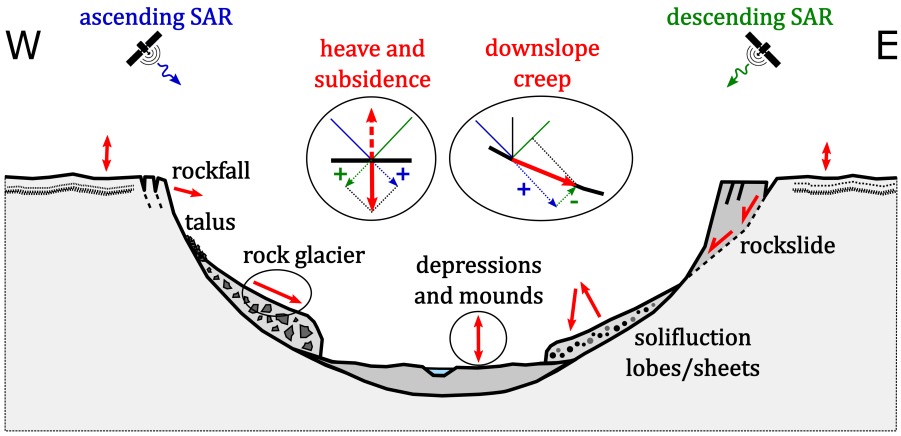

Figure 3.3: Spatial variability of the ground dynamics for an ideal example of a N–S oriented valley. The expected displacement directions of typical periglacial landforms are shown with red arrows. Detected line-of-sight measurements from ascending and descending geometries are shown with blue and green arrows, respectively. In the E–W plane, both SAR geometries can be combined to estimate the 2D displacement vector.

Temporal implications of InSAR measurements

When applying MT techniques, displacement time series can be computed to study the temporal behaviour of landforms (Papers I, II and IV). In cold and wet environments, InSAR time series are discontinuous due to snow cover during the winter seasons. The analysis requires to focus on selected snow-free periods, or to include interferograms with annual temporal baselines to connect two consecutive seasons. The second alternative is only possible when the annual displacement rate of the landforms under study is excepted to be under the maximal detection limit (Paper V). In Norwegian periglacial landscapes, the observation window is practically reduced to three to six months per year depending on the considered area and period (*Figure 3.4*). Spatially and temporally variable coherence levels makes it challenging to select reliable interferograms and pixels based on coherence information. Even if the snow

is absent in most of the landscape during the summer, high mountains can be snow-covered for a longer period (*Figure 3.2, b*), which leads to disconnected patches of reliable pixels that may cause errors during the conversion from cyclic to absolute phase differences (unwrapping) (Lauknes et al., 2010b).

To visualise MT InSAR displacements on a map and discuss their distribution, the results are often averaged over a chosen period (Papers I, III and V). For this purpose, it is essential to consider the expected temporal pattern of the target. As discussed in *Section 2.3*, the temporal behaviour is highly variable depending on the analysed landform (*Section 2.3*). In the case of flat terrain affected by seasonal heave and subsidence (*Figure 3.4, a*), seasonal displacement amplitude can be up to several cm–dm but may lead to a net annual movement close to zero if the pattern is fully cyclic. In that case, a mean annual velocity has little relevance if the study focuses on the seasonal cycles. The maximal seasonal displacement and its timing can instead be extracted and mapped (Paper II). On slopes, creeping landforms such as rock glaciers are experiencing large accelerations in summer (*Figure 3.4, b*) (Delaloye et al., 2010), which may lead to an overestimation of the annual velocities when exploiting snow-free images. This limitation must be acknowledged when documenting the overall magnitude order of the landform creep rate.

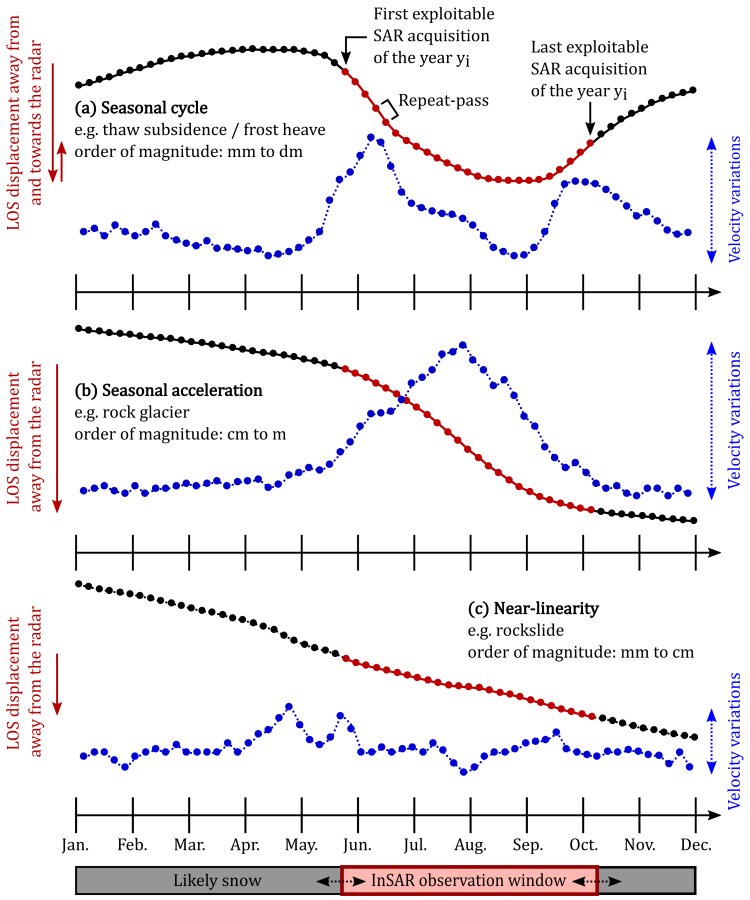

Figure 3.4: Temporal behaviour of the ground dynamics in periglacial landscapes and InSAR measurements illustrated with synthetic displacement time series with a 6-day temporal sampling (Sentinel-1). Cumulative displacements are shown in black and red. Velocity variations are shown in blue. The duration and timing of the snow-free period varies from year to year and according to the location, but is typically between June and October in Northern Norway and Svalbard. The snow-free period determines the InSAR observation window (red lines and bar).

The need for complementary measurements

All remotely sensed measurements indirectly documenting ground surface parameters require the use of complementary datasets. Due to the previously discussed drawbacks of the technique, InSAR can not be considered as standalone when applied to periglacial applications. One specific dataset always needs to be compared or combined with complementary information, to directly validate the measurements or indirectly assess their consistency, and complement the results when major limitations are identified. This is typically done through three main approaches:

1. When in-situ measurements documenting ground displacements are available, such as those based on Differential Global Navigation Satellite System (dGNSS), the results can be directly compared to evaluate their reliability (Paper III);

2. When other remote sensing datasets are available, the results can be cross-validated or combined using complementary sensors/platforms (Papers I and IV) or processing techniques (Papers III, IV and V);

3. When other indirectly related properties are documented, for instance ground temperature (Papers I and II), geomorphological maps and inventories (Paper I and III) or field observations (Papers IV and V), they can be used to assess the consistency and relevance of the final results.

For each of these approaches, the fundamental differences of measurement properties in terms of resolution, dimensionality and time period must always be kept in mind and discussed in the analysis.

Chapter 4

Thesis papers

Chapter 4 briefly introduces the five manuscripts, forming the basis of this thesis. The research scope, data and methods are summarised in *Tables 4.1, 4.2 and 4.3*. Author contributions are shown in *Table 4.4*.

4.1 Paper I

Rouyet, L. Lauknes, T. R., Christiansen, H. H., Strand, S. M. and Larsen, Y. 2019. **Seasonal dynamics of a permafrost landscape, Adventdalen, Svalbard, investigated by InSAR**. *Remote Sensing of Environment*, *231*, 111236. `https://doi.org/10.1016/j.rse.2019.111236`.

Paper I studies InSAR-based ground movement in an approximately 300 km^2 study area centered around Adventdalen, in the central part of Nordenskiöld Land, Spitsbergen, Svalbard. The region is characterised by a landscape that combines high-relief and lowlands, and encompasses a large variety of periglacial processes leading to a highly dynamic ground surface. We processed TerraSAR-X StripMap Mode (2009–2017) and Sentinel-1 Interferometric Wide Swath Mode (2015–2017) SAR images using multi-annual Stack-

ing and seasonal Small Baseline Subset (SBAS) InSAR. We analysed the spatial variability of the ground dynamics based on decomposed vertical and E–W horizontal displacement rates from multi-geometry TerraSAR-X Stacking and compared the results to a simplified geomorphological map. Continuous SBAS time series from Sentinel-1 in June–December 2017 were compared with ground temperatures measured in the active layer.

We show that InSAR results from both sensors highlight consistent seasonal displacement patterns (a summer rate of cm–dm). In the flat valley bottoms, thaw subsidence is detected and the magnitude varies depending on the water availability and frost-susceptibility of the sediments. On valley slopes, downslope displacements combining vertical and horizontal components are detected and their magnitude varies depending on the involved creep process. Based on seasonal time series, we identify ground displacement variations related to active layer thawing and freezing over flat or low-inclined slopes, where the seasonal change from subsidence to heave dominates the displacement pattern. We show that the timing of the thaw subsidence and heave matches the ground thawing and freezing periods measured in two boreholes. The results suggest that the temporal behaviour of the ground surface is primarily controlled by the thermal response of the active layer to atmospheric forcing, highlighting novel ways to investigate ground surface dynamics in permafrost landscapes.

4.2 Paper II

Rouyet, L., Liu, L., Strand, S. M., Christiansen, H. H., Larsen, Y., Lauknes, T. R. **Seasonal InSAR displacements documenting the active layer freeze and thaw progression in central–western Spitsbergen, Svalbard**. Submitted to *Remote Sensing*.

Dataset: `https://doi.org/10.5281/zenodo.4775398`

The findings from Paper I highlighted that InSAR can be exploited to infer the thermal dynamics of the active layer. In Paper II, we investigate the potential of using seasonal SBAS time series to map the timing of the subsidence maxima and use this as a proxy of the maximal active layer thawing. We processed Sentinel-1 images between June 22 and November 25, 2017 for three study areas in central and western Spitsbergen: Adventdalen, Kapp Linné and Ny-Ålesund. The study focuses on flat terrain that undergoes thaw subsidence and frost heave. We propose a methodology to identify the subsidence maxima of the time series and its Day of Year (DOY), and analyse the variability of the observed displacement patterns between and within the study areas. The measured time series are compared with a normalized and rescaled composite index model based on the Stefan equation using air and ground surface temperature records from weather stations and boreholes in the three study areas.

Clear seasonal cyclic patterns are identified in all study areas, but the amplitude, timing and progression of the displacements vary. We show that the subsidence maxima occurred considerably later on the warm and wet western coast (Kapp Linné and Ny-Ålesund) compared to the colder and drier interior (Adventdalen). The composite index model based on ground surface temperature is generally able to explain the vertical variations. In Adventdalen, the model matches the SBAS time series extracted at the location of the borehole. In Kapp Linné and Ny-Ålesund, larger deviations are found at pixel-scale, but kilometric or regional averaging allows for improving the fit. The contrasting results for the different areas are used to discuss the advantages and limitations of the proposed method and applied model. The study highlights the potential for future development of dedicated InSAR products able to depict the cyclicity of displacements in flat periglacial terrain with permafrost, to identify the timing of the maximal subsidence and to exploit the results to indirectly document the active layer thermal dynamics at both the local and regional scale.

4.3 Paper III

Rouyet, L., Lilleøren, K. S., Böhme M., Vick, L., Etzelmüller, B., Delaloye, R., Larsen, Y., Lauknes, T. R., Blikra, L. H. **Regional InSAR inventory of slope movement in Northern Norway**. Under review in *Frontiers in Earth Science: Cryospheric Sciences*.

Dataset: `https://doi.pangaea.de/10.1594/PANGAEA.930856`

Paper III studies the slope processes of the Lyngen–Kåfjord mountainous region in Troms and Finnmark county, Northern Norway. We developed semi-quantitative classified InSAR products to summarise kinematic information within the 7500 km^2 study area and relate moving areas to several periglacial processes. We applied a multiple temporal baseline InSAR Stacking procedure based on 2015–2019 ascending and descending Sentinel-1 images to take advantage of a large set of interferograms and exploit different detection capabilities. Moving areas were classified according to six velocity brackets (<0.3, 0.3–1, 1–3, 3–10, 10-30, >30 cm/yr) and related to six landform types (rock glaciers, rockslides, glaciers/moraines, talus/scree deposits, solifluction/cryoturbation and composite landforms), based on visual interpretation of optical imagery. We complemented the velocity classes with three additional layers emphasizing typical InSAR limitations in mountainous environments and allowing for differentiating the areas where there is no or little movement, areas with no data and those where the available information must be treated carefully.

The kinematic inventory shows that the velocity ranges and distribution of the different types of slope processes vary greatly within the study area. The InSAR products are used to update existing rock glacier (RG) and rockslide (RS) inventories. Landform delineations are refined, and newly detected landforms (54 RG and 20 RS) are incorporated into the databases. A kinematic attribute documenting the magnitude order of the ground velocity is assigned to the inventoried landforms. The InSAR results are compared with dGNSS

velocities from the network of monitored RS and we show that for 15 out of 17 comparable landforms, the kinematics are similarly categorised. The new inventories consist of 414 RG units within 340 single- or multi-unit(s) systems and 117 RS. Topo-climatic variables influence the spatial distribution of the RG. Their mean elevation increases toward the continental interior with a dominance of relict landforms close to the land-sea margin and an increasing occurrence of active landforms further inland. Both RG and RS are mostly located on west-facing slopes, in areas characterised by strongly foliated rocks, which suggests the influence of geological preconditioning factors. The study emphasises the complementarity of kinematic and morphological approaches for the inventory of slope processes and shows the value of simplifying complex InSAR datasets for geoscientific exploitation in periglacial environments.

4.4 Paper IV

Eriksen, H. Ø., Rouyet, L., Lauknes, T. R., Berthling, I., Isaksen, K., Hindberg, H., Larsen, Y., Corner, G. D. 2018. **Recent Acceleration of a Rock Glacier Complex, Ádjet, Norway, Documented by 62 Years of Remote Sensing Observations**. *Geophysical Research Letters*, *45*(16), 8314–8323. `https://doi.org/10.1029/2018GL077605`.

In the similar region as Paper III, a local study has been performed to document the spatio-temporal kinematic changes of a fast-moving rock glacier complex. Paper IV focuses on two destabilised lobes, located on the southwest-facing slope of Ádjet mountain in the Skibotn valley. The main lobe has an elevation ranging from 690 to 1080 m a.s.l, close to the regional altitudinal limit of mountain permafrost (600–800 m a.s.l.). We combined displacement data from front and feature tracking (FT) based on orthorectified aerial optical images, TerraSAR-X (TSX) InSAR Stacking based on 11 days interferometric pairs, TSX offset-tracking (OT), and Terrestrial Radar Interferometry (TRI)

based on Gamma Portable Radar Interferometer (GPRI) images. The integration of these remote sensing methods allow for spanning 62 years of observation (1954–2016). We show that TSX InSAR fails to document the main lobes due to velocity exceeding the detection limit of the sensor/technique, but OT and TRI allow to overcome this limitation.

We show that the rock glacier velocity has increased since 1954 and a significant acceleration is documented over the last ten years. Average annual horizontal velocity measured by FT increased from 0.5 m/yr (1954–1977) to 3.6 m/yr (2006–2014). TSX OT shows that the averaged velocity recently increased from 4.9 to 9.8 m/yr (2009-–2016), with maximum values from 12 to 69 m/yr. The kinematic analysis reveals different spatio-temporal trends in the upper and the lower parts of the rock glacier complex, suggesting irregular overloading in the upper part and progressive detachment of the faster front. Temperature, precipitation and snow depth data indicate that the climate has changed during the considered period. Mean annual air temperature (MAAT) increased by 1.8 °C in 62 years and by 0.91 °C when comparing the averaged values of the first and second half of the period. The annual precipitation and the snow depth increased by 330 mm (55 %) and 58 cm (56 %), respectively. The comparison of the displacement time series against topo-climatic data suggests that local topography, permafrost warming and increased water access to internal shear zones are causing the rock glacier acceleration. The work shows the need for combining several remote sensing sensors and processing techniques to document the kinematic behaviour of destabilised permafrost landforms over long time periods.

4.5 Paper V

Rouyet, L., Karjalainen, O., Niittynen, P., Aalto, J., Luoto, M., Lauknes, T. R., Larsen, Y., Hjort, J. **Environmental Controls of InSAR-based Periglacial Ground Dynamics in a Sub-Arctic Landscape**. Under review in *Journal of Geophysical Research: Earth Surface*.

Dataset: `http://doi.org/10.5281/zenodo.4173256`

Paper V analyses the distribution of InSAR-based ground movement in a 148 km^2 study area centred around the Geaidnogáisá and Rásttigáisá mountains in Troms and Finnmark, Northern Norway. We used multi-geometry Sentinel-1 InSAR to map the E–W horizontal and vertical components of the mean annual ground velocity. Statistical modelling primarily based on a generalized boosting method (GBM) was employed to examine the environmental controls of the periglacial ground velocity. To characterise the climatic, geomorphic, hydrological and biological conditions within the area, we compiled a set of seven explanatory variables documenting the distribution of the mean annual air temperature (MAAT), the snow cover duration (SCD), the slope angle, the percent of peat and boulder fields cover, the topographic wetness index (TWI) and the normalized difference vegetation index (NDVI).

Two-dimensional (2D) InSAR results document low mean annual ground velocities with a magnitude in the order of mm/yr to cm/yr and values up to 15 mm/yr. Vertical and horizontal velocity components in the E–W plane show variable spatial distribution over flat and sloping terrain. The statistical models have contrasted model performance depending on the velocity component used as a response variable (R^2 between 0.24 and 0.47). The slope angle and MAAT variables are the most important environmental factors explaining the distribution of the InSAR velocity. NDVI and SCD variables also have a notable contribution, interpreted as indicators of the ground material and moisture conditions. The relative importance of the environmental factors varies

for the two components of the 2D velocity. The vertical velocity is mostly influenced by the air temperature and the vegetation, while the main variable controlling the variability of the horizontal component is the slope angle, followed by the air temperature and the snow cover. These results are attributed to the characteristics of cryoturbation and solifluction processes, operating differently over flat areas and slopes. The study discusses the potential and limitations of coupling InSAR and explanatory statistical modelling for a better understanding of the environmental factors controlling periglacial ground dynamics at the regional scale and suggests ideas for further research.

Table 4.1: Research topics and studied processes/landforms of the thesis papers.

Paper	Processes/Landforms	Main research scope	Spatial focus	Time frame
Paper I	Frost heave and thaw subsidence, solifluction, rock glacier	Spatial variability; temporal behaviour	Flat and sloping terrain; regional study	Seasonal series; multi-seasonal average
Paper II	Frost heave and thaw subsidence	Temporal behaviour; spatial variability	Flat terrain; regional study	Seasonal series
Paper III	Rock glacier, rockslide, solifluction	Spatial variability	Sloping terrain; regional study	Multi-seasonal average
Paper IV	Rock glacier	Temporal behaviour; spatial variability	Sloping terrain; local study	Seasonal average; decadal series
Paper V	Solifluction and cryoturbation	Spatial variability	Flat and sloping terrain; regional study	Multi-annual average

Table 4.2: Geographical locations and periglacial contexts of the thesis papers.

Paper	Location	Geographical context	Permafrost extent
Paper I	Svalbard	Lowland and mountain	Continuous
Paper II	Svalbard	Lowland	Continuous
Paper III	Northern Norway	Mountain	Isolated to discontinuous
Paper IV	Northern Norway	Mountain	Isolated to discontinuous
Paper V	Northern Norway	Mountain	Isolated to discontinuous

Table 4.3: Radar sensors, applied processing methods and complementary datasets of the thesis papers. Acronyms refer to Sentinel-1 (S1), TerraSAR-X (TSX), Gamma Portable Radar Interferometer (GPRI), Synthetic Aperture Radar Interferometry (InSAR), Small Baseline Subset (SBAS), Terrestrial Radar Interferometry (TRI), Offset Tracking (OT), Feature Tracking (FT), Digital Elevation Model (DEM), differential Global Navigation Satellite System (dGNSS), Persistent Scatterer Interferometry (PSI), Mean Annual Air Temperature (MAAT), Snow Cover Duration (SCD), Normalized Difference Vegetation Index (NDVI) and Topographic Wetness Index (TWI).

Paper	Radar sensors	Main processing methods	Complementary datasets
Paper I	S1, TSX	InSAR Stacking, SBAS	Geomorphological map, DEM, ground temperature, optical imagery
Paper II	S1	InSAR SBAS	Air and ground surface temperature, DEM, optical imagery
Paper III	S1	InSAR Stacking	dGNSS, PSI maps, DEM, geological map, optical imagery
Paper IV	TSX, GPRI	OT, InSAR Stacking, TRI	Optical FT, DEM, air temperature, precipitation, snow depth
Paper V	S1	InSAR SBAS	DEM, MAAT, SCD, NDVI, TWI, landcover map, optical imagery, field-based activity rating

Table 4.4: Author contributions of the thesis papers

Contributions	Paper I	Paper II	Paper III	Paper IV	Paper V
Conceptualisation	**LR**, TRL	**LR**, **LL**	**LR**, RD, LHB	**HØE**, **TRL**	**LR**, **JH**, OK
Funding and administration	**LR**, TRL	**LR**, TRL	**LR**, RD, TRL	**TRL**, HØE	**LR**, JH, TRL
Methodology and software	**LR**, TRL, YL	**LR**, **LL**, TRL, YL	**LR**, RD TRL, YL	**HØE**, **TRL**, HH, YL, LR	**LR**, **OK** TRL, YL
Data gathering and processing	**LR**, HHC, SMS, TRL	**LR**, SMS, HHC, TRL	**LR**, KSL, MB, YL	**HØE**, TRL, LR, HH	**LR**, **OK**, PN, JA, YL
Results visualisation and interpretation	**LR**, HHC, SMS, TRL	**LR**, LL, SMS, HHC	**LR**, KSL, MB, LV, BE, RD, LHB	**HØE**, **LR** IB, KI, GDC	**LR**, **OK**, PN, JA, ML, JH
Manuscript writing and editing	**LR**, HHC, SMS, TRL, YL	**LR**, LL, HHC, SMS, TRL, YL	**LR**, MB, LV, BE, KSL, RD, TRL, YL, LHB	**HØE**, **LR**, GDC, TRL, IB, KI, YL, HH	**LR**, OK, JA, PN, JH, TRL, ML, YL

*Bold initials are leading contributions. Initials in standard font are supporting contributions.

Aalto, Juha = JA
Berthling, Ivar = IB
Corner, Geoffrey Douglas = GDC
Blikra, Lars Harald = LHB
Böhme, Martina = MB
Christiansen, Hanne Hvidtfeldt = HHC
Delaloye, Reynald = RD
Eriksen, Harald Øverli = HØE
Etzelmüller, Bernd = BE
Hindberg, Heidi = HH
Hjort, Jan = JH
Isaksen, Ketil = KI
Karjalainen, Olli = OK
Larsen, Yngvar = YL
Lauknes, Tom Rune = TRL
Lilleøren, Karianne Staalesen = KSL
Liu, Lin = LL
Luoto, Miska = ML
Niittynen, Pekka = PN
Rouyet, Line = LR
Strand, Sarah Marie = SMS
Vick, Louise = LV

Chapter 5

Synthesis

This chapter discusses the main outcomes of the five papers in relation with the initial research questions (RQs 1–4, *Section 1.1*). The results are first summarised by separately considering the findings related to the spatial variability and the temporal behaviour of the periglacial ground dynamics investigated using InSAR, before discussing the overall contribution of the thesis in the field of InSAR applied to periglacial research. *Figure 5.1* proposes a schematic summary of the findings and relates them to suggestions for future research, further presented in *Chapter 6*.

5.1 Spatial variability of ground dynamics

This thesis aims to document the spatial distribution of the magnitude and direction of the ground movement driven by frost action and/or gravity (RQ1) and analyse the environmental controls of this variability at different scales (RQ3). To consider a wide range of environmental contexts and periglacial landforms, as well as discuss the ability of InSAR to depict various kinematic signatures, we included case studies in different regions of the Norwe-

gian periglacial environment. At the interface of the traditional subdivision of the periglacial domains characterising the polar and mountainous regions, the Norwegian environment encompasses a rich combination of processes that is valuable to investigate the advantages and limitations of InSAR in different environments.

The presented results demonstrate the capability of InSAR technology to provide dense kinematic observations to document the movement rates of various periglacial processes (Paper I), to refine the inventory and delineation of specific landforms (Paper III) and to compare ground dynamics with environmental variables at the regional scale (Paper V). The combination of multiple radar geometries and 2D InSAR decomposition is proven valuable to map the variability of the movement direction, in flat and sloping terrain (Papers I and V), while the integration of many interferograms with different temporal baselines allows for increasing the range of detection capabilities (minimal–maximal velocities) (Paper III). Although this thesis is primarily based on Sentinel-1, the results from Papers I and IV show the value of exploiting higher resolution images, such as from the TerraSAR-X satellites, for a detailed mapping of small landforms.

The common denominator of the thesis papers is the comparison of the InSAR results with other datasets contributing to understand the distribution of the ground movement. This analysis is either based on field mapping (geomorphological units, Paper I) and landform inventories (rock glaciers and rockslides, Paper III), or on remotely sensed environmental variables documenting the climatic, geomorphic, hydrologic and biologic conditions (Paper V) (*Figure 5.1*). The kinematic signature varies for different ground material (e.g. eolian vs fluvial sediments) or landform type (e.g. rock glaciers vs rockslides). In Svalbard, larger horizontal movement is found on rock glaciers compared to solifluction lobes/sheets and larger seasonal subsidence is detected in eolian compared to fluvial sediments. The seasonal vertical displacements have mm

to dm seasonal amplitudes depending on the frost-susceptibility and water content of the ground (Paper I). In Northern Norway, higher velocities are measured on glaciers and ice cored moraines and rock glaciers, compared to solifluction and rockslides (Papers III and V). Rock glaciers creep rate ranges from mm–cm/yr to m/yr and allows for updating the activity category (relict, transitional or active) within the regional inventory (Paper III). Significant overlap in the distribution of the velocity values prevents a complete automation of InSAR exploitation for geomorphological mapping. However, the results suggest that InSAR can be a supporting tool for periglacial mapping and inventorying, as also shown by other recent research (Barboux et al., 2014; Dini et al., 2019; Vick et al., 2020; Crippa et al., 2021).

Environmental factors largely influence the direction and spatial distribution of the detected movement. In Geaidnogáisá–Rásttigáisá (Northern Norway), statistical modelling suggests that the mean annual air temperature and the slope angle are the key factors explaining the spatial variability of the ground movement associated with solifluction and cryoturbation, but their relative contribution is variable depending on the velocity direction (horizontal/vertical components) (Paper V). In Kåfjord–Lyngen (Northern Norway), the updated rock glacier inventory suggests that the overall landform distribution and activity are controlled by their location along the E–W climatic gradient, in combination with the strength of the rock mass (Paper III). A comprehensive comparison between the study areas of Svalbard and mainland Norway has at this stage not been performed due to the different processing strategies chosen in each study, but the products developed as part of Papers II (classified InSAR velocity) and Paper III (maximal subsidence of seasonal time series) could provide comparable results in the future, if similarly generated in all regions.

5.2 Temporal behaviour of ground dynamics

This thesis studies the temporal behaviour of various periglacial landforms (RQ2) and discusses the drivers of the kinematic variability at seasonal to decadal timescales (RQ3). A temporal analysis has been performed in central and western Spitsbergen and in Northern Norway, mostly in flat terrain undergoing vertical subsidence and heave due to the seasonal active layer freezing and thawing (Papers I and II) and on rock glaciers (Papers I and IV). The temporal component of the movement has been investigated using both InSAR and in-situ measurements documenting associated environmental variables. The displacement time series were primarily compared with climatic variables such as air and ground temperature, precipitation and snow depth (*Figure 5.1*).

At the seasonal scale, Sentinel-1 InSAR time series in the continuous permafrost landscape of Svalbard highlight a clear differentiation between flat or low-inclined areas dominated by a cyclic seasonal pattern (subsidence–heave due to active layer freeze and thaw) and slopes characterised by gradual creeping processes, such as permafrost creep or glacial flow (Paper I). The results concur with contemporary studies showing that Sentinel-1 contributes to documenting seasonal progression of frost- and/or gravity-driven ground displacement with dense temporal sampling (Strozzi et al., 2018; Bartsch et al., 2019; L. Wang et al., 2020; Reinosch et al., 2020). Both the transition of the subsidence to heave in InSAR series and more subtle variations (e.g. deceleration of the subsidence in the second half of the summer and slower heave in mid-November) match the fluctuations of the active layer temperature measured in boreholes (Paper I). The initial results highlight that displacement time series can indirectly document the changes of the ground thermal regime. This finding instigated a following investigation, which aimed to map and compare the timing of the thaw subsidence maxima in three areas of Svalbard (Paper II). The timing of the maximal subsidence occurs earlier in Adventdalen

(mid-September) compared to Kapp Linné and Ny-Ålesund (early–mid October), in agreement with the expected E–W climatic gradient in Spitsbergen. The comparison with a model based on temperature suggests that the seasonal displacement patterns are primarily controlled by the thermal response of the active layer to atmospheric forcing. While single time series may be affected by errors or unrepresentative local phenomena, the results suggest that spatial averaging reduces the noise level and dampens the effect of specific small-scale effects to focus on the main temperature-controlled trends. In general, the results highlight the value of using InSAR for indirectly documenting the ground thermal dynamics and suggest new strategies for future product development in the Svalbard archipelago, as well as in other polar environments.

At the decadal scale, the comparison between the creep rates of the Ádjet rock glacier complex (Northern Norway) and climatic variables (air temperature and precipitation) suggest that permafrost warming and increased amounts of liquid water in internal shear zones have contributed to the destabilisation of the landform located at the altitudinal limit of the mountain permafrost in the region. However, the study of the spatio-temporal kinematic patterns also highlights that the irregular sediment overloading and the topographic variability have an influence on the landform velocity. The local scale of the study and the complex interactions of various environmental factors do not allow for a conclusive statement on the impact of climate change in this specific case. However, the study highlights the value of combining multiple remote sensing techniques to document the decadal changes of rock glacier kinematics. Monitoring strategies based on radar remote sensing and complemented by optical imagery could in the future be implemented on several Norwegian landforms to further study the relationship between rock glacier kinematics and climatic variables, as also discussed in several recent studies (Brencher et al., 2020; Strozzi et al., 2020; Kääb et al., 2021).

5.3 InSAR applied to periglacial research

InSAR applied to geosciences has had a rapid development from its first application to earthquakes, volcanoes and subsidence in temperate areas (Gabriel et al., 1989; Massonnet et al., 1993) to the onset of its exploitation in periglacial environments (Z. Wang & Li, 1999; Rignot et al., 2002; Kenyi & Kaufmann, 2003). Nowadays, the large coverage of freely available SAR images such as Sentinel-1 enables the development of operational InSAR services, able to map and monitor entire regions, countries or even continents (Dehls et al., 2019; Larsen et al., 2020; Casagli et al., 2021). However, the current size of the datasets exacerbates the challenge of relating the detected moving areas to the various natural processes characterizing complex periglacial landscapes.

One motivation for this thesis was to contribute to bridging the gap between technological advances and geoscientific applications by suggesting novel ways to exploit InSAR data for periglacial applications at the large scale. Detailed mapping of moving landforms and comprehensive understanding of the processes controlling their kinematics is paramount in identifying potentially hazardous objects and understanding the landscape evolution in changing environments. Although InSAR only measures an effect, by studying the relationships between the spatio-temporal displacement patterns and the environmental variables, InSAR observations can indirectly document periglacial processes and their controlling factors. We show that regional InSAR datasets can refine the mapping of geomorphological units (Paper I) and update the inventory of specific landforms (Paper III). Furthermore, InSAR can enhance our knowledge on the drivers of the periglacial landforms (Papers I and V) and indirectly document the ground thermal regime (Papers I and II). To increase the geoscientific value of InSAR results, the first attempts to couple the measurements with modelling (Papers II and V) have been performed and show the potential for taking advantage of both physical and statistical models to

explain the detected displacements. Inversely, the findings also suggest that InSAR can possibly be used to constrain these models, for example by providing semi-automated solutions for landform categorisation at the large scale, or for the monitoring of temporally-variable active layer thaw depths. In parallel, the development of methods providing dedicated products exploitable for specific geoscientific applications is needed, as it is also discussed by Liu et al. (2012), Zwieback & Meyer (2021) and Crippa et al. (2021). This thesis contributes to this objective in both periglacial lowlands and mountainous landscape by proposing simple post-processing strategies to map cyclic patterns in flat terrain (Paper II) and categorise slope movement at the large scale (Paper III).

Despite the demonstrated value of InSAR technology in periglacial environments, limitations are also acknowledged and discussed (RQ4). Decorrelation on very fast-moving landforms (e.g. Papers III and IV) or on wet or snow-covered surfaces (e.g. Papers I and II) show the need for combining various sensors and techniques with different measurement properties. The Ádjet rock glacier (Paper IV) is a clear example, for which spaceborne InSAR had to be complemented by other remote sensing techniques (e.g. TRI and SAR OT) to document the movement rates of destabilised lobes. The way to analyse the results and integrate InSAR measurements in statistical and physical models of ground dynamics is also subject to several challenges. Paper II concludes that a simplistic physical model only based on temperature data is not fully able to account for all the temporal patterns of subsidence and heave, due to the ignored effects of complex hydrological processes in the active layer. Paper V suggests that further research is needed to effectively couple InSAR and statistical modelling due to the discrepancy between the spatial resolution of the remote sensing products and the studied processes, as well as the complex relationships between the environmental controls, the expected processes and the InSAR observations. These limitations highlight the potential for future research, further presented in *Section 6.2*.

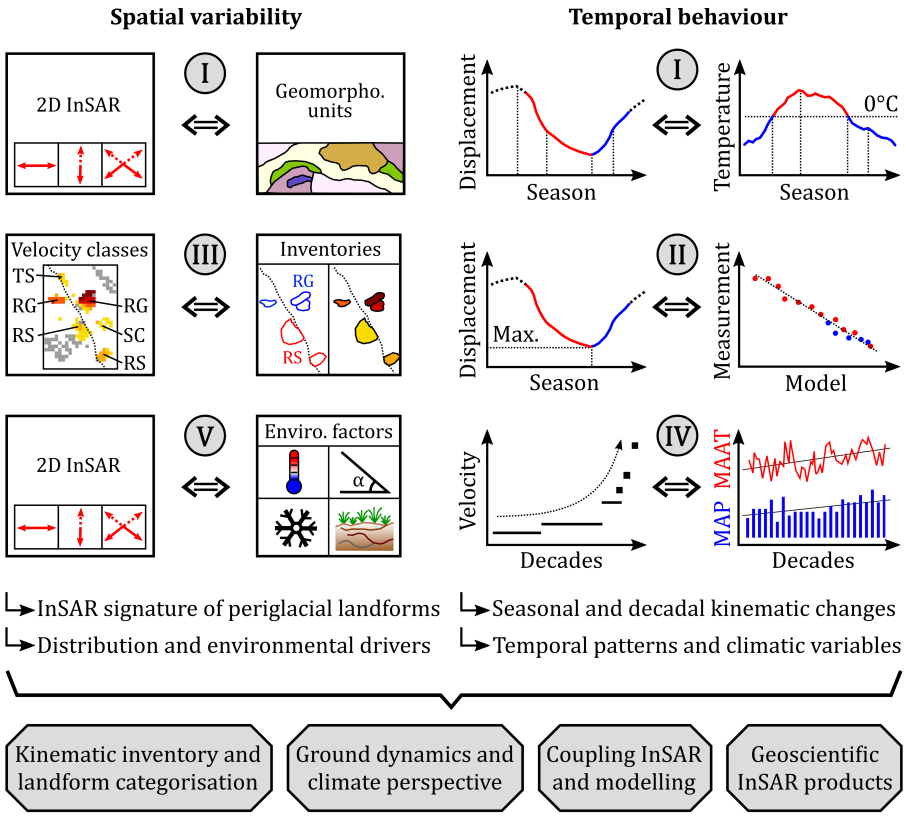

Figure 5.1: Synthesis of the results and perspectives for future research within the scope of InSAR applied to periglacial research. Roman letters refer to the five papers summarised in Chapter 4. Abbreviations and acronyms refer to geomorphological (geomorpho.), environmental (enviro.), subsidence maximum (max.), talus–scree (TS), solifluction–cryoturbation (SC), rock glaciers (RG), rockslides (RS), mean annual air temperature (MAAT) and mean annual precipitation (MAP).

Chapter 6

Conclusion

6.1 Summary

In this thesis, the potential of exploiting InSAR to document periglacial ground dynamics was studied in different regions of Svalbard and Northern Norway. The main goals were to analyse the spatio-temporal kinematic patterns of different landform types, and to relate the remotely sensed measurements to specific periglacial processes and their drivers. The main findings are summarised here:

1. **InSAR signature of periglacial landforms:**
   InSAR documents specific movement magnitudes and directions on various periglacial landforms both in permafrost lowlands and on mountain slopes. The results allow for documenting movement rates ranging from approximately mm/yr to m/yr on various widespread landforms characterising the Norwegian periglacial environment. Ground displacements documented at the regional scale provide novel information that is not directly obtainable by in-situ measurements. InSAR complements traditional mapping methods based on morphological indicators. Regional In-

SAR maps contribute to upscaling the identification and categorisation of moving landforms, and refining our geomorphological understanding of periglacial landscapes.

2. **Distribution and environmental drivers:**

   The ground movement varies spatially in relation to climatic, topographic and geologic variables. Satellite InSAR increases the density of the observations in remote and hard-to-access areas. It contributes to systematically mapping ground movement across entire regions and comparing it to environmental factors at the similar scale. The results show that the ground material types determine the amplitude of the seasonal thaw subsidence in Svalbard. Altitudinal and longitudinal climatic gradients influence the distribution and kinematics of rock glaciers, solifluction and cryoturbation processes in Northern Norway.

3. **Seasonal and decadal kinematic changes:**

   Seasonal InSAR time series in Svalbard highlight distinctive displacement patterns in flat areas dominated by a cyclic heave and subsidence due to the active layer freezing and thawing, compared to sloping terrain characterised by gradual creeping processes. In Northern Norway, decadal time series based on a combination of optical and radar remote sensing techniques provide evidence of the recent acceleration of a fast-moving rock glacier complex.

4. **Temporal patterns and climatic variables:**

   Displacement time series compared with temperature and precipitation measurements show that meteorological factors influence the temporal behaviour of the ground. In permafrost lowlands, the seasonal displacement progression is well explained by the ground temperature and the results indicate that the subsidence maxima can be used as a proxy for the timing of the active layer maximal thawing. In Skibotndalen, a significant

increase in temperature and precipitation is documented simultaneously to 62 years of kinematic time series. The results suggest that the permafrost warming and the increase of liquid water have contributed to the acceleration of the Ádjet rock glacier the last decade.

6.2 Future research

The results highlight the need for future interdisciplinary work in the field of InSAR applied to periglacial research. Four main research topics are presented below:

1. **Kinematic inventory and landform categorisation:**
   Periglacial environments are characterised by different processes that are spatially connected or even superimposed. When the objective is to identify potentially hazardous unstable rock slopes across a whole country (Hermanns et al., 2014) or to refine the permafrost zonation in entire mountainous ranges based on rock glacier distribution (Lilleøren et al., 2012), the main challenge is to comprehensively identify the objects of interest at the large scale and distinguish them from other irrelevant landforms. The research shows that different landforms are characterised by specific spatial and temporal patterns. However, these two components have mostly been considered separately in this thesis. The joint analysis of key spatio-temporal kinematic parameters would be required for a semi-automation of InSAR-based landform categorisation based on machine learning. Further research is still needed in this field, to design relevant strategies to exploit thousands km^2 of InSAR maps, while also investigating several years of displacement time series.

2. **Ground dynamics and climate perspective:**
   In mountainous environments, rock glaciers tend to accelerate on an inter-

annual basis under warmer conditions. Measurements in the European Alps showed that the landforms have a concomitant regional behaviour (Delaloye et al., 2010). This suggests that rock glacier kinematics can be used as an indicator of climate change if systematically documented over many landforms (IPA, 2020). With this objective, satellite InSAR, complemented with other radar and optical techniques, could be applied on many rock glaciers. In Troms, this would allow for determining if the acceleration of the Ádjet rock glacier is part of a regional trend. In Svalbard, the next step of the analysis of seasonal time series could be to repeat the processing for each snow-free season and analyse the inter-annual changes of the subsidence–heave patterns. If systematically generated, InSAR products documenting the timing of the thaw subsidence maxima could be compared with other key environmental variables, such as vegetation phenology and snow cover (Karlsen et al., 2014; Vickers et al., 2020). In areas where the ground elevation does not significantly change between the end of the documented InSAR period (fall) and the start of the consecutive season (spring), inter-seasonal interferograms could also be integrated to provide fully connected time series, as demonstrated in other research (Strozzi et al., 2018). In the long-term perspective, InSAR may contribute to the development of products used as indicators of climate change that could be integrated in operational monitoring strategies, such as the Svalbard Integrated Arctic Earth Observation System (SIOS) (Christiansen et al., 2021).

3. **Coupling InSAR and modelling:**

   Papers II and V propose first attempts for coupling InSAR with physical and statistical modelling. However, several limitations are identified due to simplistic assumptions made at this stage. Further research including other geospatial datasets could contribute to better representing the complex thermo-hydro-mechanical relations controlling perigla-

cial ground movement (Thomas et al., 2009). In addition, the objective of this thesis was to use the physical and statistical models to analyse and explain the InSAR results. Further research could also reverse the approach. Using statistical modelling, InSAR could for example be integrated as an explanatory variable among others to model the distribution of specific landforms. In Svalbard, the analysis of the subsidence–heave patterns suggests that time series averaging provides more robust information about the temperature-controlled temporal patterns. Kilometric products may be favoured in future research, to keep documenting spatial variability while providing more robust information about the general trends. At this scale, displacement time series could easily be compared and coupled with transient modelling of thermal conditions based on remotely sensed surface temperature at a similar resolution (Westermann et al., 2017; Obu et al., 2019). InSAR could potentially contribute to constraining such models by exploiting the subsidence rate to indirectly document the ground ice content (Zwieback & Meyer, 2021).

4. **Geoscientific InSAR products:**

   Finally, the general ambition of the presented research was to increase the geoscientific value of InSAR data to upscale the investigation of periglacial landforms. In an era where the quality and quantity of satellite imagery keeps increasing, InSAR is becoming an undeniable asset for the operational mapping and monitoring of ground movement. Upcoming SAR missions with complementary measurement properties, such as the L-band NISAR and ROSE-L (Sentinel-12), will most likely open the door to new research opportunities in the coming years. In parallel to the technological advances, the need for studies focusing on the development of dedicated products exploitable for specific geoscientific applications, such as periglacial landforms mapping and monitoring of permafrost variables, will keep increasing.

References

Aalto, J., Harrison, S. & Luoto, M. (2017). Statistical modelling predicts almost complete loss of major periglacial processes in Northern Europe by 2100. *Nature Communications*, *8*, 515. doi:10.1038/s41467-017-00669-3

Anisimov, O. A. & Nelson, F. E. (1997). Permafrost zonation and climate change in the Northern Hemisphere: Results from transient general circulation models. *Climatic Change*, *35*(2), 241–258. doi:10.1023/A:1005315409698

Antonova, S., Kääb, A., Heim, B., Langer, M. & Boike, J. (2016). Spatio-temporal variability of X-band radar backscatter and coherence over the Lena River Delta, Siberia. *Remote Sensing of Environment*, *182*, 169–191. doi:10.1016/j.rse.2016.05.003

Ballantyne, C. K. (2018). *Periglacial geomorphology*. John Wiley & Sons.

Bamler, R. & Hartl, P. (1998). Synthetic aperture radar interferometry. *Inverse Problems*, *14*(4), R1. doi:10.1088/0266-5611/14/4/001

Barboux, C., Delaloye, R. & Lambiel, C. (2014). Inventorying slope movements in an Alpine environment using DInSAR. *Earth Surface Processes and Landforms*, *39*(15), 2087–2099. doi:10.1002/esp.3603

Bartsch, A., Leibman, M., Strozzi, T., Khomutov, A., Widhalm, B., Babkina, E., Mullanurov, D., Ermokhina, K., Kroisleitner, C. & Bergstedt, H. (2019). Seasonal Progression of Ground Displacement Identified with Satellite Radar Interferometry and the Impact of Unusually Warm Conditions on Permafrost at the Yamal Peninsula in 2016. *Remote Sensing*, *11*(16), 1865. doi:10.3390/rs11161865

Berardino, P., Fornaro, G., Lanari, R. & Sansosti, E. (2002). A new algorithm for surface deformation monitoring based on small baseline differential SAR inter-

ferograms. *IEEE Transactions on Geoscience and Remote Sensing*, *40*(11), 2375–2383. doi:10.1109/TGRS.2002.803792

Berthling, I. (2011). Beyond confusion: Rock glaciers as cryo-conditioned landforms. *Geomorphology*, *131*(3-4), 98–106. doi:10.1016/j.geomorph.2011.05.002

Berthling, I. & Etzelmüller, B. (2011). The concept of cryo-conditioning in landscape evolution. *Quaternary Research*, *75*(2), 378–384. doi:10.1016/j.yqres.2010.12.011

Berthling, I., Schomacker, A. & Benediktsson, Í. (2013). Chapter 8.28. The Glacial and Periglacial Research Frontier: Where from Here? In J. F. Shroder (Ed.), *Treatise on Geomorphology* (Vol. 8, pp. 479–499). doi:10.1016/B978-0-12-374739-6.00224-4

Biskaborn, B. K., Smith, S. L., Noetzli, J., Matthes, H., Vieira, G., Streletskiy, D. A., Schoeneich, P., Romanovsky, V. E., Lewkowicz, A. G., Abramov, A. et al. (2019). Permafrost is warming at a global scale. *Nature Communications*, *10*, 264. doi:10.1038/s41467-018-08240-4

Blikra, L. H. & Christiansen, H. H. (2014). A field-based model of permafrost-controlled rockslide deformation in northern Norway. *Geomorphology*, *208*, 34–49. doi:10.1016/j.geomorph.2013.11.014

Bodin, X., Krysiecki, J.-M., Schoeneich, P., Le Roux, O., Lorier, L., Echelard, T., Peyron, M. & Walpersdorf, A. (2017). The 2006 collapse of the Bérard rock glacier (Southern French Alps). *Permafrost and Periglacial Processes*, *28*(1), 209–223. doi:10.1002/ppp.1887

Böhme, M., Hermanns, R. L., Gosse, J., Hilger, P., Eiken, T., Lauknes, T. R. & Dehls, J. F. (2019). Comparison of monitoring data with paleo–slip rates: Cosmogenic nuclide dating detects acceleration of a rockslide. *Geology*, *47*(4), 339–342. doi:10.1130/G45684.1

Boike, J., Juszak, I., Lange, S., Chadburn, S., Burke, E., Overduin, P. P., Roth, K., Ippisch, O., Bornemann, N., Stern, L. et al. (2018). A 20-year record (1998–2017) of permafrost, active layer and meteorological conditions at a high Arctic permafrost research site (Bayelva, Spitsbergen). *Earth System Science Data*, *10*(1), 355–390. doi:10.5194/essd-10-355-2018

Bonnaventure, P. P. & Lamoureux, S. F. (2013). The active layer: A conceptual review of monitoring, modelling techniques and changes in a warming climate. *Progress in Physical Geography*, *37*(3), 352–376. doi:10.1177/0309133313478314

Brencher, G., Handwerger, A. L. & Munroe, J. S. (2020). InSAR-based characterization of rock glacier movement in the Uinta Mountains, Utah, USA. *The Cryosphere Discussions*, 1–36. doi:10.5194/tc-2020-274

Brown, J., Ferrians, O. J., Heginbottom, J. A. & Melnikov, E. (2002). *Circum-Arctic map of permafrost and ground-ice conditions, Version 2*. NSIDC: National Snow and Ice Data Center. Boulder, Colorado USA. doi:10.7265/skbg-kf16

Cable, S., Elberling, B. & Kroon, A. (2018). Holocene permafrost history and cryostratigraphy in the High-Arctic Adventdalen Valley, central Svalbard. *Boreas*, *47*(2), 423–442. doi:10.1111/bor.12286

Caduff, R., Schlunegger, F., Kos, A. & Wiesmann, A. (2015). A review of terrestrial radar interferometry for measuring surface change in the geosciences. *Earth Surface Processes and Landforms*, *40*(2), 208–228. doi:10.1002/esp.3656

Casagli, N., Bianchini, S., Ciampalini, A., Del Soldato, M., Ezquierro, P., Montalti, R., Shan, M., Solari, L. & Raspini, F. (2021). Sentinel-1 InSAR Data for the Continuous Monitoring of Ground Deformation and Infrastructures at Regional Scale. In V. Singhroy (Ed.), *Advances in Remote Sensing for Infrastructure Monitoring* (pp. 63–80). Springer, Cham. doi:10.1007/978-3-030-59109-0_3

Chen, C. W. & Zebker, H. A. (2002). Phase unwrapping for large SAR interferograms: Statistical segmentation and generalized network models. *IEEE Transactions on Geoscience and Remote Sensing*, *40*(8), 1709–1719. doi:10.1109/TGRS.2002.802453

Christiansen, H. H. (2005). Thermal regime of ice-wedge cracking in Adventdalen, Svalbard. *Permafrost and Periglacial Processes*, *16*(1), 87–98. doi:10.1002/ppp.523

Christiansen, H. H., Etzelmüller, B., Isaksen, K., Juliussen, H., Farbrot, H., Humlum, O., Johansson, M., Ingeman-Nielsen, T., Kristensen, L., Hjort, J. et al. (2010). The thermal state of permafrost in the Nordic area during the International Polar Year 2007–2009. *Permafrost and Periglacial Processes*, *21*(2), 156–181. doi:10.1002/ppp.687

Christiansen, H. H., Gilbert, G. L., Neumann, U., Demidov, N., Guglielmin, M., Isaksen, K., Osuch, M. & Boike, J. (2021). Chapter 12. Ground ice content, drilling methods and equipment and permafrost dynamics in Svalbard 2016–2019 (PermaSval). In *SESS report 2020 – The State of Environmental Science in Svalbard.* Svalbard Integrated Arctic Earth Observing System, Longyearbyen. doi:10.5281/zenodo.4294095

Christiansen, H. H., Humlum, O. & Eckerstorfer, M. (2013). Central Svalbard 2000–2011

Meteorological Dynamics and Periglacial Landscape Response. *Arctic, Antarctic, and Alpine research*, *45*(1), 6–18. doi:10.1657/1938-4246-45.16

Cicoira, A., Beutel, J., Faillettaz, J. & Vieli, A. (2019). Water controls the seasonal rhythm of rock glacier flow. *Earth and Planetary Science Letters*, *528*, 115844. doi:10.1016/j.epsl.2019.115844

Corner, G. D. (2005). Chapter 13. Scandes Mountains. In M. Seppälä (Ed.), *The physical geography of Fennoscandia* (pp. 229–254). Oxford University Press.

Crippa, C., Valbuzzi, E., Frattini, P., Crosta, G. B., Spreafico, M. C. & Agliardi, F. (2021). Semi-automated regional classification of the style of activity of slow rock-slope deformations using PS InSAR and SqueeSAR velocity data. *Landslides*, 1–19. doi:10.1007/s10346-021-01654-0

Dehls, J. F., Fischer, L., Böhme, M., Saintot, A., Hermanns, R., Oppikofer, T., Lauknes, T., Larsen, Y. & Blikra, L. (2012). Landslide Monitoring in western Norway using high resolution TerraSAR-X and Radarsat-2 InSAR. In E. Eberhardt, C. Froese, K. Turner & S. Leroueil (Eds.), *Landslides and Engineered Slopes: Protecting Society through Improved Understanding* (pp. 1321–1325).

Dehls, J. F., Larsen, Y., Marinkovic, P., Lauknes, T. R., Stødle, D. & Moldestad, D. A. (2019). INSAR.No: A National Insar Deformation Mapping/Monitoring Service In Norway–From Concept To Operations. In *IGARSS 2019 – IEEE International Geoscience and Remote Sensing Symposium* (pp. 5461–5464). doi:10.1109/IGARSS.2019.8898614

Delaloye, R., Lambiel, C. & Gärtner-Roer, I. (2010). Overview of rock glacier kinematics research in the Swiss Alps. *Geographica Helvetica*, *65*(2), 135–145. doi:10.5194/gh-65-135-2010

Delaloye, R., Morard, S., Barboux, C., Abbet, D., Gruber, V., Riedo, M. & Gachet, S. (2013). Rapidly moving rock glaciers in Mattertal. In C. Graf (Ed.), *Mattertal–ein tal in bewegung* (Vol. 29, pp. 21–31). Publikation zur Jahrestagung der Schweizerischen Geomorphologischen Gesellschaft.

Delaloye, R., Perruchoud, E., Avian, M., Kaufmann, V., Bodin, X., Hausmann, H., Ikeda, A., Kääb, A., Kellerer-Pirklbauer, A., Krainer, K. et al. (2008). Recent interannual variations of rock glacier creep in the European Alps. In *Proc. of the 9th International Conference on Permafrost, Fairbanks, Alaska, 29 June 2008 – 3 July 2008* (pp. 343–348).

University of Zurich.

Dini, B., Daout, S., Manconi, A. & Loew, S. (2019). Classification of slope processes based on multitemporal DInSAR analyses in the Himalaya of NW Bhutan. *Remote Sensing of Environment*, *233*, 111408. doi:10.1016/j.rse.2019.111408

Duguay, C. R., Zhang, T., Leverington, D. W. & Romanovsky, V. E. (2005). Satellite remote sensing of permafrost and seasonally frozen ground. In C. R. Duguay & A. Pietroniro (Eds.), *Remote Sensing in Northern Hydrology: Measuring Environmental Change* (Vol. 163, p. 91). Geophysical Monograph Series - American Geophysical Union. doi:10.1029/163GM06

Eckerstorfer, M., Eriksen, H. Ø., Rouyet, L., Christiansen, H. H., Lauknes, T. R. & Blikra, L. H. (2018). Comparison of geomorphological field mapping and 2D-InSAR mapping of periglacial landscape activity at Nordnesfjellet, northern Norway. *Earth Surface Processes and Landforms*, *43*(10), 2147–2156. doi:10.1002/esp.4380

Eldevik, T., Risebrobakken, B., Bjune, A. E., Andersson, C., Birks, H. J. B., Dokken, T. M., Drange, H., Glessmer, M. S., Li, C., Nilsen, J. E. Ø. et al. (2014). A brief history of climate – the northern seas from the Last Glacial Maximum to global warming. *Quaternary Science Reviews*, *106*, 225–246. doi:10.1016/j.quascirev.2014.06.028

Emardson, T. R., Simons, M. & Webb, F. (2003). Neutral atmospheric delay in interferometric synthetic aperture radar applications: Statistical description and mitigation. *Journal of Geophysical Research: Solid Earth*, *108*(B5). doi:10.1029/2002JB001781

Eriksen, H. Ø., Bergh, S. G., Larsen, Y., Skrede, I., Kristensen, L., Lauknes, T. R., Blikra, L. H. & Kierulf, H. P. (2017b). Relating 3D surface displacement from satellite-and ground-based InSAR to structures and geomorphology of the Jettan rockslide, northern Norway. *Norwegian Journal of Geology*, *97*(4), 283–303. doi:10.17850/njg97-4-03

Eriksen, H. Ø., Lauknes, T. R., Larsen, Y., Corner, G. D., Bergh, S. G., Dehls, J. & Kierulf, H. P. (2017a). Visualizing and interpreting surface displacement patterns on unstable slopes using multi-geometry satellite SAR interferometry (2D InSAR). *Remote Sensing of Environment*, *191*, 297–312. doi:10.1016/j.rse.2016.12.024

Etzelmüller, B., Guglielmin, M., Hauck, C., Hilbich, C., Hoelzle, M., Isaksen, K., Noetzli, J., Oliva, M. & Ramos, M. (2020). Twenty years of European mountain permafrost dynamics – the PACE legacy. *Environmental Research Letters*, *15*(10), 104070. doi:10.1088/1748-9326/abae9d

Etzelmüller, B., Ødegård, R. S., Berthling, I. & Sollid, J. L. (2001). Terrain parameters and remote sensing data in the analysis of permafrost distribution and periglacial processes: principles and examples from southern Norway. *Permafrost and Periglacial Processes*, *12*(1), 79–92. doi:10.1002/ppp.384

Etzelmüller, B., Schuler, T. V., Isaksen, K., Christiansen, H. H., Farbrot, H. & Benestad, R. (2011). Modeling the temperature evolution of Svalbard permafrost during the 20th and 21st century. *The Cryosphere*, *5*(1), 67–79. doi:10.5194/tc-5-67-2011

Farbrot, H., Isaksen, K., Etzelmüller, B. & Gisnås, K. (2013). Ground thermal regime and permafrost distribution under a changing climate in northern Norway. *Permafrost and Periglacial Processes*, *24*(1), 20–38. doi:10.1002/ppp.1763

Ferretti, A. (2014). *Satellite InSAR Data: Reservoir Monitoring from Space* (Vol. EET 9). EAGE European Association of Geoscientists and Engineers.

Ferretti, A., Prati, C. & Rocca, F. (2001). Permanent scatterers in SAR interferometry. *IEEE Transactions on Geoscience and Remote Sensing*, *39*(1), 8–20. doi:10.1109/36.898661

French, H. (2007). *The Periglacial Environment, 3rd Edition*. John Wiley and Sons Ltd.

French, H. & Thorn, C. E. (2006). The changing nature of periglacial geomorphology. *Géomorphologie: Relief, Processus, Environnement*, *12*(3). doi:10.4000/geomorphologie.119

Gabriel, A. K., Goldstein, R. M. & Zebker, H. A. (1989). Mapping small elevation changes over large areas: Differential radar interferometry. *Journal of Geophysical Research: Solid Earth*, *94*(B7), 9183–9191. doi:10.1029/JB094iB07p09183

Geertsema, M., Clague, J. J., Schwab, J. W. & Evans, S. G. (2006). An overview of recent large catastrophic landslides in northern British Columbia, Canada. *Engineering geology*, *83*(1-3), 120–143. doi:10.1016/j.enggeo.2005.06.028

Genxu, W., Guangsheng, L., Chunjie, L. & Yan, Y. (2012). The variability of soil thermal and hydrological dynamics with vegetation cover in a permafrost region. *Agricultural and Forest Meteorology*, *162–163*, 44–57. doi:10.1016/j.agrformet.2012.04.006

Gischig, V. S., Moore, J. R., Evans, K. F., Amann, F. & Loew, S. (2011). Thermomechanical forcing of deep rock slope deformation: 1. Conceptual study of a simplified slope. *Journal of Geophysical Research: Earth Surface*, *116*(F4). doi:10.1029/2011JF002006

Gisnås, K., Etzelmüller, B., Lussana, C., Hjort, J., Sannel, A. B. K., Isaksen, K., Wester-

mann, S., Kuhry, P., Christiansen, H. H., Frampton, A. et al. (2017). Permafrost Map for Norway, Sweden and Finland. *Permafrost and Periglacial Processes*, *28*(2), 359–378. doi:10.1002/ppp.1922

Gisnås, K., Westermann, S., Schuler, T. V., Litherland, T., Isaksen, K., Boike, J. & Etzelmüller, B. (2014). A statistical approach to represent small-scale variability of permafrost temperatures due to snow cover. *The Cryosphere*, *8*(6), 2063–2074. doi:10.5194/tc-8-2063-2014

Goldstein, R. M., Zebker, H. A. & Werner, C. L. (1988). Satellite radar interferometry: Two-dimensional phase unwrapping. *Radio Science*, *23*(4), 713–720. doi:10.1029/RS023i004p00713

Grøneng, G., Christiansen, H. H., Nilsen, B. & Blikra, L. H. (2011). Meteorological effects on seasonal displacements of the åknes rockslide, western Norway. *Landslides*, *8*(1), 1–15. doi:10.1007/s10346-010-0224-x

Haeberli, W., Hallet, B., Arenson, L., Elconin, R., Humlum, O., Kääb, A., Kaufmann, V., Ladanyi, B., Matsuoka, N., Springman, S. et al. (2006). Permafrost creep and rock glacier dynamics. *Permafrost and Periglacial Processes*, *17*(3), 189–214. doi:10.1002/ppp.561

Hanssen, R. F. (2001). *Radar Interferometry: Data Interpretation and Error Analysis* (Vol. 2). Springer Science & Business Media.

Harbitz, C., Glimsdal, S., Løvholt, F., Kveldsvik, V., Pedersen, G. & Jensen, A. (2014). Rockslide tsunamis in complex fjords: From an unstable rock slope at Åkerneset to tsunami risk in western Norway. *Coastal engineering*, *88*, 101–122. doi:10.1016/j.coastaleng.2014.02.003

Harland, W. B. (1997). Chapter 1. Svalbard. In W. B. Harland (Ed.), *The Geology of Svalbard* (pp. 3–15). Geological Society, London, Memoir No. 17. doi:10.1144/GSL.MEM.1997.017.01.01

Harris, C., Arenson, L. U., Christiansen, H. H., Etzelmüller, B., Frauenfelder, R., Gruber, S., Haeberli, W., Hauck, C., Hoelzle, M., Humlum, O. et al. (2009). Permafrost and climate in Europe: Monitoring and modelling thermal, geomorphological and geotechnical responses. *Earth-Science Reviews*, *92*(3–4), 117–171. doi:10.1016/j.earscirev.2008.12.002

Harris, C. & Davies, M. C. (2000). Gelifluction: Observations from Large-Scale

Laboratory Simulations. *Arctic, Antarctic, and Alpine Research*, *32*(2), 202–207. doi:10.1080/15230430.2000.12003356

Harris, C., Kern-Luetschg, M., Christiansen, H. H. & Smith, F. (2011). The role of interannual climate variability in controlling solifluction processes, Endalen, Svalbard. *Permafrost and Periglacial Processes*, *22*(3), 239–253. doi:10.1002/ppp.727

Harris, C., Kern-Luetschg, M., Murton, J., Font, M., Davies, M. & Smith, F. (2008). Solifluction processes on permafrost and non-permafrost slopes: results of a large-scale laboratory simulation. *Permafrost and Periglacial Processes*, *19*(4), 359–378. doi:10.1002/ppp.630

Hermanns, R. L., Oppikofer, T., Anda, E., Blikra, L. H., Böhme, M., Bunkholt, H., Crosta, G. B., Dahle, H., Devoli, G., Fischer, L. et al. (2013). Hazard and risk classification for large unstable rock slopes in Norway. *Italian Journal of Engineering Geology and Environment*, *2013*, 245–254. doi:10.4408/IJEGE.2013-06.B-22

Hermanns, R. L., Oppikofer, T., Molina, F. X. Y., Dehls, J. F. & Böhme, M. (2014). Approach for systematic rockslide mapping of unstable rock slopes in Norway. In K. Sassa, P. Canuti & Y. Yin (Eds.), *Landslide Science for a Safer Geoenvironment* (pp. 129–134). Springer. doi:10.1007/978-3-319-04996-0_21

Hjort, J., Karjalainen, O., Aalto, J., Westermann, S., Romanovsky, V. E., Nelson, F. E., Etzelmüller, B. & Luoto, M. (2018). Degrading permafrost puts Arctic infrastructure at risk by mid-century. *Nature Communications*, *9*, 5147. doi:10.1038/s41467-018-07557-4

Humlum, O. (2000). The geomorphic significance of rock glaciers: estimates of rock glacier debris volumes and headwall recession rates in West Greenland. *Geomorphology*, *35*(1-2), 41–67. doi:10.1016/S0169-555X(00)00022-2

Humlum, O., Instanes, A. & Sollid, J. L. (2003). Permafrost in Svalbard: a review of research history, climatic background and engineering challenges. *Polar Research*, *22*(2), 191–215. doi:10.1111/j.1751-8369.2003.tb00107.x

Hungr, O., Leroueil, S. & Picarelli, L. (2014). The Varnes classification of landslide types, an update. *Landslides*, *11*(2), 167–194. doi:10.1007/s10346-013-0436-y

Ikeda, A. & Matsuoka, N. (2002). Degradation of talus-derived rock glaciers in the Upper Engadin, Swiss Alps. *Permafrost and Periglacial Processes*, *13*(2), 145–161. doi:10.1002/ppp.413

Ikeda, A., Matsuoka, N. & Kääb, A. (2008). Fast deformation of perennially frozen debris in a warm rock glacier in the Swiss Alps: An effect of liquid water. *Journal of Geophysical Research: Earth Surface*, *113*(F1). doi:10.1029/2007JF000859

IPA. (2020). Rock glacier kinematics as an associated parameter of ECV Permafrost. *International Permafrost Association (IPA) Action Group Rock glacier inventories and kinematics*. Retrieved from `https://www3.unifr.ch/geo/geomorphology/en/research/ipa-action-group-rock-glacier`

Isaksen, K., Christiansen, H. H. & Westermann, S. (2019). Chapter 7.1. Permafrost temperature and active layer thickness. In I. Hanssen-Bauer, E. Førland, H. Hisdal, S. Mayer, A. Sandø & A. Sorteberg (Eds.), *Climate in Svalbard 2100* (pp. 105–110). NCCS report no 1/2019. Retrieved from `https://bora.uib.no/bora-xmlui/handle/1956/19136`

Isaksen, K., Sollid, J. L., Holmlund, P. & Harris, C. (2007). Recent warming of mountain permafrost in Svalbard and Scandinavia. *Journal of Geophysical Research: Earth Surface*, *112*(F2). doi:10.1029/2006JF000522

Kääb, A. (2008). Remote sensing of permafrost-related problems and hazards. *Permafrost and Periglacial Processes*, *19*(2), 107–136. doi:10.1002/ppp.619

Kääb, A., Frauenfelder, R. & Roer, I. (2007). On the response of rockglacier creep to surface temperature increase. *Global and Planetary Change*, *56*(1-2), 172–187. doi:10.1016/j.gloplacha.2006.07.005

Kääb, A., Strozzi, T., Bolch, T., Caduff, R., Trefall, H., Stoffel, M. & Kokarev, A. (2021). Inventory, motion and acceleration of rock glaciers in Ile Alatau and Kungöy Ala-Too, northern Tien Shan, since the 1950s. *The Cryosphere*, *15*, 927–949. doi:10.5194/tc-15-927-2021

Karjalainen, O., Luoto, M., Aalto, J. & Hjort, J. (2019). New insights into the environmental factors controlling the ground thermal regime across the Northern Hemisphere: a comparison between permafrost and non-permafrost areas. *The Cryosphere*, *13*(2), 693–707. doi:10.5194/tc-13-693-2019

Karlsen, S. R., Elvebakk, A., Høgda, K. A. & Grydeland, T. (2014). Spatial and temporal variability in the onset of the growing season on Svalbard, Arctic Norway – Measured by MODIS-NDVI satellite data. *Remote Sensing*, *6*(9), 8088–8106. doi:10.3390/rs6098088

Kenyi, L. W. & Kaufmann, V. (2003). Estimation of rock glacier surface deformation using SAR interferometry data. *IEEE Transactions on Geoscience and Remote Sensing*, *41*(6), 1512–1515. doi:10.1109/TGRS.2003.811996

Keuschnig, M., Hartmeyer, I., Höfer-Öllinger, G., Schober, A., Krautblatter, M. & Schrott, L. (2015). Permafrost-related mass movements: Implications from a rock slide at the Kitzsteinhorn, Austria. In *Engineering Geology for Society and Territory - volume 1* (pp. 255–259). Springer. doi:10.1007/978-3-319-09300-0_48

Kokelj, S. V. & Jorgenson, M. T. (2013). Advances in thermokarst research. *Permafrost and Periglacial Processes*, *24*(2), 108–119. doi:10.1002/ppp.1779

Konrad, J.-M. & Morgenstern, N. R. (1980). A mechanistic theory of ice lens formation in fine-grained soils. *Canadian Geotechnical Journal*, *17*(4), 473–486. doi:10.1139/t80-056

Larsen, Y., Marinkovic, P., Dehls, J. F., Bredal, M., Bishop, C., Jøkulsson, G., Gjøvik, L.-P., Frauenfelder, R., Salazar, S. E., Vöge, M. et al. (2020). European Ground Motion Service: Service Implementation Plan and Product Specification Document. *EGMS – Copernicus Land Monitoring Service*. Retrieved from `https://land.copernicus.eu/user-corner/technical-library/egms-specification-and-implementation-plan`

Lauknes, T. R., Shanker, A. P., Dehls, J. F., Zebker, H. A., Henderson, I. H. C. & Larsen, Y. (2010a). Detailed rockslide mapping in northern Norway with small baseline and persistent scatterer interferometric SAR time series methods. *Remote Sensing of Environment*, *114*(9), 2097–2109. doi:10.1016/j.rse.2010.04.015

Lauknes, T. R., Zebker, H. A. & Larsen, Y. (2010b). InSAR deformation time series using an L1-norm small-baseline approach. *IEEE Transactions on Geoscience and Remote Sensing*, *49*(1), 536–546. doi:10.1109/TGRS.2010.2051951

Lilleøren, K. S., Etzelmüller, B., Schuler, T. V., Gisnås, K. & Humlum, O. (2012). The relative age of mountain permafrost – estimation of Holocene permafrost limits in Norway. *Global and Planetary Change*, *92–93*, 209–223. doi:10.1016/j.gloplacha.2012.05.016

Liu, L., Schaefer, K., Zhang, T. & Wahr, J. (2012). Estimating 1992–2000 average active layer thickness on the Alaskan North Slope from remotely sensed surface subsidence. *Journal of Geophysical Research: Earth Surface*, *117*(F1). doi:10.1029/2011JF002041

Liu, L., Zhang, T. & Wahr, J. (2010). InSAR measurements of surface deformation over permafrost on the North Slope of Alaska. *Journal of Geophysical Research: Earth Surface*, *115*(F3). doi:10.1029/2009JF001547

Mangerud, J., Gyllencreutz, R., Lohne, Ø. & Svendsen, J. I. (2011). Chapter 22. Glacial history of Norway. In *Developments in Quaternary Sciences* (Vol. 15, pp. 279–298). Elsevier. doi:10.1016/B978-0-444-53447-7.00022-2

Massonnet, D. & Feigl, K. L. (1998). Radar interferometry and its application to changes in the Earth's surface. *Reviews of Geophysics*, *36*(4), 441–500. doi:10.1029/97RG03139

Massonnet, D., Rossi, M., Carmona, C., Adragna, F., Peltzer, G., Feigl, K. & Rabaute, T. (1993). The displacement field of the Landers earthquake mapped by radar interferometry. *Nature*, *364*(6433), 138–142. doi:10.1038/364138a0

Matsuoka, N. (2001). Solifluction rates, processes and landforms: a global review. *Earth-Science Reviews*, *55*(1-2), 107–134. doi:10.1016/S0012-8252(01)00057-5

Matsuoka, N., Hirakawa, K., Watanabe, T. & Moriwaki, K. (1997). Monitoring of periglacial slope processes in the Swiss Alps: the first two years of frost shattering, heave and creep. *Permafrost and Periglacial Processes*, *8*(2), 155–177. doi:10.1002/(SICI)1099-1530(199732)8:2<155::AID-PPP248>3.0.CO;2-N

Nitze, I., Grosse, G., Jones, B. M., Romanovsky, V. E. & Boike, J. (2018). Remote sensing quantifies widespread abundance of permafrost region disturbances across the Arctic and Subarctic. *Nature Communications*, *9*, 5423. doi:10.1038/s41467-018-07663-3

Nordvik, T., Blikra, L. H., Nyrnes, E. & Derron, M.-H. (2010). Statistical analysis of seasonal displacements at the Nordnes rockslide, northern Norway. *Engineering geology*, *114*(3-4), 228–237. doi:10.1016/j.enggeo.2010.04.019

Obu, J., Westermann, S., Barboux, C., Bartsch, A., Delaloye, R., Grosse, G. & Wiesmann, A. (2020). ESA Permafrost Climate Change Initiative (Permafrost_cci): Permafrost active layer thickness for the Northern Hemisphere, v2.0. *Centre for Environmental Data Analysis, 02 November 2020*. doi:10.5285/29c4af5986ba4b9c8a3cfc33ca8d7c85

Obu, J., Westermann, S., Bartsch, A., Berdnikov, N., Christiansen, H. H., Dashtseren, A., Delaloye, R., Elberling, B., Etzelmüller, B., Kholodov, A. et al. (2019). Northern hemisphere permafrost map based on TTOP modelling for 2000–2016 at 1 km^2 scale. *Earth-Science Reviews*, *1932*, 299–316. doi:10.1016/j.earscirev.2019.04.023

Peel, M. C., Finlayson, B. L. & McMahon, T. A. (2007). Updated world map of the

Köppen-Geiger climate classification. *Hydrology and Earth System Sciences*, *11*(5), 1633–1644. doi:10.5194/hess-11-1633-2007

Pissart, A. (2002). Palsas, lithalsas and remnants of these periglacial mounds. A progress report. *Progress in Physical Geography*, *26*(4), 605–621. doi:0.1191/0309133302pp354ra

Reinosch, E., Buckel, J., Dong, J., Gerke, M., Baade, J. & Riedel, B. (2020). InSAR time series analysis of seasonal surface displacement dynamics on the Tibetan Plateau. *The Cryosphere*, *14*(5), 1633–1650. doi:10.5194/tc-14-1633-2020

Rempel, A. W. (2007). Formation of ice lenses and frost heave. *Journal of Geophysical Research: Earth Surface*, *112*(F2). doi:10.1029/2006JF000525

Rignot, E., Hallet, B. & Fountain, A. (2002). Rock glacier surface motion in Beacon Valley, Antarctica, from synthetic-aperture radar interferometry. *Geophysical Research Letters*, *29*(12), 48–1. doi:10.1029/2001GL013494

Riseborough, D., Shiklomanov, N., Etzelmüller, B., Gruber, S. & Marchenko, S. (2008). Recent advances in permafrost modelling. *Permafrost and Periglacial Processes*, *19*(2), 137–156. doi:10.1002/ppp.615

Romanovsky, V. E., Marchenko, S. S., Daanen, R., Sergeev, D. O. & Walker, D. A. (2008). Soil climate and frost heave along the permafrost/ecological North American Arctic transect. In *Proc. of the 9th International Conference on Permafrost* (Vol. 2, pp. 1519–1524).

Rosen, P. A., Hensley, S., Joughin, I. R., Li, F. K., Madsen, S. N., Rodriguez, E. & Goldstein, R. M. (2000). Synthetic aperture radar interferometry. In *Proceedings of the ieee* (Vol. 88, pp. 333–382). doi:10.1109/5.838084

Sandwell, D. T. & Price, E. J. (1998). Phase gradient approach to stacking interferograms. *Journal of Geophysical Research: Solid Earth*, *103*(B12), 30183–30204. doi:10.1029/1998JB900008

Schuh, C., Frampton, A. & Christiansen, H. H. (2017). Soil moisture redistribution and its effect on inter-annual active layer temperature and thickness variations in a dry loess terrace in Adventdalen, Svalbard. *The Cryosphere*, *11*(1), 635–651. doi:10.5194/tc-11-635-2017

Shur, Y., Hinkel, K. M. & Nelson, F. E. (2005). The transient layer: Implications for geocryology and climate-change science. *Permafrost and Periglacial Processes*, *16*(1),

5–17. doi:10.1002/ppp.518

Singhroy, V., Alasset, P.-J., Couture, R. & Poncos, V. (2007). InSAR monitoring of landslides on permafrost terrain in Canada. In *2007 IEEE International Geoscience and Remote Sensing Symposium, 23–28 July 2007, Barcelona, Spain* (pp. 2451–2454). doi:10.1109/IGARSS.2007.4423338

Slaymaker, O. (2009). Proglacial, periglacial or paraglacial? *Geological Society, London, Special Publications*, *320*(1), 71–84. doi:10.1144/SP320.6

Smith, M. W. (1985). Chapter 6. Models of soil freezing. In M. Church & O. Slaymaker (Eds.), *Field and Theory: Lectures in Geocryology* (pp. 96–120). University of British Columbia Press.

Stead, D. & Wolter, A. (2015). A critical review of rock slope failure mechanisms: The importance of structural geology. *Journal of Structural Geology*, *74*, 1–23. doi:10.1016/j.jsg.2015.02.002

Stefan, J. (1891). Über die Theorie der Eisbildung, insbesondere über die Eisbildung im Polarmeere. *Annalen der Physik und Chemie*, *42*, 269–286.

Stoffel, M., Tiranti, D. & Huggel, C. (2014). Climate change impacts on mass movements – Case studies from the European Alps. *Science of the Total Environment*, *493*, 1255–1266. doi:10.1016/j.scitotenv.2014.02.102

Strozzi, T., Antonova, S., Günther, F., Mätzler, E., Vieira, G., Wegmüller, U., Westermann, S. & Bartsch, A. (2018). Sentinel-1 SAR Interferometry for Surface Deformation Monitoring in Low-Land Permafrost Areas. *Remote Sensing*, *10*(9), 1360. doi:10.3390/rs10091360

Strozzi, T., Caduff, R., Jones, N., Barboux, C., Delaloye, R., Bodin, X., Kääb, A., Mätzler, E. & Schrott, L. (2020). Monitoring Rock Glacier Kinematics with Satellite Synthetic Aperture Radar. *Remote Sensing*, *12*(3), 559. doi:10.3390/rs12030559

Strozzi, T., Kääb, A. & Frauenfelder, R. (2004). Detecting and quantifying mountain permafrost creep from in situ inventory, space-borne radar interferometry and airborne digital photogrammetry. *International Journal of Remote Sensing*, *25*(15), 2919–2931. doi:10.1080/0143116042000192330

Thomas, H. R., Cleall, P., Li, Y.-C., Harris, C. & Kern-Luetschg, M. (2009). Modelling of cryogenic processes in permafrost and seasonally frozen soils. *Geotechnique*, *59*(3), 173–184. doi:10.1680/geot.2009.59.3.173

Torsvik, T. H. & Cocks, L. R. M. (2005). Norway in space and time: A Centennial cavalcade. *Norwegian Journal of Geology*, *85*, 73–86.

Van Vliet-Lanoë, B. (1991). Differential frost heave, load casting and convection: Converging mechanisms; a discussion of the origin of cryoturbations. *Permafrost and Periglacial Processes*, *2*(2), 123–139. doi:10.1002/ppp.3430020207

Vick, L. M., Böhme, M., Rouyet, L., Bergh, S. G., Corner, G. D. & Lauknes, T. R. (2020). Structurally controlled rock slope deformation in northern Norway. *Landslides*, *17*(8), 1745–1776. doi:10.1007/s10346-020-01421-7

Vickers, H., Karlsen, S. R. & Malnes, E. (2020). A 20-year MODIS-based snow cover dataset for Svalbard and its link to phenological timing and sea ice variability. *Remote Sensing*, *12*(7), 1123. doi:10.3390/rs12071123

Wang, L., Marzahn, P., Bernier, M. & Ludwig, R. (2020). Sentinel-1 InSAR measurements of deformation over discontinuous permafrost terrain, Northern Quebec, Canada. *Remote Sensing of Environment*, *248*, 111965. doi:10.1016/j.rse.2020.111965

Wang, Z. & Li, S. (1999). Detection of winter frost heaving of the active layer of Arctic permafrost using SAR differential interferograms. In *1999 IEEE International Geoscience and Remote Sensing Symposium. IGARSS'99 (Cat. No. 99ch36293), 28 June–2 July 1999, Hamburg, Germany* (Vol. 4, pp. 1946–1948). doi:10.1109/IGARSS.1999.774995

Watanabe, T., Matsuoka, N. & Christiansen, H. H. (2012). Mudboil and ice-wedge dynamics investigated by electrical resistivity tomography, ground temperatures and surface movements in Svalbard. *Geografiska Annaler: Series A, Physical Geography*, *94*(4), 445–457. doi:10.1111/j.1468-0459.2012.00470.x

Werner, C., Strozzi, T., Wiesmann, A. & Wegmüller, U. (2008). GAMMA's portable radar interferometer. In *Proc. of the 13th FIG Symposium on Deformation Measurement and Analysis* (pp. 1–10). LNEC, Lisbon, 2008 May 12–15.

Westermann, S., Peter, M., Langer, M., Schwamborn, G., Schirrmeister, L., Etzelmüller, B. & Boike, J. (2017). Transient modeling of the ground thermal conditions using satellite data in the Lena River delta, Siberia. *The Cryosphere*, *11*(3), 1441–1463. doi:10.5194/tc-11-1441-2017

Woodhouse, I. H. (2006). *Introduction to Microwave Remote Sensing*. CRC press.

Zebker, H. A. & Villasenor, J. (1992). Decorrelation in interferometric radar echoes. *IEEE*

Transactions on Geoscience and Remote Sensing, *30*(5), 950–959. doi:10.1109/36.175330

Zhang, T., Barry, R., Knowles, K., Heginbottom, J. & Brown, J. (2008). Statistics and characteristics of permafrost and ground-ice distribution in the Northern Hemisphere. *Polar Geography*, *31*(1-2), 47–68. doi:10.1080/10889370802175895

Zhang, T., Barry, R., Knowles, K., Ling, F. & Armstrong, R. (2003). Distribution of seasonally and perennially frozen ground in the Northern Hemisphere. In *Proc. of the 8th International Conference on Permafrost* (Vol. 2, pp. 1289–1294). AA Balkema Publishers. Zürich, Switzerland.

Zhang, T., Barry, R. G. & Armstrong, R. L. (2004). Application of Satellite Remote Sensing Techniques to Frozen Ground Studies. *Polar Geography*, *28*(3), 163–196. doi:10.1080/789610186

Zhang, X., Zhang, H., Wang, C., Tang, Y., Zhang, B., Wu, F., Wang, J. & Zhang, Z. (2019). Time-series InSAR monitoring of permafrost freeze-thaw seasonal displacement over Qinghai–Tibetan Plateau using Sentinel-1 data. *Remote Sensing*, *11*(9), 1000. doi:10.3390/rs11091000

Zwieback, S. & Hajnsek, I. (2014). The impact of vegetation growth on DInSAR coherence regions and estimated deformations. In *2014 IEEE Geoscience and Remote Sensing Symposium, 13–18 July 2014, Quebec, Canada* (pp. 966–969). doi:10.1109/IGARSS.2014.6946587

Zwieback, S., Hensley, S. & Hajnsek, I. (2015). Assessment of soil moisture effects on L-band radar interferometry. *Remote Sensing of Environment*, *164*, 77–89. doi:10.1016/j.rse.2015.04.012

Zwieback, S. & Meyer, F. J. (2021). Vulnerable top-of-permafrost ground ice indicated by remotely sensed late-season subsidence. *The Cryosphere*, *15*, 2041-–2055. doi:10.5194/tc-15-2041-2021

Appendices

Paper I: Seasonal dynamics of a permafrost landscape, Adventdalen, Svalbard, investigated by InSAR

Rouyet, L., Lauknes, T. R., Christiansen, H. H., Strand, S. M., Larsen, Y.

Published in *Remote Sensing of Environment*, *231*, 111236, 2019.

Article and Supplements:
https://doi.org/10.1016/j.rse.2019.111236

Remote Sensing of Environment 231 (2019) 111236

Contents lists available at ScienceDirect

Remote Sensing of Environment

journal homepage: www.elsevier.com/locate/rse

Seasonal dynamics of a permafrost landscape, Adventdalen, Svalbard, investigated by InSAR

Line Rouyet[a,b,c,*], Tom Rune Lauknes[a], Hanne H. Christiansen[c], Sarah M. Strand[c,d], Yngvar Larsen[a]

[a] NORCE Norwegian Research Centre AS, Siva Innovasjonssenter, P.O. Box 6434, 9294, Tromsø, Norway
[b] Department of Geosciences, The Arctic University of Norway (UiT), P.O. Box 6050, Langnes, 9037, Tromsø, Norway
[c] Arctic Geology Department, The University Centre in Svalbard (UNIS), P.O. Box 156, 9171, Longyearbyen, Norway
[d] Department of Geosciences, University of Oslo (UiO), P.O. Box 1047, Blindern, 0316, Oslo, Norway

ARTICLE INFO

Edited by Jing M. Chen

Keywords:
InSAR
Permafrost
Svalbard
Arctic
Thaw subsidence
Frost heave
Creep
Periglacial landforms

ABSTRACT

Nordenskiöld Land in Central Spitsbergen, Svalbard is characterized as a high latitude, high relief periglacial landscape with permafrost occurring both in mountains and lowlands. Freezing and thawing of the active layer causes seasonal frost heave and thaw subsidence, while permafrost-related mass-wasting processes induce downslope ground displacements on valley sides. Displacement rate varies spatially and temporally depending on environmental factors. In our study, we apply Satellite Synthetic Aperture Radar Interferometry (InSAR) to investigate the magnitude, spatial distribution and timing of seasonal ground displacements in and around Adventdalen using TerraSAR-X StripMap Mode (2009–2017) and Sentinel-1 Interferometric Wide Swath Mode (2015–2017) SAR images. First, we show that InSAR results from both sensors highlight consistent patterns and provide a comprehensive overview of the distribution of displacement rates. Secondly, two-dimensional (2D) TerraSAR-X InSAR results from combined ascending and descending geometries document the spatial variability of the vertical and east-west horizontal displacement rates for an average of nine thawing seasons. The remote sensing results are compared to a simplified geomorphological map enabling the identification of specific magnitudes and orientations of displacements for 14 selected geomorphological units. Finally, June to December 2017 6-day sampling interval Sentinel-1 time series was retrieved and compared to active layer ground temperatures from two boreholes. The timing of the subsidence and heave detected by InSAR matches the thawing and freeze-back periods measured by in-situ sensors. Our results highlight the value of InSAR to obtain landscape scale knowledge about the seasonal dynamics of complex periglacial environments.

1. Introduction

Permafrost is defined as subground material remaining at or below 0 °C for at least two consecutive years (French, 2007). It exists in approximately 24% of the terrestrial land areas of the Northern Hemisphere (Zhang et al., 2003). The uppermost part of the ground above the permafrost, which thaws in summer and refreezes in winter, is the active layer (Shur et al., 2005). During this seasonal freezing and thawing, the water-ice phase change in the ground can induce cm-scale heave and subsidence (Harris et al., 2011; Romanovsky et al., 2008). The magnitude of such displacements varies spatially depending on the active layer thickness (ALT), the amount and availability of water and the frost-susceptibility of the ground, which is largely controlled by grain size (Harris et al., 1995; Matsuoka et al., 2003; Zhang and Michalowski, 2015). On slopes, mass-wasting processes create various creeping landforms (e.g. rock glaciers, solifluction lobes/sheets) depending on climate, topography, ground material, water content, etc. (Haeberli et al., 2006; Matsuoka, 2001).

Climate change impacts the properties and distribution of frozen ground (Nelson et al., 2002), and changes of the ground thermal regime can modify the distribution, magnitude and timing of ground heave, subsidence and creep. Moreover, the seasonal freeze/thaw cycles affect slope stability (Blikra and Christiansen, 2014) and infrastructure (Harris et al., 2009). Thus, measuring ground dynamics in permafrost landscapes is important. Various monitoring networks exist that document ALT (Shiklomanov et al., 2012), permafrost thermal state (Romanovsky et al., 2010) and creep behaviour in rock glaciers (Delaloye et al., 2010), but these measurements are typically sparse and

* Corresponding author at: NORCE Norwegian Research Centre AS, P.O. Box 6434, Siva Innovasjonssenter, 9294 Tromsø, Norway.
E-mail address: line.rouyet@norceresearch.no (L. Rouyet).

https://doi.org/10.1016/j.rse.2019.111236
Received 2 October 2018; Received in revised form 29 May 2019; Accepted 1 June 2019
Available online 19 June 2019

unevenly distributed.

Satellite remote sensing provides a valuable tool to explore large and hard-to-access periglacial areas, allowing the Earth's surface to be imaged at high spatial and temporal resolution. Permafrost, as a subsurface condition, cannot be directly observed from satellites, but its impact on the surface can be documented by remote sensing (Bartsch et al., 2016; Trofaier et al., 2017). The use of Synthetic Aperture Radar (SAR) satellites is especially suitable in the Arctic as SAR imaging is independent of solar insolation and meteorological conditions. Repeat-pass Differential SAR Interferometry (InSAR) can detect ground displacements at millimetre to centimetre scales along the radar line-of-sight (LOS) and has been proven valuable for geoscience applications (Gabriel et al., 1989; Massonnet and Feigl, 1998).

InSAR in permafrost landscapes can measure creep on slopes and heave/subsidence in low-relief areas. Kenyi and Kaufmann (2001) and Rignot et al. (2002) used InSAR to measure rock glacier surface motion. Recent studies exploited the regional coverage of SAR satellites for inventorying creeping landforms (Barboux et al., 2014, 2015; Delaloye et al., 2007; Strozzi et al., 2004) or investigating temporal variations of velocity using long time series (Strozzi et al., 2010; Eriksen et al., 2018). The first cases of vertical seasonal displacements detected by InSAR in Alaska were documented by Rykhus and Lu (2008) and Wang and Li (1999). InSAR has then been used to map seasonal thaw subsidence, to identify terrain stability issues (Short et al., 2014; Wang et al., 2017; Wolfe et al., 2014) and to estimate ALT over large areas (Liu et al., 2012; Schaefer et al., 2015). Recent research modelled the relationship between InSAR displacements and climatic factors (Zhao et al., 2016), evidenced the importance of ground water content (Daout et al., 2017) and documented the inter-annual ground surface changes (Rudy et al., 2018; Strozzi et al., 2018). These studies show that InSAR is a promising technique for documenting slope movement processes and studying seasonal landscape dynamics related to ground freezing and thawing. However, little research has focused on landscapes combining high-relief and lowland permafrost-related processes. The capability of InSAR to inventory individual landforms based on their displacement patterns, and to contribute to geomorphological investigation in such complex environments, still needs to be investigated.

Here we study to what degree InSAR can identify seasonal frost- and thaw-related ground displacements in Svalbard. Based on pre-existing InSAR techniques, the novelty of our study is to combine the spatial and temporal measurement capability of complementary SAR datasets to provide new insights into the seasonal dynamics of the Svalbard landscape. Our study objectives are to (1) analyse the spatial distribution of 2D InSAR results documenting thaw subsidence and creep at the landscape scale, and study the variability of the displacement patterns for different geomorphological units; (2) investigate the temporal variations in InSAR displacements and compare the results to in situ ALT ground temperature measurements; (3) discuss the complementarity of two SAR sensors and the value of Sentinel-1 for studies of periglacial landscape dynamics.

2. Study area

The study area is centred in Adventdalen valley and adjacent parts of central Nordenskiöld Land, on the Spitsbergen Island, in the Svalbard archipelago (Fig. 1). The landscape has complex topography with mountain tops over 1000 m a.s.l. and glacially eroded – now periglacially dominated – valleys extending down to sea level (Norwegian Polar Institute, 2014a). The large-scale geomorphology is dominated by mountain plateaus with a sub-horizontal stratification of sedimentary bedrock (Dallmann et al., 2001; Major et al., 2001).

Following regional deglaciation, the landscape has been modified by weathering, local glaciation and periglacial processes (Gilbert et al., 2018; Härtel and Christiansen, 2014; Sørbel et al., 2001; Tolgensbakk et al., 2001). Bedrock is exposed mainly on rock noses in the upper steep part of the slopes composed of the resistant Firkanten formation of Tertiary sediments (Dallmann et al., 2001; Major et al., 2001). The plateaus are covered by extensive blockfields. The lower and central parts of Adventdalen and the neighbouring valleys (Fig. 1, right) are characterized by fluvial, alluvial and eolian (loess) deposits with typical permafrost-related landforms, such as ice-wedge polygons and pingos (Sørbel et al., 2001). The valley slopes are covered by allochthonous weathered material, colluvium and alluvial fans, that have been further reworked by mass-wasting processes, such as by debris-flows (André, 1995), solifluction (Harris et al., 2011), snow avalanche activity (Eckerstorfer et al., 2013), and talus-derived rock glaciers (Humlum, 2000).

Svalbard is characterized by a polar-tundra climate (Köppen–Geiger classification, Peel et al., 2007) and has continuous permafrost with a thickness varying from < 100 m in valley bottoms and coastal areas to 500 m in the mountains (Humlum et al., 2003). Gilbert et al. (2018) highlighted the complex Holocene history of sedimentary infilling and permafrost aggradation in Adventdalen, suggesting that permafrost is predominantly epigenetic. Considering the period 1912–2011, air temperature records show an increase by 2.5 °C at the Svalbard airport meteorological station. During the last decades, the average increase reached 1.0–1.2 °C per decade, but 2–3 °C per decade during the winter season (Førland et al., 2011). Ground temperature monitoring in boreholes since 2008 indicates that the permafrost has warmed from 0.06 to 0.15 °C/year (Isaksen et al., 2019). ALT increased by 0.6 cm/year in lower Adventdalen (UNISCALM monitoring site) based on 2000–2017 measurements (Isaksen et al., 2019). Modelling for the twenty-first century suggests future increases of ground temperatures and ALT (Etzelmüller et al., 2011; Isaksen et al., 2019). However, the intra- and inter-annual meteorological variability, as well as the influence of local conditions (water content, ground characteristics, snow cover, vegetation) are not negligible (Christiansen and Humlum, 2008; Christiansen et al., 2013; Harris et al., 2011; Schuh et al., 2017). ALT is generally in the range of 100 to 200 cm (Isaksen et al., 2019) and the amount of ice in the upper permafrost has high spatial variability (Cable et al., 2018; Christiansen et al., 2010).

The study area corresponds to the overlap of the available SAR datasets and the geomorphological map (see Section 3). The processed SAR areas were chosen to maximize the comparable area. The north-eastern part of the geomorphological map is not covered by the TerraSAR-X scenes in ascending geometry leading to a slightly reduced overlap area (Fig. 1, right). The size of the geomorphologically mapped area is approximately 331 km^2, and the overlap area is about 297 km^2.

3. Data and methods

3.1. SAR data

SAR datasets from the TerraSAR-X (TSX) satellite (2009–2017) and the Sentinel-1 (S1) satellites of the European Union's Copernicus Programme (2015–2017) were used to compare the results and to exploit their complementary radar wavelengths, spatial coverages, spatial resolutions, revisit times and data availability. We selected snow-free scenes from TSX in StripMap (SM) mode in ascending and descending geometries, and from S1 in Interferometric Wide Swath (IWS) mode in ascending geometry only (before 2018, IWS mode in descending geometry was not available over Svalbard). Characteristics of the datasets are further described in Table 1.

3.2. InSAR processing

InSAR results were obtained using the NORCE GSAR software (Larsen et al., 2005). Parameters used for InSAR processing are summarized in Table S1 (Supplementary material). We co-registered and multi-looked single-look complex (SLC) images using a range/azimuth multi-looking factor of 5 × 5 (TSX) and 8 × 2 (S1), providing a ground

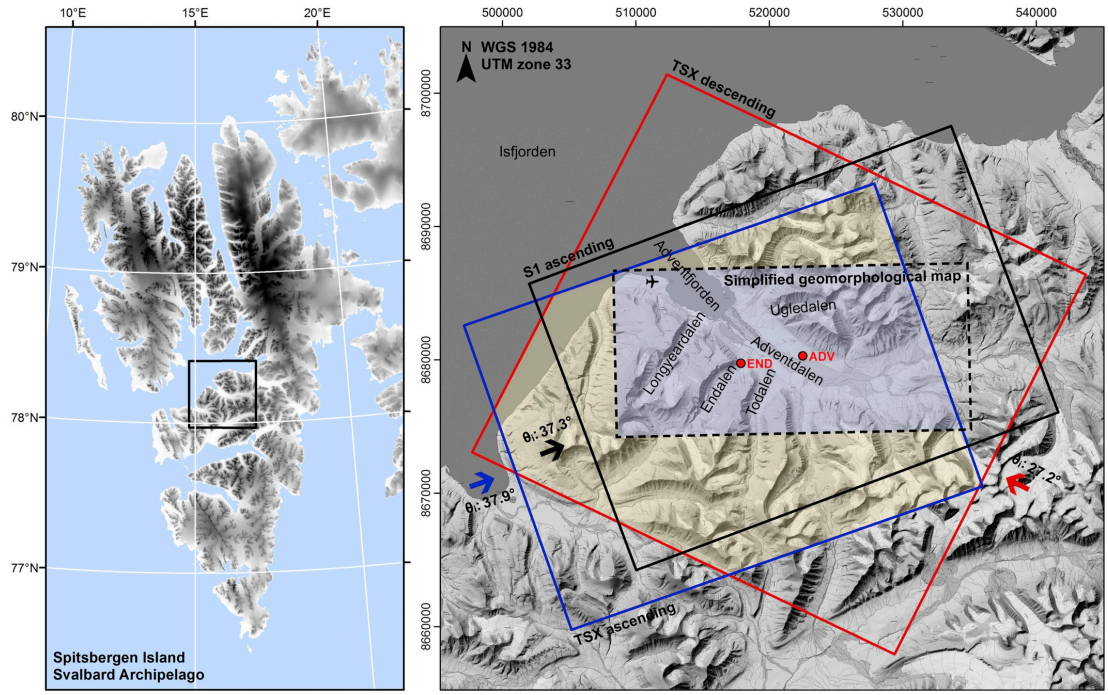

Fig. 1. Left: Location of the study area on Spitsbergen Island in the Svalbard archipelago. Black square: extent of the map shown in the right part of the figure. Right: Extent of the processed areas and the geomorphological map (blue rectangle: TerraSAR-X ascending; red rectangle: TerraSAR-X descending; solid black rectangle: Sentinel-1 ascending; dashed black rectangle: simplified geomorphological map). The common area of both TerraSAR-X geometries is shown in light yellow. The overlap with the geomorphological map is shown in light blue. The arrows indicate the line-of-sight (LOS) orientations (label θ_i: incidence angles). The red dots mark the location of two boreholes continuously monitoring ground temperature (ADV: Adventdalen, END: Endalen). Backgrounds: shaded relief from 20 m resolution Digital Elevation Model (Norwegian Polar Institute, 2014a) and topographical map (Norwegian Polar Institute, 2014b). (For interpretation of the references to colour in this figure legend, the reader is referred to the web version of this article.)

resolution of approximately 15 × 15 m (TSX) and 40 × 40 m (S1). Due to the large variety of processes under study and the high velocity expected on several landforms (e.g. rock glaciers, debris-covered glaciers), interferograms were generated with a maximal temporal baseline of 22 days (TSX) and 24 days (S1) to preserve coherence and minimize phase ambiguities. Aliasing occurs when the displacement rate exceeds a quarter of the wavelength during the time interval of the generated interferograms, i.e. 0.78 cm in 11–22 days for TSX and 1.39 cm in 6–24 days for S1. The detectable LOS velocities in this specific study are thus 0.4–0.7 mm/day for TSX and 0.6–2.3 mm/day for S1. The spatial baseline has not been restricted; the effective maximal values being clearly under the critical baseline limit (Table S1, column 4). For TSX, the interferogram stacks in both geometries include SAR combinations during the thawing periods (June to September 2009–2017). For S1, we focused on two different periods, processed using different InSAR methods (Table S1, column 2). First, we included SAR combinations during the thawing periods (June–September 2015–2017) for comparison with TSX results. Secondly, we used scenes from June to December 2017 to document the thawing period (June to October) and the start of the freezing period (October to December). We ended the series in December because snowfall later in winter leads to decorrelation. The noise-level was reduced in all interferograms by applying a spatially adaptive coherence-dependent Goldstein filter (Goldstein and Werner, 1998; Baran et al., 2003). Strongly decorrelated interferograms were removed and pixels affected by layover were masked out. The contribution from the stratified atmosphere was mitigated by a data driven approach where we fit a linear relation between residual phase and topography (Cavalié et al., 2007) using a

Table 1
Characteristics of SAR datasets from TerraSAR-X and Sentinel-1 satellites.

SAR sensor	SAR mode/geometry	Frequency band	Revisit time	Number of selected scenes	Observation period (first–last selected scenes)	LOS (orientation/ incidence angle)
TerraSAR-X	StripMap (SM) Ascending	X (λ: 3.11 cm)	11 days	67	22.08.2009–28.09.2017	70.9° 37.9°
TerraSAR-X	StripMap (SM) Descending	X (λ: 3.11 cm)	11 days	65	14.07.2009–03.10.2017	297.5° 27.2°
Sentinel-1	Interferometric Wide Swath (IWS) Ascending	C (λ: 5.55 cm)	12 days until 25.09.2016 6 days after	46	14.08.2015–01.12.2017	69.5° 37.3°

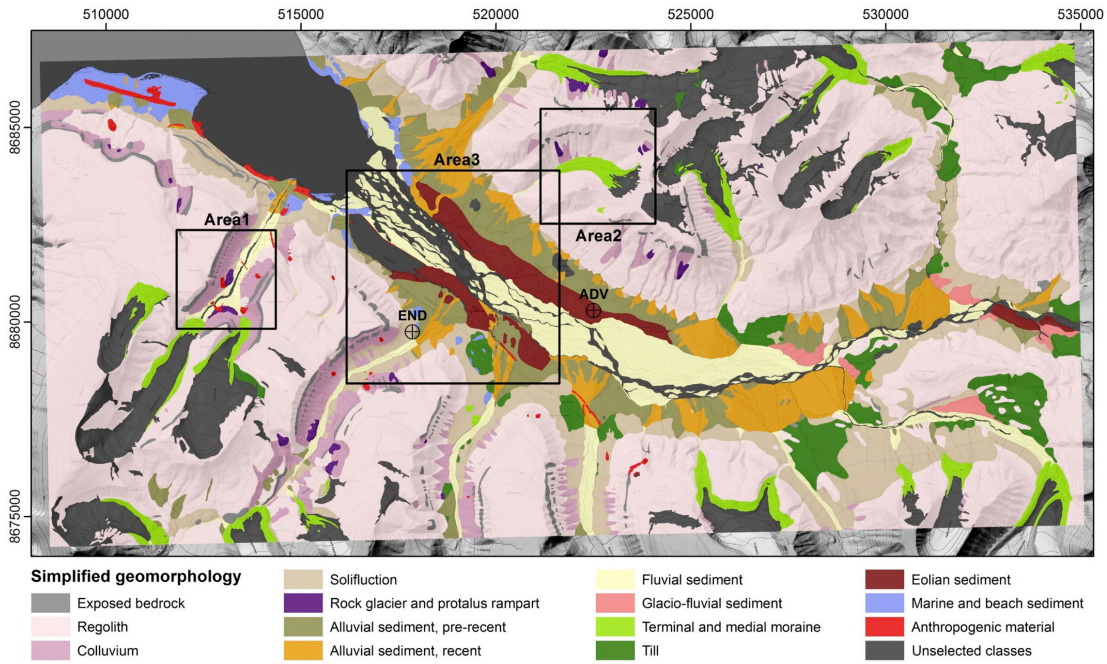

Fig. 2. Simplified geomorphological map. Based on map from Härtel and Christiansen (2014) and Tolgensbakk et al. (2001). Black squares indicate the location of the areas shown in Fig. 4. The black crossed circles mark the location of two boreholes (ADV: Adventdalen, END: Endalen). Background: topographical map (Norwegian Polar Institute, 2014b). Location of the 3000 selected InSAR pixels per geomorphological unit is shown in Fig. S5 (Supplementary material).

Digital Elevation Model (DEM) at 20 m resolution (Norwegian Polar Institute, 2014a). Based on a redundant set of interferograms, we further solved for the stratified delay per scene using a network-based approach (Lauknes, 2011). Pixels affected by noise were removed by applying a coherence filter (coherence above 0.3–0.48 in 50% of the interferograms depending on the dataset, Table S1, column 6). The interferograms were unwrapped using the SNAPHU software (Chen and Zebker, 2002) and we performed a second manual quality check of the unwrapped interferograms to remove those affected by major unwrapping errors. For the S1 processing based only on June to December 2017 scenes, we additionally corrected the interferograms by averaging all pairs centred on common acquisitions and using the redundancy to iteratively estimate the atmospheric contribution of each scene (Tymofyeyeva and Fialko, 2015). Different reference points were tested and a common reference for all datasets was chosen in an area assumed to be stable on the main building of Svalbard airport (Table S1, column 7; black star in Figs. 3, 5 and 6). All InSAR results are spatially relative to this reference point. Sets of 71–99 selected interferograms, depending on the dataset, were used to retrieve ground displacement information (Table S1, column 5 and Figs. S1–S4 in Supplementary material).

Using maximal temporal baselines of 22 days (TSX) and 24 days (S1), the multi-year datasets include gaps during the winter periods. To take advantage of the large stacks of interferograms from disconnected subsets, we applied a multi-year averaging technique (stacking) based on interferograms from the thawing periods (2009–2017 for TSX and 2015–2017 for S1). The applied stacking is a simple averaging of all selected interferograms weighted by the temporal intervals between the scenes. InSAR stacking reduces the atmospheric effects, assuming temporally uncorrelated tropospheric effects (Lyons and Sandwell, 2003; Peltzer et al., 2001; Sandwell and Price, 1998). Using S1 interferograms, we selected a temporally connected set of interferograms between June–December 2017 and we estimated displacement time series using the Small Baseline Subset (SBAS) method (Berardino et al., 2002). The phase inversion was performed using a L1-norm-based cost function, which is more robust than L2-norm with respect to unwrapping errors (Lauknes et al., 2011). For the atmospheric filtering, we used a spatial filter of 500 m spatial filter and a temporal filter of 12 days. All results were geocoded using a DEM at 20 m resolution (Norwegian Polar Institute, 2014a).

InSAR stacking results for each dataset (TSX ascending, TSX descending, S1 ascending) correspond to one-dimensional (1D) displacement rates along the LOS (Table 1, column 7), based on several years. All maps based on stacking results highlight the average multi-year displacement rates during the 4-month thawing periods (June—September), expressed in mm/summer. The results from ascending and descending geometries were combined to estimate 2-dimensional (2D) vectors in the plane spanned by the ascending and descending LOS directions (Eriksen et al., 2017). The results were decomposed into vertical (upwards-downwards) and horizontal (eastwards-westwards, E-W) components. 2D InSAR results were retrieved for TSX dataset only, due to unavailability of S1 IWS in descending geometry before 2018. It should be noted that the radar is still blind to movement orthogonal to the LOS plane, which leads to an underestimation of the displacement rates in case of a large horizontal component in the north-south (N-S) direction. To avoid misinterpretation when comparing InSAR to geomorphology, we masked out pixels in areas where a significant horizontal component towards N or S is expected (Eckerstorfer et al., 2018). The mask consists of areas with slope angles over 5° and azimuth angles ± 22.5° around 360° (N) and 180° (S) (337.5–22.5° and 157.5–202.5°). All areas with slope angles below 5° were included assuming that they are mainly affected by vertical displacements. To keep a large amount of pixels for the comparison between InSAR and geomorphology, we included areas with NE, NW, SE and SW aspects

Table 2
Information about boreholes, their monitoring instrumentation and the temperature data used in this study.

Borehole	Coordinates (UTM 33N) and altitude	Slope angle and orientation	Geomorphological unit	Total depth	Temperature measurements and additional information
ADV	N 8680294 E 522504 16.7 m a.s.l.	0.4° 293.7° (WNW)	Eolian sediment	3 m	Sensor spacing: every ~0.25 m until 2.5 m depth Data logging: every hour Missing data in November–December 2017
END	N 8679744 E 517857 49.6 m a.s.l.	8.0° 85.8° (E)	Solifluction	20 m	Sensor spacing: every ~0.25 m until 10 m depth, every 2–4 m until 20 m Data logging: every 6 h The ground surface has subsided 0.25 m since 2008, exposing the upper sensors closer to the ground.

assuming that they have a significant E-W displacement component. As a drawback, some areas may be affected by underestimation if the displacements also include a significant N-S component.

The S1 SBAS results provide time series of LOS displacements temporally relative to the first scene of the set (10.06.2017) and spatially relative to the reference point (Table S1, column 7). Based on ground temperature data and onset of frost heave on InSAR time series, we estimated an average initiation date of ground freezing (02.10.2017) used to map separately the ground displacements of the thawing period (102 days between June and October 2017) and the start of the freezing period (60 days between October and December 2017). In practice, the onset of frost heave varies spatially, but a unique date was chosen to present the results in a homogenous way.

3.3. Comparing 2D InSAR to geomorphology

The TSX 2D InSAR displacement rates were compared to a detailed geomorphological map available for this area (Härtel and Christiansen, 2014), which is the most updated version of a geomorphological and quaternary geological map in Adventdalen (modified from Tolgensbakk et al., 2001). Geomorphological units were extracted, simplified and partly renamed from the existing maps to allow for direct comparison with InSAR (Fig. 2). Punctual (e.g. individual boulders or forms) and linear (e.g. gullies or ridges) forms were discarded. Initially separated units 'Weathered material, autochthonous' and 'Weathered material, allochthonous' were merged into 'Regolith', just as 'Fluvial material, recent' and 'Fluvial material, pre-recent' and 'Braided-river plain' were merged into 'Fluvial sediment'. The classes 'Sea and lake', 'Foreshore flat' and 'Glacier' are not taken into account (unselected, dark grey in Fig. 2) as InSAR provides no relevant information on these surfaces. The units 'Alluvial fans' and 'Talus cones' are not differentiated and are displayed according to their sediment type 'Alluvial sediment, recent', 'Alluvial sediment, pre-recent' or 'Colluvium' respectively. For statistical reasons (too few comparable pixels), the units 'Organic material' and 'Pingo' were not taken into account (unselected, dark grey in Fig. 2). Solifluction is defined as surficial material in the original maps despite that it is a landform, not a material type. It is called 'Solifluction' in the simplified map. The final simplified map is composed of 14 units including 11 corresponding to natural sediments and bedrock, two corresponding to landforms ('Solifluction' and 'Rock glacier and protalus rampart') and one corresponding to artificial surficial material ('Anthropogenic material').

The 14 units have large differences in spatial extent, from approximately 1 km^2 of 'Rock glacier and protalus rampart' to approximately 158 km^2 of 'Regolith'. In addition, the coverage of InSAR maps is not continuous due to low coherence and layover/shadow areas that have been masked out. This causes high variability in the distribution of InSAR pixel numbers corresponding to the different geomorphological units. For further comparison, we randomly selected 3000 2D InSAR pixels per unit following the methodology described by Eckerstorfer et al. (2018). The location of the selected pixels is shown in Fig. S5 (Supplementary material). For each unit, the median, first and third quartiles, inter-quartile range, maximal/minimal values were calculated. Significance tests (F-test of Fisher and Welch two sample *t*-tests) were performed to compare the variance and mean of each geomorphological unit and estimate if they significantly differ. The pixel frequency per class of 10 mm displacement rate was analysed for the vertical and horizontal components separately and scatter plots combining the two components were created to visualise the 2D behaviours of each single pixel.

3.4. Comparing InSAR time series to ground temperature

The S1 InSAR time series was compared to ground temperature data from two boreholes in the central part of the study area: Adventdalen (ADV) and Endalen (END) (Figs. 1 and 2). ADV is located north of the river flowing in Adventdalen (Adventelva) in a flat area covered by eolian sediment. END is located on the north-western slope of Endalen affected by solifluction. Information about the boreholes is summarized in Table 2. The analysis consists of a comparison of timing and trends between InSAR and temperature time series. Due to the intrinsic differences of physical measures and data properties (unit, temporal sampling, spatial resolution, etc.), the analysis is based on a visual interpretation of the respective trends.

4. Results

4.1. InSAR results

The results of the multi-year InSAR stacking for each SAR dataset provide a spatial overview of the average LOS displacement rates based on three (S1) to nine (TSX) thawing seasons (Fig. 3). Fig. 4 shows detailed results for three smaller areas. For comparison, we focus on TSX and S1 results both in ascending geometry, expressed in average displacements (mm) along their respective LOS during the 4-month thawing periods (summer). The results from TSX descending stacking are available in the Supplementary material (Fig. S6). Positive values show an increase of the sensor-to-ground distance (displacements away from the radar), whereas negative values show a decrease of the sensor-to-ground distance (displacements towards the radar). As indicated in Table 1 and with black arrows in Figs. 3 and 4, the LOS is quite similar for both datasets.

At a regional scale, the main patterns on both maps are similar, both in terms of magnitude of displacements and spatial variations. Thanks to its C-band sensor and 6-day revisit time, S1 provides a better spatial coverage in fast moving and moist ground in Adventdalen due to higher coherence. The sediments on the terraces surrounding the Adventdalen braided river are largely settling due to the phase change from ice to water in the active layer. Maximal average values are up to ca 230 mm/summer (Fig. 4, area 3), but the results highlight spatial variations partly following the delineation of geomorphological units. In the adjacent valley bottoms (Longyeardalen, Endalen, Todalen) and in low flat areas such as in the north-western part of the study area (Svalbard airport area), displacement rates are generally lower. On west-facing

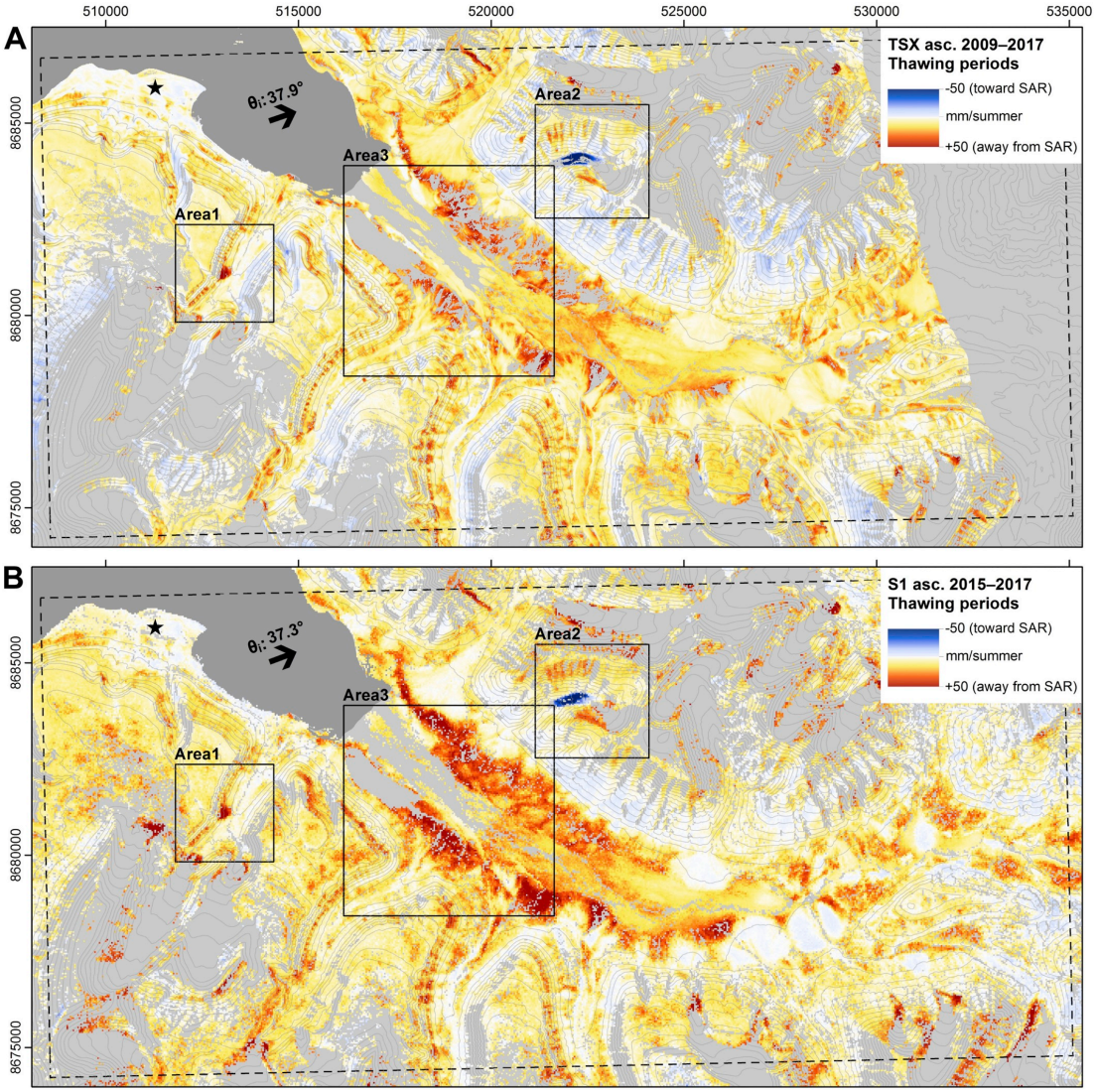

Fig. 3. Multi-year InSAR stacking LOS displacement rates during the 4-month thawing periods (June to September). A. Results from TerraSAR-X stacking, StripMap Mode, ascending geometry. B. Results from Sentinel-1 stacking, Interferometric Swath Mode, ascending geometry. Note that the observation period is not similar (2009–2017 for TerraSAR-X, 2015–2017 for Sentinel-1) and that the colour scale is saturated for visualisation. Black arrows: LOS orientations (label θ_i: incidence angles). Black squares: areas shown in Fig. 4. Dashed black rectangle: extent of geomorphological map shown in Fig. 2. Black star: reference point (Svalbard airport building). Background: land/sea masks and 50 m contour lines (Norwegian Polar Institute, 2014b).

slopes, little displacement is detected due to the unfavourable orientation compared to the ascending LOS. Some areas show a decrease of sensor-to-ground distance highlighting a horizontal component towards the radar. The most obvious example is located in Ugledalen where a debris-covered glacier is moving towards the radar with maximal average values up to ca 370 mm/summer (Fig. 4, area 2). On east-facing slopes, more active areas are mapped due to the more favourable slope orientation compared to the LOS. These displacements away from the radar can be associated with rock instabilities on rock noses, regolith and colluvium in upper parts of the slopes, and creep processes on solifluction sheets, rock glaciers and protalus ramparts in the middle and lower parts of the slopes (Fig. 4, areas 1–3). The most obvious example is located in Longyeardalen and corresponds to a rock glacier moving towards east (away from the radar) with maximal average values up to ca 320 mm/summer (Fig. 4, area 1). Areas without any InSAR result (grey in Figs. 3 and 4) are either affected by significant changes in surface properties due to e.g. moisture, snow or fast displacements (coherence under chosen thresholds), or by layover or shadow (see Section 3.2). The differences between TSX and S1 results are related to intrinsic differences between the sensors and datasets

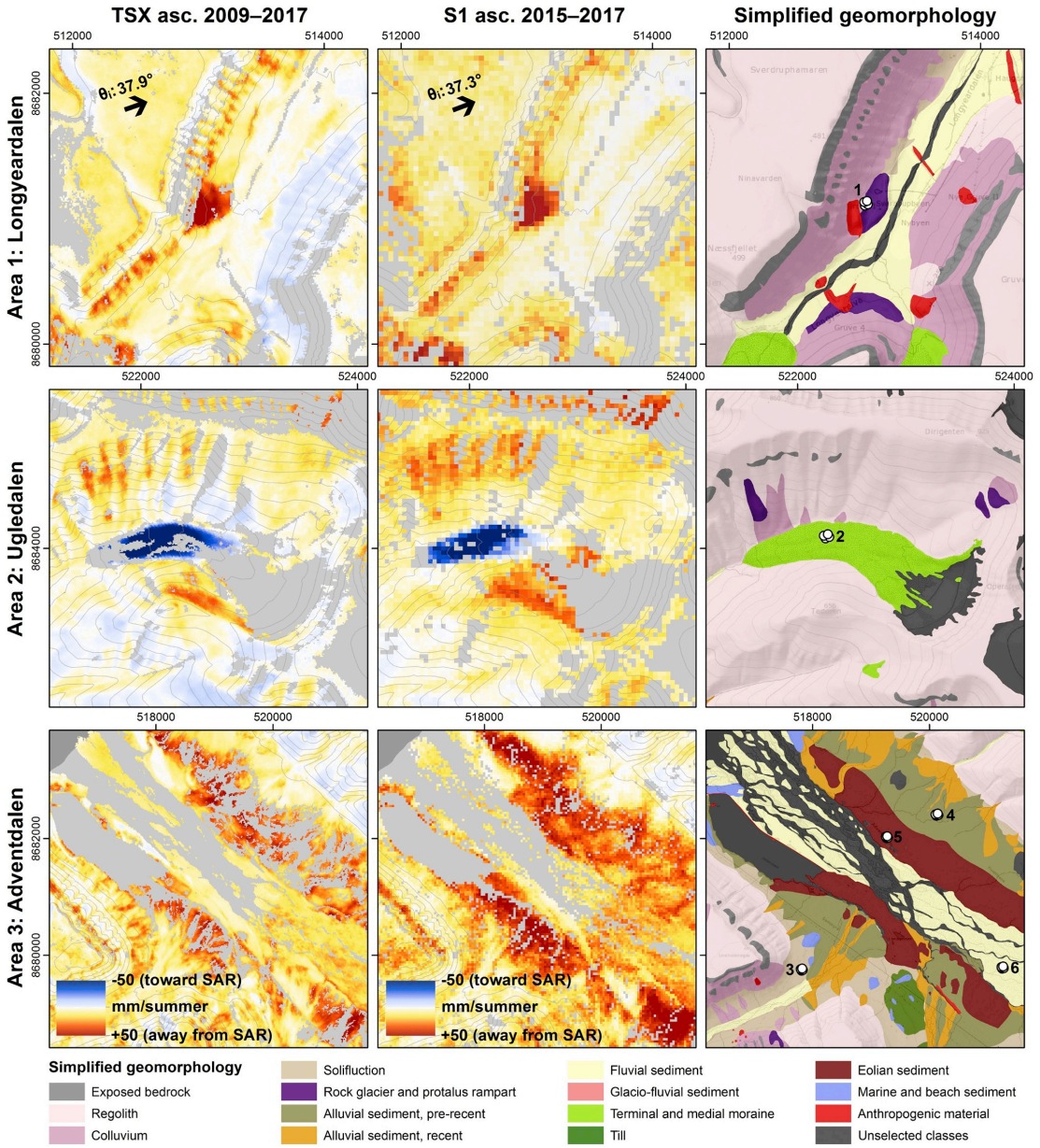

Fig. 4. Comparison of TerraSAR-X and Sentinel-1 ascending multi-year stacking LOS displacement rates during the 4-month thawing periods (June to September 2009–2017 for TerraSAR-X, 2015–2017 for Sentinel-1) with the simplified geomorphological map in areas of measured high displacement rates. Locations of the areas are shown in Figs. 2 and 3. In first and second columns: black arrows show the LOS orientations (label θ_i: incidence angles). In third column: circled white dots show the location of time series presented in Fig. 7.

(observation periods, temporal and spatial resolutions, sensor wavelengths, LOS, etc.) and are further discussed in Section 5.1.

Fig. 5 shows the results of the vertical (upwards-downwards, Fig. 5, A) and horizontal (eastwards-westwards, Fig. 5, B) decomposition based on the combination of TSX ascending and descending InSAR stacking. The map of the magnitude of 2D vectors is available in the Supplementary material (Fig. S7). The steep incidence angle of the descending geometry (Table 1) induces extensive layover on slopes facing the radar, which unfortunately leads to a reduced common 2D InSAR area on east-facing slopes. As explained in Section 3.2, N-S slopes affected by rate underestimation are masked out (black mask, Fig. 5). The results show settlement caused by thaw subsidence at variable rate

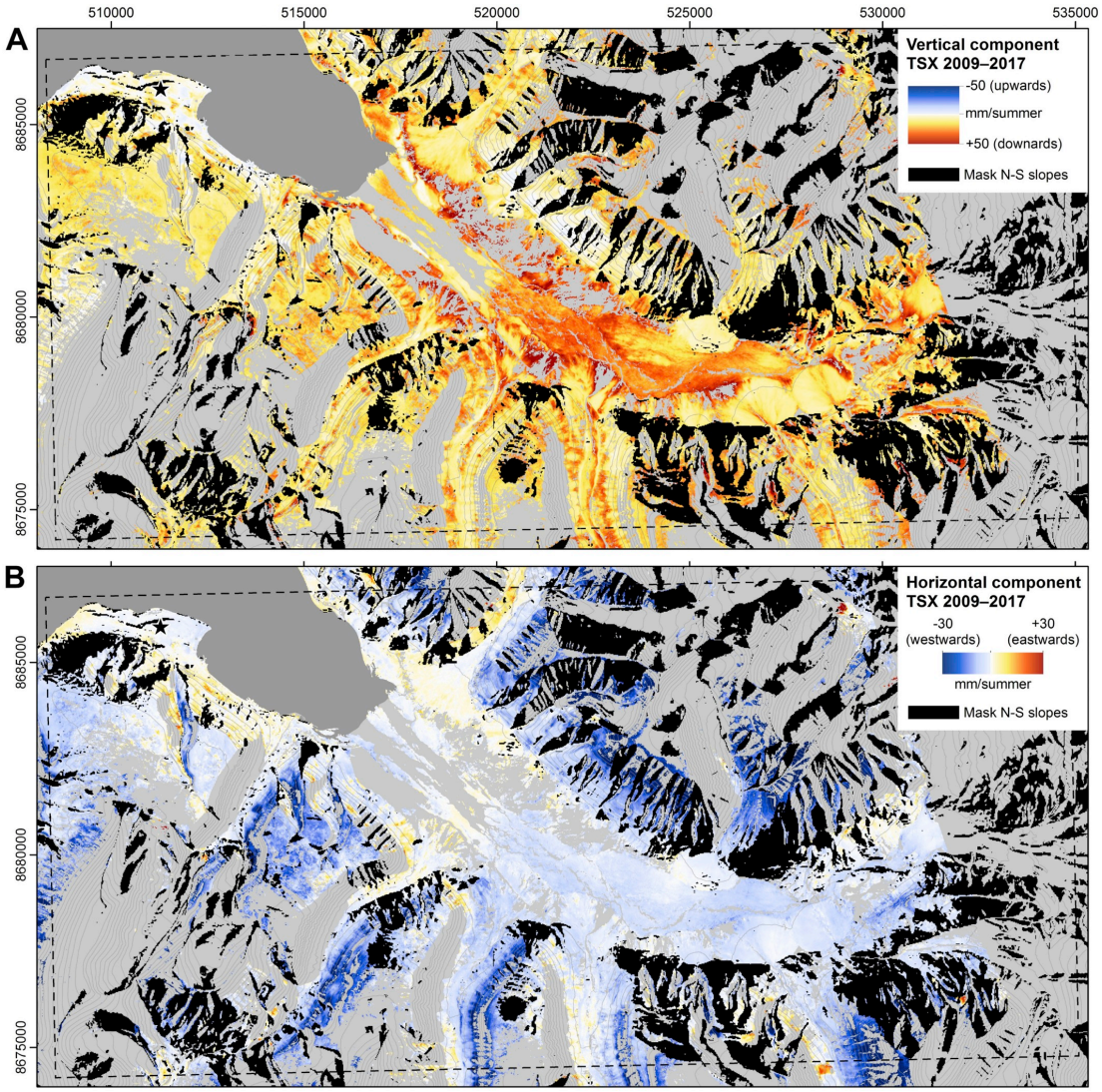

Fig. 5. Vertical/horizontal decomposition based on combination of TerraSAR-X ascending and descending multi-year stacking displacement rates during the 4-month thawing periods (June to September 2009–2017). A. Vertical component. B. Horizontal component. Black star: reference point (Svalbard airport building). The magnitude of 2D vectors is shown in Fig. S7 (Supplementary material). Background: land/sea masks and 50 m contour lines (Norwegian Polar Institute, 2014b).

over flat areas and the combination of vertical and horizontal displacement components on slopes. As expected, flat areas in valley bottoms, on mountain plateaus and on the lowland raised marine deposits have a low horizontal component of displacement.

The S1 SBAS time series retrieved between June and December 2017 highlights the change from subsidence to heave in beginning of October in most of the flat areas (Fig. 6). Between June and beginning of October, the sensor-to-ground distance generally increased on flat areas (Fig. 6, A) due to thaw subsidence, while it generally decreased from September to December due to frost heave (Fig. 6, B). On the slopes, the time series does not necessarily follow the same subsidence and heave pattern due to gravity-driven processes and their impact on the detected displacements with respect to the LOS. Lower subsidence and heave amplitude can also be explained by less frost-susceptible coarse material and lower water content as it drains downhills and accumulates in valley bottoms. It should be noted that even after having masked out low coherence pixels, the quality of the results on the top of the plateaus is variable. Especially in the south-western part of the area, large variations of values at short intervals in space and time indicate that pixels may be affected by noise most likely related to changes in surface properties due to snow and moisture. This is further discussed in Section 5.1.

S1 2017 time series on selected sediments and landforms (Fig. 7) shows clear seasonal variability in the movement pattern. The

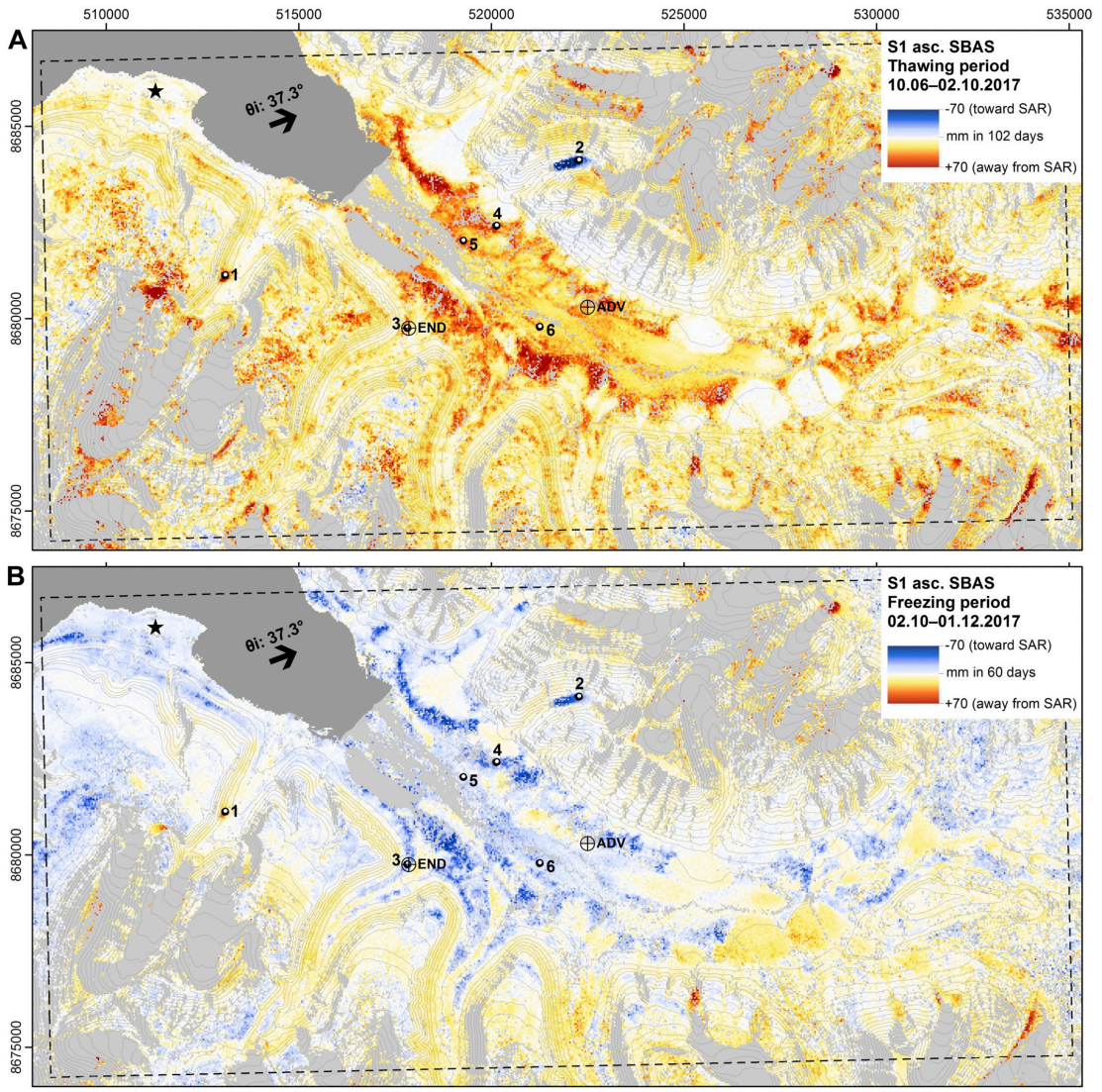

Fig. 6. Total Sentinel-1 SBAS LOS displacements during the thawing period (June to October) and the start of the freezing period (October to December) 2017. A. 10.06 to 02.10.2017 total LOS displacements highlighting thaw subsidence, especially in the lowlands. B. 02.10 to 01.12.2017 total LOS displacements highlighting frost heave, especially in the lowlands. Black arrows: LOS orientations (label θ_i: incidence angles). Circled white dots: location of time series presented in Fig. 7. Black crossed circles: location of Endalen (END) and Adventdalen (ADV) boreholes. Black star: reference point (Svalbard airport building). Background: land/sea masks and 50 m contour lines (Norwegian Polar Institute, 2014b).

comparison of four neighbouring pixels shows the consistency of the displacement patterns and the magnitude of the spatial variability for an 80 m × 80 m window. Located on slopes with 10–14° angles, the rock glacier and the debris-covered glacier (Fig. 7A, graphs 1 and 2) are mainly controlled by gravity-driven processes. The velocity varied during the measurement period (Fig. 7B, lines 1 and 2) but no clear trend related to the active layer thawing and freezing can be highlighted due to the superimposed downslope creeping process. LOS displacements reached 80 to 120 mm in 6 months (away from the radar for the rock glacier in Longyeardalen due to its eastward orientation, towards the radar for the debris-covered glacier due to its westward orientation). For the solifluction sheet (Fig. 7A, graph 3), creep is also expected due to the 8.8° slope angle at this location, but the subsidence and heave related to the active layer thawing and freezing are large enough to dominate the measured displacement pattern. Velocity was at its maximum during the initial thawing period from mid-June to early July (Fig. 7B, line 3). It then decreased and stayed relatively stable through the summer before it increased again between the end of September and mid-October. Graphs 4–6 (Fig. 7A) show examples of different sediments in the bottom of Adventdalen. Due to the nearly flat

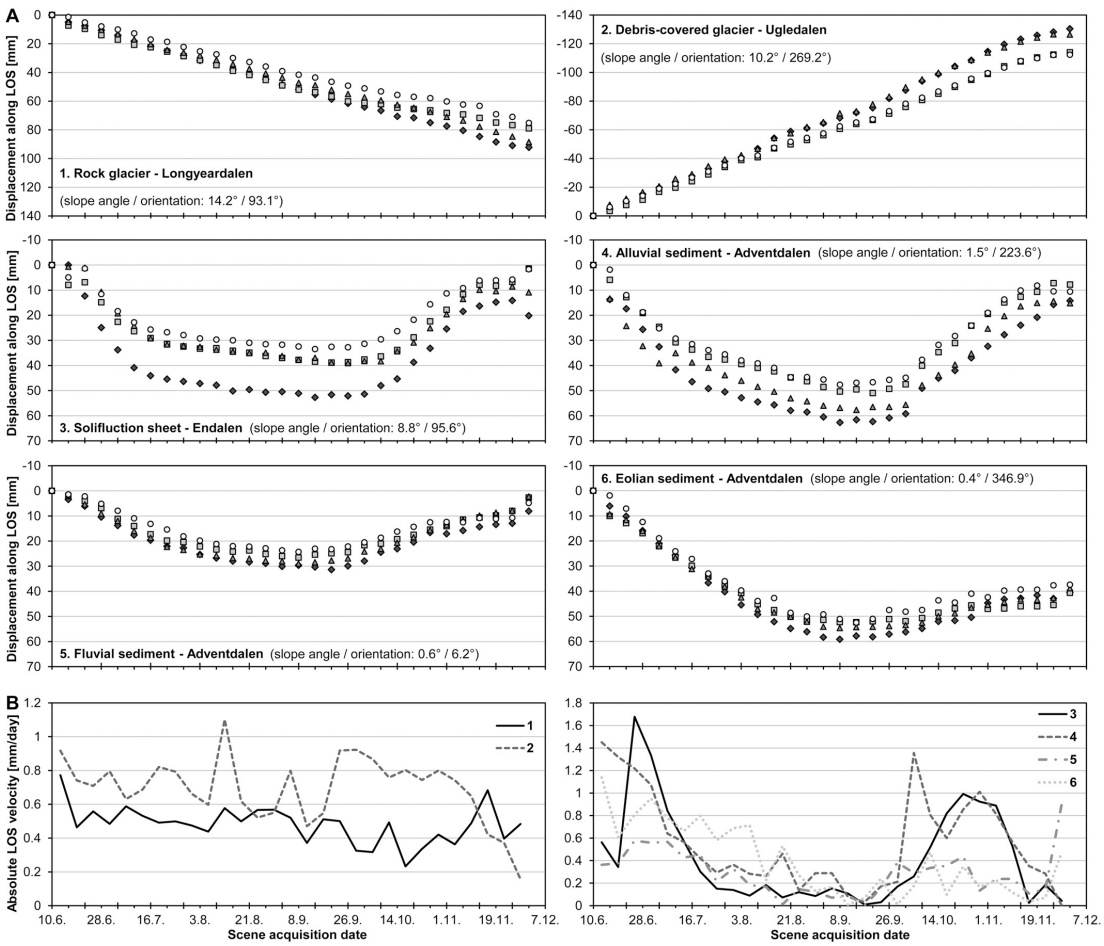

Fig. 7. A. Sentinel-1 SBAS June to December 2017 LOS displacement time series at six locations with different sediments and landforms. The four different symbols show the time series for four neighbouring pixels, highlighting the magnitude of the spatial variability for an 80 m × 80 m window. Time series 1. and 3. are located on east-facing slopes, 2. on west-facing slope, 3–6 on flat Adventdalen valley bottom. Locations of the time series are represented by the white dots in Figs. 4 and 6. B. Absolute LOS velocity between consecutive acquisitions based on the average of the four neighbouring pixels at the six selected locations. 1. and 2. are landforms mainly controlled by gravity-driven processes and thus dominated by a downslope pattern, 3–6 are landforms mainly controlled by the active layer dynamics and thus dominated by a subsidence/heave pattern. Note that the range of values on vertical axes varies for the different graphs.

topography (slope angles: 0.4–1.5°), the measurements are clearly dominated by thaw subsidence and frost heave at different magnitudes. At its maximum, the detected subsidence reached 60 mm in alluvial (Fig. 7A, graph 4) and eolian sediments (Fig. 7A, graph 6), but only 30 mm in fluvial sediment (Fig. 7A, graph 5). For all subsidence/heave-dominated time series (Fig. 7B, lines 3–6), velocity was high in June and early July and decreased later in the summer. The ground surface was generally stable in September, and the heave started quickly at the beginning of October before slowing down in mid-November. Even if the different landforms highlight a similar trend, the magnitude varies significantly depending on the location. The identification of specific displacement rates for different geomorphological units highlights the need for more detailed investigation of the InSAR spatial variability, presented in Section 4.2. Further interpretations of the temporal variations are presented in Section 4.3.

4.2. Comparing 2D InSAR to geomorphology

Statistics of the 2D InSAR average displacements during the thawing seasons 2009–2017 are analysed for each of the 14 selected geomorphological units (see Section 3.3). Three main observations show that there is a relationship between the magnitude of the 2D InSAR displacements during the thawing periods and the geomorphological units (Fig. 8): (1) the median value per unit varies between 4.5 mm/summer and 29.5 mm/summer, with minimum values in 'Marine and beach sediment' and 'Anthropogenic material' and a maximum value in 'Eolian sediment'; (2) 'Rock glacier and protalus rampart', 'Terminal and medial moraine', and 'Eolian sediment' have a median > 5 mm/summer over the median of all pixels, while 'Marine and beach sediment' and 'Anthropogenic material' have a median > 5 mm/summer below; (3) the interquartile range (IQR) varies between certain units: 'Terminal and medial moraine' and 'Eolian sediment' have an IQR at

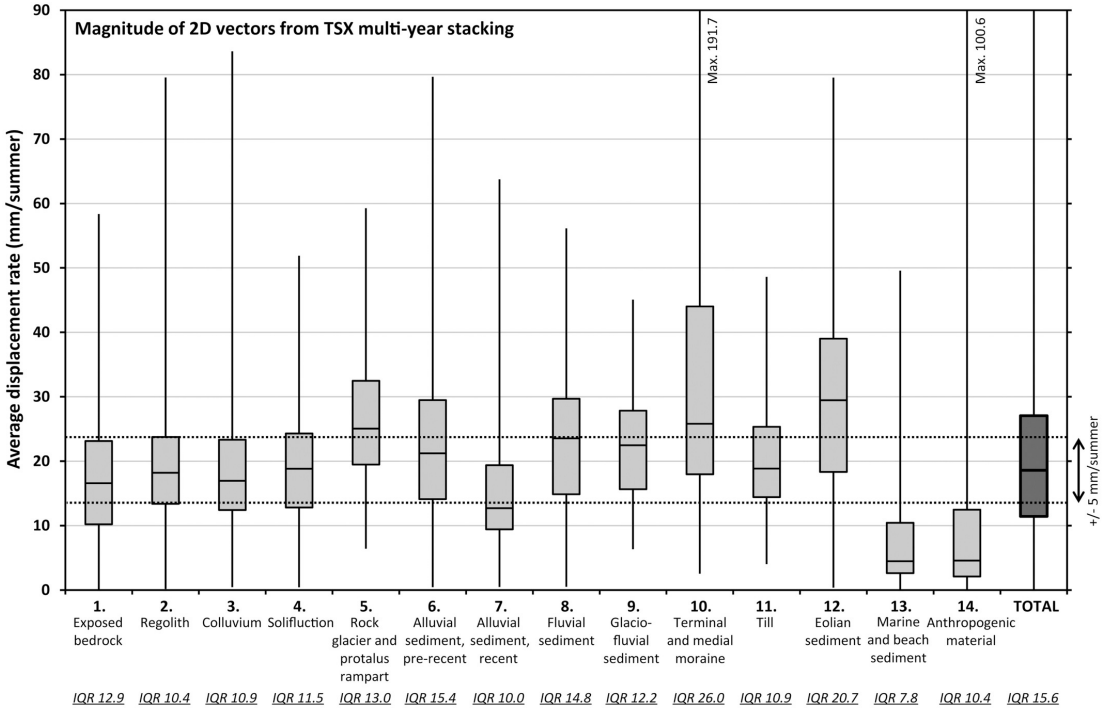

Fig. 8. Magnitude of 2D vectors from TerraSAR-X multi-year stacking for each geomorphological unit during the 4-month thawing periods (June–September 2009–2017). For scaling and visualisation purposes, the maximum displacement rates of 'Terminal and medial moraine' and 'Anthropogenic material' are higher than the upper limit shown. The last box on the right corresponds to statistics of all 42,000 pixels together. The dotted line shows the ± 5 mm/summer limits over/under the median of all pixels. IQR values are the interquartile range for each unit. Note that the bedrock is exposed mainly in rock noses in the upper steep part of the slopes. As some of these areas are unstable, high displacement rates are expected.

least 5 mm/summer higher than for the overall pixel average. 'Regolith', 'Alluvial sediment, recent', 'Marine and beach sediment' and 'Anthropogenic material' have an IQR at least 5 mm/summer lower.

Results from significance tests show that the hypothesis of no difference between the means of all pairs of geomorphological units can be rejected in most cases, confirming that the displacement rate differs significantly depending on the geomorphology (Fig. S8 in Supplementary material). Despite these differences, there are large overlaps in the 2D value ranges for most of the units and statistical similarities are found between some of them. *P*-values are over 0.05 between 'Regolith' and 'Colluvium', 'Alluvial sediment, pre-recent' and 'Fluvial sediment', and 'Glacio-fluvial sediment' and 'Fluvial sediment'. *P*-values are over 0.01 between 'Regolith' and 'Solifluction', 'Colluvium' and 'Solifluction', and 'Alluvial sediment, pre-recent' and 'Glacio-fluvial sediment' (Fig. S8).

The vertical and horizontal components provide more information (boxplots in Figs. S9–S10 in Supplementary material), and can also be analysed by studying the pixel frequency per class of 10 mm/summer displacement rates (Fig. 9 and magnitude of 2D vectors in Fig. S11 of the Supplementary material). Four main observations highlight the value of the 2D InSAR decomposition: (1) for low values of displacement rates (0 to +20 mm/summer for the vertical component, −10 to +10 mm/summer for the horizontal), all geomorphological units are represented with a frequency between 3 and 15% of the pixels; (2) for higher positive rates for the vertical component (over 50 mm/summer downwards), 'Alluvial sediment, pre-recent', 'Terminal and medial moraine' and 'Eolian sediment' represent over 80% of the pixels; (3) for higher absolute displacement rates for the horizontal component (over 30 mm/summer), 'Rock glacier and protalus rampart', 'Terminal and medial moraine' and 'Anthropogenic material' represent over 60% of the pixels; (4) vertically, the presence of low negative rates (upwards, min: −6.5 mm/summer) mainly for 'Marine and beach sediment' and 'Anthropogenic material' can be attributed to a slight shift due to subsidence at the reference point (further discussed in Section 5.1).

The limitation of this histogram analysis is that it artificially separates vertical and horizontal components that can, if analysed in combination, provide further information about the orientation of the displacements. To visualise the 2D behaviour of each single pixel, results are presented as scatter plots. Six of the most widespread geomorphological units are shown (Fig. 10). The remaining results are available in the Supplementary material (Fig. S12). The variability of the 2D InSAR results highlights the control of the topography. On slopes, gravity-driven processes induce downslope movement combining vertical and horizontal components. 'Solifluction' (Fig. 10, plot A) is affected both by horizontal (up to 32 mm/summer) and vertical displacements (up to 50 mm/summer). The vertical component is overall higher than horizontal component, which fits with field measurements (Harris et al., 2011). 'Rock glacier and protalus rampart' (Fig. 10, plot B) has a higher horizontal component (up to 50 mm/summer, mainly westwards due to the overrepresentation of west-facing slopes) combined with high vertical components (up to 53 mm/summer). In the lowlands, the horizontal component is negligible due to low slope angles. 'Fluvial sediment' (Fig. 10, plot C) and 'Eolian sediment' (Fig. 10, plot D) are mainly distributed along the vertical axis with high subsidence rates up to 40 and 60 mm/summer respectively, but characteristically without much horizontal movement. Measured low horizontal rates can, however, be

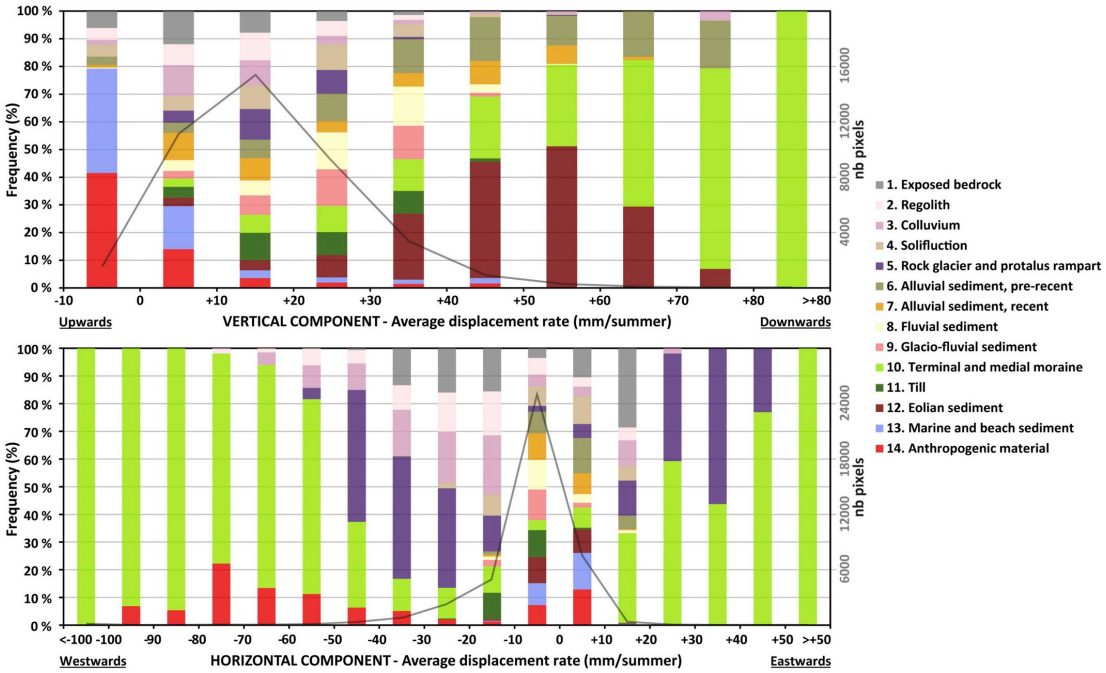

Fig. 9. Pixel frequency per class of 10 mm/summer displacement rates based on 2D InSAR from TerraSAR-X multi-year stacking during the 4-month thawing periods (June–September 2009–2017). Upper: Vertical component. Lower: Horizontal component. The geomorphological units and attributed colours are similar to those presented in Fig. 2. The grey curves indicate the number of pixels per class of 10 mm/summer displacement rates showing that 100% at high displacement rates correspond to fewer pixels than low rates. The shift of the horizontal displacements towards the west is due to the overrepresentation of west-facing slopes. Magnitude of 2D vectors is shown in Fig. S11 (Supplementary material).

due to creep on low-angled slopes and the slight shift towards negative values is again due to an overrepresentation of west-facing slopes. The difference of magnitude between 'Fluvial sediment' and 'Eolian sediment' can be related to the ground porosity, the frost-susceptibility of the material, as well as the water content and availability. The sand-gravel portion in fluvial sediment constrains both the porosity and frost-susceptibility. Fine-grained eolian sediment is more favourable to cryosuction, which controls the supply of water at the freezing front and thus enable ice segregation and ice lens formation (French, 2007; Smith, 1985), lifting the ground surface during freezing. 'Terminal and medial moraine' (Fig. 10, plot E) shows a core of values with rather low rates, but a large number of outliers with extreme rates in both components (up to 187 mm/summer horizontally and 102 mm/summer vertically). These areas are highly dynamic as they are located at the front or on the edges of retreating land-terminating glaciers. InSAR documents several potential processes going on in these landforms: mass-wasting, thawing of ice-cores, or creep of glaciers that are debris-covered but have been mapped as moraines. For 'Anthropogenic material' (Fig. 10, plot F), two different patterns are highlighted: vertical displacements at low rates over infrastructure in lowlands (mainly below 20 mm/summer), and higher rates including a large horizontal component corresponding to mining deposits located on valley slopes. This indicates that some mining piles are moving downslope. Composed of coarse material and located on steep slopes (> 30°), the behaviour of these artificial landforms can be compared to natural permafrost creep process.

4.3. Comparing InSAR time series to ground temperatures

The S1 InSAR time series between June and December 2017 highlights clear seasonal variations (Fig. 7) that can be compared to in situ temperature measurements between the ground surface and 2 m depth at the Adventdalen (ADV) and Endalen (END) boreholes (see Section 3.4).

Due to loss of coherence on snow and wet surfaces, the InSAR results potentially miss the start of the thaw subsidence and more importantly part of the frost heave when the ground gets snow-covered. Thus, the results are not able to provide the absolute magnitude of the subsidence and heave through a one-year cycle. In addition, InSAR time series correspond to displacements along LOS, regardless of the slope angle and orientation. Consequently, we focus on the timing and the relative changes of trends rather than on the absolute displacement values. The analysis provides information about the temporal variations of movement, compared to the field-measured ground temperatures.

The time series documents the summer thawing, the autumn freezing and the start of the winter cooling, as described in Zhao et al., 2000. In Fig. 11, the match between the ground temperature variations and InSAR displacement is obvious during four time periods: (1) Subsidence starts at – or rapidly after – the beginning of the ground thawing, when SAR scenes become snow-free and exploitable for InSAR analysis. The first acquisitions can, however, be affected by noise and phase ambiguities attributed to moisture or too fast movements (between 10.06.2017 and 22.06.2017 at END). Fast subsidence due to the quick thawing of the top active layer is measured during approx. two months. (2) From beginning of August, a second period is characterized by slower subsidence, when surface and shallow temperature starts

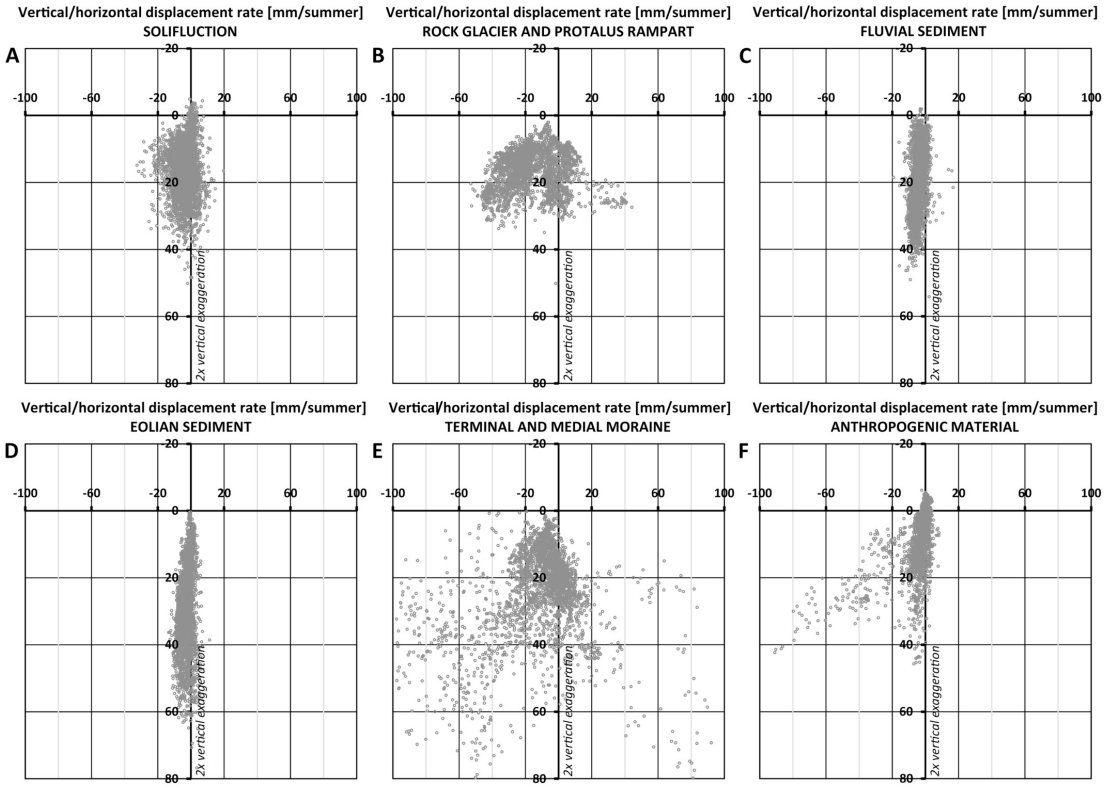

Fig. 10. Scatter plots showing the horizontal (x-axis) and vertical (y-axis) displacement rates of the 3000 randomly selected pixels for six geomorphological units based on 2D InSAR from TerraSAR-X multi-year stacking during the 4-month thawing periods (June–September 2009–2017). Note that E has the same scale as A–F for comparison, so pixels with large rates are not visible. In Fig. S12 (K in Supplementary material), the limits of the axis have been doubled to see all values.

decreasing but the deeper active layer slowly still develops. The second period lasts approx. two months. (3) Short transition from subsidence to heave recorded by InSAR matches the initiation of the active layer freeze-back period, which occurs between the end of September and the beginning of October at both sites. (4) Even short-term temperature fluctuations appear to have a halting impact on ground displacements; for example in beginning of November at ADV and more clearly in the middle of November at END, the heave slows down before speeding up again, corresponding to a short-term ground surface warming.

The seasonal evolution of the ground surface dynamics resolved into subsidence and heave correspond to patterns documented in previous studies also based on in-situ and remote sensing measurements (Daout et al., 2017; Harris et al., 2011; Smith, 1985; Strozzi et al., 2018). Modelling the variations of the thaw/freeze depths based on the Stefan function (Nelson et al., 1997) and proportionally relating the depth of the thawing/freezing front to displacements caused by the phase change of ground water (Hu et al., 2018) have shown that the cyclic elevation changes are primarily controlled by the thermal response of the active layer to atmospheric forcing. In Adventdalen and Endalen, we show that the high temporal resolution of S1-based InSAR results can be used as an indirect tool for monitoring active layer temperature changes in permafrost environments. This is further discussed in Section 5.3.

5. Discussion

5.1. Multi-sensor and multi-geometry complementarity

Our results highlight the complementarity of multi-sensor and multi-geometry InSAR. At the regional scale, the patterns detected on stacking results based on ascending geometries from S1 and TSX sensors are consistent overall (Fig. 3). However, several differences related to the intrinsic properties of the two sensors and datasets highlight the value of taking benefit of their respective advantages. The C-band wavelength and 6-days revisit time of S1 provide less decorrelation and better coherence on wet and fast moving surfaces, compared to X-band and 11-days revisit time of TSX (e.g. valley bottom, Fig. 4, area 3), as also discussed by Antonova et al. (2018) and Strozzi et al. (2018). Comparison between S1 SBAS time series and ground temperatures shows the value of the S1 short revisit time to document seasonal patterns. The scene coverage of 250 km (swath wide) and the open data policy of the Copernicus Programme are valuable for upscaling the investigation of periglacial landscapes and make possible the development of operational monitoring services. On the other hand, the 15 m spatial resolution of TSX after multilooking (compared to 40 m for S1) allows for more detailed investigation of small-scale landforms (e.g. rock glaciers and debris-covered glaciers, Fig. 4, areas 1 and 2). Comparison between TSX 2D InSAR results and geomorphology shows the value of the availability of two geometries allowing for 2D InSAR decomposition. Until the end of 2017, no descending image was available

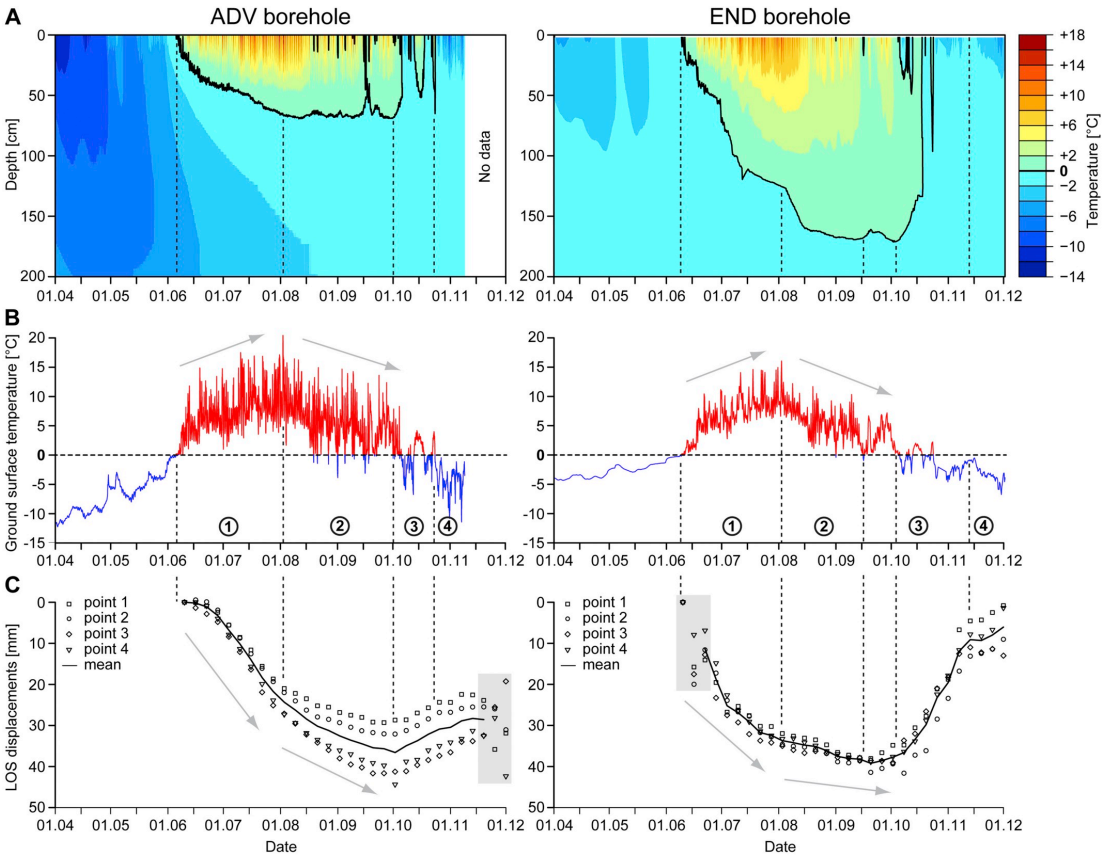

Fig. 11. 2017 ground temperature and Sentinel-1 SBAS displacement time series during summer thawing, autumn freezing and start of winter cooling at borehole locations. Left: Adventdalen (ADV) borehole. Right: Endalen (END) borehole. A. Temperature from the ground surface down to 200 cm depth. B. Ground surface temperature. C. InSAR displacements at the four neighbouring pixels closest to the two boreholes. The vertical dashed lines and circled numbers correspond to the four identified matching time periods. Grey areas: acquisitions affected by noise. Information about the two boreholes is summarized in Table. 2 and their locations are shown Figs. 1, 2 and 6.

for S1 Interferometric Wide Swath mode in the study area. Other differences may be related to the different observation periods, spatial and temporal resolutions and LOS.

Error sources and uncertainties in InSAR results have to be taken into account. Large scale unwrapping problems have been mitigated by manually discarding affected interferograms. However, some local unwrapping errors can be expected, especially on small areas isolated by non-coherent ones (e.g. south-western part of the study area, Fig. 3). The mitigation of the tropospheric effect is performed by stacking (averaging) of interferograms or using a network-based approach for SBAS. The standard deviation of the retrieved velocity depends on the number of interferograms (71–99) and the maximum temporal baseline (22–24 days) used for the processing. Using Eq. 11 from Emardson et al. (2003) and assuming a standard deviation of 5 mm per interferogram due to the atmosphere, the standard deviation of the stacking results in Adventdalen is estimated to 2.5–3.5 mm/summer. Other unwanted phase change components related to changes of surface properties (vegetation, snow, moisture) can also have an impact on the accuracy of the results, but are unfortunately difficult to assess quantitatively. Seasonal change of ground moisture is most likely the main error source in this study. It induces differential propagation of the electromagnetic wave into the ground, leading to a biased detection of sensor-to-ground change of distance (De Zan et al., 2014). The bias of the phase measurements due to ground moisture variability increases with the radar wavelength and can reach 10–20% of the wavelength (Zwieback et al., 2017). Thus, S1 results are more susceptible to this effect than TSX. The bias typically corresponds to an overestimation of the subsidence during the thawing season (due to a decrease of the wave velocity as the ground gets moister). Though the magnitude of the detected displacements, the consistency of the patterns from both sensors (Fig. 3) and the clear inversion from subsidence to heave fitting the timing of ground thawing and freezing (Figs. 7, 11) tend to indicate that our results are overall robust, this issue would definitely benefit from further research. As discussed by Zwieback et al. (2017), the sensitivity of InSAR to ground moisture can in addition become valuable if this phase contribution can be isolated. Finally, due to the highly dynamic Svalbard environment, finding a stable reference point is not easy. Some upward values over flat areas on the stacking results based on the thawing periods may indicate an upward shift of the mean velocity (< 7 mm/summer) due to slight subsidence at the pixel chosen as reference point.

5.2. InSAR contribution for geomorphological investigation

Our results highlight that vertical and horizontal displacement patterns in and around Adventdalen vary for different geomorphological units. On slopes, InSAR results provide good delineation of creeping landforms (e.g. rock glaciers, debris-covered glaciers, solifluction sheets). The landforms combine vertical and horizontal components of displacement at variable rates controlled by the involved processes. Over low-relief areas, vertical displacements naturally dominate and the seasonal amplitude is particularly large in fine-grained frost-susceptible materials (e.g. eolian sediment) and areas assumed to have good water availability (e.g. outer part of alluvial fans). This confirms the findings of Daout et al. (2017) who highlighted that seasonal ground displacements are largely controlled by ground properties and water content in the sedimentary basins of the Tibet Plateau. For example, in Adventdalen, some outer and drier parts of the river terraces, with an eolian cover, do not exhibit the same magnitude of seasonal subsidence and heave as the lower parts of the fans/terraces (Figs. 3, 4 and 6). This makes sense, as the water content is generally lower in the outer river terraces than in the lower alluvial fans (Cable et al., 2018).

The 2D InSAR displacement rates for different geomorphological units overlap significantly (Fig. 8), which makes direct classification impossible, as also discussed by Eckerstorfer et al. (2018). The effect of the different spatial resolutions, the georeferencing inaccuracy, the simplification of the geomorphological units and the mapping scale partially explain the overlaps. For example, the delineation of 'Alluvial sediment, pre-recent', 'Alluvial sediment, recent' and 'Fluvial sediment' units in highly dynamic valley bottoms is subject to inaccuracies. 'Terminal and medial moraine' also includes debris-covered glaciers and 'Anthropogenic material' includes both infrastructure in valley bottoms and mining deposits creeping on slopes. In addition, the complex behaviours under investigation imply that different processes can have similar displacement rates, or that similar processes under variable environmental contexts can have different rates. Jointly analysing vertical and horizontal components determined from the 2D InSAR method allows, however, for more valuable information to differentiate sediments, bedrock and landforms (Figs. 9, 10 and S12). Without additional information, a completely automatic processing of InSAR displacements for mapping geomorphology remains unfeasible, but the findings highlight the potential of using InSAR to refine the inventory and delineation of specific landforms on existing maps, or as a supporting tool for geomorphological or geocryological mapping, as the spatial distribution of InSAR displacements is related to the distribution of frost-susceptible sediments and the variability of water content available for ground ice formation in the active layer. When used in combination with other environmental information such as topography, geology, climate, vegetation and/or hydrology, InSAR may also be valuably integrated into statistically-based geomorphological distribution modelling (Hjort and Luoto, 2013).

5.3. InSAR contribution for investigation of ground thermal conditions

With the increase of repeat-pass frequency of recent SAR satellites such as S1, InSAR can be used to monitor the temporal variations of ground displacements at seasonal scale. This has direct applications like in geohazard studies, but can also provide indirect findings. Our results show that there is a clear correspondence between active layer thermal regime and the InSAR measured displacements at the location of two boreholes, with the timing of the subsidence and heave onsets matching the observed ground surface and active layer thawing and freezing (Fig. 11). This confirms that InSAR can be a valuable tool for the indirect monitoring of active layer dynamics over landforms dominated by subsidence and heave patterns, as in the flat bottom of Adventdalen or on gentle solifluction slopes in Endalen. In high-relief contexts where the processes are mainly gravity-driven, InSAR can provide information about the temporal variability of the creep velocity (Fig. 7), but the time series have to be interpreted carefully due to the complex orientation of the real displacements and their relations with the LOS measurements.

In the lowlands, previous research has studied and modelled the relationship between InSAR time series and active layer dynamics, often with the objective of exploiting InSAR for ALT retrieval. The Stefan equation (Stefan, 1891) allows for a simple calculation of the development of thaw depth through the season, based on the accumulated thawing-degree days derived from air temperature. Assuming homogenous ground, a defined amount of ground ice and that all pore ice turns into water during the thawing, the InSAR-measured subsidence can be converted into thaw depth (Liu et al., 2012). More recent models combine the use of thawing and freezing indices to more realistically depict short term variations and take into account eventual transient summer freezing (Hu et al., 2018) or investigate how other climatic factors such as precipitation affect the ground surface dynamics (Zhao et al., 2016).

These models can perform well in homogenous areas and their simplicity is valuable for upscaling investigations in permafrost areas, where little additional data is available. However, they also have some limitations. Major elements besides climatic variables are often neglected. Our results show that the displacement magnitude and timing are geomorphologically-controlled, largely determined by the sediment, bedrock or landform types, and thus cannot be explained only by climatic variables. Other variables have to be considered, such as the heterogeneity of the ground properties and the water available for ground ice formation in the active layer (Shiklomanov et al., 2010), as well as the presence of different ice types in the ground (e.g. pore and segregated ice) and the factors controlling ice lens formation (Rempel, 2007). Both elements impact the ground thermal regime (e.g. due to porosity, thermal conductivity, release/absorption of latent heat of fusion of water) and how the surface is affected by a phase change (e.g. due to melting of ice lenses vs. pore ice only). Comparing InSAR results to field data, Daout et al. (2017) showed that the magnitude and timing of the ground displacement patterns are controlled by ground properties and water availability. Their conclusions from the Tibet Plateau concur with our findings which suggest that, especially in complex periglacial landscapes encompassing a wide range of topographical, geomorphological and hydrological conditions, InSAR is a valuable tool for the investigation of freeze and thaw processes at large scale, but may benefit from further combination with in situ data and modelling techniques.

6. Conclusion

Our study demonstrates the value of multi-sensor and multi-geometry InSAR for investigating complex permafrost landscapes containing both high-relief and lowlands. The analysis of the spatial variability of ground displacement rates based on decomposed vertical and east-west horizontal TerraSAR-X InSAR results compared to a simplified geomorphological map show that it is possible to identify specific 2D displacement patterns for different geomorphological units. In the flat valley bottoms, thaw subsidence is detected and the magnitude varies according to the water availability and frost-susceptibility of the sediments. On valley slopes, downslope displacements combining vertical and horizontal components are detected and their magnitude varies depending on the involved creep process. Based on 6-month continuous time series from Sentinel-1 in June–December 2017, we were able to correctly identify ground displacement variations related to active layer thawing and freezing over flat or low-inclined slopes, where the seasonal change from thaw subsidence to frost heave dominates the displacement pattern. Through comparison with in situ ground temperature measurements in the active layer, we show that the timing of the InSAR seasonal subsidence and heave patterns matches the ground thawing and freezing periods measured in two boreholes.

The identified spatio-temporal relations between ground surface displacements and environmental variables evidence the potential for further exploitation of InSAR technology for understanding, mapping and monitoring the dynamics of remote periglacial landscapes. The findings support the development of more advanced models to remotely and indirectly retrieve variables related to permafrost such as active layer thickness, which is one of the two Essential Climate Variables for permafrost.

Acknowledgements

Line Rouyet's PhD study is part of the research project FrostInSAR (2017–2021) funded by the Space Programme of the Research Council of Norway (Project Nr: 263005). The development of the GSAR processing chain and previous research applying InSAR in periglacial environments have been supported by the Norwegian Space Centre, the Research Council of Norway (Project Nr: 212022) and the European Space Agency (Project Nr: 4000106830 and 4000119115). TerraSAR-X scenes were provided by the German Aerospace Center (DLR) under the TSX-AO project contracts #GEO0565 and #GEO3519. Sentinel-1 scenes were provided as part of the EU Copernicus data service (2015–2017). We acknowledge the work and valuable feedback from three anonymous reviewers and the editor Prof. Dar Roberts who contributed to improve the manuscript. We thank Markus Eckerstorfer for his contribution to the previous PermaSAT and PermaSAR projects that led to the initiation of the current FrostInSAR project. We are grateful for the interest and inputs of Stefanie Cable shared during various discussions. We acknowledge the work of the ESA GlobPermafrost and CCI+ Permafrost initiatives providing a great international framework and inspiration for research on remote sensing of permafrost landscapes.

Appendix A. Supplementary data

Supplementary data to this article can be found online at https://doi.org/10.1016/j.rse.2019.111236.

References

André, M.F., 1995. Holocene climate fluctuations and geomorphic impact of extreme events in Svalbard. Geografiska Annaler: Series A, Physical Geography 77 (4), 241–250. https://doi.org/10.1080/04353676.1995.11880444.

Antonova, S., Sudhaus, H., Strozzi, T., Zwieback, S., Kääb, A., Heim, B., Langer, M., Bornemann, N., Boike, J., 2018. Thaw subsidence of a Yedoma landscape in Northern Siberia, measured in situ and estimated from TerraSAR-X interferometry. Remote Sens. Environ. 10 (4), 494. https://doi.org/10.3390/rs10040494.

Baran, I., Stewart, M.P., Kampes, B.M., Perski, Z., Lilly, P., 2003. A modification to the Goldstein radar interferogram filter. IEEE Trans. Geosci. Remote Sens. 41 (9), 2114–2118. https://doi.org/10.1109/TGRS.2003.817212.

Barboux, C., Delaloye, R., Lambiel, C., 2014. Inventorying slope movements in an Alpine environment using DInSAR. Earth Surf. Process. Landf. 39 (15), 2087–2099. https://doi.org/10.1002/esp.3603.

Barboux, C., Strozzi, T., Delaloye, R., Wegmüller, U., Collet, C., 2015. Mapping slope movements in Alpine environments using TerraSAR-X interferometric methods. ISPRS J. Photogramm. Remote Sens. 109, 178–192. https://doi.org/10.1016/j.isprsjprs.2015.09.010.

Bartsch, A., Grosse, G., Kääb, A., Westermann, S., Strozzi, T., Wiesmann, A., Duguay, C., Seifert, F.M., Obu, J., Goler, R., 2016. GlobPermafrost – how space-based earth observation supports understanding of permafrost. In: Proc. Living Planet Symposium 2016, Prague, Czech Republic, 9–13 May 2016. vol. 740. pp. 332.

Berardino, P., Fornaro, G., Lanari, R., Sansosti, E., 2002. A new algorithm for surface deformation monitoring based on small baseline differential SAR interferograms. IEEE Trans. Geosci. Remote Sens. 40 (11), 2375–2383. https://doi.org/10.1109/TGRS.2002.803792.

Blikra, L.H., Christiansen, H.H., 2014. A field-based model of permafrost-controlled rockslide deformation in northern Norway. Geomorphology 208, 34–49. https://doi.org/10.1016/j.geomorph.2013.11.014.

Cable, S., Elberling, B., Kroon, A., 2018. Holocene permafrost history and cryostratigraphy in the High-Arctic Adventdalen Valley, central Svalbard. Boreas 47 (2), 423–442. https://doi.org/10.1111/bor.12286.

Cavalié, O., Doin, M.P., Lasserre, C., Briole, P., 2007. Ground motion measurement in the Lake Mead area, Nevada, by differential synthetic aperture radar interferometry time series analysis: probing the lithosphere rheological structure. Journal of Geophysical Research: Solid Earth (B3), 112. https://doi.org/10.1029/2006JB004344.

Chen, C., Zebker, H.A., 2002. Phase unwrapping for large SAR interferograms: statistical segmentation and generalized network models. IEEE Trans. Geosci. Remote Sens. 40 (8), 1709–1719. https://doi.org/10.1109/TGRS.2002.802453.

Christiansen, H., Humlum, O., 2008. Interannual variations in active layer thickness in Svalbard. In: Proc. Ninth International Conference on Permafrost, Fairbanks, Alaska, U.S.A., 29 June–3 July, pp. 257–262.

Christiansen, H.H., Etzelmüller, B., Isaksen, K., Juliussen, H., Farbrot, H., Humlum, O., Johansson, M., Ingeman-Nielsen, T., Kristensen, L., Hjort, J., Holmlund, P., Sannel, A.B.K., Sigsgaard, C., Åkerman, H.J., Foged, N., Blikra, L.H., Pernosky, M.A., Ødegård, R.S., 2010. The thermal state of permafrost in the nordic area during the international polar year 2007–2009. Permafr. Periglac. Process. 21 (2), 156–181. https://doi.org/10.1002/ppp.687.

Christiansen, H.H., Humlum, O., Eckerstorfer, M., 2013. Central Svalbard 2000–2011 meteorological dynamics and periglacial landscape response. Arct. Antarct. Alp. Res. 45 (1), 6–18. https://doi.org/10.1657/1938-4246-45.16.

Dallmann, W.K., Kjærnet, T., Nøttvedt, A., 2001. Geological Map of Svalbard 1:100,000. Sheet C9G Adventdalen (Text). Norwegian Polar Institute (Temakart No. 31/32).

Daout, S., Doin, M.P., Peltzer, G., Socquet, A., Lasserre, C., 2017. Large-scale InSAR monitoring of permafrost freeze-thaw cycles on the Tibetan Plateau. Geophys. Res. Lett. 44 (2), 901–909. https://doi.org/10.1002/2016GL070781.

De Zan, F., Parizzi, A., Prats-Iraola, P., López-Dekker, P., 2014. A SAR interferometric model for soil moisture. IEEE Trans. Geosci. Remote Sens. 52 (1), 418–425. https://doi.org/10.1109/TGRS.2013.2241069.

Delaloye, R., Lambiel, C., Lugon, R., Raetzo, H., Strozzi, T., 2007. Typical ERS InSAR signature of slope movements in a periglacial mountain environment (Swiss Alps). In: Proc. ENVISAT Symposium 2007, Montreux, Switzerland, 23–27 April 2007, ESA SP-636.

Delaloye, R., Lambiel, C., Gärtner-Roer, I., 2010. Overview of rock glacier kinematics research in the Swiss Alps. Geographica Helvetica 65, 135–145. https://doi.org/10.5194/gh-65-135-2010. 2010.

Eckerstorfer, M., Christiansen, H.H., Vogel, S., Rubensdotter, L., 2013. Snow cornice dynamics as a control on plateau edge erosion in central Svalbard. Earth Surf. Process. Landf. 38 (5), 466–476. https://doi.org/10.1002/esp.3292.

Eckerstorfer, M., Eriksen, H.Ø., Rouyet, L., Christiansen, H.H., Lauknes, T.R., Blikra, L.H., 2018. Comparison of geomorphological field mapping and 2D-InSAR mapping of periglacial landscape activity at Nordnesfjellet, northern Norway. Earth Surf. Process. Landf. 43 (10), 2147–2156. https://doi.org/10.1002/esp.4380.

Emardson, T.R., Simons, M., Webb, F.H., 2003. Neutral atmospheric delay in interferometric synthetic aperture radar applications: statistical description and mitigation. Journal of Geophysical Research: Solid Earth 108 (B5), 2231. https://doi.org/10.1029/2002JB001781.

Eriksen, H.Ø., Lauknes, T.R., Larsen, Y., Corner, G.D., Bergh, S.G., Dehls, J., Kierulf, H.P., 2017. Visualizing and interpreting surface displacement patterns on unstable slopes using multi-geometry satellite SAR interferometry (2D InSAR). Remote Sens. Environ. 191, 297–312. https://doi.org/10.1016/j.rse.2016.12.024.

Eriksen, H.Ø., Rouyet, L., Lauknes, T.R., Berthling, I., Isaksen, K., Hindberg, H., Larsen, Y., Corner, G.D., 2018. Recent acceleration of a rock glacier complex, Ádjet, Norway, documented by 62 years of remote sensing observations. Geophys. Res. Lett. 45 (16), 8314–8323. https://doi.org/10.1029/2018GL077605.

Etzelmüller, B., Schuler, T.V., Isaksen, K., Christiansen, H.H., Farbrot, H., Benestad, R., 2011. Modeling the temperature evolution of Svalbard permafrost during the 20th and 21st century. Cryosphere 5 (1), 67. https://doi.org/10.5194/tc-5-67-2011.

Førland, E.J., Benestad, R., Hanssen-Bauer, I., Haugen, J.E., Skaugen, T.E., 2011. Temperature and precipitation development at Svalbard 1900–2100. Adv. Meteorol. 2011. https://doi.org/10.1155/2011/893790.

French, H.M., 2007. The Periglacial Environment, Third edition. John Wiley & Sons, Chichester, England.

Gabriel, A.K., Goldstein, R.M., Zebker, H.A., 1989. Mapping small elevation changes over large areas: differential radar interferometry. Journal of Geophysical Research: Solid Earth 94 (B7), 9183–9191. https://doi.org/10.1029/JB094iB07p09183.

Gilbert, G.L., O'Neill, H.B., Nemec, W., Thiel, C., Christiansen, H.H., Buylaert, J.P., 2018. Late Quaternary sedimentation and permafrost development in a Svalbard fjord-valley, Norwegian high Arctic. Sedimentology. https://doi.org/10.1111/sed.12476.

Goldstein, R.M., Werner, C.L., 1998. Radar interferogram filtering for geophysical applications. Geophys. Res. Lett. 25 (21), 4035–4038. https://doi.org/10.1029/1998GL900033.

Haeberli, W., Hallet, B., Arenson, L., Elconin, R., Humlum, O., Kääb, A., Kaufmann, V., Ladanyi, B., Matsuoka, N., Springman, S., Mühll, D.V., 2006. Permafrost creep and rock glacier dynamics. Permafr. Periglac. Process. 17 (3), 189–214. https://doi.org/10.1002/ppp.561.

Harris, C., Davies, M.C., Coutard, J.P., 1995. Laboratory simulation of periglacial solifluction: significance of porewater pressures, moisture contents and undrained shear strengths during soil thawing. Permafr. Periglac. Process. 6 (4), 293–311. https://doi.org/10.1002/ppp.3430060403.

Harris, C., Arenson, L.U., Christiansen, H.H., Etzelmüller, B., Frauenfelder, R., Gruber, S., Haeberli, W., Hauck, C., Hölzle, M., Humlum, O., Isaksen, K., Kääb, A., Kern-Lütschg, M.A., Lehning, M., Matsuoka, N., Murton, J.B., Nötzli, J., Phillips, M., Ross, N., Seppälä, M., Springman, S.M., Von der Mühll, D., 2009. Permafrost and climate in Europe: monitoring and modelling thermal, geomorphological and geotechnical responses. Earth Sci. Rev. 92 (3–4), 117–171. https://doi.org/10.1016/j.earscirev.2008.12.002.

Harris, C., Kern-Lütschg, M.A., Christiansen, H.H., Smith, F., 2011. The role of interannual climate variability in controlling solifluction processes, Endalen, Svalbard. Permafr. Periglac. Process. 22 (3), 239–253. https://doi.org/10.1002/ppp.727.

Härtel, S., Christiansen, H.H., 2014. Geomorphological and Cryological map of Adventdalen, Svalbard. PANGAEA. https://doi.org/10.1594/PANGAEA.833048.

Hjort, J., Luoto, M., 2013. Statistical methods for geomorphic distribution modeling. In: Schroder, J. (Editor in Chief), Baas, A.C.W. (Eds.), Treatise on Geomorphology. Quantitative Modeling of Geomorphology, vol. 2. Academic Press, San Diego, pp. 59–73. https://doi.org/10.1016/B978-0-12-374739-6.00028-2.

Hu, Y., Liu, L., Larson, K.M., Schaefer, K.M., Zhang, J., Yao, Y., 2018. GPS interferometric reflectometry reveals cyclic elevation changes in thaw and freezing seasons in a permafrost area (Barrow, Alaska). Geophys. Res. Lett. 45, 5581–5589. https://doi.

org/10.1029/2018GL077960.
Humlum, O., 2000. The geomorphic significance of rock glaciers: estimates of rock glacier debris volumes and headwall recession rates in West Greenland. Geomorphology 35 (1–2), 41–67. https://doi.org/10.1016/S0169-555X(00)00022-2.
Humlum, O., Instanes, A., Sollid, J.L., 2003. Permafrost in Svalbard: a review of research history, climatic background and engineering challenges. Polar Res. 22 (2), 191–215. https://doi.org/10.3402/polar.v22i2.6455.
Isaksen, K., Christiansen, H.H., Westermann, S., 2019. 7.1 permafrost temperature and active layer thickness. In: Hanssen-Bauer, I., Førland, E.J., Hisdal, H., Mayer, S., Sandø, A.B., Sorteberg, A. (Eds.), Climate in Svalbard 2100, pp. 105–110 NCCS report no 1/2019.
Kenyi, L.W., Kaufmann, V., 2001. Estimation of alpine permafrost surface deformation using InSAR data. In: Proc. Geoscience and Remote Sensing Symposium, IGARSS'01, Sydney, Australia, 9–13 July 2001. vol. 3. IEEE 2001 International, pp. 1107–1109. https://doi.org/10.1109/IGARSS.2001.976761.
Larsen, Y., Engen, G., Lauknes, T.R., Malnes, E., Høgda, K.A., 2005. A generic differential interferometric SAR processing system, with applications to land subsidence and snow-water equivalent retrieval. In: Proc. Fringe 2005 Workshop, Frascati, Italy, 28 November–2 December 2005. vol. 61 (ESA SP-610).
Lauknes, T.R., 2011. InSAR tropospheric stratification delays: correction using a small baseline approach. IEEE Geosci. Remote Sens. Lett. 8 (6), 1070–1074. https://doi.org/10.1109/LGRS.2011.2156381.
Lauknes, T.R., Zebker, H.A., Larsen, Y., 2011. InSAR deformation time series using an L1-norm small-baseline approach. IEEE Trans. Geosci. Remote Sens. 49 (1), 536–546. https://doi.org/10.1109/TGRS.2010.2051951.
Liu, L., Schaefer, K., Zhang, T., Wahr, J., 2012. Estimating 1992–2000 average active layer thickness on the Alaskan North Slope from remotely sensed surface subsidence. Journal of Geophysical Research: Earth Surface 117 (F1). https://doi.org/10.1029/2011JF002041.
Lyons, S., Sandwell, D., 2003. Fault creep along the southern San Andreas from interferometric synthetic aperture radar, permanent scatterers, and stacking. Journal of Geophysical Research: Solid Earth 108 (B1). https://doi.org/10.1029/2002JB001831.
Major, H., Haremo, W.K., Dallmann, W.K., Andresen, A., 2001. Geological Map of Svalbard 1:100,000. Sheet C9G Adventdalen (Map). Norwegian Polar Institute (Temakart No. 31/32).
Massonnet, D., Feigl, K.L., 1998. Radar interferometry and its application to changes in the earth's surface. Rev. Geophys. 36 (4), 441–500. https://doi.org/10.1029/97RG03139.
Matsuoka, N., 2001. Solifluction rates, processes and landforms: a global review. Earth Sci. Rev. 55 (1–2), 107–134. https://doi.org/10.1016/S0012-8252(01)00057-5.
Matsuoka, N., Abe, M., Ijiri, M., 2003. Differential frost heave and sorted patterned ground: field measurements and a laboratory experiment. Geomorphology 52 (1–2), 73–85. https://doi.org/10.1016/S0169-555X(02)00249-0.
Nelson, F.E., Shiklomanov, N.I., Mueller, G.R., Hinkel, K.M., Walker, D.A., Bockheim, J.G., 1997. Estimating active-layer thickness over a large region: Kuparuk River basin, Alaska, USA. Arct. Alp. Res. 29 (4), 367–378. https://doi.org/10.1080/00040851.1997.12003258.
Nelson, F.E., Anisimov, O.A., Shiklomanov, N.I., 2002. Climate change and hazard zonation in the circum-Arctic permafrost regions. Nat. Hazards 26 (3), 203–225. https://doi.org/10.1023/A:1015612918401.
Norwegian Polar Institute, 2014a. Terrengmodell Svalbard (S0 Terrengmodell). Norwegian Polar Institute. 10.21334/npolar.2014.dce53a47.
Norwegian Polar Institute, 2014b. Kartdata Svalbard 1:100 000 (S100 Kartdata)/Map Data. Norwegian Polar Institute. 10.21334/npolar.2014.645336c7.
Peel, M.C., Finlayson, B.L., McMahon, T.A., 2007. Updated world map of the Köppen-Geiger climate classification. Hydrol. Earth Syst. Sci. Discuss. 4 (2), 439–473. https://doi.org/10.5194/hess-11-1633-2007.
Peltzer, G., Crampé, F., Hensley, S., Rosen, P., 2001. Transient strain accumulation and fault interaction in the Eastern California shear zone. Geology 29 (11), 975–978. https://doi.org/10.1130/0091-7613(2001)029<0975:TSAAFI>2.0.CO;2.
Rempel, A.W., 2007. Formation of ice lenses and frost heave. Journal of Geophysical Research: Earth Surface (F2), 112. https://doi.org/10.1029/2006JF000525.
Rignot, E., Hallet, B., Fountain, A., 2002. Rock glacier surface motion in Beacon Valley, Antarctica, from synthetic aperture radar interferometry. Geophys. Res. Lett. 29 (12). https://doi.org/10.1029/2001GL013494.
Romanovsky, V.E., Marchenko, S.S., Daanen, R., Sergeev, D.O., Walker, D.A., 2008. Soil climate and frost heave along the permafrost/ecological North American Arctic transect. In: Proc. Ninth International Conference on Permafrost 2005, Fairbanks, U.S.A. vol. 2. pp. 1519–1524.
Romanovsky, V.E., Smith, S.L., Christiansen, H.H., 2010. Permafrost thermal state in the polar Northern Hemisphere during the international polar year 2007–2009: a synthesis. Permafr. Periglac. Process. 21 (2), 106–116. https://doi.org/10.1002/ppp.689.
Rudy, A.C., Lamoureux, S.F., Treitz, P., Short, N., Brisco, B., 2018. Seasonal and multi-year surface displacements measured by DInSAR in a High Arctic permafrost environment. Int. J. Appl. Earth Obs. Geoinf. 64, 51–61. https://doi.org/10.1016/j.jag.2017.09.002.
Rykhus, R.P., Lu, Z., 2008. InSAR detects possible thaw settlement in the Alaskan Arctic Coastal Plain. Can. J. Remote. Sens. 34 (2), 100–112. https://doi.org/10.5589/m08-018.
Sandwell, D.T., Price, E.J., 1998. Phase gradient approach to stacking interferograms. Journal of Geophysical Research: Solid Earth 103 (B12), 30183–30204. https://doi.org/10.1029/1998JB900008.
Schaefer, K., Liu, L., Parsekian, A., Jafarov, E., Chen, A., Zhang, T., Gusmeroli, A., Panda, S., Zebker, H.A., Schaefer, T., 2015. Remotely sensed active layer thickness (ReSALT) at Barrow, Alaska using interferometric synthetic aperture radar. Remote Sens. 7 (4), 3735–3759. https://doi.org/10.3390/rs70403735.
Schuh, C., Frampton, A., Christiansen, H.H., 2017. Soil moisture redistribution and its effect on inter-annual active layer temperature and thickness variations in a dry loess terrace in Adventdalen, Svalbard. Cryosphere 11 (1), 635. https://doi.org/10.5194/tc-11-635-2017.
Shiklomanov, N.I., Streletskiy, D.A., Nelson, F.E., Hollister, R.D., Romanovsky, V.E., Tweedie, C.E., Bockheim, J.G., Brown, J., 2010. Decadal variations of active-layer thickness in moisture-controlled landscapes, Barrow, Alaska. Journal of Geophysical Research: Biogeosciences 115 (G4). https://doi.org/10.1029/2009JG001248.
Shiklomanov, N.I., Streletskiy, D.A., Nelson, F.E., 2012. Northern hemisphere component of the global circumpolar active layer monitoring (CALM) program. In: Proc. 10th Int. Conf. on Permafrost, Salekhard, Russia, 25–29 June. vol. 1. pp. 377–382.
Short, N., LeBlanc, A.M., Sladen, W., Oldenborger, G., Mathon-Dufour, V., Brisco, B., 2014. RADARSAT-2 D-InSAR for ground displacement in permafrost terrain, validation from Iqaluit Airport, Baffin Island, Canada. Remote Sens. Environ. 141, 40–51. https://doi.org/10.1016/j.rse.2013.10.016.
Shur, Y., Hinkel, K.M., Nelson, F.E., 2005. The transient layer: implications for geocryology and climate-change science. Permafr. Periglac. Process. 16 (1), 5–17. https://doi.org/10.1002/ppp.518.
Smith, M.W., 1985. Observations of soil freezing and frost heave at Inuvik, Northwest Territories, Canada. Can. J. Earth Sci. 22 (2), 282–290. https://doi.org/10.1139/e85-024.
Sørbel, L., Tolgensbakk, J., Hagne, O., Høgvard, K., 2001. Geomorphological and Quaternary Geological Map of Svalbard 1:100,000. Sheet C9Q Adventdalen (Map). Norwegian Polar Institute (Temakart No. 31/32).
Stefan, J., 1891. Über die Theorie der Eisbildung, insbesondere über die Eisbildung im Polarmeere. Ann. Phys. 278 (2), 269–286. https://doi.org/10.1002/andp.18912780206.
Strozzi, T., Kääb, A., Frauenfelder, R., 2004. Detecting and quantifying mountain permafrost creep from in situ inventory, space-borne radar interferometry and airborne digital photogrammetry. Int. J. Remote Sens. 25 (15), 2919–2931. https://doi.org/10.1080/0143116042000192330.
Strozzi, T., Delaloye, R., Kääb, A., Ambrosi, C., Perruchoud, E., Wegmüller, U., 2010. Combined observations of rock mass movements using satellite SAR interferometry, differential GPS, airborne digital photogrammetry, and airborne photography interpretation. Journal of Geophysical Research: Earth Surface 115 (F1). https://doi.org/10.1029/2009JF001311.
Strozzi, T., Antonova, S., Günther, F., Mätzler, E., Vieira, G., Wegmüller, U., Westermann, S., Bartsch, A., 2018. Sentinel-1 SAR interferometry for surface deformation monitoring in low-land permafrost areas. Remote Sens. 10, 1360. https://doi.org/10.3390/rs10091360.
Tolgensbakk, J., Sørbel, L., Høgvard, K., 2001. Geomorphological and Quaternary Geological Map of Svalbard 1:100,000. Sheet C9Q Adventdalen (Text). Norwegian Polar Institute (Temakart No. 31/32).
Trofaier, A.M., Westermann, S., Bartsch, A., 2017. Progress in space-borne studies of permafrost for climate science: towards a multi-ECV approach. Remote Sens. Environ. 203, 55–70. https://doi.org/10.1016/j.rse.2017.05.021.
Tymofyeyeva, E., Fialko, Y., 2015. Mitigation of atmospheric phase delays in InSAR data, with application to the eastern California shear zone. Journal of Geophysical Research: Solid Earth 120 (8), 5952–5963. https://doi.org/10.1002/2015JB011886.
Wang, Z., Li, S., 1999. Detection of winter frost heaving of the active layer of Arctic permafrost using SAR differential interferograms. In: Proc. Geoscience and Remote Sensing Symposium, IGARSS'99, Hamburg, Germany, 28 June–2 July 1999. IEEE 1999 International. vol. 4. pp. 1946–1948. https://doi.org/10.1109/IGARSS.1999.774995.
Wang, C., Zhang, Z., Zhang, H., Wu, Q., Zhang, B., Tang, Y., 2017. Seasonal deformation features on Qinghai-Tibet railway observed using time-series InSAR technique with high-resolution TerraSAR-X images. Remote Sensing Letters 8 (1), 1–10. https://doi.org/10.1080/2150704X.2016.1225170.
Wolfe, S.A., Short, N.H., Morse, P.D., Schwarz, S.H., Stevens, C.W., 2014. Evaluation of RADARSAT-2 DInSAR seasonal surface displacement in discontinuous permafrost terrain, Yellowknife, Northwest Territories, Canada. Can. J. Remote. Sens. 40 (6), 406–422. https://doi.org/10.1080/07038992.2014.1012836.
Zhang, T., Barry, R.G., Knowles, K., Ling, F., Armstrong, R.L., 2003. Distribution of seasonally and perennially frozen ground in the Northern Hemisphere. In: Proc. 8th International Conference on Permafrost, Zürich, Switzerland, 21–25 July. vol. 2. AA Balkema Publishers, pp. 1289–1294.
Zhang, Y., Michalowski, R.L., 2015. Thermal-hydro-mechanical analysis of frost heave and thaw settlement. J. Geotech. Geoenviron. 141 (7), 04015027. https://doi.org/10.1061/(ASCE)GT.1943-5606.0001305.
Zhao, L., Cheng, G., Li, S., Zhao, X., Wang, S., 2000. Thawing and freezing processes of active layer in Wudaoliang region of Tibetan Plateau. Chin. Sci. Bull. 45 (23), 2181–2187.
Zhao, R., Li, Z.W., Feng, G.C., Wang, Q.J., Hu, J., 2016. Monitoring surface deformation over permafrost with an improved SBAS-InSAR algorithm: with emphasis on climatic factors modeling. Remote Sens. Environ. 184, 276–287. https://doi.org/10.1016/j.rse.2016.07.019.
Zwieback, S., Hensley, S., Hajnsek, I., 2017. Soil moisture estimation using differential radar interferometry: toward separating soil moisture and displacements. IEEE Trans. Geosci. Remote Sens. 55 (9), 5069–5083. https://doi.org/10.1109/TGRS.2017.2702099.

Paper II: Seasonal InSAR displacements documenting the active layer freeze and thaw progression in central–western Spitsbergen, Svalbard

Rouyet, L., Liu, L., Strand, S. M., Christiansen, H. H., Larsen, Y., Lauknes, T.R.

Submitted to *Remote Sensing*

Dataset: https://doi.org/10.5281/zenodo.4775398

Seasonal InSAR displacements documenting the active layer freeze and thaw progression in central–western Spitsbergen, Svalbard

Line Rouyet[1,2,3], Lin Liu[4], Sarah Marie Strand[3,5], Hanne Hvidtfeldt Christiansen[3], Tom Rune Lauknes[1,2] and Yngvar Larsen[1]

[1] NORCE Norwegian Research Centre AS, Siva Innovasjonssenter, P.O. Box 6434, 9294 Tromsø, Norway
[2] Department of Geosciences, The Arctic University of Norway (UiT), P.O. Box 6050, Langnes, 9037 Tromsø, Norway
[3] Arctic Geology Department, The University Centre in Svalbard (UNIS), P.O. Box 156, 9171 Longyearbyen, Norway
[4] Earth System Science Programme, Faculty of Science, The Chinese University of Hong Kong, Hong Kong, China
[5] Department of Geosciences, University of Oslo (UiO), P.O. Box 1047, Blindern, 0316 Oslo, Norway

Keywords: Permafrost; Active Layer; InSAR; Time series; Ground displacement; Ground temperature; Displacement progression; Thaw progression; Arctic; Svalbard

Abstract

In permafrost areas, the active layer undergoes seasonal frost heave and thaw subsidence caused by ice formation and melting. The amplitude and timing of the ground displacement cycles depend on the climatic and ground conditions. Here we used Sentinel-1 Synthetic Aperture Radar Interferometry (InSAR) to document the seasonal displacement progression in three regions of Svalbard. We retrieved June–November 2017 time series and identified thaw subsidence maxima and their timing. InSAR measurements were compared with a composite index model based on ground temperature. Cyclic seasonal patterns are identified in all areas, but the timing of the displacement progression vary. The subsidence maxima occurred later on the warm western coast (Kapp Linné and Ny-Ålesund) compared to the colder interior (Adventdalen). The composite index model is generally able to explain the observed patterns. In Adventdalen, the model matches the InSAR time series at the location of the borehole. In Kapp Linné and Ny-Ålesund, larger deviations are found at the pixel-scale, but km or regional averaging improves the fit. The study highlights the potential for further development of regional InSAR products able to represent the cyclic displacements in permafrost areas and infer the active layer thermal dynamics.

1. Introduction

Permafrost, defined as ground that remains at or below 0°C for at least two consecutive years, is an essential component of the terrestrial cryosphere that is sensitive to climate change [1]. Permafrost degradation contributes to global warming by releasing greenhouse gases previously trapped in the frozen ground [2] and has direct impacts on infrastructure [3] and ecosystems [4]. The upper part of the ground, the active layer (AL), is seasonally frozen and thawed, and determines a vast set of ecological and hydrological processes occurring in permafrost landscapes [5,6]. Permafrost thermal state and AL thickness (ALT) are the two components of the Permafrost Essential Climate Variable (ECV). These variables are typically measured by in-situ techniques [7], but the scarce network of monitoring sites makes remote and large polar regions difficult to comprehensively document. This leads to large uncertainties in the estimate of the current permafrost state and future projections [8]. However, surface changes documented by satellite remote sensing allow us to indirectly investigate permafrost dynamics. The exploitation of optical [9], radar [10] and thermal [11] imagery for this purpose has significantly increased these past decades [12].

Seasonal AL freezing and thawing induces cyclic subsidence and heave of the ground surface due to ice formation and melting [5,6]. The variability of the ground thermal regime, water content and physical AL properties lead to an uneven amplitude, distribution and temporal variability of these

displacements [14,15]. Satellite Synthetic Aperture Radar Interferometry (InSAR) allows for documenting line-of-sight (LOS) ground surface displacements between radar images taken at different times [16]. InSAR-based displacement maps can cover extensive areas and document the spatial distribution of thaw subsidence [17]. InSAR has also been used to estimate the ALT [18] and map areas with high content of excess ground ice at the top of permafrost [19]. Multi-temporal InSAR techniques allow for the retrieval of displacement time series, valuable for studying the seasonal progression of the ground displacements related to freeze and thaw cycles [20–23], as well as the interannual changes of surface elevation [24–27].

In Svalbard, InSAR time series highlighted that the temporal patterns of the seasonal subsidence and heave match the AL thermal variations measured in boreholes in Adventdalen and Endalen [22]. Based on Global Positioning System Interferometric Reflectometry (GPS-IR) in an Alaskan site, Hu et al. [13] showed that a composite index model based on air temperature is able to characterize the cyclic patterns using the Stefan equation [28,29]. Both studies suggest that displacement time series can indirectly document the AL thermal regime and thus complement and upscale traditional point-based field monitoring. The results indicate that the timing of the maximal subsidence can be used as a proxy for the transition between the thawing period and the freeze-back onset. However, other studies conversely concluded that the displacement progression described by the Stefan equation does not reproduce observations, due to the unconsidered impacts of hydrologic controls [30–32]. Further research is thus necessary to compare measured and modelled displacement time series, to study the importance of the temperature control on AL displacement patterns in different environmental settings. In addition, the operational exploitation of InSAR technology for the monitoring of ground dynamics in extensive permafrost areas still needs to be demonstrated. With the development of national to multi-national InSAR mapping services based on freely available images from the Copernicus Sentinel-1 satellite mission [33,34], the ability to map ground movement at large scales is dramatically increasing. However, the currently applied processing strategies are mostly designed for moving areas with relatively constant displacement directions and the InSAR parameter chosen for mapping purpose is usually the mean annual ground velocity, which has limited applicability in areas affected by cyclic patterns. In Svalbard and similar polar environments, dedicated products that take the complex ground seasonal dynamics into account are required.

Here we aim to 1) to develop Sentinel-1 InSAR products documenting the spatial variability and timing of the seasonal thaw subsidence maxima in three regions of Svalbard characterized by different geomorphological and climatic conditions; 2) compare the displacement time series with a composite index based on temperature and evaluate how a simple model can explain the progression of subsidence and heave patterns in the study areas; 3) discuss the potential and limitations of using the timing of the maximal subsidence as a proxy for the end of the thawing season and suggest ideas for the development of alternative InSAR products in polar areas characterized by cyclic patterns.

2. Study areas

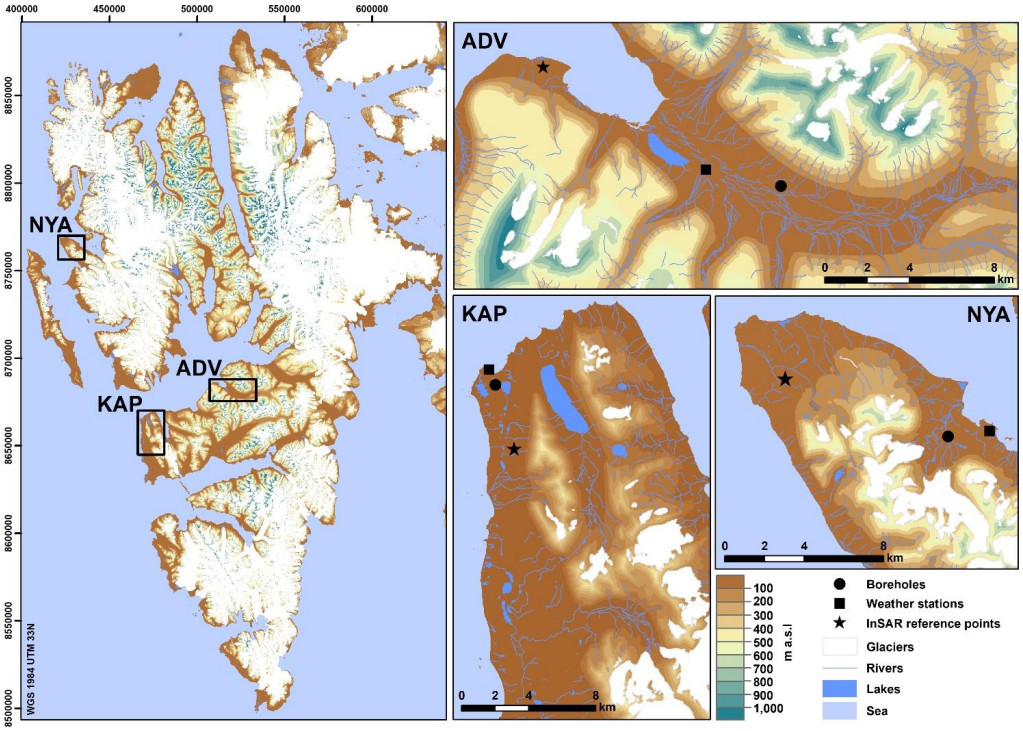

Figure 1. Location of the three study areas in central and western Spitsbergen, Svalbard: Adventdalen (ADV), Kapp Linné (KAP) and Ny-Ålesund (NYA). Digital elevation model and topographical information are from the Norwegian Polar Institute [35,36].

Svalbard is characterized by a polar-tundra climate [37], influenced by the West Spitsbergen oceanic current, which warms in particular the western parts of the archipelago [38]. The Spitsbergen island experiences a large climatic gradient with higher temperature and greater precipitation in the west compared to the more continental interior [39]. The periglacial land area has continuous permafrost, varying from approximately 100 m in thickness in valley bottoms and coastal areas to 500 m in the mountains [40]. The seasonal and inter-annual meteorological variations, as well as the diversity of local environmental conditions (water content, ground material properties, snow cover and vegetation) largely influence the ground thermal regime and consequently the dynamics of periglacial landforms [41–43]. Monitoring of ground temperature and ALT indicates that permafrost is warming and ALT is increasing [44–46]. Projections for the twenty-first century suggest similar future trends following climate change scenarios [39,47]. The study focuses on three different and well-studied areas of central and western Spitsbergen: Adventdalen, Kapp Linné and Ny-Ålesund (Figure 1). All three areas have permafrost observation sites as part of the Svalbard Integrated Arctic Earth Observing System (SIOS) [45]. The selected areas vary from 121 to 307 km^2 in size (Table 1).

The Adventdalen (ADV) area is dominated by a SE–NW oriented valley tributary to the large Isfjord system. Longyearbyen, Svalbard's main settlement and airport, is located in the western part of the study area (black star, Figure 1). ADV has a complex topography with mountain tops up to approximately 1,050 m a.s.l. and glacially eroded valleys down to sea level, carved into flat-lying

sedimentary rocks, consisting primarily of sandstones and shales [48]. Following regional deglaciation, fluvial and periglacial activities have further developed the ADV geomorphology. The valley floors are infilled by fluvial, alluvial and eolian (loess) deposits [49]. The permafrost thickness is about 100 m near the coast and increases up-valley [50]. The accumulation of eolian deposits on alluvial terraces led to the upward growth of syngenetic permafrost, underlain by epigenetic permafrost formed by the downward freezing of fluvial and marine deposits [51]. Ground ice distribution is variable [51,52], but higher contents are generally found in the top few metres of the syngenetic permafrost, especially in eolian deposits, and at the top of the underlying epigenetic permafrost [51]. Permafrost ECV observations have been carried out in this area since 2000 [46]. In 2016−2017, the mean annual temperature of the permafrost surface varied between approximatively −0.5 and −3.2 °C in two SIOS boreholes. ALT was between 0.9 and 1.8 m [45].

The Kapp Linné (KAP) area is located in the westernmost part of the Nordenskiöld peninsula and is greatly influenced by the North Atlantic maritime regime [53]. The region is characterized by the northwest-striking West Spitsbergen Fold Belt [54], and a low-lying Precambrian bedrock platform − the strandflat − mantled by raised beach deposits [55]. The Isfjord Radio weather station is situated in the northwestern part of this strandflat complex (black square, Figure 1). The Griegfjellet ridgeline, composed of pre-Cambrian phyllite [56], reaches up to approximately 780 m a.s.l. and separates the coastal strandflat from the Linné valley and its proglacial lake Linnévatnet [57]. The strandflat geomorphology is characterized by a complex assemblage of dry, coarse-grained, raised marine beach ridges, exposed weathered bedrock interspersed with thermokarst lakes, organic-rich shallow bogs with small palsas, ice-wedge polygons and sorted/unsorted circles [58,59]. Permafrost ECV observations have been carried out in this area since 2008 [44]. In 2016−2017, the mean annual temperature of the permafrost surface varied between approximatively −1.5 and −1.8 °C in two SIOS boreholes. ALT was between 1.8 and 3.0 m [45].

The Ny-Ålesund (NYA) area is located along Kongfjorden in northwestern Spitsbergen. It includes a former coal mining village, converted into a research station (black square, Figure 1). The region is characterized by a strandflat area in the outer part of the Brøggerhalvøya peninsula and steep topography with the highest peaks at 790 m a.s.l in the south-eastern part. In Brøggerhalvøya, late Paleozoic to early Triassic sedimentary sequences are overlain by Paleocene coal-rich sediments [60]. The bedrock is covered by Quaternary terrestrial and coastal sediments, consisting of till, colluvial, fluvial and raised beach deposits [61]. Fine-scale variabilities of surface temperature [62], snow cover [63] and active layer thickness [64] have been documented in the intensively studied Bayelva area (black circle, Figure 1). Here a permafrost research site collects long-term observational environmental data series since 1998 [65]. In 2016−2017, the mean annual temperature of the permafrost surface was approximatively −2.7 °C in the two SIOS boreholes in the area. ALT was between 1.5 and 2.0 m [45].

3. Data and methods

3.1. Sentinel-1 SBAS time series

InSAR results are based on SAR images from the Sentinel-1 satellites of the European Commission Copernicus Programme. The selected scenes have been acquired with the Interferometric Wide swath mode in an ascending geometry (track 14). The sensor looks obliquely downward (LOS incidence angle I_a, Table 1), towards ENE (LOS compass direction D_i, Table 1). The same period (June 22 to November 25, 2017) was selected for each study area to provide comparable time series. The chosen start and end dates are expected to reduce the risk of significant decorrelation due to extensive snow cover. It should, however, be noted that ground thawing is expected to start before June 22 (typically late May−early June in ADV) [22,46], which leads to an underestimation of the total seasonal subsidence if ground ice melts in the upper part of the active layer. This has no major implication considering that the scope of the study is to document the timing of the transition from thaw subsidence

to frost heave, occurring later within the season, and discuss the relative temporal variability of the displacement patterns.

InSAR results were processed using the NORCE GSAR software [66]. Single Look Complex (SLC) images were co-registered and multi-looked using a range/azimuth factor of 8x2. Interferometric image pairs (interferograms) were generated with a maximal temporal baseline of 48 days. After removal of strongly decorrelated interferograms (mean coherence < 0.5) due to fast movement, snow and moist surface, the effective temporal baseline is 6 to 12 days at the beginning and end of the time series. Longer temporal baselines could be included in the middle of the time series due to more stable ground conditions. The final selection includes 84 to 90 interferograms depending on the study area (Table 1 and Supplements S1–S3). The ADV time series is continuous. Acquisition 27.08.2017 in KAP is affected by major ionospheric effect, while acquisition 08.10.2017 in NYA is affected by snow. They have thus been discarded, introducing a gap in the time series. The constrained spatial baselines (maximum value: 188 m) lead to small topographical phase components that have been estimated and removed using a 20 m Digital Elevation Model (DEM) [35]. The noise-level was reduced in all interferograms by applying a spatially adaptive coherence-dependent Goldstein filter [67,68]. The contribution from the stratified atmosphere was mitigated by a data driven approach where we fit a linear relationship between residual phase and topography [69] using the available DEM [35]. Based on the redundant sets of interferograms, we further corrected the stratified delay per scene using a network-based approach [70]. The remaining turbulent component was mitigated by averaging all pairs centred on common acquisitions and using the redundancy to iteratively estimate the atmospheric contribution of each scene [71]. Pixels affected by low signal stability due to snow (e.g. glaciers, perennial patches) or water (e.g. lakes, rivers) in most of the pairs were removed by applying a coherence-based filter (0.5 in 50% of the selected interferograms). The unwrapping has been performed using the SNAPHU software [72]. InSAR is a spatially relative technique, which means that the results must be calibrated to a reference location. We tested different reference points and chose references in areas assumed to be stable. For all study areas, reference points are on low-inclined surface ($\leq 2°$) with high mean coherence (≥ 0.8), located either on infrastructure or on visible rock outcrops based on aerial imagery [73] (Table 1). We estimated ground displacement time series using the Small Baseline Subset (SBAS) method [74]. The inversion is performed using a L1-norm-based cost function, which is more robust than L2-norm with respect to unwrapping errors [75]. Atmospheric filtering used a spatial filter of 500 m and a temporal filter of 18 days.

The initial InSAR measurements correspond to one-dimensional sensor-to-ground distance changes along the LOS. The displacement times series are temporally relative to the first scene of the dataset (22.06.2017) and spatially relative to the reference points (Table 1). The results were geocoded using the 20 m DEM [35] and have a 40 m spatial resolution. The time series have a 6-day temporal resolution.

Table 1. Information about the study areas and the InSAR datasets. Locations of the InSAR reference points are shown in Figure 1. The interferogram networks are shown in Supplements S1–S3.

	Land area [km^2]	Selected number of interferograms	Line-of-sight (LOS) Incidence angle (I_a) / compass direction (D_i)	Reference points (UTM 33N)
Adventdalen (ADV)	307	90	I_a: 37.3° / D_i: 69.5°	8685931 511282
Kapp Linné (KAP)	288	88	I_a: 34.0° / D_i: 67.8°	8551011 469616
Ny-Ålesund (NYA)	121	84	I_a: 34.3° / D_i: 66.0°	8765916 423918

3.2. Thaw subsidence maxima

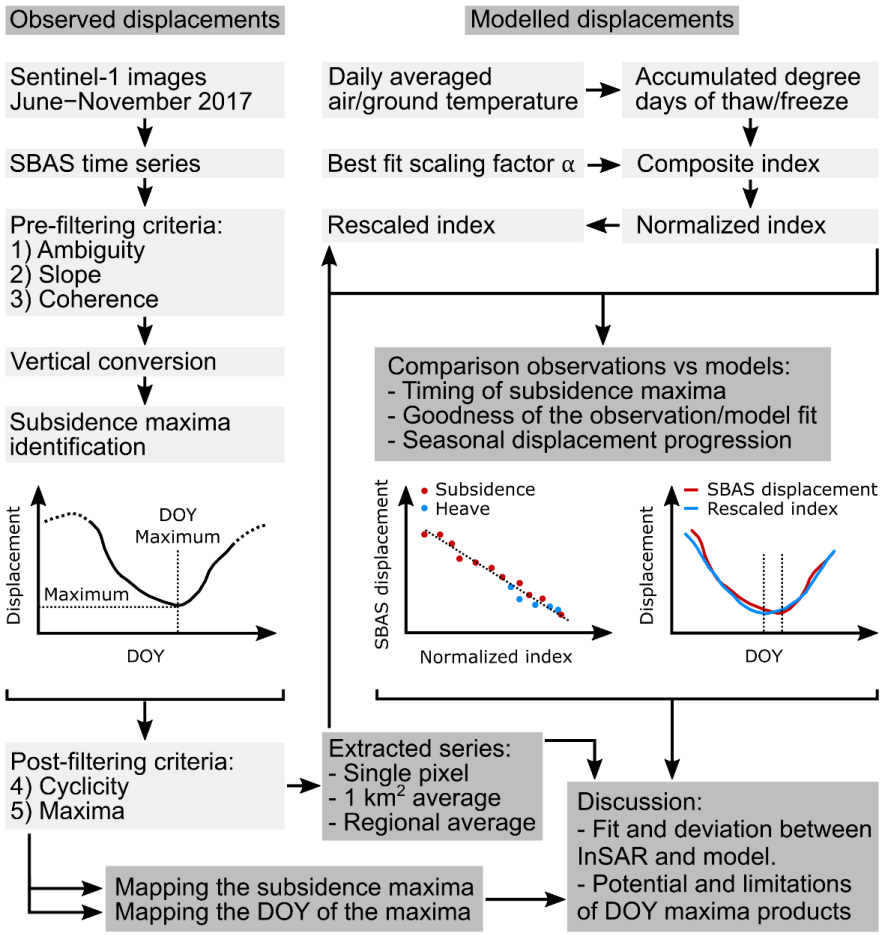

Figure 2. Schematic illustration of the study workflow. Light grey boxes show the processing steps. Dark grey boxes summarize the main outputs.

We propose a relatively simple workflow to generate high level products based on seasonal SBAS time series. We applied conservative filters to remove unreliable and irrelevant information when focusing on the timing of the thaw subsidence maxima. The procedure follows four main steps to filter the SBAS results, convert the LOS values to vertical displacements, identify the maximal subsidence and extract the acquisition date of the maxima. These steps are illustrated in Figure 2 and summarized hereafter:

1. Pre-filtering of SBAS results:
   a) Criterion 1 "Ambiguity": InSAR signal becomes aliased when the displacement gradient between adjacent pixels is higher than a quarter the wavelength during the selected time interval. The theoretical detection capability for Sentinel-1 (5.6 cm wavelength) is therefore 14 mm between the acquisitions used to build interferograms. We filtered out the results likely to

be affected by a phase ambiguity by discarding pixels with displacements over 14 mm between successive acquisitions.

b) Criterion 2 "Slope": Creep processes on slopes are likely to mask out the transition from subsidence to heave. Based on a 20 m DEM [35], we discarded all pixels with slope angle > 1.5°, computed using ArcGIS (©ESRI). Solifluction can occur on low-inclined surfaces, and has been reported on 2° slopes [76]. The conservative threshold of 1.5° was used to account for the relatively low DEM resolution, likely to underestimate local slope variabilities.

c) Criterion 3 "Coherence": Decorrelation sources due to snow, ground moisture and vegetation may affect the quality of the displacement estimates. We applied a secondary coherence thresholding more conservative than at the processing stage (Section 3.1). Pixels with mean coherence < 0.55 based on the selected interferograms (Table 1) were discarded.

2. Vertical conversion: As we focus here on flat areas, we can assume that all displacements occur vertically (subsidence and heave). We converted all results from LOS to vertical displacement using the following equation:

$$V_{disp} = \frac{LOS_{disp}}{\cos(I_a)} \quad (1)$$

where V_{disp} is the vertical displacement, LOS_{disp} is the LOS-projected displacement, and I_a is the incidence angle of the radar beam (Table 1). V_{disp} documents a subsidence (positive value) or a heave (negative value), relatively to the first acquisition date.

3. Subsidence maxima: For each time series, the maximal value was identified, and its corresponding Day of Year (DOY) was extracted. It should be noted that the DOY identification is based on the subsidence maximum only and does not take into account the entire pattern of the displacement progression, which may lead to erroneous value if the ground level flattens at the end of the thawing season.

4. Post-filtering of selected series:

a. Criterion 4 "Cyclicity": Pixels with DOY corresponding to the first or the last acquisition of the series (i.e. without any subsidence/heave pattern) were discarded, as they do not document a cyclic process. We assume that these pixels correspond to remaining low-inclined areas affected by downslope creep. For analysing the spatial distribution of the maximal subsidence, we used the results after the four first steps of filtering.

b. Criterion 5 "Maxima": For mapping the DOY, all pixels with a maximal subsidence < 10 mm were additionally discarded, as we assume that the transition between subsidence to heave in areas with low displacement amplitude is likely to be masked out by noise sources. The temporal resolution of the DOY product is 6 days (12 days when there is one missing acquisition), corresponding the repeat-pass interval of the Sentinel-1 mission.

For further comparison with temperature data (Section 3.3), we focused on time series at three different scales (local, intermediate and regional) by:

- Extracting the nearest pixels to the boreholes;
- Averaging the series for the pixels within 1 km^2 around the boreholes;
- Averaging the pixels with a DOY of the subsidence maxima within the interquartile range of all results, as we assume that they are representative of the ground behaviour at the regional scale.

3.3. Composite index model of seasonal time series

The SBAS time series were compared to a simple composite index model documenting the response of the ground surface to temperature variations, based on daily averaged air temperature from three weather stations and ground surface temperature from three boreholes in all study areas (Table 2; Figure 1). The calculation of the composite index is explained in detail by Hu et al. [13]. The four

main steps of the procedure are schematically summarized in Figure 2 and can be described as followed:

- For a given time in the season, the thawing (freezing) depth of the ground can be modelled using the Stefan equation [28,29]. The phase change of water causes volume change of the ground medium within the thawed (frozen) layer. We assume that the 1D ground medium has homogenous and constant thermal properties and water content. All the water pores within the active layer are assumed to be affected by phase change, which causes a ~9% volume decrease and increase leading to subsidence and heave. The time-variant subsidence (s) and heave (h) can be simplified as:

$$s(t) = E_T\sqrt{A_T(t)} \text{ and } h(t) = E_F\sqrt{A_F(t)} \quad (2)$$

where A(t) is the accumulated degree days of thawing (T) (units: °C days) or accumulated degree days of freezing (F) (units: °C days), and E_F and E_T are time-invariant coefficients based on ground/water properties (the soil bulk density, volumetric water content, water/ice density, latent heat of fusion for water, thermal conductivity, n-factors) [13].

- The two seasonal coefficients E_F and E_T can be related by a scaling factor α:

$$\alpha = \frac{E_F}{E_T} = \sqrt{\frac{k_F n_F}{k_T n_T}} \quad (3)$$

Where k_F and k_T are the thermal conductivities of the frozen (F) and thawed (T) ground. The n-factors n_F and n_T are ratios accounting for the offset between the air temperature and the ground surface temperature, influenced by the surface conditions (e.g. snow, vegetation) [77].

The scaling factor applied by Hu et al. [13] is 1.44 based on the ground properties of the Barrow site (Alaska, USA), and using air temperature series for the calculation of the composite index. When using ground surface temperature, the n factors are 1, so α reduces to $\sqrt{\frac{k_F}{k_T}}$, i.e. the difference of thermal responses between thawed and frozen ground. In our study, we tested and compared the results for five factors (1, 1.2, 1.4, 1.6 and 1.8), due to variable and partly unknown ground properties in the study areas.

- Based on equations 2 and 3, the composite index I_c can be expressed as:

$$I_c(t) = \sqrt{A_T(t)} - \alpha\sqrt{A_F(t)} \quad (4)$$

We set the composite index to be zero until the start of the thawing season. The initiation of the calculation starts when first daily averaged temperature above 0 °C are recorded at the weather stations or in the boreholes.

- Because we are only interested in characterizing the temporal pattern of ground displacements, we normalized the composite index with its maximum value and rescaled it by multiplying the index by the maximal value of the SBAS displacement time series:

$$d(t) = d_s\bar{I}_c(t) \quad (5)$$

Where d_s is the maximum seasonal subsidence based on the SBAS time series (units: mm) and $\bar{I}_c$ is the composite index (equation 4) normalized with its maximum value.

The comparisons between the SBAS time series and the model (normalized and rescaled composite index) consisted of:

- Comparing the timing of the transition between the subsidence and the heave between the observations and the models;

- Evaluating the goodness of the fit between the observations and the models by documenting the proportion of the variance of the seasonal SBAS displacements that is explained by the normalized index (R^2);
- Analysing the temporal variations of the entire observed displacement time series in respect to the rescaled composite index;
- Discussing the results' differences when using single pixels closest to the boreholes, 1-km^2 and regional averaged displacement time series.

We finally interpreted the fit/deviation between the observation and the model by discussing the limitations of the SBAS products and the validity/invalidity of the assumptions behind the simplified composite index model. The findings were related to the results from Section 3.2 to discuss the potential of DOY maxima products to document the cyclic dynamics of the active layer in permafrost landscapes.

Table 2. Information about the weather stations, the boreholes and the documented air and ground temperature time series in the three study areas. Locations are shown in Figure 1.

	Station and data types	Coordinates (UTM 33N)	Altitude [m a.s.l]	Site information and reference
Adventdalen (ADV)	Weather station. Air temperature.	8681070 N 518966 E	15	Adventdalen station 99870. Reference: NCCS, 2021 [78].
	Borehole. Ground temperature.	8680294 N 522504 E	17	Ice-wedge polygons in eolian deposit. The area is affected by long-term subsidence, exposing the upper sensors closer to the surface. Data from logger at –23 cm is therefore used in this study, assuming to be representative of the ground surface conditions. The borehole is part of the UNIS monitoring network and temperature data has previously been compared with InSAR in Rouyet et al., 2019 [22].
Kapp Linné (KAP)	Weather station. Air temperature.	8665721 N 468119 E	7	Isfjord Radio station 99790. Reference: NCCS, 2021 [78].
	Borehole. Ground temperature.	8664808 N 468512 E	21	Beach ridge on strandflat composed of coarse-grained beach sediment. Sensor at ground surface. GTN-P and NORPERM references: NO 36 / KL-B-2. Reference: Christiansen et al., 2010; 2021 [44,45].
Ny-Ålesund (NYA)	Weather station. Air temperature.	434216 N 8763255 E	8	Ny-Ålesund station 99910. Reference: NCCS, 2021 [78].
	Borehole. Ground temperature.	8762985 N 432118 E	25	Diamict surface with fine-grained glaciofluvial sediments. Profile C. Sensor at –1 cm. GTN-P reference: NO GE 60. Reference: Boike et al., 2018 [65].

4. Results

4.1. Thaw subsidence maxima

The final SBAS results (Sections 3.1–3.2) are presented on maps showing the distribution of the subsidence maxima and their corresponding DOY (Figure 3–5). The five criteria used for filtering significantly reduce the exploitable observations to 3–5 % of the initially documented pixels (Supplement S4) but still provide a good coverage in the flat areas, mostly in the valley bottoms in ADV, and in the strandflat areas in KAP and NYA, with total pixel numbers of 14,547 in ADV, 21,198 in KAP and 6,021 in NYA. The observed patterns are described thereafter by analysing the results at the landscape scale, as well as within selected km^2 areas around the three boreholes and over landforms experiencing a behaviour that deviated from the regional trend. Orthophoto imagery of the corresponding locations can be found in supporting material (Supplement S5).

In ADV, displacements occurring between June 22 and the day of the subsidence maxima are mostly over 20 mm (Figure 3A). The displacement distribution is geomorphologically-controlled [22]. Large displacements are detected on landforms assumed to have high water content and composed of fine-grained frost-susceptible sediments. Greatest subsidence up to approximately 100 mm are found in the outer part of alluvial fans and in the eolian terraces surrounding the ADV braided river. The timing of the subsidence maxima is quite homogenous in the valley bottom (Figure 3B), with values between 251 and 269 (mid–late September). The maxima are identified later on the valley sides, e.g. where the borehole is located (Figure 3B, area C; Figure 6C), suggesting different ground behaviour between the terraces (Supplement S4, C) and the fluvial riverbed (Supplement S4, D). Most ADV time series show a clear cyclic displacement pattern, with a distinct and quick transition between subsidence and heave that allows for a mostly unambiguous extraction of the DOY maxima (Figures 6C–D). The subsidence maxima are identified earlier on the SW blockfield plateau (Figure 3B, area E; Figure 6E), suggesting earlier freeze-back due to higher elevations (400–500 m a.s.l). The end of the time series in November is often affected by a stabilization or lowering effect (Figure 6 C and E) that may be caused by a bias due to interferences from snow or surficial icing. This presumed artefact especially affects some alluvial fans in the inner part of the valley (eastern side in Figure 3B) where outliers with late DOY maxima are identified.

In KAP, the variability of the subsidence maxima matches the complexity of the landform assemblage in the area (Figure 4A), especially in the northern part (Supplement S5, area F). Low subsidence values (typically lower than 20 mm) are detected in areas composed of exposed bedrock or coarse-grained beach ridges, but maxima up to 120 mm are found in organic-rich and fine-grained sediments in beach ridge depressions. A spatial gradation with earlier DOY along the eastern slope compared to the coastal part highlights the impact of the maritime influence within the area (Figure 4B). The timing of the subsidence maxima is mostly homogenous in the northern part, e.g. where the borehole is located (Figure 4B, area F). The subsidence maxima occur considerably later than in ADV (287 to 305, i.e. in mid–late October). The transition between subsidence and heave is clear on series from the northern part (Figures 4F, area F; Figure 6F) but becomes more ambiguous towards the South, where earlier DOY are detected (Figure 4B, areas G–H; Figure 6G–H). The flattening of the displacement curves in mid–late summer shows that the ground level stabilizes for a long period, likely due to little ice content in the lower active layer (Figure 6G–H). The ground stabilization induces uncertainties in the automatic identification of the subsidence maxima (Figure 6G–H). Nevertheless, the different behaviour observed on the beach ridges in the south-eastern part of the strandflat may also indicate specific ground conditions due to the location at the mouth of the Orustdalen valley occupied by large glacial systems in its upper part (Figure 3B, area H). This is further discussed in Section 5.

In NYA, the documented surfaces are mostly composed of coarse beach and diamict deposits. The relatively little frost-susceptibility of the material leads to subsidence values generally lower than for

the two other study areas, with maxima mostly under 40 mm (Figure 5A). Maximal subsidence, up to 80 mm, are found primarily in the western part of the peninsula, in the alluvial deposits surrounding the Kvadenhukelva riverbed. Beach ridge depressions on the strandflat show homogenous DOY values with subsidence maxima occurring approximatively at the same time as in the KAP area (287 to 299, in mid-October) (Figure 5B, e.g. in area J). The north-western part of the strandflat has considerably earlier DOY than the surroundings (Figure 5B, area J), suggesting a different ground behaviour in this exposed coastal part of the landscape. It experiences rather stable surface position, with only minor subsidence through the documented summer period, followed by quick and large heaving when freeze-back occurs (Figure 5B, area K; Figure 6K). Larger subsidence may have occurred prior the documented period as this exposed coast is likely snow-free long before the start of the InSAR series (June 22). As for the southern part of the KAP area, the early stabilization of the ground level causes uncertainties in the automatic extraction of the maxima. However, the different pattern identified at this location may also be caused by specific ground conditions characterizing the outer part of alluvial fans. In the inner part of Kongsfjorden (NE in Figure 5), some altitudinal variations and geographical zonation are visible, with earlier DOY compared to the outer part of the peninsula. Around the borehole, a heave pattern is detected in late August to mid-September prior to the main one from mid-October (Figure 6I). We further discuss the potential causes of this pattern in relation with the composite index (Section 4.2).

When comparing the results for the three areas, clear differences are identified (Figure 7). The median DOY of the subsidence maxima is earlier in ADV compared to KAP and NYA. Even considering the interquartile variability of the distribution, the values of ADV show no overlap with the two other areas (Figure 7A). KAP and NYA DOY maxima have overlapping distributions, but the detected subsidence values are lower in NYA (Figure 7A). It should be noted that the acquisition gap in the NYA time series (early October, DOY 281) may have led to an artificially later median DOY if the natural transition occurs around the missing date (Figure 7D). To focus on representative regional patterns, we averaged the time series with a DOY of the subsidence maxima within the interquartile range of the distribution of all values (Figure 8B). Cyclic patterns are visible in all areas, but the averaged time series highlight regional differences that are further discussed in Section 6.1. Time series with maxima below/over the first and third quartiles of the entire area (Figure 8 A and C) exemplify the deviation from the most common pattern. Due to long thawing periods, the averaged time series in KAP and NYA show that the ground tends to remain stable during several months in mid–late summer (Figure 8), which likely affects the reliability of the automatic extraction of the subsidence maxima. This issue is further discussed in Section 6.2.

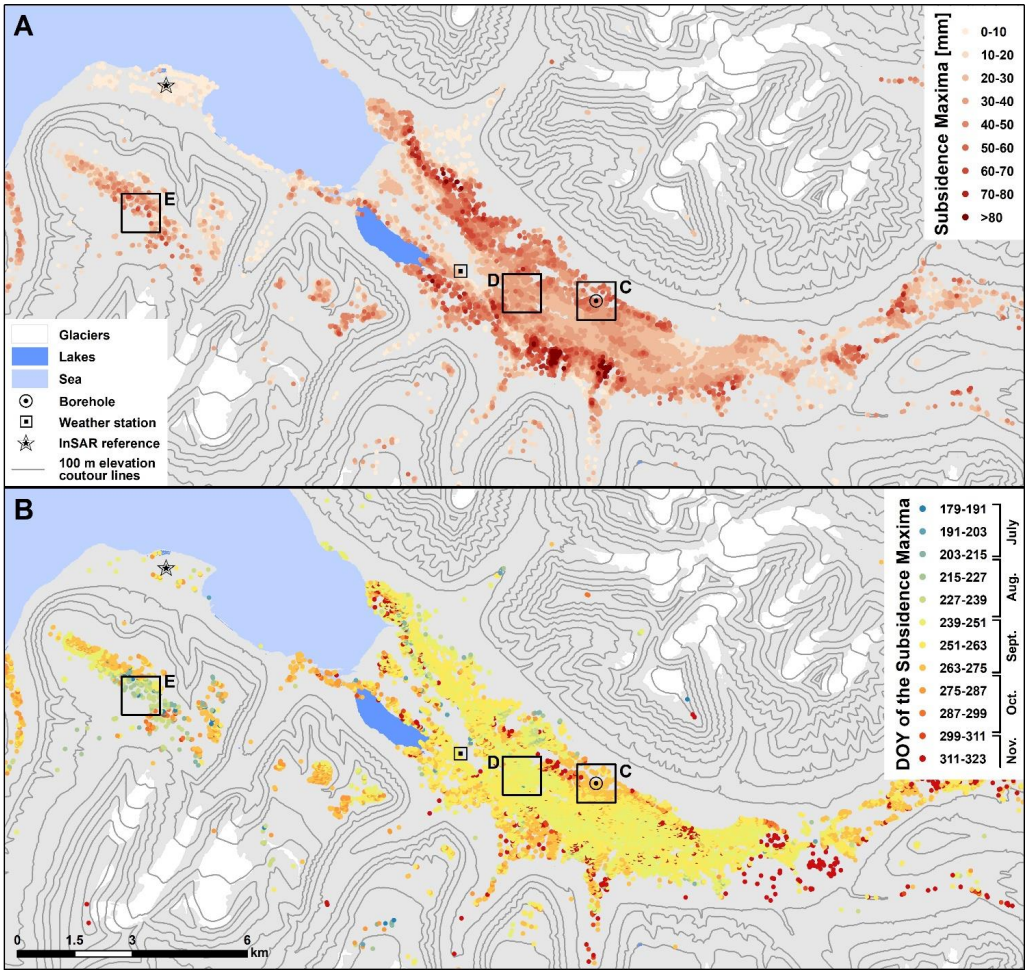

Figure 3. Spatial distribution of filtered SBAS results in Adventdalen (ADV) based on 22.06.2017–25.11.2017 time series. **A.** Subsidence maxima for the pixels selected after the four first filtering criteria (Section 3.2). **B.** Day of Year (DOY) of the subsidence maxima for the pixels selected after the five filtering criteria (Section 3.2). Black squares **C–E** show the km^2 extents used to average the time series (Figure 6C–E). Orthophoto imagery of the corresponding locations are shown in Supplement S5. 100 m elevation contour lines, glacier, sea and lake layers are from the Norwegian Polar Institute [35,36].

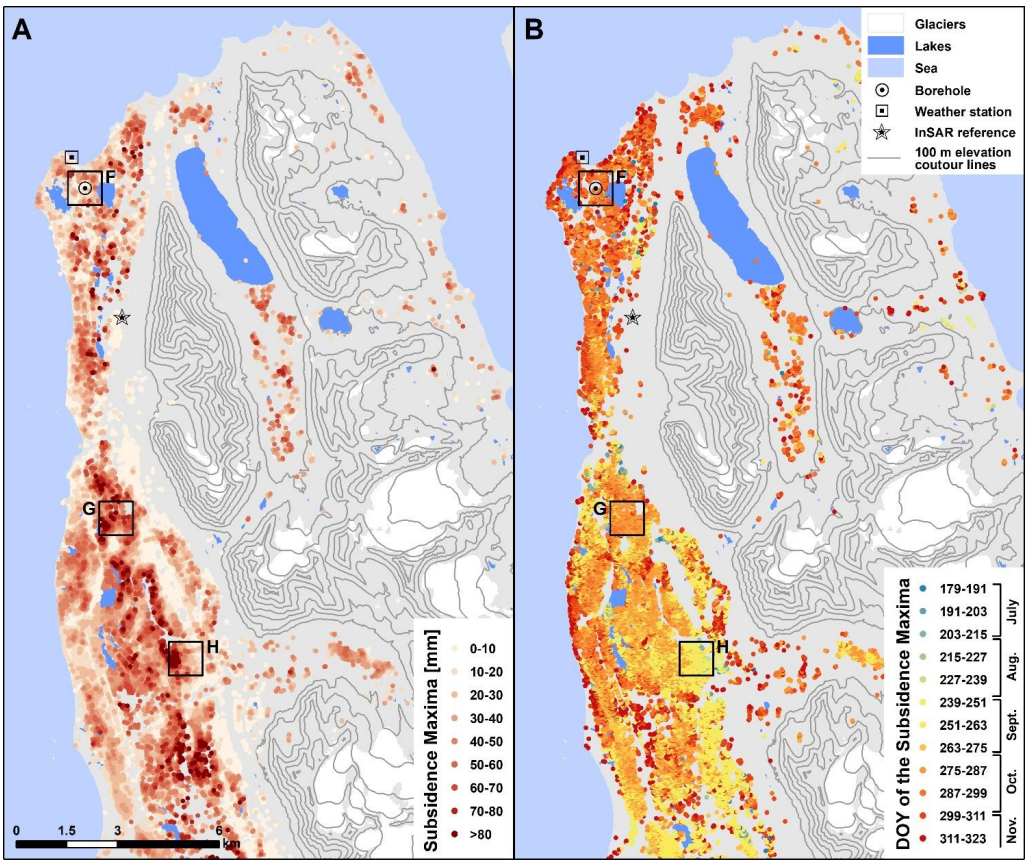

Figure 4. Spatial distribution of filtered SBAS results in Kapp Linné (KAP) based on 22.06.2017–25.11.2017 time series. **A.** Subsidence maxima for the pixels selected after the four first filtering criteria (Section 3.2). **B.** Day of Year (DOY) of the subsidence maxima for the pixels selected after the five filtering criteria (Section 3.2). Black squares **F–H** show the km^2 extents used to average the time series (Figure 6F–H). Orthophoto imagery of the corresponding locations are shown in Supplement S5. 100 m elevation contour lines, glacier, sea and lake layers are from the Norwegian Polar Institute [35,36].

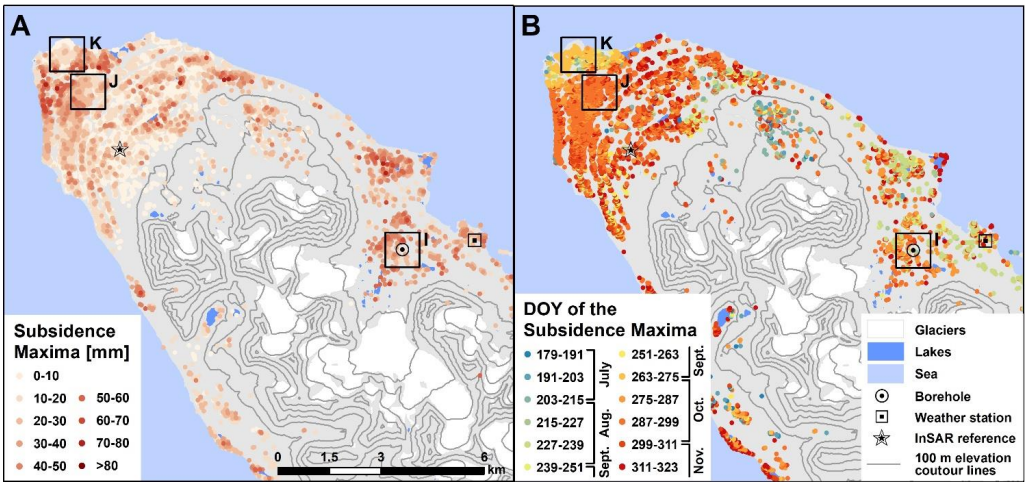

Figure 5. Spatial distribution of filtered SBAS results in Ny-Ålesund (NYA) based on 22.06.2017–25.11.2017 time series. **A.** Subsidence maxima for the pixels selected after the four first filtering criteria (Section 3.2). **B.** Day of Year (DOY) of the subsidence maxima for the pixels selected after the five filtering criteria (Section 3.2). Black squares **I–K** show the km^2 extents used to average the time series (Figure 6I–K). Orthophoto imagery of the corresponding locations are shown in Supplement S5. 100 m elevation contour lines, glacier, sea and lake layers are from the Norwegian Polar Institute [35,36].

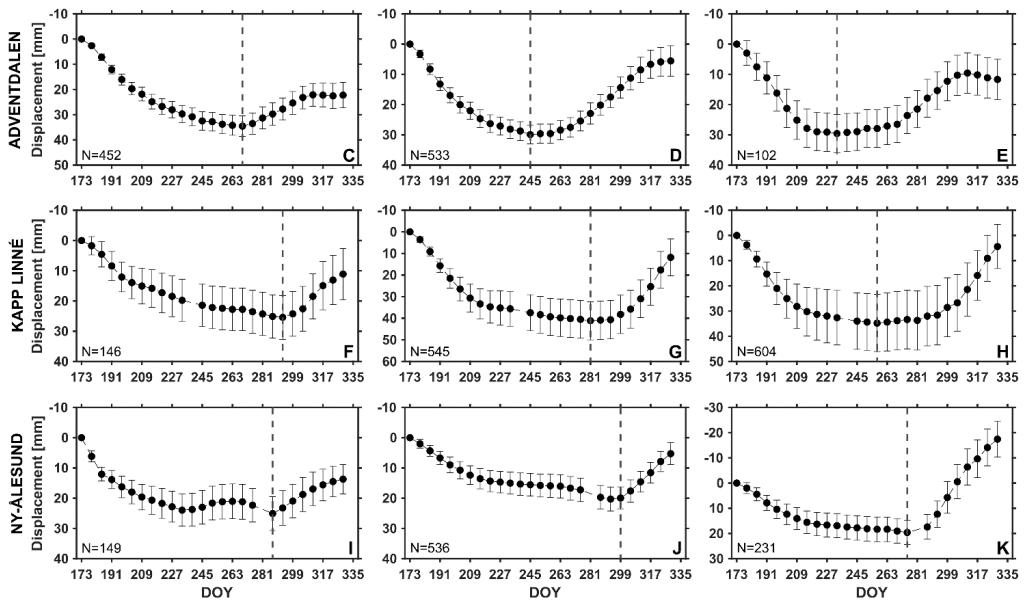

Figure 6. Examples of the spatial variability of the seasonal displacement progression and the detected DOY of the subsidence maxima for time series averaged over 1 km^2. Locations **C–K** are shown in Figures 3–5 (black squares). Orthophoto imagery of the areas are shown in Supplement S5. The vertical bars show the standard deviation of the displacement values around the mean for each acquisition time. The vertical dashed lines show the averaged detected DOY of the subsidence maxima. N value documents the number of pixels that have been averaged for each area. Note that the y-axis scale varies for each graph.

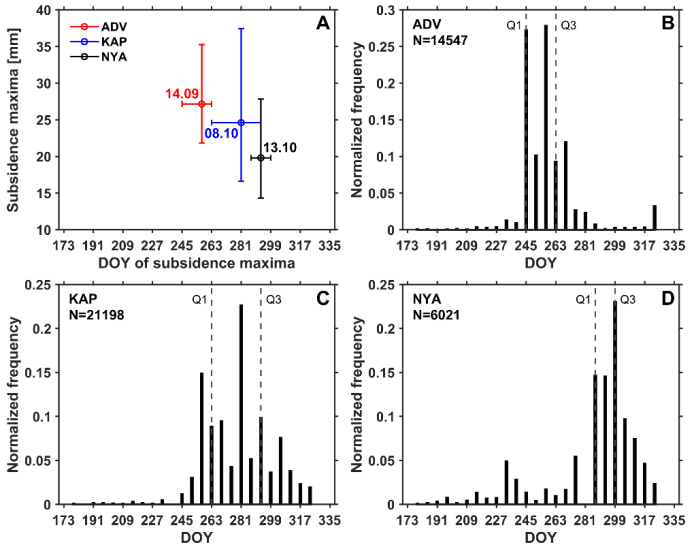

Figure 7. A. Median and interquartile range of the subsidence maxima (> 10 mm) and associated DOY. Circles and dates show the median values. The bars show the interquartile range. **B–D.** Distribution of the DOY of the subsidence maxima in Adventdalen (ADV), Kapp Linné (KAP) and Ny-Ålesund (NYA). Vertical dashed lines Q1 and Q3 show the first and third quartiles of the distribution. N values are the numbers of total pixels after filtering.

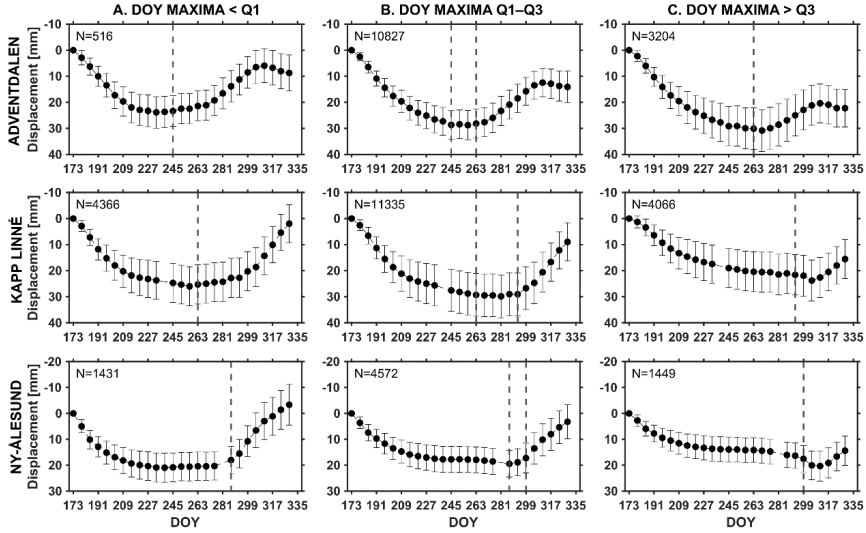

Figure 8. Averaged time series for each study area classified according to the DOY of the subsidence maxima. The vertical bars show the standard deviation of the displacement values around the mean for each acquisition time. Vertical dashed lines Q1 and Q3 show the first and third quartiles of the entire distribution. N document the number of pixels that have been averaged in each category. **A.** Average of the series with a detected DOY earlier than the first quartile (Q1) of the distribution. **B.** Average of the series with a detected DOY within the interquartile range, assumed to be representative of ground dynamics at the regional scale. **C.** Average of the series with a detected DOY later than the third quartile (Q3) of the distribution.

4.2. Composite index model of seasonal time series

The daily averaged temperature series highlight differences between the air and ground surface temperatures measured at weather stations and in boreholes in each of the three study areas (Table 2). Short-term fluctuations are reduced in the time series from the boreholes (Figure 9A) mostly due to the insulating winter and spring effects of the snow and the thermal diffusivity of the upper soil layer. Especially at the beginning of the thawing season in ADV and NYA, a thermal offset and a time lag are observable between the two series. In NYA, the ground surface temperature during snow melting remained stable around 0 °C during three weeks after air temperature became positive (Figure 9A). The start of the InSAR observation window on June 22 (measurement period, vertical black lines in Figure 9A) approximately fit the onset of ground thawing in the NYA borehole (June 20). In ADV and KAP boreholes, the ground thawing started on June 13 in ADV borehole and June 4. This is 9 days (ADV) to 18 days (KAP) before the InSAR measurement period, which highlights the importance of interpretating the subsidence maxima values in a relative manner, due to underestimation of the total seasonal subsidence. Based on the thaw depth probing at the University Centre in Svalbard Circumpolar Active Layer Monitoring network grid (UNISCALM) [43,46], early summer is indeed known to have a quick thawing rate, which may induce an undocumented subsidence if ground ice melts in the upper part of the active layer.

The composite index was calculated based on air and ground temperature data from the three weather stations and boreholes (Section 3.3) (Supplements S6–S7). After testing five scaling factors α (Section 3.3), the results showing the best fit between the observed and modelled time series have been selected (Supplements S8–S9). At the regional scale, the pixels with a DOY of the subsidence maxima within the interquartile range of all series (Figure 8B) are compared with the composite index. The results show that for all study areas, the composite index models based on ground surface temperature from the boreholes provide a better fit with the observed subsidence and heave than when using air temperature as input (Figure 9B and Supplement S10). This can be explained by the lag between air and ground temperature, especially at the thaw onset. For further analysis, we therefore used ground temperature as input to the models at all scales and for all areas.

In ADV, at the borehole location, both the timing of the transition from subsidence to heave and the whole displacement progression is well represented by the composite index (Figure 10A). Similarly, the match is good for the intermediate scale (km^2 average) (Figure 10B). At the regional average, the general shape of the curve is well represented by the model, but the measurements are shifted compared to the modelled displacements, especially during heaving (Figure 10C). The observed subsidence maxima and the following heave occur earlier than the model. This shows that the borehole is located in an area that deviates from the interquartile regional averaged series, which is also visible when examining the spatial distribution of the DOY of the subsidence maxima (Figure 3B).

In KAP, the pixel closest to the borehole shows noisy patterns, especially at the beginning and the end of the documented period (Figure 11A). The progression of the displacements is not well represented by the model, but the timing of the transition matches the composite index. The km^2 average allows for removing some variability and improves the fit between measurements and the model (Figure 11B, left), although the whole displacement progression still appears to be controlled by other factors than temperature only (Figure 11B, right). The regional average reduces short-term variability, especially during late subsidence, which is well represented by the model. However, as for ADV, the timing of the transition is slightly shifted (Figure 11C). The natural variability in this wide and geomorphologically heterogenous area does not allow for representing averaged regional displacements based on temperature from one single borehole site located on a dry beach ridge (Supplement S5, F).

In NYA, the comparison between the composite index and the InSAR time series closest to the borehole shows a clear shift (earlier for the InSAR series) and a low R^2, which suggest that processes

occurring at this specific location can not only be explained by a simple temperature-based model (Figure 12A). With a km^2 average, the InSAR series highlight an ambiguous pattern, with a small heave occurring prior to the main one (Figure 12B). It approximately occurs when the temperature drops and fluctuates around 0 °C for about a week (Figure 9A). The pattern is only visible in the highest part of the landscape (Figures 5I and 6I), which may suggest that at this location, lower temperature leads to surficial ice formation. However, the clear displacement pattern and long duration of the heave pattern compared to the relatively short freezing period indicates that the displacement is controlled by other factors than temperature only. Another important issue in the NYA series is the missing acquisition in early October (decorrelation due to snow), which is approximatively at the time of the freeze-back according to the temperature series. It contributes to a poor correspondence between the measurements and the model for the acquisition dates close to the subsidence maxima. Nevertheless, when averaging series at a regional scale, the match between the observation and the model increases considerably (Figure 12C).

The comparison of the three areas leads to contrasting conclusions. In ADV, the time series have a clear cyclic pattern that is well represented by the model at local and km^2 scales. At larger scale, the fit between the observation and the model decreases. The area where the borehole is located appears to be not representative of the regional behaviour dominated by earlier DOY in the fluvial sediments of the brained river plain. In KAP, the km^2 average provides a better fit with the model than a single pixel. The timing of the subsidence-to-heave transition generally fits the temperature records, but the whole displacement progression is not fully explained by the model. At the regional scale, inversely, the displacement progression is well represented by the model, but the subsidence-to-heave transition is somewhat shifted. As for ADV, this highlights the difficulty of representing a regional pattern based on single borehole temperature records, especially in a large area with a complex assemblage of landform types. In NYA, the observation at local scale is not explained by the model. The timing of the transition is clearly shifted compared to the temperature records. However, by averaging the series within a km^2 or at regional scale, the match improves considerably. The causes of the differences between the three areas are further discussed in Section 5.1 and used to identify the advantages and limitations of the proposed method and applied model in Section 5.2.

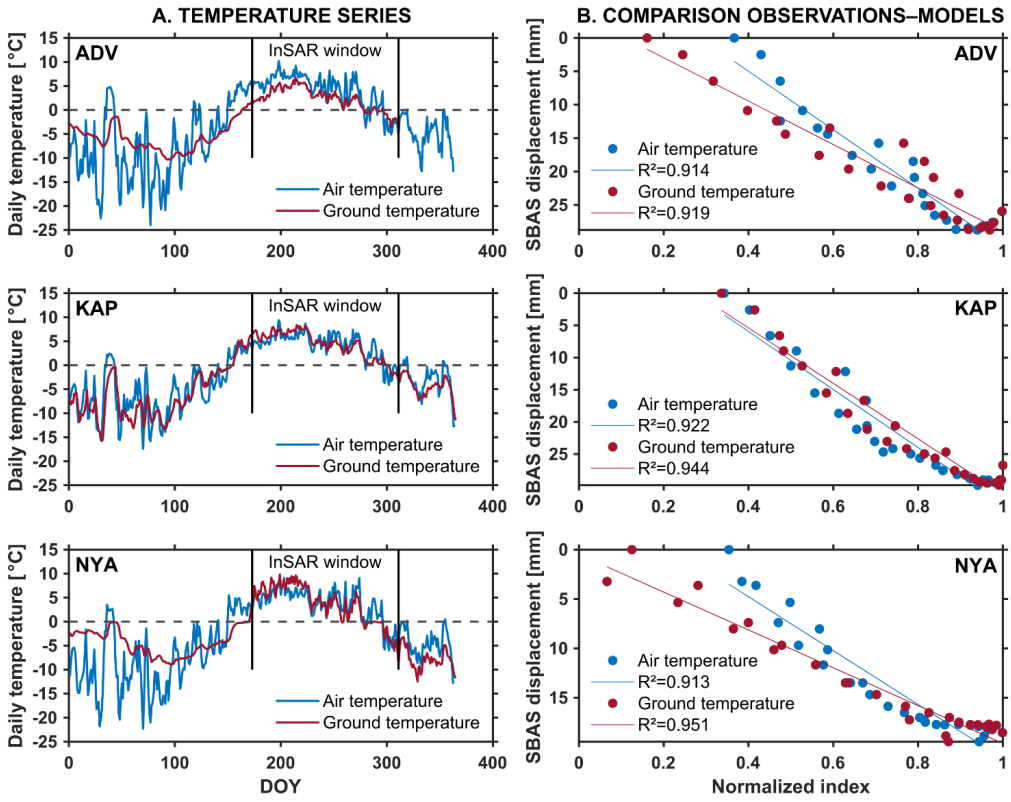

Figure 9. A. Daily air and ground surface temperatures at the weather stations and in boreholes in Adventdalen (ADV), Kapp Linné (KAP) and Ny-Ålesund (NYA) (Table 2). **B.** Comparisons between normalized composite index and SBAS displacement at the regional scale (DOY maxima Q1–Q3, Figure 8B). Comparisons between the SBAS time series and the rescaled normalized index are shown in Supplement S10. Information about temperature data is summarized in Table 2.

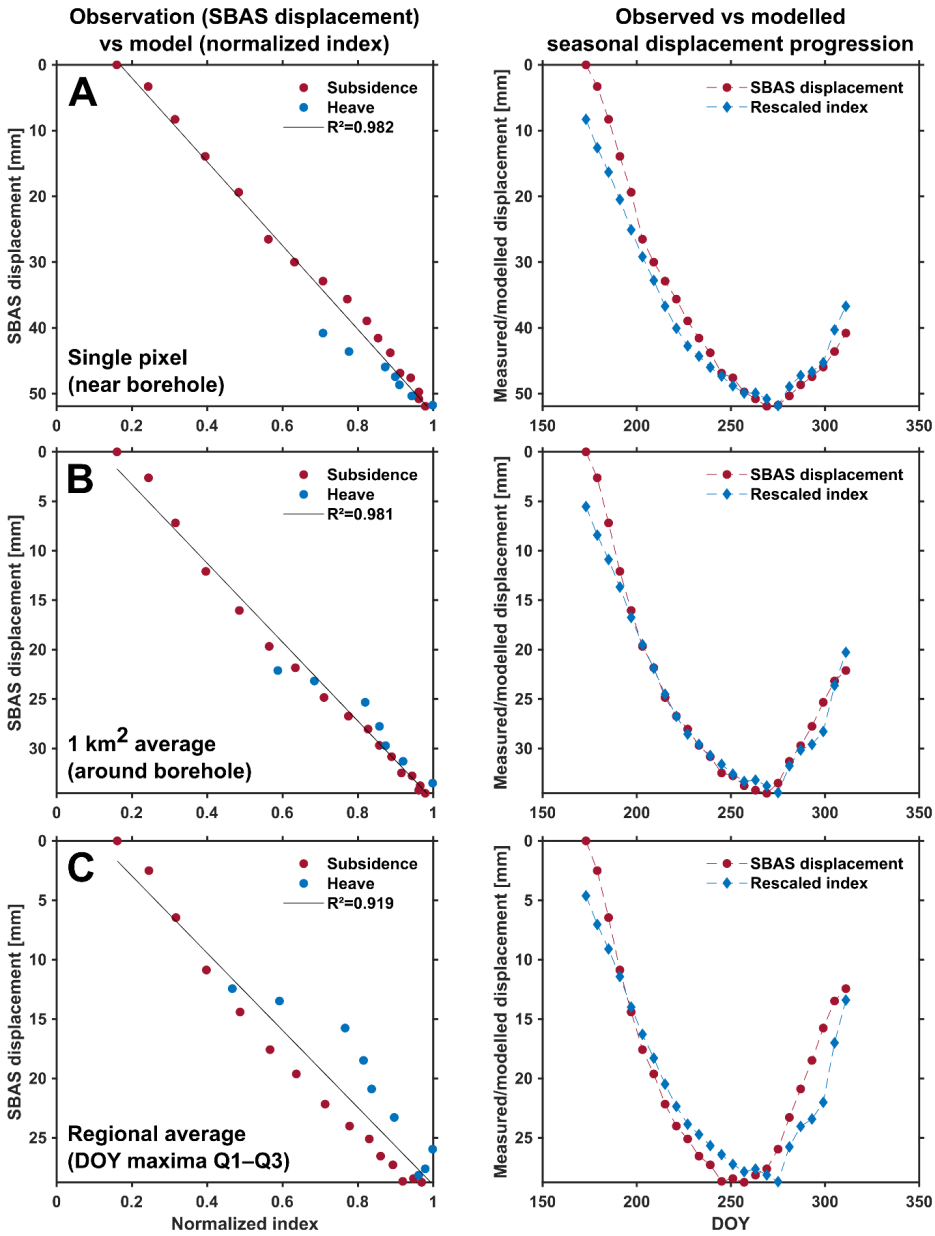

Figure 10. Comparison between the InSAR time series and the composite index at three scales in the Adventdalen (ADV) study area. **Left:** Goodness of the fit between SBAS displacement and normalized composite index. **Right:** Seasonal progression of the SBAS time series and the rescaled composite index. **A.** The selected time series corresponds to the pixel where the borehole is located. **B.** 1 km^2 average around the borehole (452 pixels). Black square C in Figure 3. **C.** Regional average of the time series with a DOY within the interquartile of all the pixels (Figure 8B). Note that the y-axis scale varies for each graph. Information about temperature data is summarized in Table 2.

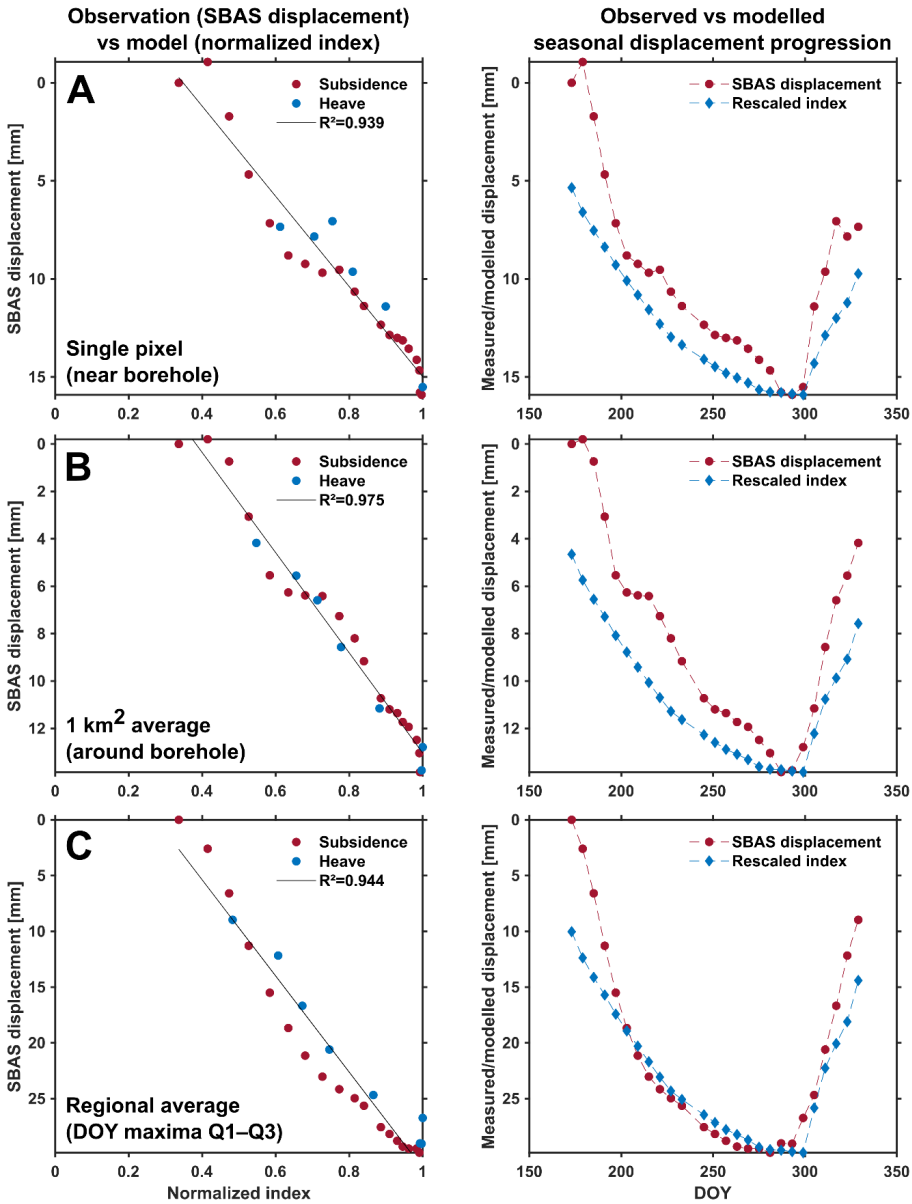

Figure 11. Comparison between the InSAR time series and the composite index at three scales in the Kapp Linné (KAP) study area. **Left:** Goodness of the fit between SBAS displacement and normalized composite index. **Right:** Seasonal progression of the SBAS time series and the rescaled composite index. **A.** The pixel at the location of the borehole has been filtered out and we therefore used the nearest available time series (pixel centre is 62 m away from the borehole, black circle in Figure 4). **B.** 1 km^2 average around the borehole (146 pixels). Black square F in Figure 4. **C.** Regional average of the time series with a DOY within the interquartile of all the pixels (Figure 8B). Note that the y-axis scale varies for each graph. Information about temperature data is summarized in Table 2.

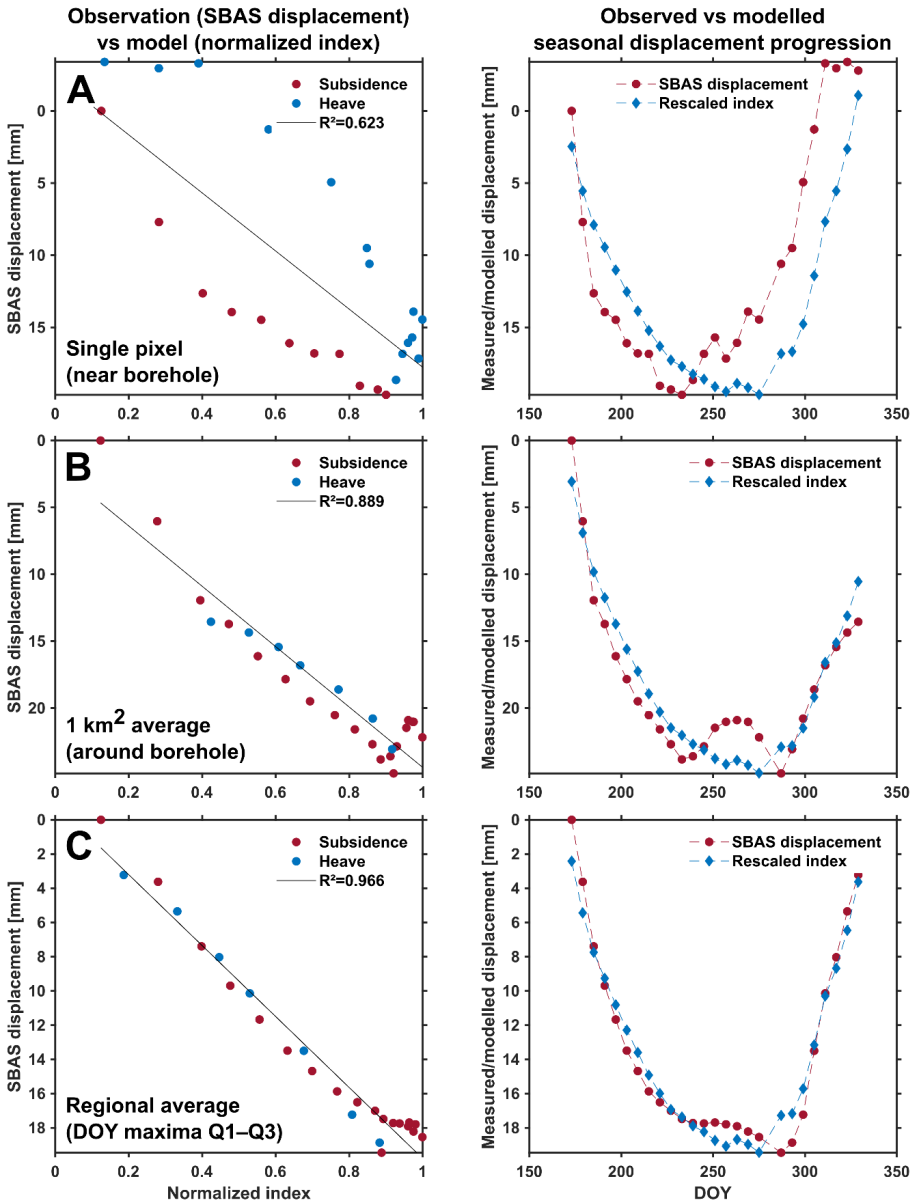

Figure 12. Comparison between the InSAR time series and the composite index at three scales in the Ny-Ålesund (NYA) study area. **Left:** Goodness of the fit between SBAS displacement and normalized composite index. **Right:** Seasonal progression of the SBAS time series and the rescaled composite index. **A.** The pixel at the location of the borehole has been filtered out and we therefore used the nearest available time series (pixel centre is 43 m away from the borehole, black circle in Figure 5). **B.** 1 km^2 average around the borehole (149 pixels). Black square I in Figure 5. **C.** Regional average of the time series with a DOY within the interquartile of all the pixels (Figure 8B). Note that the y-axis scale varies for each graph. Information about temperature data is summarized in Table 2.

5. Discussion

5.1. Seasonal displacement patterns

The documented subsidence maxima in the three areas of Western Spitsbergen (mostly within 15–35 mm, with maximum up to 120 mm) are in the commonly reported ranges of seasonal cyclic displacements in continuous permafrost areas [13,14,26] and generally agree with other observations made in Svalbard [79–81]. However, it is important to consider that the applied InSAR measurement period is underestimating the total subsidence, especially in areas where the thaw onset starts significantly earlier than the InSAR observation window, such as in KAP (Figure 10A). The NYA study area shows nevertheless clearly lower subsidence values than ADV and KAP (Figure 7A), which is most likely caused by a generally thinner and more coarse-grained sediment cover. The large variability of the displacement values within and between the study areas is assumed to be controlled by the active layer thickness and the ground conditions (ice type/content, frost-susceptibility of the material). The relationship between landform types and InSAR displacement rates has been discussed in a former Svalbard study [22] and by several authors in other continuous permafrost environments of the Northern Hemisphere, such as Siberia, Alaska and Canada [17,21,82,83].

The InSAR time series after filtering highlight clear cyclic patterns, but the timing of the displacement progression varies between the three study areas. Distinct transitions from subsidence to heave are found in ADV, while more ambiguous patterns are observed in parts of the KAP and NYA areas. The extracted DOY of the subsidence maxima vary between the three regions. The results especially highlight a clear difference between the two areas located on the West coast and ADV in central Spitsbergen. This emphasizes the maritime influence of the warm sea in KAP and NYA, compared to one of the most continental parts of Svalbard (ADV) [41,53].

In ADV, the mean annual air temperature was -2.8 °C in 2017 [78]. Ground surface temperature at borehole location shows relatively cold conditions with only 356 °C days of thaw in 2017 (Supplement S7). The area is characterized by early subsidence maxima (DOY median values: September 14) (Figure 7A). At the location of the borehole, the maximum occurs later (September 26), which approximately concurs with the ground surface temperature series (Figure 10A). The difference between the fine-grained terrasses and the coarse sediments surrounding the riverbed in the valley bottom, visible on DOY maxima maps (Figure 3B) as well as on the entire time series (Figure 6B–C), highlight a contrasting response of the ground to temperature fluctuations. It suggests that the ground reacts quickly to the first recorded negative temperature in coarse fluvial sediments, while the process is delayed on the loess terraces. The different behaviour at the location of the borehole, compared to most of the valley bottom, is also documented by in-situ measurements. At the UNISCALM site, the thaw onset is documented in late May – early June [43,46], while thawing is delayed at the location of the selected borehole (first positive temperature at ground surface on June 13) (Figure 9, Supplement S7). InSAR time series with subsidence maxima above the first third quartile (Figure 8C) appear to be affected by a systematic bias at the end of the documented period. No clear source has been identified, but we hypothesize that this may be caused by complex scattering processes due to snow or surface icing [84]. Time series with maxima below the first quartile of the entire area (Figure 8A) are mostly located in elevated parts of the landscape (blockfield plateaus) and suggest a natural earlier freezing onset due to colder, drier and/or well-drained conditions. Although less obvious, similar gradients seem to affect the two other areas. In KAP, later subsidence maxima are detected in the western part, most exposed to the maritime influence, compared to the more protected interior (Figure 4B). In NYA, early subsidence maxima are detected in the NE part (Kongsfjord interior), compared to the exposed strandflat in the outer part of the peninsula (Figure 5B).

In KAP, a large heterogeneity is highlighted both in terms of maximal subsidence values and timing of displacement progression (Figures 4 and 6 F–H), which is assumed to illustrate the complexity of

the landform assemblage in the area [58,59]. KAP has a warmer climate compared to ADV, with a mean annual air temperature of -1.5 °C in 2017 [78]. The study area experiences early ground thawing and late freezing leading to 674 °C days of thaw based on ground surface temperature (Supplement S7). The area is characterized by later subsidence maxima (DOY median value: October 8) (Figure 7A), compared to ADV (DOY median values: September 14). At the location of KAP borehole, the detected DOY (October 20) approximatively fit the end of thawing season recorded by the temperature sensors (Figure 11A). Time series with DOY of the subsidence maxima above the first third quartile (Figure 8C) appear to be affected by late summer subsidence that may indicate the thaw front reached the ice-rich top of the permafrost. A similar pattern is also visible in the NYA study area.

NYA had a mean annual air temperature of -2.9 °C in 2017 [78]. The ground surface temperature from the borehole shows 570 °C days of thaw in 2017 (Supplement S7), which corresponds to an intermediate case compared to ADV and KAP. Observations in NYA generally highlight more ambiguous results, assumed to be caused by two main elements. First, snowfall occurred in early October 2017, which led to large decorrelation in all interferograms connected to the October 8 Sentinel-1 acquisition. Data gap reduces the temporal resolution to 12 days in a critical period for documenting the detection of the subsidence maxima. Second, the air and ground temperature series show that a long period is affected by oscillations close to the freezing point from September until the clear decrease of temperature in late October (Figure 9A). These fluctuations are recorded both on time series from the weather station and the borehole, but the stabilization close to 0 °C is especially visible on ground temperature data (Figure 10A). A slight but consistent summer heave is detected at the end of the thawing season in the time series surrounding the NYA borehole (Figure 12B). A short period in mid-September shows a drop of temperature close to or under 0 °C (Figure 9A, Supplement S7), but the AL ground thermal data [65] do not show any significant refreezing able to fully explain the displacement pattern. One possible explanation is that the km^2 average is dominated by an upward effect from surficial icing occurring around the riverbed, in the meltwater plain surrounding the hill where the borehole is located. The well-developed active layer may also have favoured water migration towards the frozen layer and lead to ice formation at the permafrost table [85]. In general, the misfit between the InSAR observations and the model at the location of the borehole (Figure 12A) suggests that a simple model only based on surface temperature is not able to represent all mechanisms occurring in the active layer in this area. Similarly, an early ground stabilization and heave pattern detected in the western part of the Brøggerhalvøya peninsula may suggest complex hydrological processes, variable water flux within the active layer and potential late summer ice segregation at the top of the permafrost [30–32]. Similar processes may also explain the early pattern detected in the southern part of KAP (Figure 6F and Figure 8A). Located at the mouth of a valley with a glacier in the upper part, this area may indeed be subject to large water outflow variations.

5.2. InSAR products as proxy of the active layer thermal regime

The study has been designed with the general objective to develop InSAR products able to infer the active layer thermal regime in flat permafrost areas. This is based on the assumptions that 1) at the seasonal timescale, the subsidence and heave temporal patterns are mostly controlled by the AL thermal variations; 2) the subsidence maximum can be used as a proxy of the AL thaw maximum. The comparisons between the InSAR displacements and the composite index model show that the observations are generally well represented by the model, even if exclusively based on thawing and freezing degree days, which confirms that the seasonal changes of surface level are mostly determined by the ground thermal conditions. Models based on ground temperature performed better than when using air temperature, which concurs with several studies documenting the thermal offset and time lag between the atmosphere and the ground, in particular due to snow cover [86–88]. At the local scale in ADV (Figure 10 A) and for km or regional averages in KAP and NYA (Figures 11 and 12, B and C),

the temperature-based model well represents the observed displacement pattern (Figure 13, scenario 1), and the acquisition dates of the maximal InSAR displacement generally match the timing of transition between the thawing and freezing season (Figure 13, scenario A). In these cases, the results show that the documented subsidence maxima can be appropriately used as a proxy of the end of the AL thawing period.

However, we also highlight different inferior scenarios when 1) the model fails to provide similar displacement series as InSAR due to oversimplistic assumptions, e.g. excluding the impact of variable water content, the water flux within the active layer and/or the potential late summer ice formation at the top of the permafrost (Figure 12, scenarios 2 and 3); 2) the extracted DOY of the subsidence maxima may not correspond to the end of the thawing period, due to ground level stabilization over long periods and short-term fluctuations in the time series (Figure 13, scenarios B and C). In certain cases, the model fails to explain the whole displacement progression but the timing of the transition between subsidence and heave fits with the temperature records (Figure 13, scenario 2). This is typically the case at the local scale in KAP (Figure 11A). In other cases, the whole index is shifted compared to the measurements, such as in NYA (Figure 12A). Independently to the model validity, the extracted DOY may be erroneous, typically if the displacement time series has large variability due to summer heave or measurement noise (Figure 13B and C), and/or if the curve flattens due late summer ground stabilisation caused by little ice content in the lower AL (Figures 6F and 7A). In these cases, the DOY may be detected earlier than the actual end of the thawing season. Discontinuous series can also lead to shifted DOY identification if the natural transition occurs around the date of a discarded acquisition, such as in NYA (Figure 12C). When considering several thousand pixels in hundreds km^2 areas, the major issue is to discriminate what causes the model to fail and/or the DOY extraction to misrepresent the targeted transition time.

The identified limitations highlight potential for further research to exploit InSAR time series and document the temporal dynamics of the active layer in permafrost areas. The developed products and applied model are based on simple assumptions and may require adjustments to be exploited systematically at a larger scale. We suggest that future developments can be achieved by considering the following elements:

- InSAR processing: The InSAR procedure is currently based on a site-dependent selection of interferograms that include several manual steps (Section 3.1). The variability of the snow cover is the main challenge that can lead to spatially and temporally discontinuous coherent interferometric signals (such as in NYA). Applying automated adaptive filtering, possibly based on a combination of SAR backscatter, InSAR coherence and external meteorological information would be valuable to upscale the procedure for example to the entire glacier-free land of the Svalbard archipelago. Instead of exploiting similar acquisitions in areas with variable climatic conditions, adaptive InSAR observation windows would allow for the selection of locally relevant periods, starting from the first snow-free scene after thaw onset, and thus avoiding an underestimation of the total seasonal subsidence values (such as in ADV and KAP, Figure 9A).
- DOY extraction: To identify the timing of the transition between thawing and freezing seasons and solve the issue related to the flattening of the displacement curves visible in some time series (Figure 13, scenario C), a more sophisticated procedure could be tested, for instance by fitting a polynomial function to the entire time series and/or by analysing the displacement gradients between acquisitions, in addition or instead of simply considering the maximal value of the InSAR time series. Scenarios where primary and secondary maxima are identified could also be valuable to further study the cases of summer heave patterns (Figure 13, scenario B).
- Time series averaging: While single time series may be affected by errors or unrepresentative local phenomena (Figures 11A and 12A), the results in KAP and NYA suggest that averaging reduces the noise level and dampens the effect of specific small-scale effects to focus on the main climate-

controlled trends. Kilometric averaging may be favoured in future product development, to keep documenting spatial variability while providing more robust information about the general seasonal pattern. At this scale, InSAR processing could be performed with larger multi-looking factors to provide more robust phase statistics for each pixel. Kilometric averaged displacement time series can easily be compared and coupled with transient modelling of thermal conditions based on remotely sensed surface temperature at a similar resolution [11,89]. Comparing InSAR with modelled temperature would have the advantage of increasing the measurement density compared to weather stations and boreholes and could provide new insights on the cause of the spatial-temporal variability of the time series.

- Time series modelling: The composite model is based on the Stefan equation, with simplistic assumptions that can explain that the model fails to represent the measurements in several cases (Figure 13, scenarios 2 and 3). As discussed by Gruber [30], one main issue is related to the assumption of constant water content and absence of liquid water in the frozen layer. The model also assumes that the heave is caused by the volumetric change of pore water turning into pore ice (in-situ water freezing). It does not consider the ice segregation (formation of ice lenses), which is known to be an important factor causing frost heave [5,32,90]. Other formulations using the Leybenzon equation, the Kudryavtsev's or the Gold and Lachbruch's models [1,29] could be implemented and compared with InSAR time series. Frost heave models taken into account ice lens formation could also be used to further interpret the InSAR-based displacement patterns, as applied by Yanagiya et al. [91].
- Further result interpretation and exploitation: To further interpret the spatio-temporal variability of the ground dynamics, comparison with geological and hydrological variables based on field mapping and in-situ measurements would be valuable, following previously applied methodologies in similar environments [82,83]. Remote sensing products documenting the ground dynamics can be used to monitor the timing of the seasonal freeze and thaw processes in Svalbard and other polar regions. ALT is one of the two components of the permafrost ECV, which is mainly obtained by field probing or borehole measurements [6,46]. The ALT is often estimated based on measurements of the maximal thaw depth. When the field measurements are discontinuous, e.g. through biweekly/monthly probing, selecting the right time to measure the thaw depth can be a challenge. Providing regional remotely sensed information about the active layer dynamics with a 6-day resolution would help field scientists to target the best time of their in-situ ALT measurements. If developed systematically (for each season and at large scale), such datasets can also enhance comparison with other remotely sensed environmental variables, such as vegetation phenology and snow cover time series [92,93]. These products could also be combined with top-of-permafrost excess ground ice maps, estimated from late-summer InSAR subsidence, as developed by Zwieback & Meyer [19].

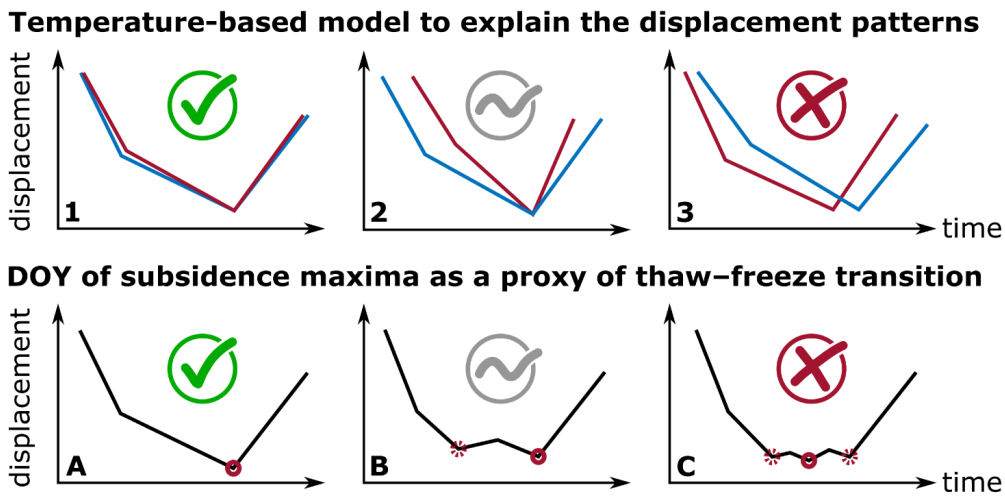

Figure 13. Examples of fit and deviation between the InSAR observations and the composite index model based on the Stefan equation (scenarios 1–3), and potential and limitations of DOY of subsidence maxima products as a proxy of the transition between the thawing and freezing season (scenarios A–C). Blue lines represent the rescaled index. Red lines are the measured InSAR time series. Red solid circles are the identified DOY of subsidence maxima. Dotted circles represent possible alternative solutions that lead to large uncertainty in the extraction of a representative value.

6. Conclusions

Using Sentinel-1 Synthetic Aperture Radar Interferometry (InSAR), we mapped the subsidence maxima and their corresponding Day of Year (DOY) in three regions in Svalbard affected by cyclic ground displacements due to active layer freeze and thaw. We analysed the seasonal time series and compared the displacements to a composite index model based on in-situ temperature measurements. Four conclusions can be drawn:

- The subsidence maxima and their timing vary between the three regions. The maxima occurred earlier in Adventdalen (mid-September) compared to Kapp Linné and Ny-Ålesund (early–mid October), located further west along the warmer coast. The identified maximal subsidence values vary within and between the regions and are assumed to depend on the active layer thickness, water/ice content and frost-susceptibility of the ground material.
- The results show clear cyclic patterns in all study areas and at the three considered scales (single pixels, km^2 and regional averages). The variable displacement progression is assumed to represent the natural variability of the climatic parameters and ground conditions. Some time series have long periods characterized by ground stabilization in late summer, which makes the identification of the subsidence maxima uncertain. Ambiguous displacement patterns are observed in Ny-Ålesund, including a secondary heave in a relatively cold period in late summer.
- Comparisons between the InSAR observations and the model show that the composite index based on ground surface temperature from the boreholes provides a better fit than the air temperature index due to thermal offset and time lag between the atmosphere and the ground, especially at the thaw onset.
- In Adventdalen, the model explains well the displacement progression extracted at the location of the borehole. In Kapp Linné and Ny-Ålesund, larger deviations are found at pixel-scale, likely due to complex hydrogeological effects occurring in the active layer. However, km or regional

averaging allows for improving the match between the models and measurements, which suggests that at this scale, the displacement patterns are primarily controlled by the thermal response of the active layer to atmospheric forcing.

The findings show that dense and frequent InSAR measurements of thaw subsidence and frost heave have the potential to upscale the documentation of the active layer thermal regime over wide permafrost areas. Limitations related to the proposed InSAR products and the simple assumptions behind the composite model are discussed and open the door to follow-up research to couple InSAR with modelling and design future operational remote sensing strategies in Svalbard.

Supplementary Materials: Figures S1–S3: Baseline plots of the Sentinel-1 interferometric pairs. Figure S4: Percent of documented pixels after the five steps of filtering. Figure S5: Orthophoto imagery of the 1 km^2 areas. Figures S6–7: Air and ground temperature, calculated ADDT/ADDF and composite index. Tables S8–9: Coefficient of determination R^2 or proportion of the variance of the InSAR displacements (at the three scales) that is explained by the composite index, based on air and ground temperature, after having tested five scaling factors α. Figure S10: Measured and modelled displacements based on air temperature.

Author Contributions: Conceptualization: L.R. and L.L.; methodology and software: L.R., L.L., Y.L. and T.R.L; formal analysis, investigation and visualization: L.R.; data curation: L.R., S.M.S., H.H.C. and T.R.L; project funding and administration: L.R. and T.R.L.; writing—original draft preparation: L.R.; writing—review and editing: L.L., H.H.C., S.M.S., T.R.L. and Y.L. All authors have read and agreed to the published version of the manuscript.

Funding: The study is part of Rouyet's Ph.D. research project FrostInSAR (2017–2021) funded by the Space Research Programme of the Research Council of Norway (grant 263005). The development of the GSAR processing chain and previous research applying InSAR in the Norwegian periglacial environment have been supported by the Norwegian Space Centre, the European Space Agency and the Research Council of Norway. L. Liu was supported by the Hong Kong Research Grants Council (CUHK14305618).

Acknowledgment: We acknowledge the five judges from the editorial board of SIOS's special issue who awarded a related presentation at the SIOS's online conference (04–05 June 2020) at the origin of the research presented in the current manuscript.

Data Availability Statement: The filtered InSAR time series, the subsidence maxima and corresponding DOY are available in Zenodo: https://doi.org/10.5281/zenodo.4775398. Additional data sources used in this study are listed in the references, included in the figures and tables, or in the supporting information associated with this publication.

Conflicts of Interest: The authors declare no conflict of interest. The funders had no role in the design of the study; in the collection, analyses, or interpretation of data; in the writing of the manuscript, or in the decision to publish the results.

References

1. French, H.M. *The Periglacial Environment - Third Edition*; John Wiley & Sons, Ltd, 2007;
2. Schuur, E.A.; McGuire, A.D.; Schädel, C.; Grosse, G.; Harden, J.W.; Hayes, D.J.; Hugelius, G.; Koven, C.D.; Kuhry, P.; Lawrence, D.M. Climate Change and the Permafrost Carbon Feedback. *Nature* **2015**, *520*, 171–179, doi:10.1038/nature14338.
3. Hjort, J.; Karjalainen, O.; Aalto, J.; Westermann, S.; Romanovsky, V.E.; Nelson, F.E.; Etzelmüller, B.; Luoto, M. Degrading Permafrost Puts Arctic Infrastructure at Risk by Mid-Century. *Nature Communications* **2018**, *9*, 1–9, doi:10.1038/s41467-018-07557-4.
4. Jorgenson, M.T.; Racine, C.H.; Walters, J.C.; Osterkamp, T.E. Permafrost Degradation and Ecological Changes Associated with a Warmingclimate in Central Alaska. *Climatic Change* **2001**, *48*, 551–579, doi:10.1023/A:1005667424292.
5. Rempel, A.W. Formation of Ice Lenses and Frost Heave. *Journal of Geophysical Research: Earth Surface* **2007**, *112*, doi:10.1029/2006JF000525.
6. Bonnaventure, P.P.; Lamoureux, S.F. The Active Layer: A Conceptual Review of Monitoring, Modelling Techniques and Changes in a Warming Climate. *Progress in Physical Geography* **2013**, *37*, 352–376, doi:10.1177/0309133313478314.

7. Biskaborn, B.K.; Smith, S.L.; Noetzli, J.; Matthes, H.; Vieira, G.; Streletskiy, D.A.; Schoeneich, P.; Romanovsky, V.E.; Lewkowicz, A.G.; Abramov, A. Permafrost Is Warming at a Global Scale. *Nature Communications* **2019**, *10*, 1–11, doi:10.1038/s41467-018-08240-4.
8. Meredith, M.; Sommerkorn, M.; Cassotta, S.; Derksen, C.; Ekaykin, A.; Hollowed, A.; Kofinas, G.; Mackintosh, A.; Melbourne-Thomas, J.; Muelbert, M.M.C. Chapter 3. Polar Regions. In *IPCC Special Report on the Ocean and Cryosphere in a Changing Climate*; The Intergovernmental Panel on Climate Change, 2019.
9. Nitze, I.; Grosse, G.; Jones, B.M.; Romanovsky, V.E.; Boike, J. Remote Sensing Quantifies Widespread Abundance of Permafrost Region Disturbances across the Arctic and Subarctic. *Nature Communications* **2018**, *9*, 1–11, doi:10.1038/s41467-018-07663-3.
10. Zhang, T.; Barry, R.G.; Armstrong, R.L. Application of Satellite Remote Sensing Techniques to Frozen Ground Studies. *Polar Geography* **2004**, *28*, 163–196, doi:10.1080/789610186.
11. Obu, J.; Westermann, S.; Bartsch, A.; Berdnikov, N.; Christiansen, H.H.; Dashtseren, A.; Delaloye, R.; Elberling, B.; Etzelmüller, B.; Kholodov, A. Northern Hemisphere Permafrost Map Based on TTOP Modelling for 2000–2016 at 1 Km2 Scale. *Earth-Science Reviews* **2019**, *193*, 299–316, doi:10.1016/j.earscirev.2019.04.023.
12. Philipp, M.; Dietz, A.; Buchelt, S.; Kuenzer, C. Trends in Satellite Earth Observation for Permafrost Related Analyses—A Review. *Remote Sensing* **2021**, *13*, 1217, doi:10.3390/rs13061217.
13. Hu, Y.; Liu, L.; Larson, K.M.; Schaefer, K.M.; Zhang, J.; Yao, Y. GPS Interferometric Reflectometry Reveals Cyclic Elevation Changes in Thaw and Freezing Seasons in a Permafrost Area (Barrow, Alaska). *Geophysical Research Letters* **2018**, *45*, 5581–5589, doi:10.1029/2018GL077960.
14. Romanovsky, V.E.; Marchenko, S.S.; Daanen, R.; Sergeev, D.O.; Walker, D.A. Soil Climate and Frost Heave along the Permafrost/Ecological North American Arctic Transect. In Proceedings of the 9th International Conference on Permafrost, Alaska, Fairbanks; 2008; Vol. 2, pp. 1519–1524.
15. Shiklomanov, N.I.; Streletskiy, D.A.; Little, J.D.; Nelson, F.E. Isotropic Thaw Subsidence in Undisturbed Permafrost Landscapes. *Geophysical Research Letters* **2013**, *40*, 6356–6361, doi:10.1002/2013GL058295.
16. Bamler, R.; Hartl, P. Synthetic Aperture Radar Interferometry. *Inverse Problems* **1998**, *14*, R1, doi:10.1088/0266-5611/14/4/001.
17. Short, N.; LeBlanc, A.-M.; Sladen, W.; Oldenborger, G.; Mathon-Dufour, V.; Brisco, B. RADARSAT-2 D-InSAR for Ground Displacement in Permafrost Terrain, Validation from Iqaluit Airport, Baffin Island, Canada. *Remote Sensing of Environment* **2014**, *141*, 40–51, doi:10.1016/j.rse.2013.10.016.
18. Liu, L.; Zhang, T.; Wahr, J. InSAR Measurements of Surface Deformation over Permafrost on the North Slope of Alaska. *Journal of Geophysical Research: Earth Surface* **2010**, *115*, doi:10.1029/2009JF001547.
19. Zwieback, S.; Meyer, F.J. Vulnerable Top-of-Permafrost Ground Ice Indicated by Remotely Sensed Late-Season Subsidence. *The Cryosphere* **2020**, *15*, 2041–2055, doi:10.5194/tc-15-2041-2021.
20. Daout, S.; Doin, M.-P.; Peltzer, G.; Socquet, A.; Lasserre, C. Large-Scale InSAR Monitoring of Permafrost Freeze-Thaw Cycles on the Tibetan Plateau. *Geophysical Research Letters* **2017**, *44*, 901–909, doi:10.1002/2016GL070781.
21. Bartsch, A.; Leibman, M.; Strozzi, T.; Khomutov, A.; Widhalm, B.; Babkina, E.; Mullanurov, D.; Ermokhina, K.; Kroisleitner, C.; Bergstedt, H. Seasonal Progression of Ground Displacement Identified with Satellite Radar Interferometry and the Impact of Unusually Warm Conditions on Permafrost at the Yamal Peninsula in 2016. *Remote Sensing* **2019**, *11*, 1865, doi:10.3390/rs11161865.
22. Rouyet, L.; Lauknes, T.R.; Christiansen, H.H.; Strand, S.M.; Larsen, Y. Seasonal Dynamics of a Permafrost Landscape, Adventdalen, Svalbard, Investigated by InSAR. *Remote Sensing of Environment* **2019**, *231*, 111236, doi:10.1016/j.rse.2019.111236.
23. Reinosch, E.; Buckel, J.; Dong, J.; Gerke, M.; Baade, J.; Riedel, B. InSAR Time Series Analysis of Seasonal Surface Displacement Dynamics on the Tibetan Plateau. *The Cryosphere* **2020**, *14*, 1633–1650, doi:10.5194/tc-14-1633-2020.
24. Liu, L.; Jafarov, E.E.; Schaefer, K.M.; Jones, B.M.; Zebker, H.A.; Williams, C.A.; Rogan, J.; Zhang, T. InSAR Detects Increase in Surface Subsidence Caused by an Arctic Tundra Fire. *Geophysical Research Letters* **2014**, *41*, 3906–3913, doi:10.1002/2014GL060533.
25. Strozzi, T.; Antonova, S.; Günther, F.; Mätzler, E.; Vieira, G.; Wegmüller, U.; Westermann, S.; Bartsch, A. Sentinel-1 SAR Interferometry for Surface Deformation Monitoring in Low-Land Permafrost Areas. *Remote Sensing* **2018**, *10*, 1360, doi:10.3390/rs10091360.
26. Antonova, S.; Sudhaus, H.; Strozzi, T.; Zwieback, S.; Kääb, A.; Heim, B.; Langer, M.; Bornemann, N.; Boike, J. Thaw Subsidence of a Yedoma Landscape in Northern Siberia, Measured in Situ and Estimated from TerraSAR-X Interferometry. *Remote Sensing* **2018**, *10*, 494, doi:10.3390/rs10040494.
27. Abe, T.; Iwahana, G.; Efremov, P.V.; Desyatkin, A.R.; Kawamura, T.; Fedorov, A.; Zhegusov, Y.; Yanagiya, K.; Tadono, T. Surface Displacement Revealed by L-Band InSAR Analysis in the Mayya Area, Central Yakutia, Underlain by Continuous Permafrost. *Earth, Planets and Space* **2020**, *72*, 1–16, doi:10.1186/s40623-020-01266-3.
28. Stefan, J. Über Die Theorie Der Eisbildung, Insbesondere Über Die Eisbildung Im Polarmeere. *Annalen der Physik und Chemie* **1891**, *42*, 269–286.

29. Riseborough, D.W.; Shiklomanov, N.; Etzelmüller, B.; Gruber, S.; Marchenko, S. Recent Advances in Permafrost Modelling. *Permafrost and Periglacial Processes* **2008**, *19*, 137–156, doi:10.1002/ppp.615.
30. Gruber, S. Ground Subsidence and Heave over Permafrost: Hourly Time Series Reveal Interannual, Seasonal and Shorter-Term Movement Caused by Freezing, Thawing and Water Movement. *The Cryosphere* **2020**, *14*, 1437–1447, doi:10.5194/tc-14-1437-2020.
31. Romanovsky, V.E.; Osterkamp, T.E. Thawing of the Active Layer on the Coastal Plain of the Alaskan Arctic. *Permafrost and Periglacial Processes* **1997**, *8*, 1–22, doi:10.1002/(SICI)1099-1530(199701)8:1<1::AID-PPP243>3.0.CO;2-U.
32. Thomas, H.R.; Cleall, P.; Li, Y.-C.; Harris, C.; Kern-Luetschg, M. Modelling of Cryogenic Processes in Permafrost and Seasonally Frozen Soils. *Géotechnique* **2009**, *59*, 173–184, doi:10.1680/geot.2009.59.3.173.
33. Dehls, J.F.; Larsen, Y.; Marinkovic, P.; Lauknes, T.R.; Stødle, D.; Moldestad, D.A. INSAR.No: A National Insar Deformation Mapping/Monitoring Service In Norway–From Concept To Operations. In Proceedings of the IGARSS 2019 – IEEE International Geoscience and Remote Sensing Symposium; 2019; pp. 5461–5464.
34. Larsen, Y.; Marinkovic, P.; Dehls, J.F.; Bredal, M.; Bishop, C.; Jøkulsson, G.; Gjøvik, L.-P.; Frauenfelder, R.; Salazar, S.E.; Vöge, M.; et al. *European Ground Motion Service: Service Implementation Plan and Product Specification Document*; Copernicus Land Monitoring Service, 2020;
35. NPI Terrengmodell Svalbard (S0 Terrengmodell) [Dataset]. Available online: https://www.doi.org/10.21334/npolar.2014.dce53a47.
36. NPI Kartdata Svalbard 1:100 000 (S100 Kartdata) / Map Data [Dataset]. Norwegian Polar Institute; 2014. Available online: https://www.doi.org/10.21334/npolar.2014.645336c7.
37. Peel, M.C.; Finlayson, B.L.; McMahon, T.A. Updated World Map of the Köppen-Geiger Climate Classification. *Hydrology and Earth System Sciences* **2007**, *11*, 1633–1644, doi:10.5194/hess-11-1633-2007.
38. Harland, W.B. Svalbard. In *The Geology of Svalbard*; Geological Society, London, Memoirs, 1997; Vol. 17, pp. 3–15.
39. Hanssen-Bauer, I.; Førland, E.J.; Hisdal, H.; Mayer, S.; AB, S.; Sorteberg, A. *Climate in Svalbard 2100*; 2019;
40. Humlum, O.; Instanes, A.; Sollid, J.L. Permafrost in Svalbard: A Review of Research History, Climatic Background and Engineering Challenges. *Polar Research* **2003**, *22*, 191–215, doi:10.1111/j.1751-8369.2003.tb00107.x.
41. Christiansen, H.H.; Humlum, O.; Eckerstorfer, M. Central Svalbard 2000–2011 Meteorological Dynamics and Periglacial Landscape Response. *Arctic, Antarctic, and Alpine Research* **2013**, *45*, 6–18, doi:10.1657/1938-4246-45.16.
42. Harris, C.; Kern-Luetschg, M.; Christiansen, H.H.; Smith, F. The Role of Interannual Climate Variability in Controlling Solifluction Processes, Endalen, Svalbard. *Permafrost and Periglacial Processes* **2011**, *22*, 239–253, doi:10.1002/ppp.727.
43. Schuh, C.; Frampton, A.; Christiansen, H.H. Soil Moisture Redistribution and Its Effect on Inter-Annual Active Layer Temperature and Thickness Variations in a Dry Loess Terrace in Adventdalen, Svalbard. *The Cryosphere* **2017**, *11*, 635–651, doi:10.5194/tc-11-635-2017.
44. Christiansen, H.H.; Etzelmüller, B.; Isaksen, K.; Juliussen, H.; Farbrot, H.; Humlum, O.; Johansson, M.; Ingeman-Nielsen, T.; Kristensen, L.; Hjort, J. The Thermal State of Permafrost in the Nordic Area during the International Polar Year 2007–2009. *Permafrost and Periglacial Processes* **2010**, *21*, 156–181, doi:10.1002/ppp.687.
45. Christiansen, H.H.; Gilbert, G.L.; Neumann, U.; Demidov, N.; Guglielmin, M.; Isaksen, K.; Osuch, M.; Boike, J. Ground ice content, drilling methods and equipment and permafrost dynamics in Svalbard 2016–2019 (PermaSval). In *The State of Environmental Science in Svalbard (SESS report 2020)*; Svalbard Integrated Arctic Earth Observing System, Longyearbyen, 2021.
46. Strand, S.M.; Christiansen, H.H.; Johansson, M.; Åkerman, J.; Humlum, O. Active Layer Thickening and Controls on Interannual Variability in the Nordic Arctic Compared to the Circum-Arctic. *Permafrost and Periglacial Processes* **2020**, *32*, 47–58, doi:10.1002/ppp.2088.
47. Etzelmüller, B.; Schuler, T.V.; Isaksen, K.; Christiansen, H.H.; Farbrot, H.; Benestad, R. Modeling the Temperature Evolution of Svalbard Permafrost during the 20th and 21st Century. *The Cryosphere* **2011**, *5*, 67–79, doi:10.5194/tc-5-67-2011.
48. Major, H.; Haremo, P.; Dallmann, W.K.; Andresen, A.; Salvigsen, O. Geological Map of Svalbard 1: 100,000, Sheet C9G Adventdalen 2001.
49. Tolgensbakk, J.; Sørbel, L.; Høgvard, K. Geomorphological and Quaternary Geological Map of Svalbard 1: 100,000. Sheet C9Q Adventdalen. Temakart 31 2001.
50. Humlum, O. Holocene Permafrost Aggradation in Svalbard. *Geological Society, London, Special Publications* **2005**, *242*, 119–129, doi:10.1144/GSL.SP.2005.242.01.11.
51. Gilbert, G.L.; O'Neill, H.B.; Nemec, W.; Thiel, C.; Christiansen, H.H.; Buylaert, J.-P. Late Quaternary Sedimentation and Permafrost Development in a Svalbard Fjord-Valley, Norwegian High Arctic. *Sedimentology* **2018**, *65*, 2531–2558, doi:10.1111/sed.12476.

52. Cable, S.; Elberling, B.; Kroon, A. Holocene Permafrost History and Cryostratigraphy in the High-Arctic Adventdalen Valley, Central Svalbard. *Boreas* **2018**, *47*, 423–442, doi:10.1111/bor.12286.
53. Retelle, M.; Christiansen, H.H.; Hodson, A.; Nikulina, A.; Osuch, M.; Poleshuk, K.; Romashova, K.; Roof, S.; Rouyet, L.; Strand, S.M. Environmental Monitoring in the Kapp Linne-Gronfjorden Region (KLEO). In *The State of Environmental Science in Svalbard (SESS report 2019)*; 2020.
54. Dallmann, W.K. *Geoscience Atlas of Svalbard*; Norwegian Polar Institute, 2015;
55. Landvik, J.Y.; Landvik, J.Y.; Salvigsen, O. The Late Weichselian and Holocene Shoreline Displacement on the West-Central Coast of Svalbard. *Polar Research* **1987**, *5*, 29–44, doi:10.1111/j.1751-8369.1987.tb00353.x.
56. Ohta, Y.; Hjelle, A. Geological Map Svalbard 1: 100,000. Isfjorden: Spitsbergen. Sheet B9G 1992.
57. Snyder, J.A.; Werner, A.; Miller, G.H. Holocene Cirque Glacier Activity in Western Spitsbergen, Svalbard: Sediment Records from Proglacial Linnévatnet. *The Holocene* **2000**, *10*, 555–563, doi:10.1191/095968300667351697.
58. Åkerman, H.J. Relations between Slow Slope Processes and Active-Layer Thickness 1972–2002, Kapp Linné, Svalbard. *Norsk Geografisk Tidsskrift - Norwegian Journal of Geography* **2005**, *59*, 116–128, doi:10.1080/00291950510038386.
59. Eckerstorfer, M.; Malnes, E.; Christiansen, H.H. Freeze/Thaw Conditions at Periglacial Landforms in Kapp Linné, Svalbard, Investigated Using Field Observations, in Situ, and Radar Satellite Monitoring. *Geomorphology* **2017**, *293*, 433–447, doi:10.1016/j.geomorph.2017.02.010.
60. Hjelle, A. Geological Map of Svalbard 1: 100,000: Sheet A7G Kongsfjorden 1999.
61. Miccadei, E.; Piacentini, T.; Berti, C. Geomorphological Features of the Kongsfjorden Area: Ny-Ålesund, Blomstrandøya (NW Svalbard, Norway). *Rendiconti Lincei* **2016**, *27*, 217–228, doi:10.1007/s12210-016-0537-3.
62. Westermann, S.; Langer, M.; Boike, J. Spatial and Temporal Variations of Summer Surface Temperatures of High-Arctic Tundra on Svalbard — Implications for MODIS LST Based Permafrost Monitoring. *Remote Sensing of Environment* **2011**, *115*, 908–922, doi:10.1016/j.rse.2010.11.018.
63. Boike, J.; Roth, K.; Ippisch, O. Seasonal Snow Cover on Frozen Ground: Energy Balance Calculations of a Permafrost Site near Ny-Ålesund, Spitsbergen. *Journal of Geophysical Research: Atmospheres* **2003**, *108*, ALT-4, doi:10.1029/2001JD000939.
64. Westermann, S.; Wollschläger, U.; Boike, J. Monitoring of Active Layer Dynamics at a Permafrost Site on Svalbard Using Multi-Channel Ground-Penetrating Radar. *The Cryosphere* **2010**, *4*, 475–487, doi:10.5194/tc-4-475-2010.
65. Boike, J.; Juszak, I.; Lange, S.; Chadburn, S.; Burke, E.; Overduin, P.P.; Roth, K.; Ippisch, O.; Bornemann, N.; Stern, L. A 20-Year Record (1998–2017) of Permafrost, Active Layer and Meteorological Conditions at a High Arctic Permafrost Research Site (Bayelva, Spitsbergen). *Earth System Science Data* **2018**, *10*, 355–390, doi:https://doi.org/10.5194/essd-10-355-2018.
66. Larsen, Y.; Engen, G.; Lauknes, T.R.; Malnes, E.; Høgda, K.A. A Generic Differential Interferometric SAR Processing System, with Applications to Land Subsidence and Snow-Water Equivalent Retrieval. In Proceedings of the ESA Fringe Workshop, Frascati, Italy, 28 November – 2 December 2005; ESA SP-610, 2005.
67. Baran, I.; Stewart, M.P.; Kampes, B.M.; Perski, Z.; Lilly, P. A Modification to the Goldstein Radar Interferogram Filter. *IEEE Transactions on Geoscience and Remote Sensing* **2003**, *41*, 2114–2118, doi:10.1109/TGRS.2003.817212.
68. Goldstein, R.M.; Werner, C.L. Radar Interferogram Filtering for Geophysical Applications. *Geophysical Research Letters* **1998**, *25*, 4035–4038, doi:10.1029/1998GL900033.
69. Cavalié, O.; Doin, M.-P.; Lasserre, C.; Briole, P. Ground Motion Measurement in the Lake Mead Area, Nevada, by Differential Synthetic Aperture Radar Interferometry Time Series Analysis: Probing the Lithosphere Rheological Structure. *Journal of Geophysical Research: Solid Earth* **2007**, *112*, doi:10.1029/2006JB004344.
70. Lauknes, T.R. InSAR Tropospheric Stratification Delays: Correction Using a Small Baseline Approach. *IEEE Geoscience and Remote Sensing Letters* **2011**, *8*, 1070–1074, doi:10.1109/LGRS.2011.2156381.
71. Tymofyeyeva, E.; Fialko, Y. Mitigation of Atmospheric Phase Delays in InSAR Data, with Application to the Eastern California Shear Zone. *Journal of Geophysical Research: Solid Earth* **2015**, *120*, 5952–5963, doi:10.1002/2015JB011886.
72. Chen, C.W.; Zebker, H.A. Phase Unwrapping for Large SAR Interferograms: Statistical Segmentation and Generalized Network Models. *IEEE Transactions on Geoscience and Remote Sensing* **2002**, *40*, 1709–1719, doi:10.1109/TGRS.2002.802453.
73. NPI Data and Services. Svalbard Orthophoto - WMTS Basemap Service. Norwegian Polar Institute; 2021. Available online: https://geodata.npolar.no/.
74. Berardino, P.; Fornaro, G.; Lanari, R.; Sansosti, E. A New Algorithm for Surface Deformation Monitoring Based on Small Baseline Differential SAR Interferograms. *IEEE Transactions on Geoscience and Remote Sensing* **2002**, *40*, 2375–2383, doi:10.1109/TGRS.2002.803792.
75. Lauknes, T.R.; Zebker, H.A.; Larsen, Y. InSAR Deformation Time Series Using an L1-Norm Small-Baseline Approach. *IEEE Transactions on Geoscience and Remote Sensing* **2010**, *49*, 536–546, doi:10.1109/TGRS.2010.2051951.

76. Matsuoka, N. Solifluction Rates, Processes and Landforms: A Global Review. *Earth-Science Reviews* **2001**, *55*, 107–134, doi:10.1016/S0012-8252(01)00057-5.
77. Riseborough, D.W. Thawing and Freezing Indices in the Active Layer. In Proceedings of the 8th International Conference on Permafrost, Zurich, Switzerland; Rotterdam: AA Balkema, 2003; Vol. 2, pp. 953–958.
78. NCCS 2017 Daily Air Temperature. Adventdalen Station 99870. Isfjord Radio Station 99790. Ny-Ålesund Station 99910. Norwegian Centre for Climate Services; 2021. Available online: https://seklima.met.no/observations/.
79. Hallet, B.; Allard, M. Measurement of Soil Motion in Sorted Circles, Western Spitsbergen. In Proceedings of the 7th International Conference on Permafrost, Yellowknife, Canada; 1998; pp. 415–420.
80. Matsuoka, N.; Hirakawa, K. Solifluction Resulting from One-Sided and Two-Sided Freezing: Field Data from Svalbard. *Polar Geoscience* **2000**, *13*, 187–201.
81. Watanabe, T.; Matsuoka, N.; Christiansen, H.H. Mudboil and Ice-wedge Dynamics Investigated by Electrical Resistivity Tomography, Ground Temperatures and Surface Movements in Svalbard. *Geografiska Annaler: Series A, Physical Geography* **2012**, *94*, 445–457, doi:10.1111/j.1468-0459.2012.00470.x.
82. Chen, J.; Wu, Y.; O'Connor, M.; Cardenas, M.B.; Schaefer, K.; Michaelides, R.; Kling, G. Active Layer Freeze-Thaw and Water Storage Dynamics in Permafrost Environments Inferred from InSAR. *Remote Sensing of Environment* **2020**, *248*, 112007, doi:10.1016/j.rse.2020.112007.
83. Rudy, A.C.A.; Lamoureux, S.F.; Treitz, P.; Short, N.; Brisco, B. Seasonal and Multi-Year Surface Displacements Measured by DInSAR in a High Arctic Permafrost Environment. *International Journal of Applied Earth Observation and Geoinformation* **2018**, *64*, 51–61, doi:10.1016/j.jag.2017.09.002.
84. Zwieback, S.; Liu, X.; Antonova, S.; Heim, B.; Bartsch, A.; Boike, J.; Hajnsek, I. A Statistical Test of Phase Closure to Detect Influences on DInSAR Deformation Estimates Besides Displacements and Decorrelation Noise: Two Case Studies in High-Latitude Regions. *IEEE Transactions on Geoscience and Remote Sensing* **2016**, *54*, 5588–5601, doi:10.1109/TGRS.2016.2569435.
85. Mackay, J.R. Downward Water Movement into Frozen Ground, Western Arctic Coast, Canada. *Canadian Journal of Earth Sciences* **1983**, *20*, 120–134, doi:10.1139/e83-012.
86. Romanovsky, V.E.; Sazonova, T.S.; Balobaev, V.T.; Shender, N.I.; Sergueev, D.O. Past and Recent Changes in Air and Permafrost Temperatures in Eastern Siberia. *Global and Planetary Change* **2007**, *56*, 399–413, doi:10.1016/j.gloplacha.2006.07.022.
87. Throop, J.; Lewkowicz, A.G.; Smith, S.L. Climate and Ground Temperature Relations at Sites across the Continuous and Discontinuous Permafrost Zones, Northern Canada. *Canadian Journal of Earth Sciences* **2012**, *49*, 865–876, doi:10.1139/e11-075.
88. Way, R.G.; Lewkowicz, A.G. Environmental Controls on Ground Temperature and Permafrost in Labrador, Northeast Canada. *Permafrost and Periglacial Processes* **2018**, *29*, 73–85, doi:10.1002/ppp.1972.
89. Westermann, S.; Peter, M.; Langer, M.; Schwamborn, G.; Schirrmeister, L.; Etzelmüller, B.; Boike, J. Transient Modeling of the Ground Thermal Conditions Using Satellite Data in the Lena River Delta, Siberia. *The Cryosphere* **2017**, *11*, 1441–1463, doi:10.5194/tc-11-1441-2017.
90. Smith, M.W. Observations of Soil Freezing and Frost Heave at Inuvik, Northwest Territories, Canada. *Canadian Journal of Earth Sciences* **1985**, *22*, 283–290, doi:10.1139/e85-024.
91. Yanagiya, K.; Furuya, M. Post-Wildfire Surface Deformation Near Batagay, Eastern Siberia, Detected by L-Band and C-Band InSAR. *Journal of Geophysical Research: Earth Surface* **2020**, *125*, e2019JF005473, doi:10.1029/2019JF005473.
92. Karlsen, S.R.; Elvebakk, A.; Høgda, K.A.; Grydeland, T. Spatial and Temporal Variability in the Onset of the Growing Season on Svalbard, Arctic Norway—Measured by MODIS-NDVI Satellite Data. *Remote Sensing* **2014**, *6*, 8088–8106, doi:10.3390/rs6098088.
93. Vickers, H.; Karlsen, S.R.; Malnes, E. A 20-Year MODIS-Based Snow Cover Dataset for Svalbard and Its Link to Phenological Timing and Sea Ice Variability. *Remote Sensing* **2020**, *12*, 1123, doi:10.3390/rs12071123.

Supplementary Material

Seasonal InSAR displacements documenting the active layer freeze and thaw progression in central–western Spitsbergen, Svalbard

Line Rouyet, Lin Liu, Sarah Marie Strand, Hanne Hvidtfeldt Christiansen, Tom Rune Lauknes, Yngvar Larsen

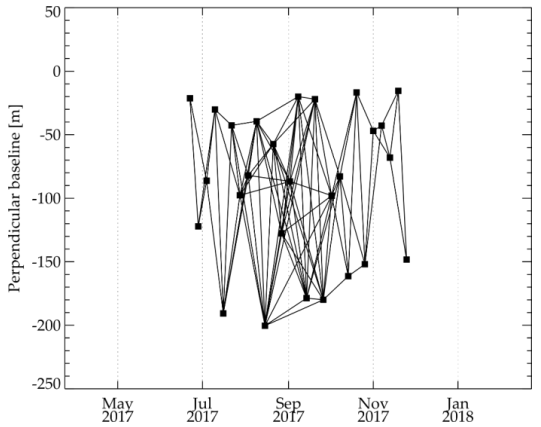

Supplement S1. Baseline plot of the Sentinel-1 interferometric pairs used in Adventdalen (ADV). Black squares: 27 SAR acquisitions (6-day sampling between 22.06.2017 and 25.11.2017). Black lines: 90 interferograms.

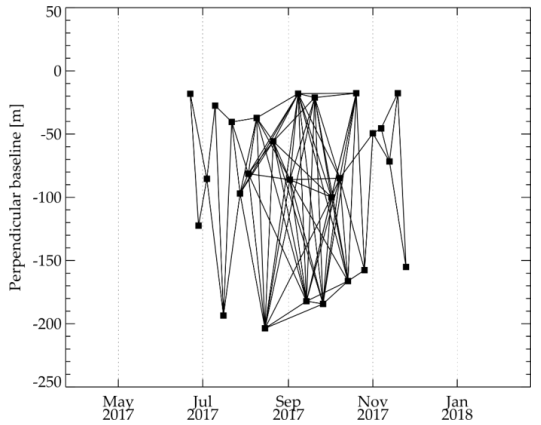

Supplement S2. Baseline plot of the Sentinel-1 interferometric pairs used in Kapp Linné (KAP). Black squares: 26 SAR acquisitions (6-day sampling between 22.06.2017 and 25.11.2017, except 27.08.2017 that has been discarded due to major ionospheric effect). Black lines: 88 interferograms.

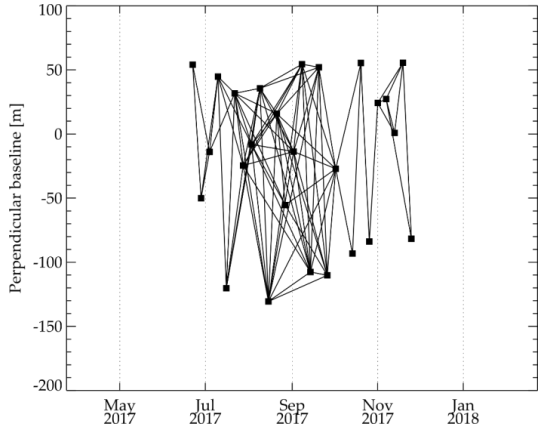

Supplement S3. Baseline plots of the Sentinel-1 interferometric pairs used for Ny-Ålesund (NYA). Black squares: 26 SAR acquisitions (6-day sampling between 22.06.2017 and 25.11.2017, except 08.10.2017 that has been discarded due to snow). Black lines: 84 interferograms.

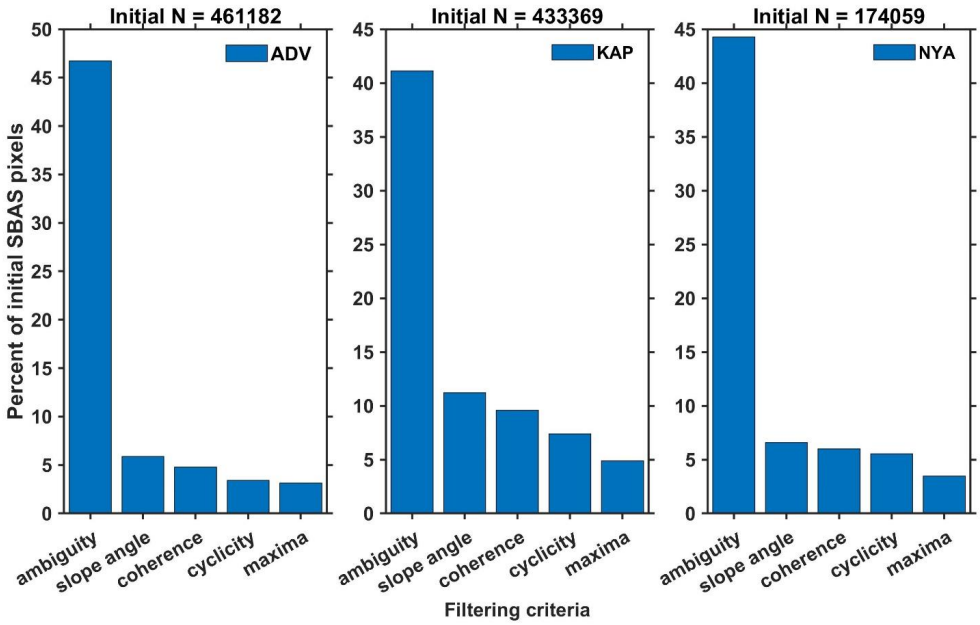

Supplement S4. Percent of documented pixels after the five steps of filtering. Initial N are the numbers of pixels after SBAS processing (Section 3.1). The results have been filtered according to five criteria to remove unreliable and irrelevant information when focusing on the cyclic thaw subsidence and frost heave patterns (Section 3.2).

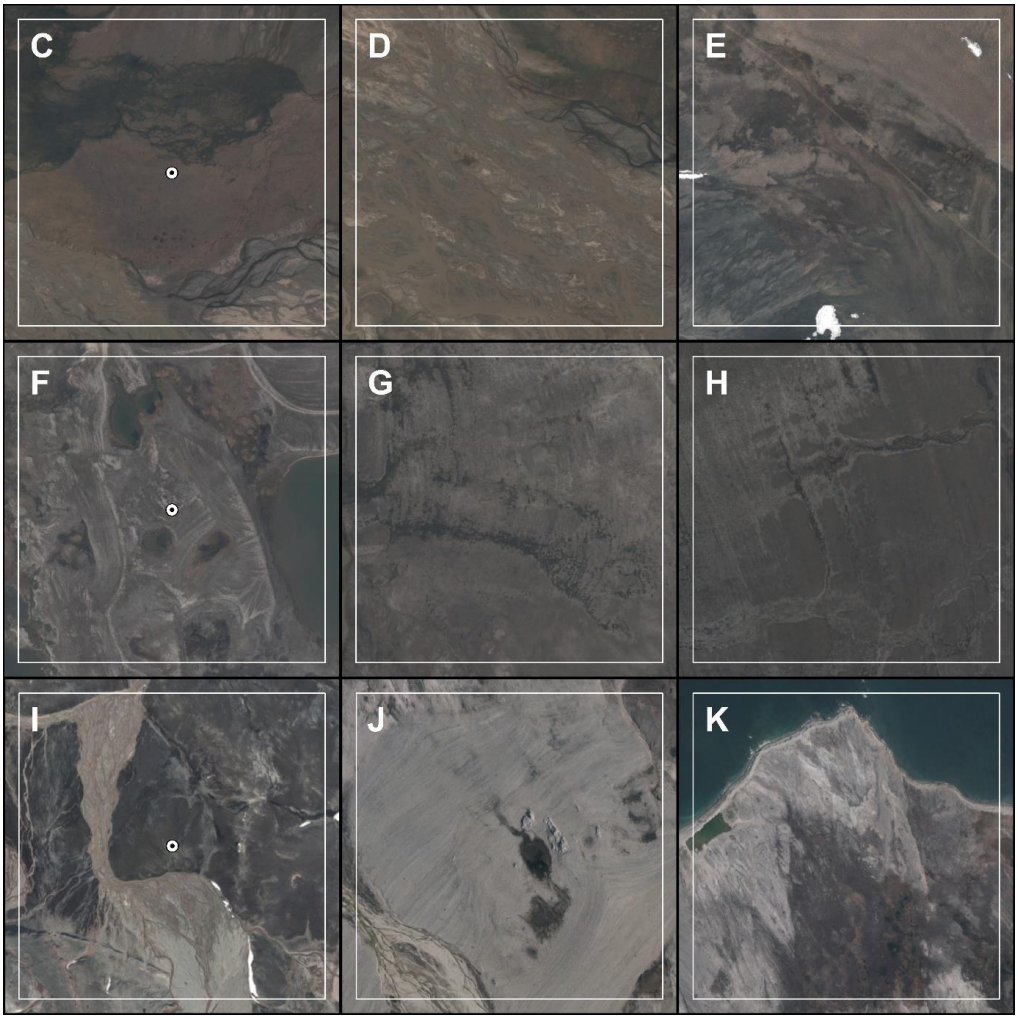

Supplement S5. Orthophoto imagery of the 1 km^2 areas (white squares) selected for the discussion of InSAR results' variability within the three regions. C–D: Selected areas in Adventdalen. C shows the loess-covered ice wedge polygons where ADV borehole is located (white circle). D shows the brained river plain and its fluvial sediments. E shows a blockfield plateau above Longyearbyen. F–H: Selected areas in the Kapp Linné strandflat dominated by beach ridges. F is centred around the KAP borehole (white circle). I–K: Selected areas in Ny-Ålesund. I shows the Bayeleva meltwater plain and the morainic hill where the NYA borehole is located (white circle). J shows beach ridges on the strandflat. K show alluvial fans in the outer part of Brøggerhalvøya. Location maps are shown in Figures 3–5. Averaged InSAR time series for each km^2 subarea are shown in Figure 6. Orthophoto imagery is from the Norwegian Polar Institute (2021) [73], also available in the *toposvalbard.npolar.no* map viewer.

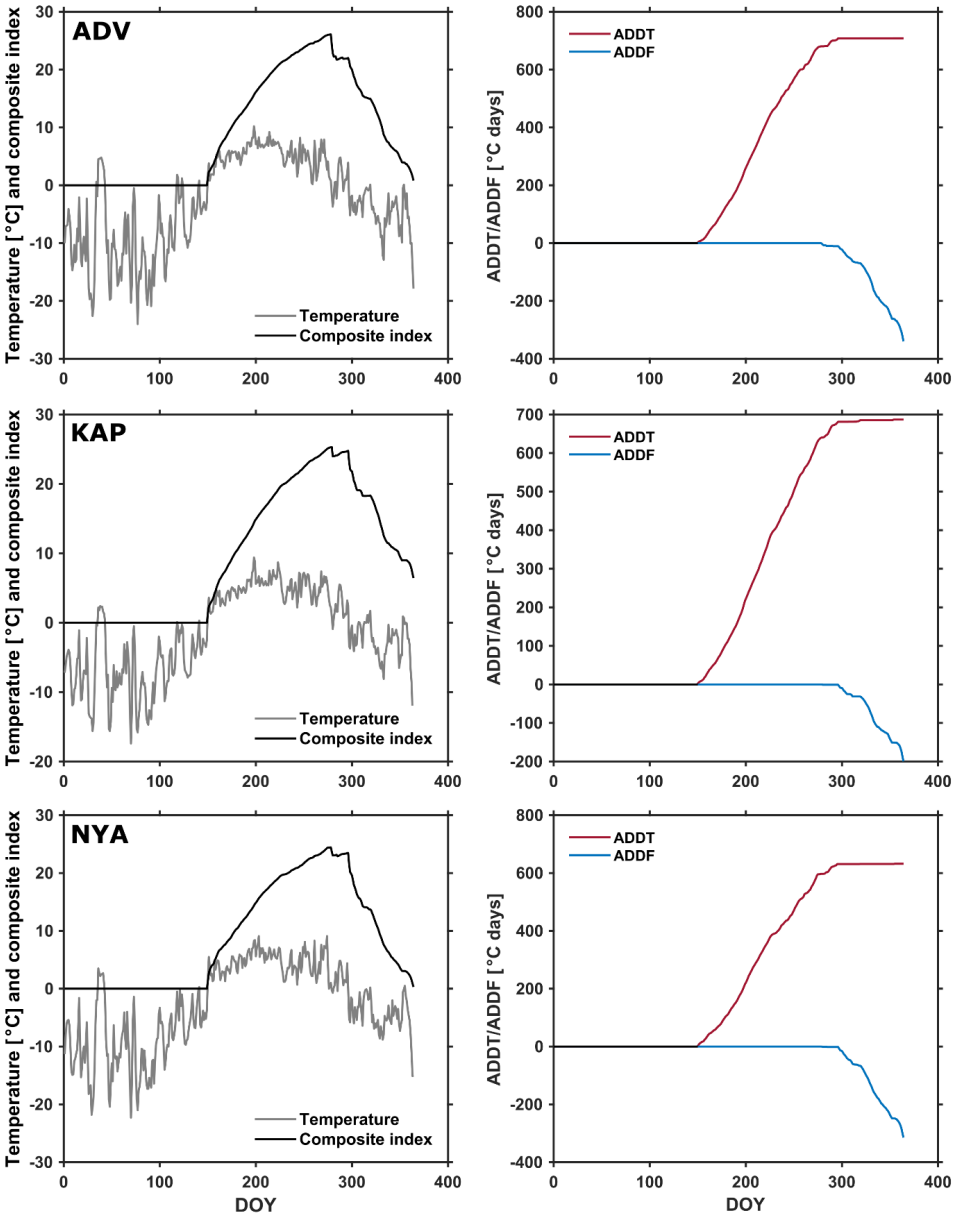

Supplement S6. Air temperature measured at three weather stations (Table 2), calculated Accumulated Degrees Days of Thaw and Freeze (ADDT/ADDF) and composite index, here based on a scaling factor α of 1.4. The calculation starts at the thaw onset based on the temperature data (the index therefore remains at zero before initiation).

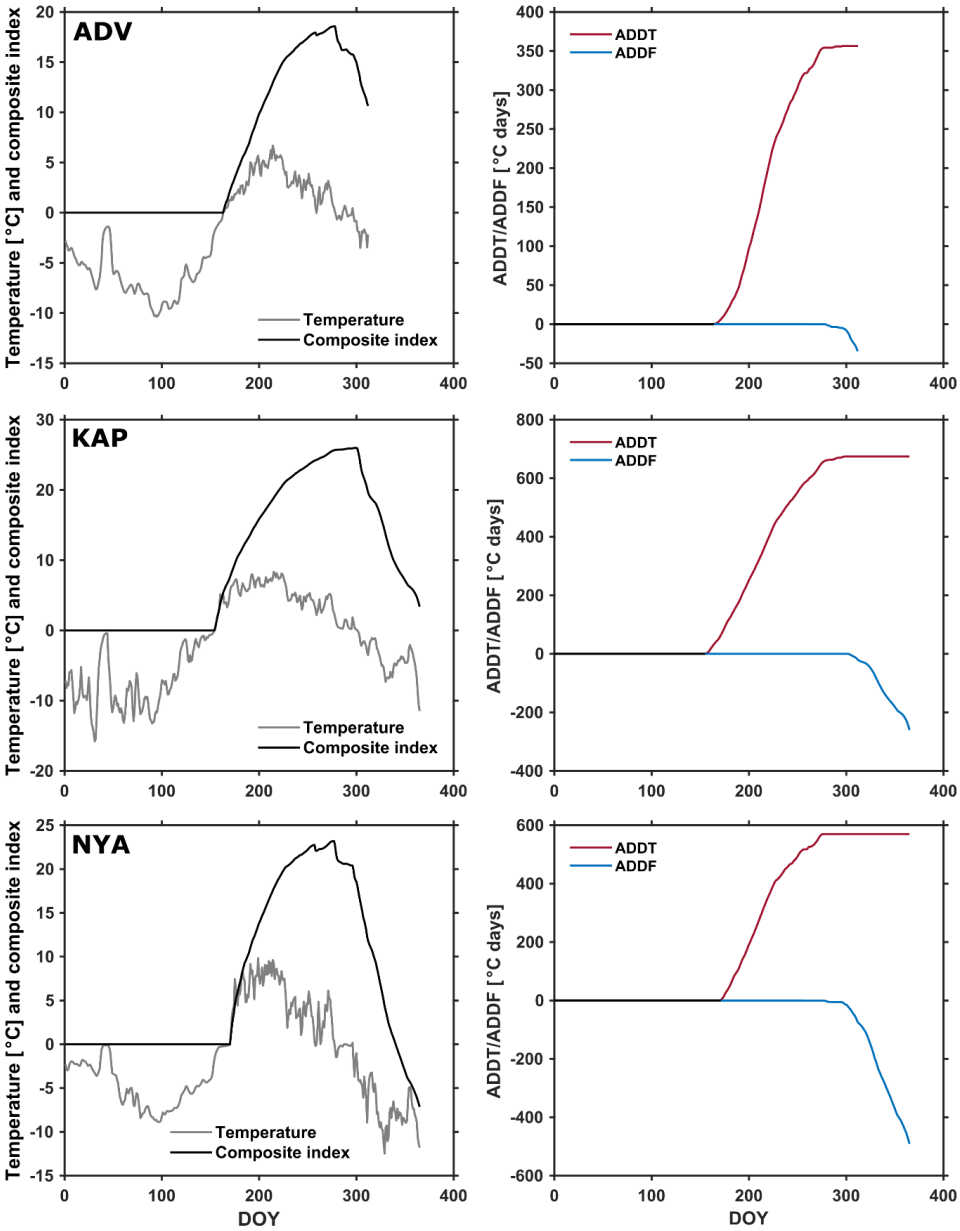

Supplement S7. Ground temperature measured in three boreholes (Table 2), calculated Accumulated Degrees Days of Thaw and Freeze (ADDT/ADDF) and composite index, here based on a scaling factor α of 1.4. The calculation starts at the thaw onset based on temperature data (the index therefore remains at zero before initiation).

Supplement S8. Coefficient of determination R^2 or proportion of the variance of the regional averaged InSAR displacements that is explained by the composite index, based on air and ground temperature. In bold are the results that are kept for visualization (Figures 9 and Supplement S10) after having tested five scaling factors α. Information about temperature data is summarized in Table 2.

		Scaling factor α				
	Temperature Series	1	1.2	1.4	1.6	1.8
Adventdalen (ADV)	Air temperature	0.807	0.858	0.893	0.912	**0.914**
	Ground temperature	0.796	0.836	0.871	0.899	**0.919**
Kapp Linné (KAP)	Air temperature	0.813	0.868	0.905	**0.922**	0.921
	Ground temperature	0.862	0.904	0.931	**0.944**	0.943
Ny-Ålesund (NYA)	Air temperature	0.807	0.879	0.913	**0.915**	0.894
	Ground temperature	0.913	0.956	**0.966**	0.951	0.920

Supplement S9. Coefficient of determination R^2 or proportion of the variance of the InSAR displacement time series (three scales: the single pixels near the boreholes, km^2 and regional averages) that is explained by the composite index based on ground temperature. In bold are the results that are kept for visualization (Figures 10–12) after having tested five scaling factors α. Information about temperature data is summarized in Table 2.

		Scaling factor α				
	InSAR Series	1	1.2	1.4	1.6	1.8
Adventdalen (ADV)	Near borehole pixel	**0.982**	0.962	0.935	0.899	0.856
	Km^2 average	0.970	0.980	**0.981**	0.973	0.957
	Regional series	0.796	0.836	0.871	0.899	**0.919**
Kapp Linné (KAP)	Near borehole pixel	0.924	**0.939**	0.938	0.924	0.987
	Km^2 average	0.950	0.970	**0.975**	0.964	0.941
	Mean series	0.862	0.904	0.931	**0.944**	0.943
Ny-Ålesund (NYA)	Near borehole pixel	0.269	0.375	0.473	0.556	**0.623**
	Km^2 average	**0.889**	0.859	0.807	0.744	0.677
	Regional average	0.913	0.956	**0.966**	0.951	0.920

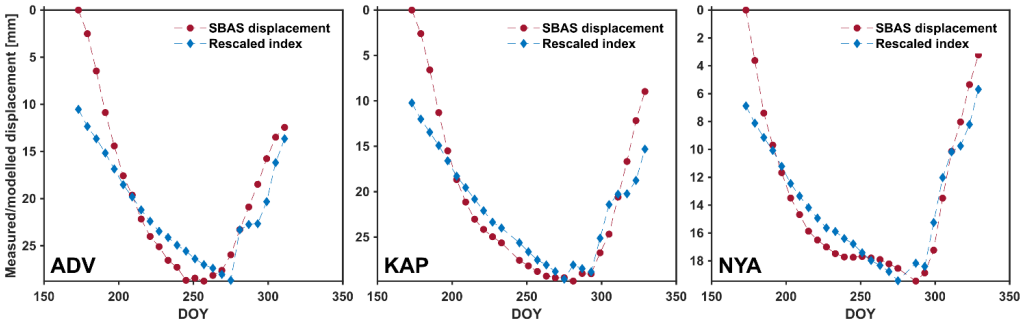

Supplement S10. Measured displacements (regionally averaged InSAR series, DOY maxima Q1–Q3, Figure 8B) compared to modelled displacements (rescaled composite index) based on air temperature. Note that the y-axis scale varies for each graph. Information about temperature data is summarized in Table 2.

Paper III: Regional InSAR inventory of slope movement in Northern Norway

Rouyet, L., Lilleøren, K. S., Böhme M., Vick, L. M., Etzelmüller, B., Delaloye, R., Larsen, Y., Lauknes, T. R., Blikra, L. H.

Under Review in *Frontiers in Earth Science: Cryospheric Sciences*

Dataset: https://doi.pangaea.de/10.1594/PANGAEA.930856

Regional InSAR inventory of slope movement in Northern Norway

Line Rouyet[1,2,3], Karianne Staalesen Lilleøren[4], Martina Böhme[5], Louise Mary Vick[2], Reynald Delaloye[6], Bernd Etzelmüller[4], Tom Rune Lauknes[1], Yngvar Larsen[1], Lars Harald Blikra[7]

[1] NORCE Norwegian Research Centre AS, Tromsø, Norway.
[2] Department of Geosciences, UiT The Arctic University of Norway, Tromsø, Norway
[3] Department of Arctic Geology, The University Centre in Svalbard (UNIS), Longyearbyen, Norway
[4] Department of Geosciences, The University of Oslo (UiO), Oslo, Norway
[5] The Geological Survey of Norway (NGU), Trondheim, Norway
[6] Department of Geosciences, The University of Fribourg (UNIFR), Fribourg, Switzerland
[7] The Norwegian Water Resources and Energy Directorate (NVE), Trondheim, Norway

Keywords: Slope movement, InSAR, Periglacial, Permafrost, Subarctic, Norway, Rock glacier, Rockslide

Abstract

Mountain slopes in periglacial environments are affected by frost- and gravity-driven processes that shape the landscape. Both rock glaciers and rockslides have been intensively inventoried worldwide. Although most inventories are traditionally based on morphological criteria, kinematic approaches based on satellite remote sensing have more recently been used to identify moving landforms at the regional scale.

In this study, we developed simplified ground velocity products based on Interferometric Synthetic Aperture Radar (InSAR) to inventory slope movements in a region in Northern Norway covering approximately 7500 km^2. We used a multiple temporal baseline InSAR stacking procedure based on 2015–2019 ascending and descending Sentinel-1 images to take advantage of a large set of interferograms and exploit different detection capabilities.

First, moving areas are classified according to six velocity brackets, and morphologically associated to six landform types (rock glaciers, rockslides, glaciers/moraines, talus/scree deposits, solifluction/cryoturbation and composite landforms). The kinematic inventory shows that the velocity ranges and spatial distribution of the different types of slope processes vary greatly within the study area.

Second, we exploit InSAR to update pre-existing inventories of rock glaciers and rockslides in the region. Landform delineations and divisions are refined, and newly detected landforms (54 rock glaciers and 20 rockslides) are incorporated into the databases. The updated inventories consist of 414 rock glacier units within 340 single- or multi-unit(s) systems and 117 rockslides. An InSAR-based kinematic attribute assigned to each inventoried landform documents the magnitude order of the movement.

Finally, we show that topo-climatic variables influence the spatial distribution of the rock glaciers. Their mean elevation increases toward the continental interior with a dominance of relict landforms close to the land-sea margin and an increased occurrence of active landforms further inland. Both rock glaciers and rockslides are mostly located on west-facing slopes and in areas characterized by strongly foliated rocks, which suggests the influence of geological preconditioning factors.

The study demonstrates the value of semi-quantitative InSAR products to characterize kinematical information at large scale and exploit the results for periglacial research. It highlights the complementarity of both kinematic and morphological approaches for inventorying slope processes.

1 Introduction

Mountainous regions are affected by a wide range of periglacial processes leading to ground movement (Ballantyne, 2018; Gruber and Haeberli, 2009; Jaboyedoff et al., 2013). Gravity induces certain landforms on slopes, such as rock glaciers and rockslides. They have specific characteristics depending on the material they convey (rock, unconsolidated sediments, ice), their movement rates and their environmental controlling factors. One common denominator of these landforms is the potential hazard they represent in case of failure (Blikra et al., 2006; Kääb et al., 2005).

Located in seasonally or perennially frozen ground, most periglacial landforms are influenced by freeze and thaw cycles (French, 2007). Rock glaciers, defined here as creeping permafrost landforms consisting of an ice/rock mixture (Berthling, 2011), are often used as a proxy for permafrost occurrence or paleo-permafrost extents (Etzelmüller et al., 2020; Karjalainen et al., 2020; Lilleøren and Etzelmüller, 2011; Scotti et al., 2013). In mountainous areas where large topographic variability and site-specific conditions determine the local occurrence of permafrost, rock glacier inventories are valuable to complement global kilometric-resolution permafrost products (Obu et al., 2019). Rock glacier kinematics are considered as an indicator of climate change due to the increasing evidence of relations between creep rate and ground temperature (Delaloye et al., 2010; Kääb et al., 2020). Several studies have evidenced that climate change has consequences on the permafrost thermal state and the ice/water contents of rock glaciers (Ikeda et al., 2008), which cause in a first response their acceleration (Delaloye et al., 2010; Kääb et al., 2007), their destabilization (Delaloye et al., 2013; Eriksen et al., 2018; Roer et al., 2008;), exceptionally their collapse (Bodin et al., 2017), but also conversely, as degradation continues, their progressive stabilization (Delaloye et al., 2017; Ikeda and Matsuoka, 2002).

Permafrost and seasonal frost also influence the dynamics of certain rockslides (Blikra and Christiansen, 2014; Keuschnig et al., 2015) and changing climate has an impact on their stability (Geerstema et al., 2006; Patton et al., 2019; Stoffel et al., 2014). Mapping of unstable rock slopes prone to catastrophic failure are made in many mountainous regions around the globe. Inventories of unstable rock masses, hereafter referred to as rockslides, are typically produced to identify geohazards and understand their distribution and mechanisms (Crosta et al., 2013; Hermanns et al., 2013; Pedrazzini et al., 2016).

To document large areas, satellite remote sensing techniques have become widely applied to identify, map and inventory slope movement. Satellite Interferometric Synthetic Aperture Radar (InSAR) is especially valuable to detect millimetre to centimetre scale ground movement in the radar line-of-sight (LOS). InSAR has been extensively used for studies of periglacial landforms, such as rock glaciers (Delaloye et al., 2007; Kääb et al., 2020; Liu et al., 2013; Villarroel et al., 2018; Wang et al., 2017) or rockslides (Bouali et al., 2018; Böhme et al., 2019; Lauknes et al., 2010; Rosi et al., 2017; Vick et al., 2020). In the Western Swiss Alps, Barboux et al. (2014; 2015) mapped and inventoried slope movement using InSAR and categorized the detected moving objects by velocity classes and landform types (solifluction, rockslides, push-moraines, rock glaciers). In Bhutan, Dini et al. (2019) categorized different slope processes using InSAR and were able to distinguish between irreversible (gravitational, e.g. rock glaciers or rockslides) and reversible processes (seasonal, e.g. related to freeze/thaw or hydromechanical forces). In Norway, Iceland and Svalbard, various studies also showed that InSAR can be used to identify specific magnitude and orientation of displacement for different periglacial landforms and surficial material types (Eckerstorfer et al., 2018; Eriksen et al., 2017a; Lilleøren et al., 2013; Rouyet et al., 2019).

Several InSAR techniques have been developed depending on the expected movement rate, the conditions of the study area and the scope of the research. In mountainous environments, landforms moving at dm/yr to m/yr rates are typically investigated by manual analysis of interferometric image pairs (Delaloye et al., 2007; Barboux et al., 2014), while more advanced time series methods perform

well on landforms with a mm/yr to cm–dm/yr velocity but tend to fail on fast-moving landforms (Barboux et al., 2015; Rosi et al., 2017; Vick et al., 2020). Nowadays, the development of national to multi-national InSAR mapping services (Dehls et al., 2019; Larsen et al., 2020) allows for identifying moving areas over entire mountain ranges, but understanding these movements and relating them to specific processes remain a challenging task. Research towards a more comprehensive use of large stacks of Synthetic Aperture Radar (SAR) images to categorize the ground velocity and relate detected moving areas to specific landforms is needed to scale up the exploitation of InSAR technology in geosciences.

Here we propose a multiple temporal baseline approach based on InSAR stacking (Lyons and Sandwell, 2003; Sandwell and Price, 1998), to combine complementary strengths of existing techniques and consider a large range of velocities. We inventory slope movements in a study area in Northern Norway, encompassing a cluster of rock glaciers and rockslides, and compare them to morphological inventories. We aim to 1) develop simple high order InSAR products that summarize the kinematic information and semi-quantitatively document slope movement over large areas; 2) categorize the identified moving areas and relate them to inferred slope processes; 3) combine kinematic and morphological approaches to update the existing inventories of rock glaciers and rockslides; 4) interpret the kinematic variability and distribution of different landform types and discuss the values and limitations of InSAR for regional periglacial studies.

2 Study area

The study area is located in Troms and Finnmark county, Northern Norway and covers 7500 km^2, 6300 km^2 of which is on land (Figure 1). Shaped over more than 20 glacial cycles (Corner, 2005), the alpine topography is characterized by a high altitudinal gradient with deep narrow fjords and high mountain peaks up to ca. 1800 m a.s.l. in the central part of the area (Lyngen Alps). Towards East, multiple valleys lead from the fjord heads towards a flat-topped terrain (ca. 1000 m a.s.l.) near the Finnish and Swedish borders.

The geology of the region consists of Caledonian nappes of the Upper Allochthon (Andresen, 1985), with basement rocks of the Fennoscandian Shield outcropping in erosion windows and in coastal areas (Zwaan, 1988; Bergh et al., 2007). The thrust nappes were metamorphosed, imbricated, and folded during multiple events, resulting in a dominance of medium- to high-grade metamorphic lithologies (Augland et al., 2014; Zwaan, 1988). The major structures, i.e. faults, shear zones, thrusts and foliation, dip dominantly to the NW, aligning with the complex fold-thrust belt architecture. The Lyngen Alps are metagabbro-dominated, while the western and eastern parts of the study area are characterized by metasedimentary rocks, such as mica schist and phyllite (NGU, 2020a; Zwaan, 1988; Zwaan et al., 1998).

The study area lies within the subarctic climate zone, characterised by long cold winters and short cool summers (NCCS, 2021). The region is influenced by the warm North Atlantic Current, with a large climatic gradient between the temperate and humid coasts and the cold and dry continental interior. Due to the general orientation of the land-sea margin in this region (Figure 1, bottom-right inset), the climatic gradient follows a NW–SE orientation, parallel to profile P–P' (Figure 1, black crosses). At stations close to sea level, mean annual air temperature and precipitation recorded the past ten years are respectively 4.8°C and 1197 mm in Botnhamn/Hekkingen on the west coast, 3.7°C and 1051 mm in Tromsø and 3.2°C and 436 mm in Skibotn (East of Storfjord) (NCCS, 2021). The permafrost distribution follows a similar gradient. The lower elevation limit of the discontinuous zones, where permafrost underlies 50–90% of the landscape, is estimated at around 1000 m a.s.l. in coastal sites and decreases to below 400 m a.s.l. towards the interior. Around Kåfjord, the lower discontinuous permafrost limit is estimated at 800–900 m a.s.l. (Farbrot et al., 2013; Gisnås et al., 2017), but isolated-sporadic permafrost, where permafrost underlies < 50% of the landscape, can be found down to 500 m

a.s.l (Hjort et al., 2014). The permafrost is relatively warm with temperature close or just below 0°C (Christiansen et al., 2010). In-situ ground temperature measurements indicate that the permafrost is warming and degrading in Northern Norway (Farbrot et al., 2013; Isaksen et al., 2007). In the study area, this is documented by six instrumented boreholes in Guolasjávri, Lávkavággi and Nordnes, all East of Storfjord (Farbrot et al., 2013). Models project that this trend is likely to continue in the coming decades (Gisnås et al., 2013; Farbrot et al., 2013).

Due to its geological and geomorphological history, the area presents a cluster of unstable rock slopes (Blikra et al., 2006; Braathen et al., 2004; Bunkholt et al., 2012; Osmundsen et al., 2009; Vick et al., 2020). Several rockslides are intensively investigated (Hermanns et al., 2016) and monitored (Blikra and Kristensen, 2013), due to potential major consequences in case of a collapse into the valleys or fjords, as well as connected secondary effects such as displacement waves. Detailed mapping and inventories of rock glaciers and ice-cored moraines have also been performed, especially in the Kåfjord area (Lilleøren and Etzelmüller, 2011; Tolgensbakk and Sollid, 1988; Sollid and Sørbel, 1992). Recent research evidenced a fast creep and acceleration trend in a rock glacier complex in Skibotndalen (Eriksen et al., 2018). Other periglacial landforms, such as solifluction lobes and sheets, have also been studied (Hjort et al., 2014; Eriksen et al., 2017a).

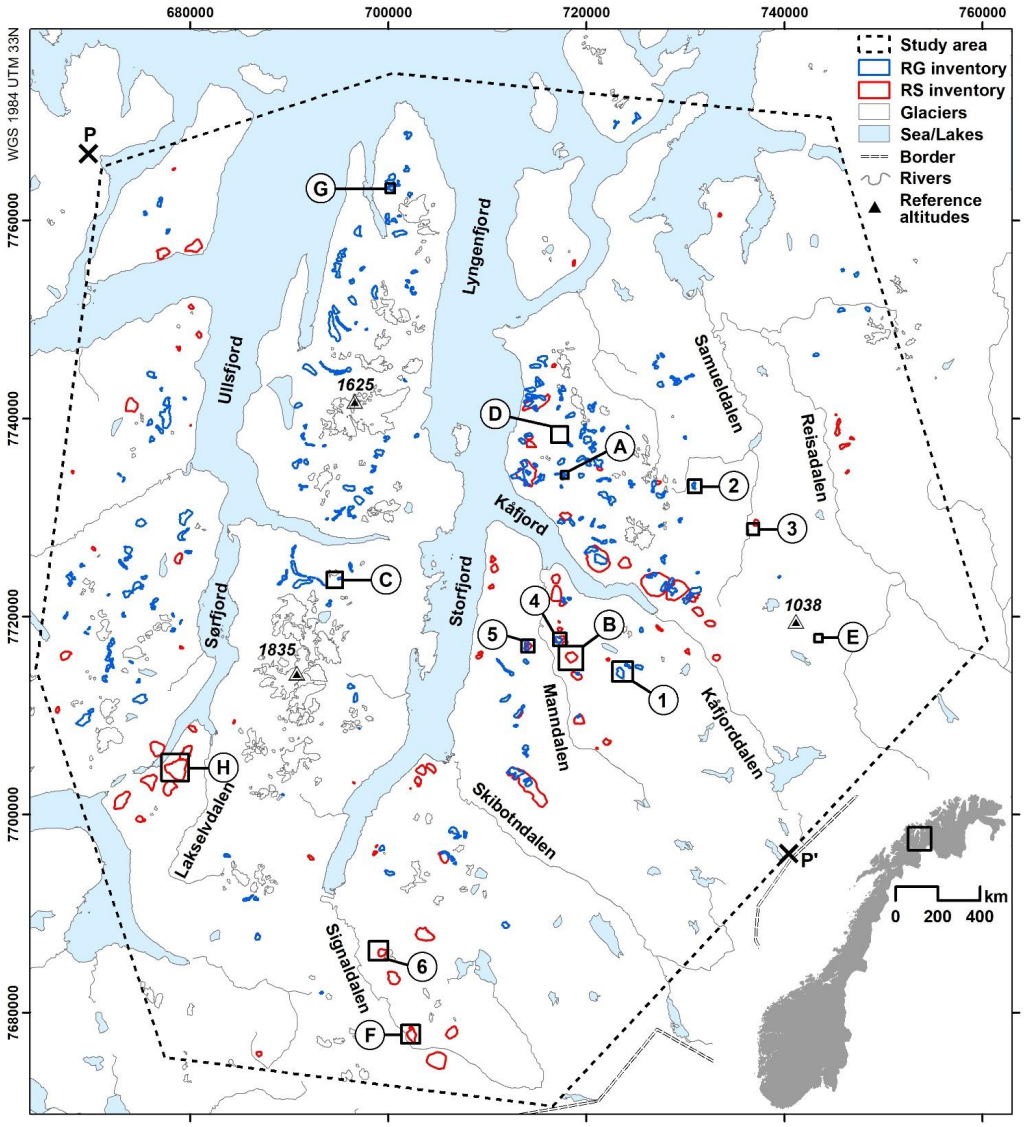

Figure 1. Location map of the study area in Northern Norway with landforms from the initial rock glacier (RG) and rockslide (RS) inventories. Detailed maps **(A–H)** and **(1–6)** are shown in Figures 3, 6, 8 and 10. P–P' show the limits of the profile used in Section 6.3. Glacier inventory from ndreassen and Winsvold (2012) and Winsvold et al. (2014). Sea, lakes, rivers, border and reference altitudes/names from NMA (2020a).

3 Datasets

3.1 Sentinel-1 Interferometric Wide Swath mode scenes

The InSAR processing is based on images from Sentinel-1 C-band (5.6 cm wavelength) SAR satellites of the European Commission Copernicus Programme. Sentinel-1 is a constellation of two satellites providing a repeat-pass of 6 days. SAR images from ascending (track 58) and descending (track 95) snow-free SAR images (Interferometric Wide Swath mode) between 2015 and 2019 (June–October) were used. The sensor is looking obliquely downward (mean LOS incidence angles: 38.9° in ascending; 27.4° in descending), towards East-Northeast (ENE) for ascending acquisitions and towards West-Northwest (WNW) for descending acquisitions (mean LOS orientations: 77.4° in ascending; 282.6° in descending). An 8 x 2 (range x azimuth) spatial multi-looking factor was applied, providing a final ground resolution of approximately 40 x 40 m.

3.2 Initial morphological inventories and in-situ data

The polygonal morphological inventories used in this study are based on an inventory of cryogenic landforms from the University of Oslo and an inventory of unstable rock slopes from the Geological Survey of Norway.

With the study area, the cryogenic landforms inventory from Lilleøren and Etzelmüller (2011) consists of 345 rock glaciers, protalus ramparts, ice-cored moraines, debris-covered glaciers, and morainic glacier-forefield. In the present study, we differentiate permafrost from glacial landforms. We discarded 59 landforms to focus on rock glaciers and protalus ramparts, the latter being considered as 'embryonic rock glaciers' experiencing permafrost creep (Scapozza et al., 2011). The initial inventory of rock glaciers (RG) consists of 286 landforms (Figure 1, blue polygons). The inventory is primarily based on geomorphological or quaternary geological maps (Østrem, 1964; Sollid and Torp, 1984; Tolgensbakk and Sollid, 1988) and optical imagery (NMA, 2011). The activity of the rock glaciers was defined as active, inactive, or relict based on morphological evidence. The delineation follows an extended geomorphological footprint definition, including the frontal and lateral margins/aprons. It must be noted that the quality of the optical images was variable at the time of the inventory and may have led to inaccurate detection and delineation, especially in the upper boundary, due to image distortion in steep areas, shadows and snow cover.

The initial unstable rock slope inventory, hereafter referred to as rockslides (RS), consists of 97 landforms in the study area (NGU, 2020b) (Figure 1, red polygons). It considers areas where signs of gravitational and post-glacial rock mass deformation have been identified by the Geological Survey of Norway (e.g. backscarps, open fractures) and could lead to a rock avalanche in case of failure (Hermanns et al., 2013; Oppikofer et al., 2015). The mapping programme focuses on rockslides that present a risk to society and therefore is not exhaustive. It must be noted that the reliability of the RS polygonal delineations varies depending on the level of investigation. In areas without detailed geological information, the delineation is indicative, especially at the lower limit. Within the study area, three RS are permanently monitored (high risk objects: Gámánjunni 3, Jettan and Indre Nordnes) (Blikra et al., 2009; Blikra et al., 2015; Böhme et al., 2016; 2019; Eriksen et al., 2017b) and 21 RS have corner reflectors for InSAR monitoring and/or periodic differential Global Navigation Satellite System (dGNSS) measurements (Bunkholt et al., 2011; Lauknes, 2011a). Of those last, 13 are showing displacement, four are not moving (certain data), four are uncertain due to short series or bad measurement locations. In total, measurements over 20 RS were used for comparison with the InSAR results of this study. Their location is shown in supplementary material (Figure S1).

4 Methods

The use of InSAR to map slope movements in mountainous environments is well-spread and usually based on two types of techniques, both with advantages and drawbacks. The analysis of individual interferometric pairs (interferograms) has proven to be valuable in identifying landforms with fast movement (Delaloye et al., 2007; Barboux et al., 2014). It reduces the risk of a biased estimate of the displacement and exploits information from decorrelated areas, when related to fast-moving landforms (Barboux et al., 2014). However, such analysis requires laborious manual work considering the extensive SAR data archives and may exaggerate the importance of some interferograms with short-term nonrepresentative patterns. Slow-moving landforms (e.g. mm/yr to cm/yr on large rockslides) may be hard to detect due to uncorrected atmospheric effects. Multi-temporal InSAR techniques (Ferretti et al., 2001; Berardino et al., 2002), including automated conversion from cyclic to continuous phase difference, so-called unwrapping (Chen and Zebker, 2002), have been developed to process large SAR stacks, allowing for mitigating more robustly atmospheric effects and providing submillimetric accuracy. However, due to InSAR decorrelation during snow-covered periods, time series methods usually require the integration of interferograms with long temporal intervals, which may lead to ambiguous displacement estimates on fast-moving landforms, especially when the movement is nonlinear (Wasowski and Bovenga, 2014).

We apply here a multiple temporal baseline InSAR stacking methodology to combine the strengths of the single interferogram analysis and multi-temporal InSAR techniques (Section 4.1). Mean annual ground velocity was classified to inventory kinematics at the regional scale (Section 4.2). The results were then used to update the morphological RG and RS inventories and include a kinematic attribute into the databases (Sections 4.3) (Figure 2).

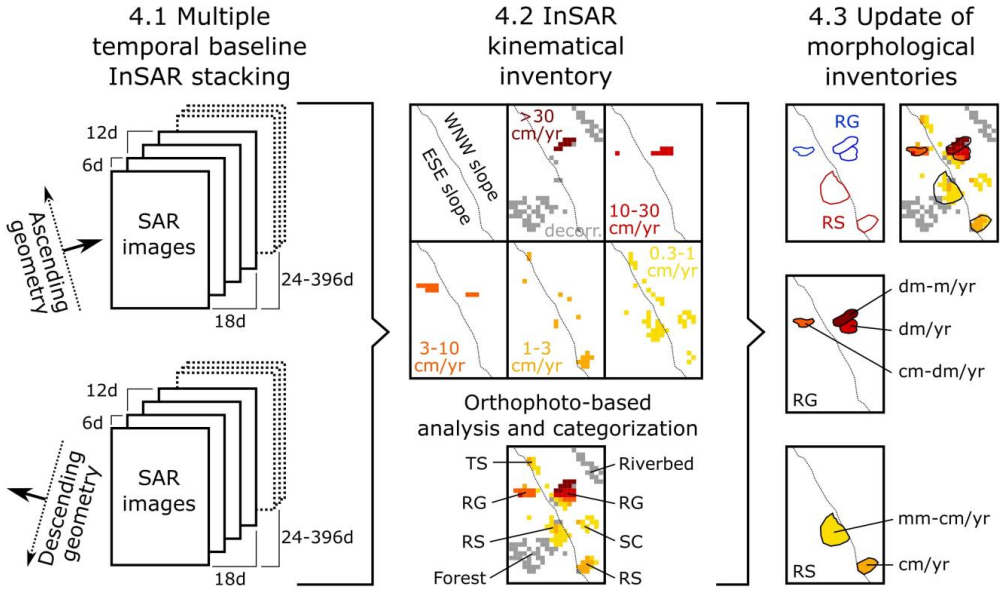

Figure 2. Methodological sketch. Acronyms refer to rock glacier (RG), rockslide (RS), talus/scree deposit (TS), solifluction/cryoturbation (SC).

4.1 Multiple temporal baseline InSAR stacking

InSAR results have been processed using the NORCE GSAR software (Larsen et al., 2005). All June to October seasonal and one-year pairs were first generated leading to two sets of 2705 (track 58) and 2533 (track 95) interferograms. The spatial baseline has not been restricted, the effective maximum being under the critical baseline limit. The noise level was reduced by applying a spatially adaptive coherence-dependent Goldstein filter (Goldstein and Werner, 1998; Baran et al., 2003). Interferograms were preselected based on a measure of the signal stability (mean coherence > 0.4), leading to two sets of 1221 (track 58) and 1308 (track 95) interferograms. The contribution from the stratified atmosphere was mitigated (Cavalié et al., 2007; Lauknes, 2011b) using a 10 m DEM (NMA, 2016). A similar calibration point at a location expected to be stable in the central part of the study area has been used in both geometries (69°30'52''/20°25'45'', black star in Figure 4). Unwrapping was performed using the SNAPHU software (Chen and Zebker, 2002). Interferograms affected by large unwrapping errors were discarded.

We used a weighted averaging method based on multiple unwrapped interferograms (InSAR stacking, e.g. Lyons and Sandwell, 2003; Sandwell and Price, 1998), to mitigate atmospheric artefacts and provide an estimate of the assumed linear velocity. It should be noted that although the results are expressed as mean annual velocities, they are based on snow-free scenes, which exaggerate the importance of the summer seasons. InSAR stacking has here been processed with five complementary ranges of temporal intervals between the SAR acquisitions (temporal baselines BT, Table 1), in order to combine different detection capabilities. Large BT (e.g. one year) provide good sensitivity to low displacement rates. Small BT (e.g. 6 days) allows for higher detectable maximal velocities. In 54–150 days and 336–396 days stacks, fast moving areas are decorrelated but the results are used only for velocities < 3 cm/yr. In the 6 days stack, the noise level is expected to be higher, but the results are used only for velocities > 30 cm/yr. The procedure has been performed both for ascending and descending datasets, leading to a set of 10 mean velocity maps. The large number of interferograms in each stack (56 to 326, Table 1) contributed to mitigate the effects from turbulences in the troposphere. Additionally, the results have been spatially smoothed using a 10 km filter to remove remaining large-scale unwanted phase trends (atmospheric components).

Table 1. Summary of the InSAR processing settings for the five stacks in each SAR geometry. Acronyms refer to ASC (ascending), DESC (descending), BT (temporal baseline, i.e. time interval between SAR acquisitions)

Stack	Min. BT [days]	Max. BT [days]	Max. velocity [cm/yr]	Nb interferograms (preselected based on mean coherence >0.4)		Nb interferograms (after manual check of unwrapping results)		Use for velocity classes (see Table 2)
				ASC	DESC	ASC	DESC	
1	336	396	1.29	353	375	299	326	Classes 1 and 2
2	54	150	3.41	146	168	125	148	Class 2
3	18	48	10.65	252	251	219	219	Class 3
4	6	12	42.58	126	129	111	114	Class 4
5	6	6	85.17	67	66	56	57	Classes 5 and Decorrelated

4.2 InSAR kinematic inventory

The InSAR kinematic inventory is a catalogue of ground movement comprising pixels assigned to six mean annual velocity classes. The processing strategy has been designed for a semi-quantitative mapping at a regional scale. To document movement on both east- and west-facing slopes, ascending and descending results were combined. The velocity classes are meant to document half a magnitude

order, as recommended by the International Permafrost Association (IPA) Action Group on rock glaciers inventories and kinematics (IPA, 2020; IPA, 2020b).

Five classes are based on the actual velocity values (classes 1 to 5, Table 2). When a pixel was covered by results from different stacks or geometries, we selected the value that corresponds to the highest velocity class to keep the most adequate information in respect to line-of-sight and detection capability. This assumes that for example a movement on a west-facing slope could be underestimated in ascending results and a fast-moving area is affected by phase ambiguity using long BT. The maximum detection capability for displacement between two neighbouring pixels corresponds to a quarter of the wavelength of the sensor (5.6 cm for Sentinel-1) during the time interval used to build the interferograms. For a stack including interannual interferograms (336–396 days BT, stack 1 in Table 1), phase ambiguities can occur when the velocity is over ca. 1.3 cm/yr. The results of this stack were thus used for the class 1, i.e. 0.3–1 cm/yr (Table 2). For a stack including only 6 days interferograms (stack 5 in Table 1), the detection capability rises to ca. 85 cm/yr. The results of this stack were thus used for the class 5, i.e. > 30 cm/yr (Table 2). The similar rationale was applied to the intermediate velocity classes 2–4, based on the stacks 1–5 (Table 2).

Three additional classes were generated (Table 2). The class 'Decorrelated' corresponds to the pixels under the coherence thresholds both in ascending and descending results using the stack 5 (6 days BT). Fjord and large lakes have been removed to focus on land. Decorrelation is typically caused by 1) dense vegetation, 2) snow or surface water, 3) too high velocities (> 85 cm/yr). Over specific landforms with morphological signs of high activity, if there is no visual sign indicating that 1) or 2) are the decorrelation causes (based on orthophotos, NMA, 2020b), the third hypothesis can be reasonably kept. The class 'Layover/Shadow' shows where no information can be exploited from any SAR geometry. The class 'N-S slopes' consists of a semi-opaque mask of the North- and South-facing slopes (compass directions 337.5–22.5°/157.5–202.5° on slope angles > 2°) highlighting where InSAR is likely to provide underestimated values if the horizontal component of the true displacement vector is large. This mask corresponds to ca. 21% of the land area (1313 km^2). When mapping all together the five velocity classes and the three additional classes, the transparent areas can reasonably be considered as under the detection limit (< 0.3 cm/yr), i.e. corresponding to no or little movement (class 0). The multiple temporal baseline InSAR stacking applied here does not allow for an accurate discrimination of velocities under this limit.

Based on the InSAR kinematic inventory, we analysed the type and velocity classes of the identified moving pixels, independently of any previously made morphological inventory. The main InSAR-detected moving areas consists of clusters of typically > 10 pixels (ca. 160,000 m^2) from similar or adjacent classes. They were first manually located with a point without interpreting which process induce the movement. This procedure is not meant to be fully exhaustive but aims to provide a representative sample of what InSAR is able to detect in the study area. Due to the focus on slope processes, only pixels on slopes stepper than 5 degrees were considered at this stage. Secondly, each identified location was associated with a category of periglacial landform through a visual interpretation of orthophotos (NMA, 2020b). Six main categories have been chosen for this purpose (Figure 3): rock glacier (RG), rockslide (RS), glacier/moraine (GM), talus/scree deposit (TS), solifluction/cryoturbation (SC), composite (CO). The expected dominant movement type associated with these landforms are: permafrost creep (for RG), rock mass sliding/deformation (for RS), glacial flow or ice-core deformation/melting (for GM), superficial displacement of debris (for TS), thaw subsidence, frost creep and gelifluction (for SC). A seventh category (UD: undefined) is used when no clear process is identified. The CO class is further divided into RS+S (rockslide+superficial), RG+S (rock glacier+superficial) and RS+RG (rockslide+rock glacier). Superficial here means either talus/scree deposit or solifluction/cryoturbation. The dominant velocity class was associated to each

identified area and moving areas significantly overlapped by the 'N-S slopes' mask were flagged as 'Uncertain'.

Table 2. Velocity classification based on InSAR results from five stacks in both geometries (see Table 1)

Velocity class, no data and N-S mask	**Min. velocity**	**Max. velocity**	**Information**
	[cm/yr]		
Class 0	< 0.3		Transparent on maps, i.e. no detected movement
Class 1	0.3	1	Based on 336-396 days BT (stack 1)
Class 2	1	3	Based on a combined product from 54–150 days BT (1.5–3 cm/yr) and 336–396 days BT (1–1.5 cm/yr) (stacks 1–2)
Class 3	3	10	Based on 18–48 days BT stack (stack 3)
Class 4	10	30	Based on 6–12 days BT (stack 4)
Class 5	> 30		Based on 6 days BT (stack 5)
Decorrelated	No data due to decorrelation on land (in both ascending and descending stacks)		Decorrelation may indicate too high velocities (> 85 cm/yr) if no other decorrelation source is identified (dense vegetation, snow or surface water)
Layover/shadow	No data due to radar layover or shadow (in both ascending and descending stacks)		No information can be exploited in these areas.
N-S slopes	Uncertain		The N-S mask (227.5–22.5°/157.5–202.5° on slope angles >2°) shows where the InSAR information must be treated carefully due to LOS measurements.

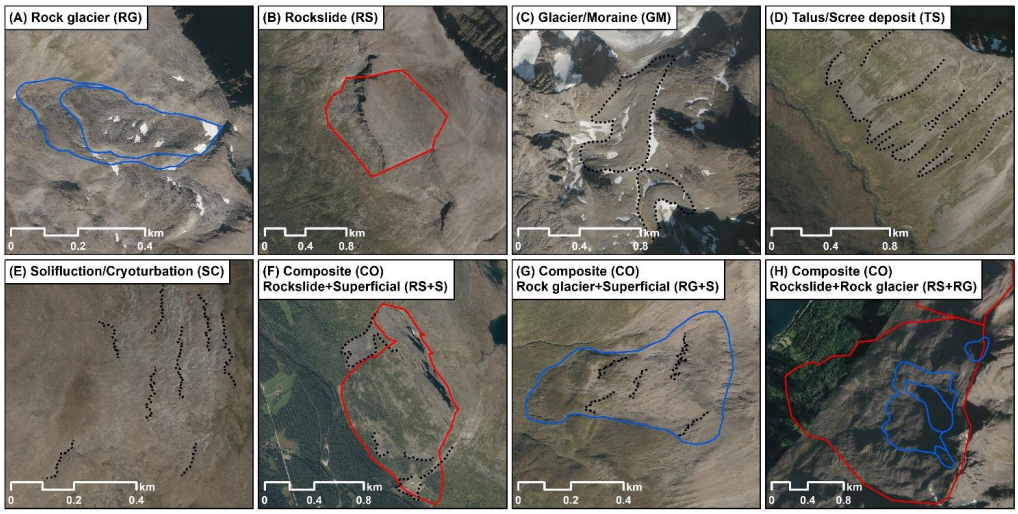

Figure 3. Orthophotos with examples of the landform categories. Locations **(A–H)** of these detailed maps are shown in Figures 1 and 4. The lines highlight the indicative landform delineations for morphological interpretation (blue: rock glaciers; red: rockslides, dashed black: others, in **(C)**: debris-covered glacier and ice-cored moraine; in **(D)**: gullies and talus cones; in **(E)** and **(G)**: solifluction lobes). *Norge i bilder* orthophotos from NMA (2020b).

4.3 Update of the rock glacier and rockslide inventories

The initial RG and RS inventories were updated by 1) including a kinematic attribute to a previously identified landform, when there is no significant limitation on the reliability of the attribution; 2) updating the delineation/units when the InSAR results fit morphological evidence that were not considered in the initial inventories; 3) adding newly detected objects, when RG/RS/CO categories have been identified but are missing in the initial inventories.

The kinematic attribute assigned to rock glaciers follows 'order of magnitude' categories (e.g. cm/yr, dm/yr, m/yr). The criteria for the assignment of the kinematic attribute, based on the velocity classes of the InSAR moving areas, are following the recent recommendations from the IPA Action Group on rock glacier inventories and kinematics (IPA, 2020a). Translation rules from velocity classes to kinematic attribute are explained in IPA (2020b) and are meant to account for some spatial and temporal heterogeneities over the inventoried landforms. If decorrelation is likely due to velocity above the threshold (Section 4.2; Table 2), the attribute 'm/yr' is used. The dominant category is used if several velocity classes are present over one landform. If there is too much heterogeneity, the category 'Undefined' is chosen, or the landform is divided into several morphological units where appropriate. If a landform is to a large extent located on N-S slopes, the reliability is low and the kinematic attribute remains 'undefined'. Based on the new kinematic information, the categorization of the rock glacier activity was also updated, following the new recommended classes (active, transitional, relict; IPA, 2020a). In general, units with kinematic attribute < 0.3 cm/yr or mm–cm/yr associated with other superficial movement (e.g. solifluction) are interpreted as relict. Units with mm–cm/yr to cm/yr kinematic attribute are interpreted as transitional. Landforms documented with cm–dm/yr to m/yr kinematics are interpreted as active. Morphological criteria are also taken into account, such as RG with undefined kinematic attribute have also been categorized as active, transitional, or relict (IPA, 2020a). According to the new delineations, one rock glacier system can be composed of a single unit or multiple units (coalescent or adjacent). The spatial connection of a rock glacier to the geomorphological unit located directly over the rock glaciers is also documented, as recommended by IPA (2020a). The relevant categories for this study are 'talus-connected', 'landslide-connected', 'glacier-connected', 'glacier forefield-connected' and 'poly-connected'. It should be noted that the spatial connection to an upslope unit does not necessarily mean that there is a dynamic or genetic connection (IPA, 2020a).

For rockslides, similar categories of kinematic attributes were used. However, in many cases, the detected velocity cannot be directly associated with the movement of the rock mass, because other processes take place in the superficial part of the inventoried landform. The landform was kinematically categorized only if the signal is assumed to correspond to the movement of the rock mass (over a rock plateau or in absence of superficial deposits). The kinematic attribute remains 'Undefined' if superficial processes are likely to dominate the InSAR signal, e.g. when talus/scree deposits, solifluction lobes or rock glaciers are superimposed. The applied stacking technique does not allow for detection capability < 0.3 cm/yr. However, multi-temporal InSAR based on a Persistent Scatterers Interferometry (PSI) algorithm can be used for this purpose. Based on the open-access Norwegian Ground Motion Mapping Service (InSAR Norway, insar.ngu.no; NGU, 2020c; Dehls et al., 2019), an additional category 'mm/yr' is added to document slow-moving landforms.

5 Results

5.1 InSAR classified products

The multi temporal baseline InSAR stacking method led to the identification of moving pixels with velocities > 0.3 cm/yr (classes 1–5) corresponding to ca. 2 % of the land area (152 km^2) (Supplementary Table S0, rows 1–2). Ca. 72 % of the land area (4527 km^2) are under the detection limit of 0.3 cm/yr.

Ca. 24 % of the land area (1525 km^2) are decorrelated in 6 days due to vegetation, snow, surface water or too fast movement. Areas affected by layover/shadow in both ascending/descending geometries cover ca. 1 % of land area (57 km^2). The fraction of areas documented by moving pixels slightly increases when discarding N-S slopes (Supplementary Table S0, rows 3–4).

Figure 4 shows the distribution of all classified InSAR results in the study area. Each landform category is presented on separated maps in supplementary material (Figures S2–S8). A high density of movement is detected on the Njárgavárri/Badjánvárri mountain slope along Kåfjorddalen, where the moving areas match the delineation of the initial RG/RS inventories at several locations (Figure 4, lower-right inset). This is especially clear for a large rock glacier complex, which is homogenously covered by the 10–30 cm/yr velocity class. This area has also been documented by Eriksen et al. (2017a), who measured similar velocity ranges. High velocity is also detected over Ádjet mountain slope along Skitbotndalen (Figure 4, upper-left inset), with several locations covered by the > 30 cm/yr velocity class. Over two initially inventoried rock glaciers, the class 'Decorrelated' covers the frontal parts of the lobes, highlighting that these areas are moving over the threshold of 85 cm/yr. These rock glaciers have been studied in detail by Eriksen et al. (2018), who documented velocities up to tens of m/yr, with an acceleration the past decades.

The analysis of the InSAR kinematic inventory led to the identification of 763 moving areas that have been associated with the six main landform categories (Figure 5). Moving areas identified on N-S slopes are inventoried but the velocity is likely to be underestimated and the attributed velocity class therefore remains 'Uncertain'. Clusters of multiple and composite processes are identified in the Piggtind area (between Lakselvdalen and Sørfjord), Manndalen, Northern Kåfjord, as well as in Skibotndalen and Signaldalen (Figure 5). Fast-moving glacier/moraine (GM) landforms are mostly identified in the Lyngen peninsula (between Storfjord/Lyngenfjord and Ullsfjord). The flat-topped terrain in the eastern part of the study area is dominated by low velocity solifluction/cryoturbation (SC) processes. Figure 6 shows detailed maps with examples of InSAR results from each landform category (similar locations as Figure 3).

The large number of identified moving areas categorized by landform type provides a representative sample to compare their velocity ranges. The total number of moving areas attributed to each category varies greatly (Figure 7A). Among the 763 locations, 357 (47%) are attributed to solifluction/cryoturbation (SC) processes. Many landforms are also identified for the composite landforms (139 CO, 18%), the talus/scree deposits (131 TS, 17%) and the rock glaciers (83 RG, 11%). Among the CO landforms, the combination of rockslides and rock glaciers (RS+RG), as well as rockslides and superficial (RS+S), are dominating with 58 and 70 landforms, respectively. RS and GM include only 16 to 24 landforms (2–3 %), respectively. The velocity ranges clearly vary depending on the landform category (Figure 7B). In > 60 % of the documented cases, GM has velocity ≥ 10 cm/yr. TS, SC and RS are dominated by low velocities (> 70% with 0.3–3 cm/yr). RG has the largest variety of velocity ranges, but ca. 50 % of the identified landforms have velocities > 3 cm/yr. Velocities of the composite category vary depending on the CO type (Figure 7C). CO RS+RG has overall the same distribution of velocity ranges as RG, highlighting that the signal from these landforms is likely dominated by the creep of the rock glaciers. CO RG+S mostly consists of relict rock glaciers with superficial processes (SC or TS) and is dominated by low velocity ranges. CO RS+S is an intermediate case with velocity ranges clearly higher than the RS category, highlighting that the detected velocity of these landforms can not only be explained by the movement of the main rock mass. Remaining 13 moving areas that could not be associated to a specific landform remained undefined (UD). Some are due to shadow, snow or distortions on orthophoto images. Others, located in areas surrounding by decorrelated pixels are possibly due to small extent unwrapping errors.

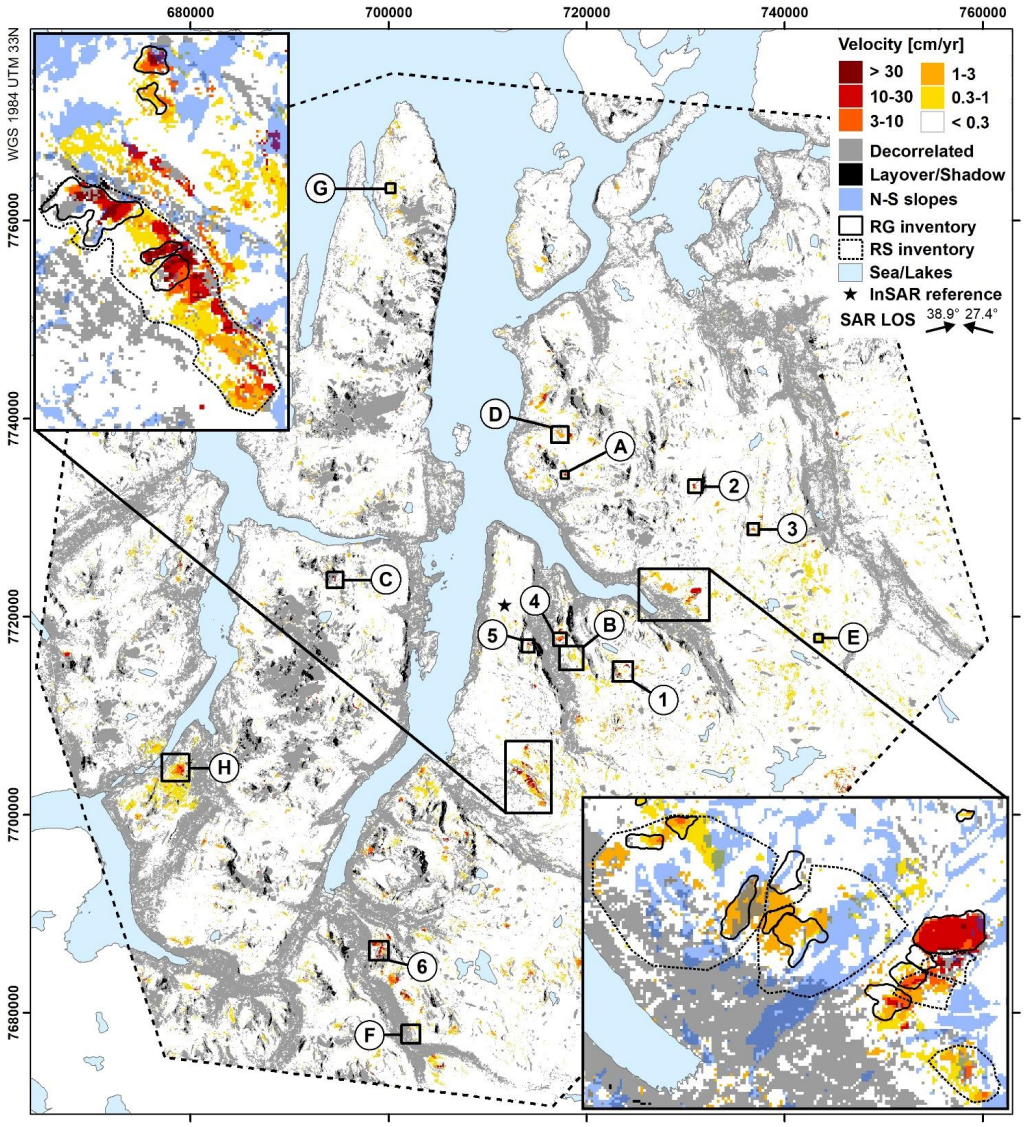

Figure 4. All classified InSAR results and detailed views over Ádjet in Skibotndalen (upper-left) and Njárgavárri/Badjánvárri in Kåfjorddalen (lower-right). Polygons in detailed maps: initial inventories of rock glaciers (RG, back solid lines) and rockslides (RS, black dashed lines). Note that the N-S slopes mask is here displayed only on the detailed maps for the sake of visualization. Locations **(A–H)** and **(1–6)** are the areas detailed in Figures 6, 8 and 10. Arrows in legend: line-of-sight (LOS) orientation. Sea and lakes from NMA (2020a).

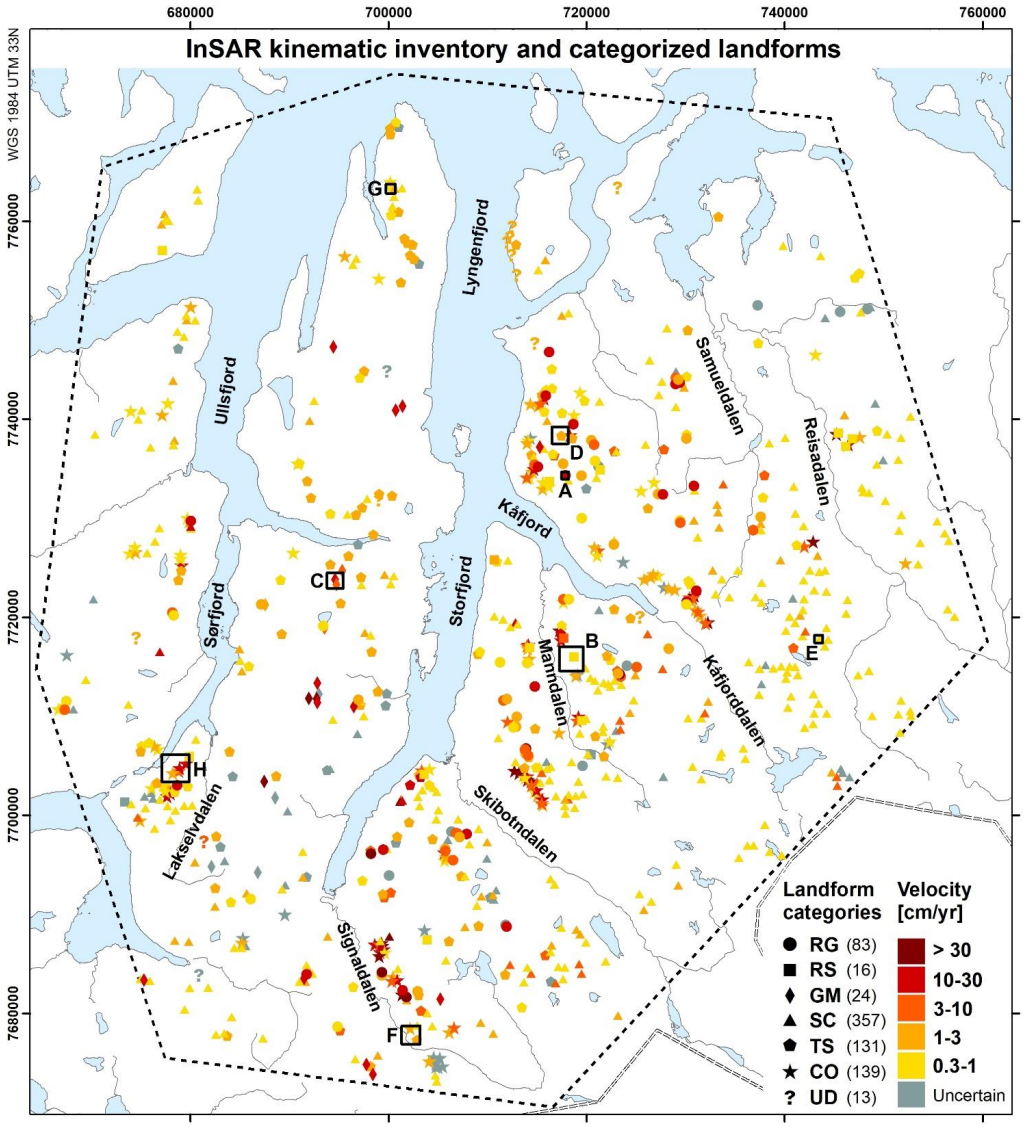

Figure 5. InSAR kinematic inventory: slope movement categorized by landform type. Acronyms refer to rock glacier (RG), rockslide (RS), glacier/moraine (GM), talus/scree deposit (TS), solifluction/cryoturbation (SC), composite (CO) and undefined (UD). Numbers in parentheses in the legend are the total numbers of identified areas for each landform category. Grey symbols correspond to areas where slope movement has been detected and the landform type categorized, but the velocity is uncertain due to location on N-S slopes. Locations **(A–F)** are the areas detailed in Figures 3 and 6. Sea, lakes, rivers and border from NMA (2020a).

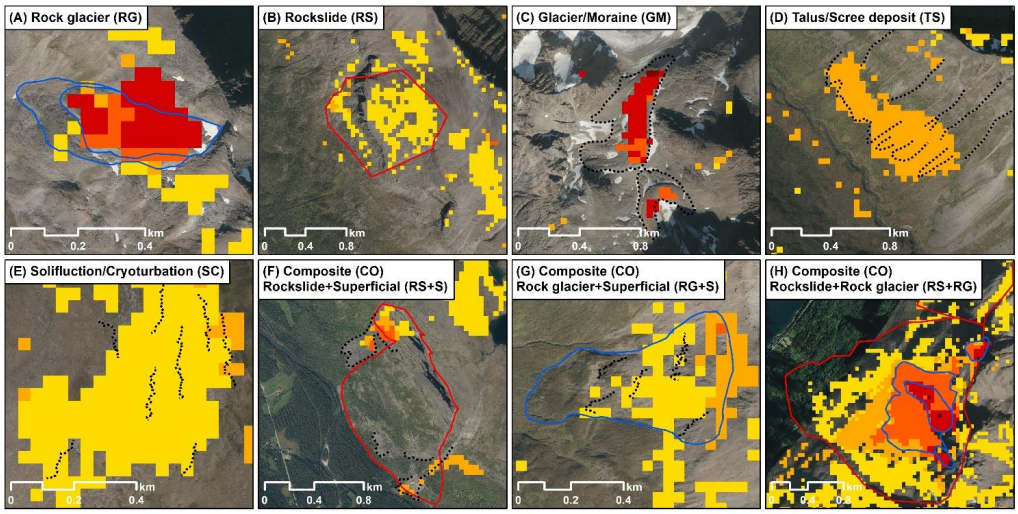

Figure 6. Classified InSAR results for each landform category (based on Figure 3). Locations **(A–H)** are shown in Figures 4 and 5. The lines highlight indicative delineations for morphological interpretation (blue: rock glaciers; red: rockslides, dashed black: others, in **(C)**: debris-covered glacier and ice-cored moraine; in **(D)**: gullies and talus cones; in **(E)** and **(G)**: solifluction lobes). The velocity colour scale is similar as the one used in Figures 4 and 5. Note that the classes 'Decorrelated', 'Layover/Shadow' and 'N-S slopes' are not displayed for the sake of visualization. *Norge i bilder* orthophotos from NMA (2020b).

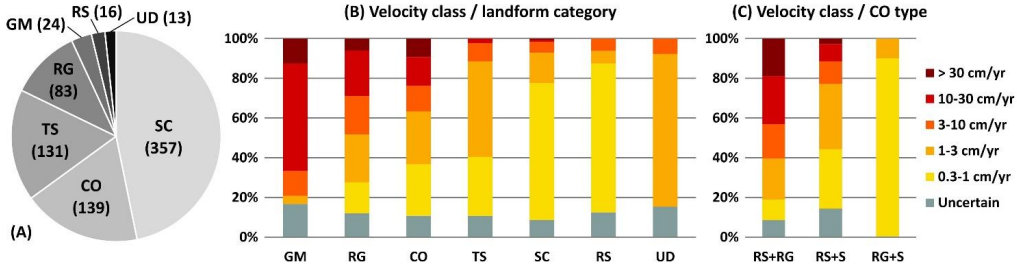

Figure 7. Statistics of the dominant velocity classes per landform category. **(A)** Number of identified landforms by landform category**. (B)** Velocity class by landform category. **(C)** Velocity class by composite type. Acronyms refer to rock glacier (RG), rockslide (RS), glacier-moraine (GM), talus/scree deposit (TS), solifluction/cryoturbation (SC), composite (CO), undefined (UD) and superficial (S). In grey: areas where slope movement has been detected and the landform type categorized but the velocity is uncertain due to location on N-S slopes

5.2 Update of the rock glacier inventory

The RG inventory consists of 340 systems (54 newly detected), including 290 single units and 124 units within 50 RG systems (414 units in total). In some cases, the update consisted in revising the delineation of the landforms or dividing previously inventoried single units into multi-units within a system, when the variability of the kinematics matched morphological evidence (Figures 8, examples 1–2). In other cases, newly identified landforms categorized as RG or CO RS+RG/RG+S (InSAR kinematic inventory, Section 5.1) were added to the inventory (Figure 8, example 3). A kinematic attribute < 0.3 cm/yr (no detected movement) is assigned to 240 units and 21 units remain kinematically

undefined (highly heterogeneous, no data or mostly located on N-S slopes). The remaining 153 units have kinematics between mm–cm/yr and m/yr (Figure 9, pie chart). The kinematic attributes contribute to the update of the activity assessment. In total, 92 units are estimated as active, 104 as transitional and 218 as relict. The distribution of the activity attribute is shown in supplementary material (Figure S9).

The kinematic attribute is spatially distributed with a clear NW–SE trend, with lower creep rates towards the NW part of the study area (Figure 9). A high density of rock glaciers with variable kinematics is found between Skibotndalen, Kåfjord and Samueldalen (Figure 9, inset map). Several active landforms are also inventoried in Piggtind area (between Lakselvdalen and Sørfjord) and in Signaldalen. The spatial connection of a rock glacier to the geomorphological unit located directly above is also documented: 285 units are talus-connected, 67 units are landslide-connected, 6 units are glacier-connected and 12 units are glacier-forefield connected. The category 'poly-connected' is used for 44 units combining a talus and landslide connection, or a talus, glacier and/or glacier-forefield connection. The importance of both categories 'landslide-connected' and 'poly-connected' highlight the challenge of multiple and combined processes in this study area. The distribution of the spatial connection to the upslope unit attribute is shown in supplementary material (Figure S10).

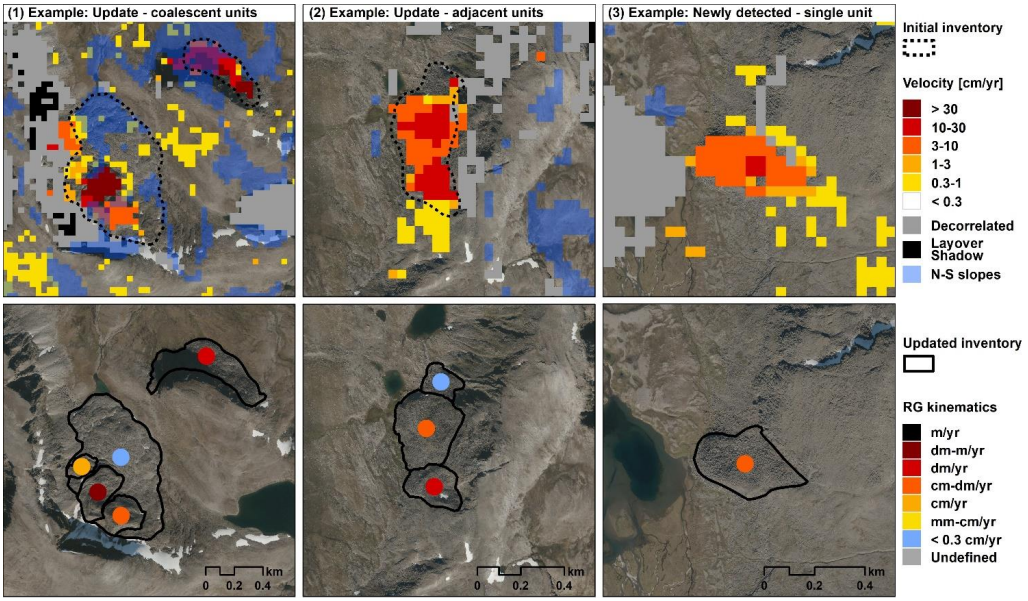

Figure 8. Update of the rock glacier (RG) inventory. Examples of **(1)** coalescent units within two systems, **(2)** adjacent units within one system, **(3)** newly detected single unit. Upper panel: classified InSAR results and initial inventory. Lower panel: updated inventory with associated kinematic attribute for each unit. Locations of these detailed maps are shown in Figure 9. *Norge i bilder* orthophotos from NMA (2020b).

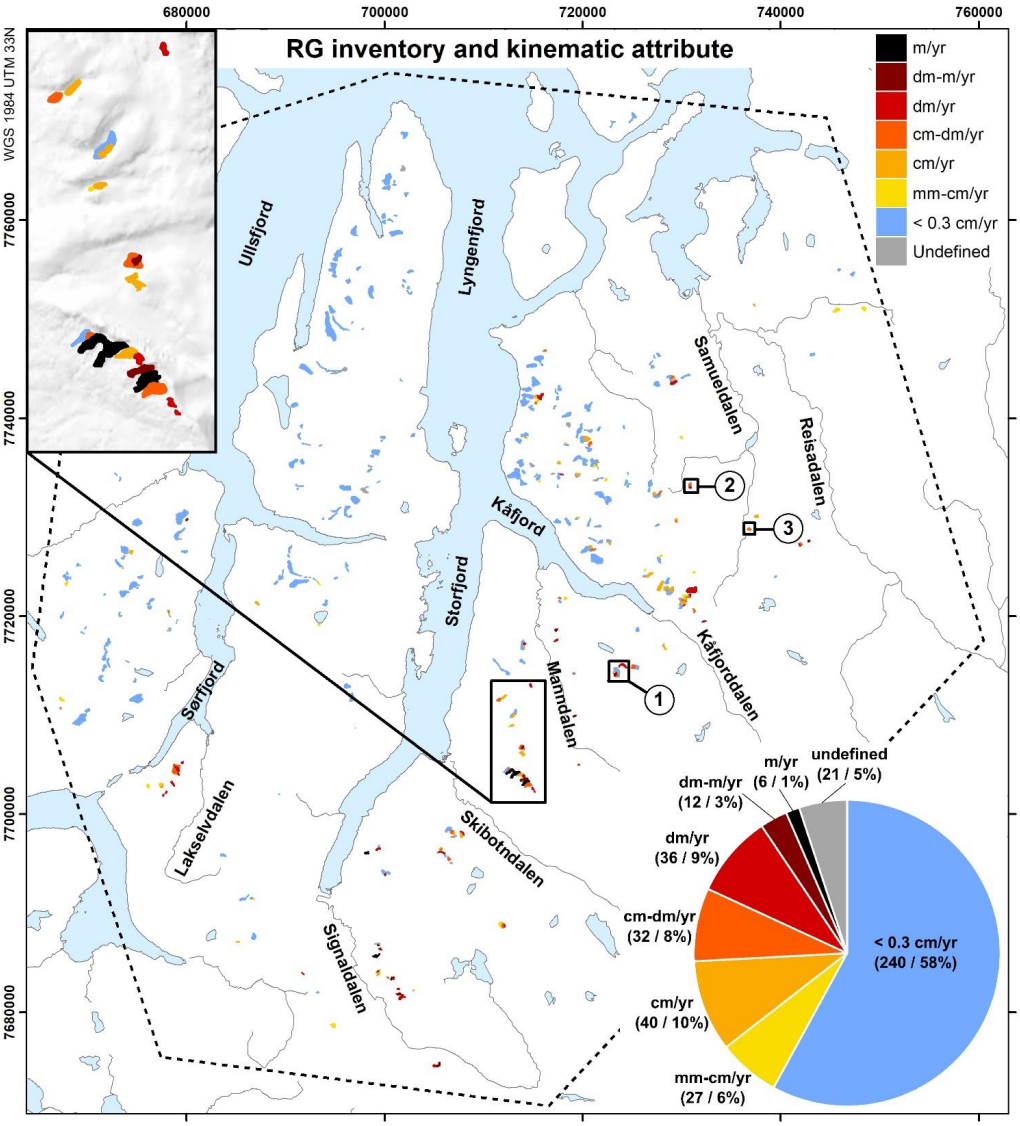

Figure 9. Updated rock glacier (RG) inventory consisting of 414 units in 340 systems and variability of the kinematic attribute in the study area. Inset map (upper-left corner): detailed view over an area including several landforms with variable kinematic attributes. Pie chart (lower-right corner): kinematic attributes for all inventoried RG units. Numbers 1–3 are the locations of examples shown in Figure 8. Sea, lakes, rivers and reference names from NMA (2020a).

5.3 Update of the rockslide inventory

The RS inventory consists of 117 landforms (20 newly detected). In many cases, the InSAR detects velocity both related to movement of the main rock mass and to processes taking place superficially (CO RS+RG or RS+S in InSAR kinematic inventory, Section 5.1). When a homogenous velocity is located in an area that can reliably be attributed to the RS kinematics based on morphological criteria (e.g. over top rock plateaus), a kinematic attribute has been attributed (Figure 10, examples 4–5). When superficial processes are masking out the potential signal from the rock mass, the kinematic attribute remains undefined (Figure 10, example 6).

High density of RS can be seen along Kåfjord, Kåfjordalen, Manndalen and Storfjord-Lyngenfjord (Figure 11, inset map). Several landforms are also identified in the Piggtind area (between Lakselvdalen and Sørfjorden) and Signaldalen, as for the RG inventory. The inventory includes 24 RS with kinematics in mm–cm/yr, cm/yr or cm–dm/yr ranges. Taking advantage of the complementary data available on the Norwegian Ground Motion Mapping Service InSAR Norway (Section 4.3), a mm/yr kinematic attribute is additionally assigned to 16 landforms. Over 50 % of the landforms remain undefined, 17 RS due to no exploitable data, and 45 RS due to superficial processes masking the potential signal from the rock mass (Figure 11, pie chart).

When comparing the InSAR-based kinematics with in-situ measurements for 20 RS (Section 3.2), we see that 15 RS fall into the expected categories, three are not comparable and two are mismatching. Two RS are inventoried in the cm/yr and cm–dm/yr categories: Jettan along Storfjord and Gámánjunni 3 in Manndalen. These are two high-risk objects continuously monitored, for which the InSAR-based categorization fits with monitoring data (1–3 cm/yr for Jettan and 3–10 cm/yr for Gámánjunni 3). Three RS are mostly under the 0.1 cm/yr detection limit, four RS have with mm/yr velocities and six RS have with mm–cm/yr velocities. Three landforms are not comparable due to undefined InSAR-based kinematics and for two others, there is a mismatch between the dGNSS and InSAR measurements. Falsnesfjellet 1 along Storfjord has < 0.1 cm/yr InSAR-based kinematics but a dGNSS-measured velocity of a few mm/yr. This case may indicate underestimation due to LOS measurements, but also highlights the different spatio-temporal properties of the dGNSS and InSAR measurements (Section 6.1). In Gámánjunni 1 in Manndalen, we find the opposite discrepancy between dGNSS and InSAR with no significant dGNSS movement but mm–cm/yr InSAR kinematics. This may indicate that the dGNSS measurements are not representative of the whole mass at these specific locations. Detailed maps showing the locations of the discussed RS are shown in supplementary material (Figure S1).

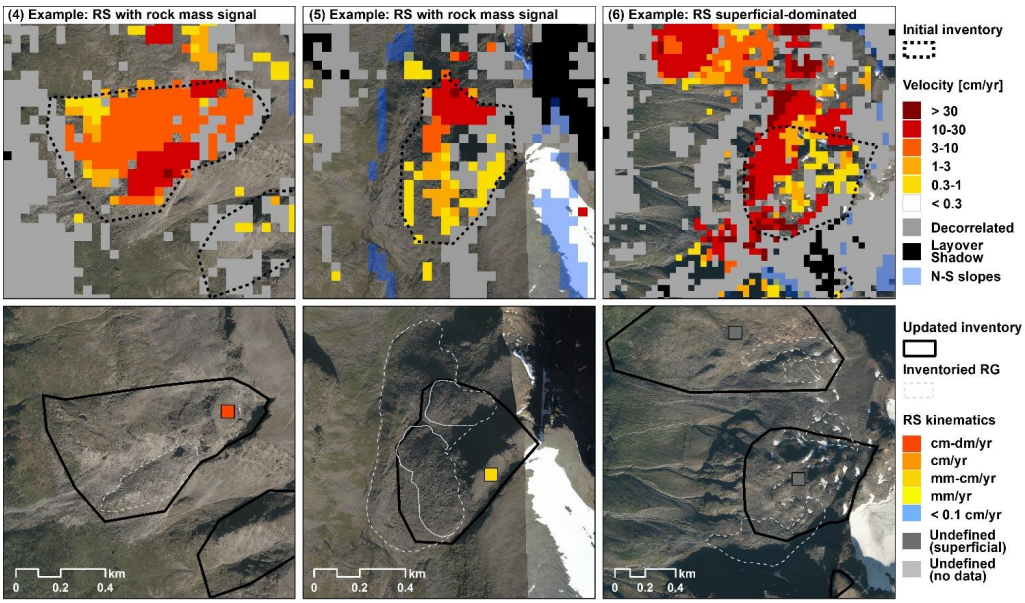

Figure 10. Update of the rockslide (RS) inventory. **(4–5)** Examples of composite landforms where the InSAR signal can reliably be attributed to the movement to the rock mass at specific locations (top rock plateaus). **(6)** Example of composite landform where the InSAR results are dominated by superficial processes masking the potential signal from the rock mass. Locations of these detailed maps are shown in Figure 11. *Norge i bilder* orthophoto from NMA (2020b).

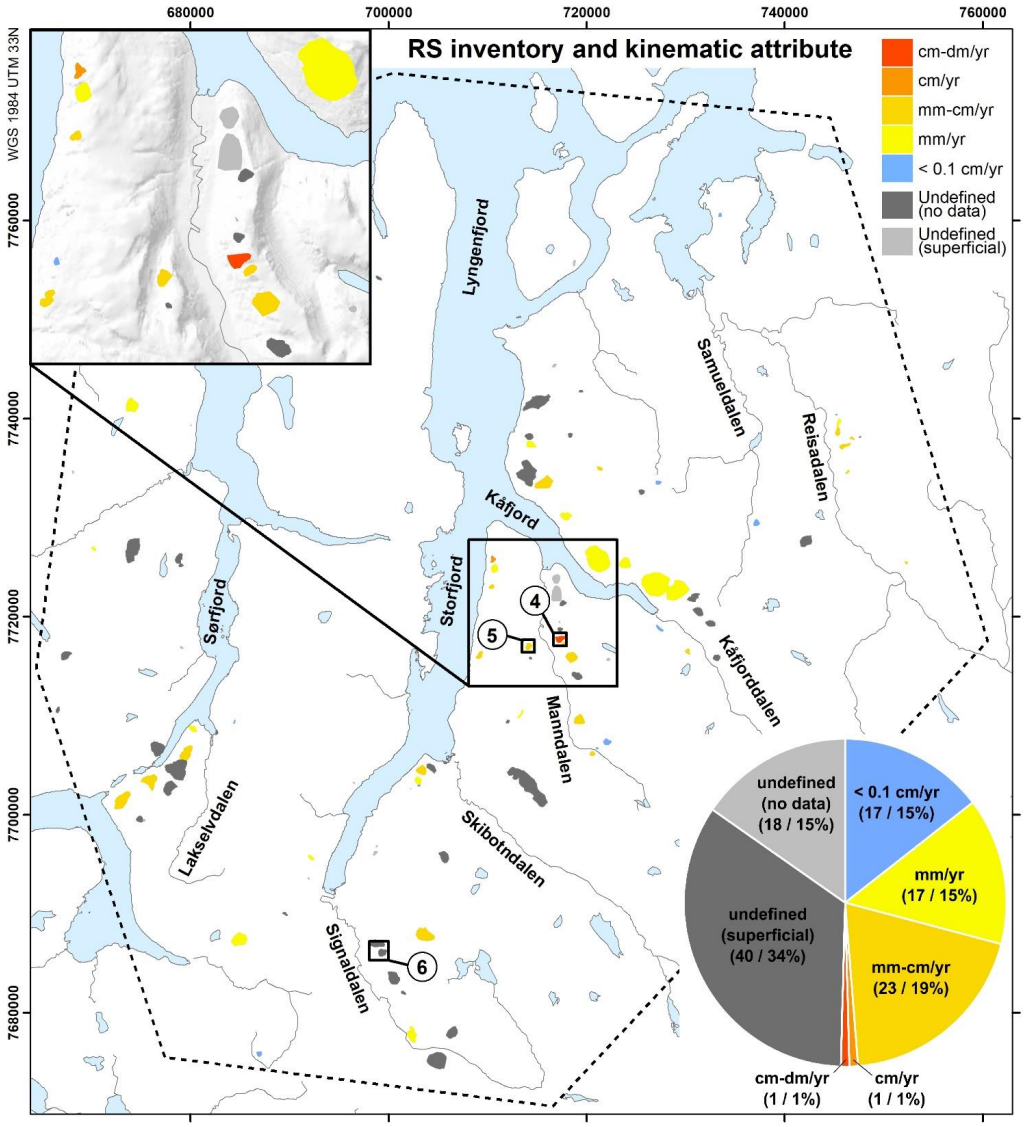

Figure 11. Updated rockslide (RS) inventory consisting of 117 landforms and variability of the kinematic attribute in the study area. Inset map (upper-left corner): detailed view over an area including several landforms with variable kinematic attributes. Pie chart (lower-right corner): kinematic attributes for all inventoried RS. Locations **(4–6)** are the examples shown in Figure 10. Sea, lakes, rivers and reference names from NMA (2020a).

6 Discussion

6.1 InSAR classified products: potential and limitations

Validation possibilities within the study are constrained by the few available complementary datasets. For rock glaciers and solifluction lobes, kinematic measurements have been performed based on a set of complementary optical and radar sensors. In Skibotndalen, Kåfjord, Manndalen and Nordnes, the documented rates are in agreement with our results (Eriksen et al., 2017a; 2017b; 2018). When comparing the InSAR-based kinematics with in-situ data for 20 RS, we identified two cases where dGNSS velocities and InSAR-based kinematics do not match. One cause of mismatch is that InSAR is likely to underestimate the movement rate if the displacement vector significantly deviates from the LOS orientation. For low velocity landforms, this can typically be interpreted as not moving, although a few mm/yr are measured by dGNSS. Another reason is that InSAR provides averaged values over 40 m pixels based on snow-free periods only, while dGNSS data are point measurements based on the entire year. If the movement is heterogenous over the landform or if the dGNSS point is not representative of the whole mass, the remotely sensed and in-situ measurements may document different elements of the landform. If the seasonal patterns lead to a velocity decrease in winter, InSAR measures would provide a higher averaged value than dGNSS. Despite these elements, we could see that 15 out of 17 comparable RS are similarly categorized, which is considered as acceptable given the differences of measurement properties.

There are however five limitations that need to be further discussed:

1. The results are presented as annual velocities for all landforms although the results are based on snow-free images only. Seasonal variations are expected, especially for landforms driven by ground freeze/thaw processes (Gruber, 2020). On slopes, the gravitational downslope displacement of material can be combined with cyclic processes (frost heave and thaw subsidence, e.g. on solifluction lobes, Harris et al., 2008). Rock glaciers have strong intra-annual velocity variations, with acceleration and deceleration that can sometimes exceed 50% of the annual average (Delaloye and Staub, 2016). These seasonal patterns are driven by changes in temperature and water supply (Cicoira et al., 2019; Kenner et al., 2017). Velocity variations of rockslide are typically comparatively smaller and more spread over the year as many external drivers may impact the strength degradation, internal shearing and progressive failure of rock bridges (Eberhardt et al., 2016), although seasonal influence in relation with freeze/thaw cycles has also been evidenced in periglacial environment (Blikra and Christiansen, 2014; Keuschnig et al., 2015). Based on InSAR, the differentiation of gravitational/irreversible and seasonal/reversible components of the movement and the quantification of the seasonal variations of velocity can be performed by analysing time series (Dini et al., 2019; Rouyet et al., 2019; Strozzi et al., 2020). This was beyond the scope of the current study, focusing on the inventory, the analysis of distribution and the relative comparison of movement magnitude. It is however important to keep in mind that the kinematics may be overestimated on landforms accelerating in summer.
2. When considering only E-W slopes (compass directions 22.5–257.5°/202.5–227.5°), the fraction of areas documented by moving pixels slightly increases (ca. 3 %), while class 0 (< 0.3 cm/yr) decreases (ca. 70 %) (Section 5.1). This shows that the velocity is underestimated on N-S facing slopes due the measurements along LOS, which justify the use of the N-S mask to highlight parts of the landscape with lower reliability. It should however be noted that the applied thresholds (compass directions 22.5–257.5°/202.5–227.5°) are not exhaustively masking out all areas where a N-S movement component can occur, as NE, NW, SE and SE slope orientations are still included. For a better documentation of the true displacement vector, multi-geometry methods can be applied (e.g. Eckerstorfer et al., 2018; Eriksen et al., 2017a; Rouyet et al., 2019).

3. The multiple temporal baseline InSAR stacking procedure has a detection limit of 0.3 cm/yr that is not fully optimised for the relative slow velocity of the rockslides (Section 5.3). The Norwegian Ground Motion Mapping Service (InSAR Norway) with submillimetric detection capability is more adapted for slow-moving processes, and higher-resolution PSI-based results also improve the identification of small areas not affected by superficial processes. Conversely, InSAR Norway is not designed for velocities over cm–dm/yr, which shows the importance of combining different InSAR processing techniques for documenting all expected landform types (e.g. Barboux et al., 2015; Lauknes, 2010a).
4. Although 20 new RS were included in the inventory based on InSAR detected movement, the kinematics could not be reliably determined for 16 of them due the presence of superficial processes likely to have dominated the InSAR signal (Section 5.3). It highlights that remote sensing information has always to be treated carefully when applied in complex environments encompassing a large range of processes, partly overlapping. The technique measures surface movements, that is not necessarily caused by the process one specific user is interested in. In the case of rockslides, the results have still been valuable to identify hotspots, later interpreted as including a deep rock deformation mechanism. Even if not kinematically assigned, these sites may be further investigated by geologists in the future, especially where high risk for population and infrastructure is assessed.
5. A kinematic approach is not standalone when inventorying periglacial landforms. This is especially obvious when considering relict RG or very slow RS that could not have been detected based on InSAR only. The results show the value of combining morphological and kinematic information to document slope processes.

6.2 InSAR kinematic inventory and categorized landforms

The kinematic inventory shows that the velocity ranges and spatial distribution of the different types of slope processes vary greatly within the study area (Section 5.1). The solifluction/cryoturbation (SC) category is the dominant landform type in the study area (47 % of the 763 identified moving areas), which is as expected in a region at the interface between seasonal frost and isolated to discontinuous permafrost. Solifluction can be found below the limit for discontinuous permafrost, but usually above the limit of sporadic permafrost, i.e. 500–800 m a.s.l in Kåfjord area (Hjort et al., 2014). The identified SC moving areas are widely distributed in the eastern part of the study area, towards the Finnish and Swedish borders, where the altitude of the permafrost limit decreases and the average elevation of the flat-topped terrain is ca. 600–1000 m a.s.l. Velocities within the 0.3–1 cm/yr and 1–3 cm/yr classes are dominating the SC category, which is in the expected range for mountainous and subarctic areas (Gruber, 2020; Smith, 1987; Matsuoka, 2001). Similar velocities have been documented by two-dimensional TerraSAR-X InSAR results in the same region (Nordnesfjellet, South of Kåfjord) (Eriksen et al., 2017a).

The composite (CO) category is the second largest identified in the area (18%), comprising combination of rockslides, rock glaciers and superficial processes (RS+RG, RS+S, RG+S). The high frequency of these co-occurring landforms highlights the challenge and complexity of interpreting ground movement in a highly dynamic region. The co-occurrence of these objects infers some degree of interaction, for example in the case of the combination of rockslide and rock glacier (RS+RG). It indicates that fractured/disaggregated rock material and rock fall deposits in RS inventoried areas contribute to feed rock glaciers. Sediment input is recognized as an important controlling factor of the rock glacier dynamics (Delaloye et al., 2013; Müller et al., 2016). Rock slope deformation within the permafrost zone may favour the development/preservation of rock glaciers, which emphasizes the general co-dependency of landform genesis in peri-/paraglacial landscapes (Ballantyne, 2002; Luckmann, 2017; Wilson, 2009). The CO RS+RG category encompasses a large range of velocity,

mostly > 3 cm/yr, similarly to the standalone RG category, while RS has clearly lower rates. This shows that for composite landforms, RG tends to mask out the signal from the rock mass and the remotely sensed information is dominated by the movement from more superficial processes. Interestingly, velocity rates for CO RS+RG are also slightly higher than the standalone RG category, which seems to indicate that the presence of a deep rock deformation has an influence on rock glacier dynamics.

Talus/scree deposits (TS) are distributed as expected on the steepest slopes in the area. Although InSAR is not able to detect abrupt rockfall and avalanche occurring almost instantaneously and leading to decorrelation, the gradual displacement of the sediments over the deposits themselves can be captured (mostly 0.3–3 cm/yr). The glaciers/moraines (GM) category includes only 24 landforms, which can easily be explained by the loss of InSAR coherence (decorrelation) on debris-free glacial surfaces (due to snow, ice melt and/or too fast movement) and perennial snow largely present at the considered altitudes. The documented GM are moving at high rates (mostly 10–30 cm/yr or >30 cm/yr). They are mainly located in the Lyngen peninsula, which is characterized by the highest elevations of the study area and influenced by large glacier systems (Andreassen and Winsvold, 2012; Winsvold et al., 2014). The category includes debris-covered glaciers and ice-cored moraines for which the detected movement is possibly caused by a combination of processes (glacial flow, ice melt, creep/superficial erosion and debris redistribution). On debris-covered glaciers, the measurements do not necessarily represent the glacial flow, but may include a significant vertical component (subsidence due to ice melt) (Thompson et al., 2016).

6.3 Rock glaciers and rockslides: distribution and controlling factors

By focusing on two specific types of periglacial previously inventoried landforms in the study area, the advantages of both a morphological and a kinematic approach have been combined (Sections 5.2–5.3). The updated inventories allow for studying the relations between the landform distribution, the kinematics and the topo-climatic factors. The mean elevation and the creep rate of the inventoried rock glacier (RG) increase toward the continental interior (Figure 12A). The western and central parts of the area are dominated by relict RG (kinematic attribute < 0.3 cm/yr), located at low altitude. The highest parts of the terrain are either permafrost-free (e.g. in the westernmost part of the study area), or occupied by large glacial systems (e.g. Lyngen peninsula). The occurrence of active landforms increases towards SE. Most of the active landforms have over 600 m a.s.l mean elevation. A cluster of active RG with kinematics between cm/yr and m/yr is found 65–85 km along a NW–SE profile following the continental gradient. These RG are mostly located above 800 m a.s.l. (Figure 12A) This corresponds to the area East from Storfjord-Lyngenfjord, where permafrost limit has been reported at similar elevations (Farbrot et al., 2013; Gisnås et al., 2017). A similar cluster is found for the rockslides (RS) (Figure 12B), but the elevation/continentality trend is less pronounced, which indicates that the distribution of these landforms is likely controlled by other factors. Most of RS with mean elevation over 800 m a.s.l remain undefined kinematically, mostly due the dynamics of superimposed periglacial processes that mask out the movement of the rock mass, such as RG. The analysis of the mean slope angle and slope orientation highlight a cluster of RG and RS landforms on west-facing slopes (Figure 12, C–D). Low-angled RG are mostly relict (kinematic attribute < 0.3 cm/yr) (Figure 12C).

The control of geological factors is studied by analysing the proportion of inventoried landforms within the major lithology types, based on a geological map from the Geological Survey of Norway (NGU, 2020a; Zwaan, 1988; Zwaan et al., 1998). For sake of simplification, the initial map has been divided into three main categories based on their lithologies and the assumed strength of the rock mass, inspired by the classification applied in Erener et al. (2010): 1) massive rocks (such as gabbro, tonalite and peridotite), 2) strongly foliated rocks (such as mica shist, quartz schist and phyllite), and 3) weakly foliated rocks (such as marble, metasandstone and quartzite) (Figure 13A). Comparing the fraction of

landforms falling into each geological category with the overall distribution in the land area, we see that both RG and RS are clearly over-represented in strongly foliated rocks (Figure 13B). This category corresponds to 40% of the land area, but 283 RG units (68% of the inventoried sites) and 90 RS (77% of the inventoried sites) take place in this rock type. The mean slope orientation at the sites is also analysed, which highlights an over-representation of landforms on west-facing slopes (225–315° compass dip direction). While 28% of the land area have a W-orientation, 249 RG units (60 %) and 70 RS (60 %) are represented in this category. This can indicate a topo-climatic influence, but is also consistent with the general architecture of trusted nappe complex, controlling the orientation of the dominant foliation, the major faults, joints and shear zones (Figure 13A, black lines). It is in line with the documented evidence of structural control of rock slope deformation in the area (Blikra et al., 2006; Braathen et al., 2004; Bunkholt et al., 2012; Osmundsen et al., 2009; Vick et al., 2020). It also concurs with the conclusions on other studies highlighting the significance of geological preconditioning factors in the development of both on rock glaciers (Falaschi et al., 2014; Johnsen et al., 2007; Onaca et al., 2017) and rockslides (Crosta et al., 2013; Dini et al., 2020; Pedrazzini et al., 2016; Stead and Wolter, 2015).

Here we proposed a first attempt of discussion about the distribution, dynamics and controlling factors of RG and RS in Northern Norway, focusing on climatic, topographic and geological variables. The updated regional inventories including a kinematic information constitute a new valuable dataset to be exploited in future studies about the controls of slope processes in subarctic environments. Comprehensive rock glaciers inventories can be further used to complement the kilometric global permafrost products (Obu et al., 2019) and refine the mapping of permafrost zones in mountainous regions, as also discussed by Marcer et al. (2017) and Colucci et al. (2019). The relationship between environmental factors, landform distribution and movement rates can bring forward our understanding of geomorphological processes in cryo-conditioned landscapes. It may provide complementary datasets to constrain or validate landscape evolution modelling (Hilger et al., 2021; Lilleøren et al., 2012). Analysing jointly RG and RS distribution and kinematics may also highlight new findings about the significance of composite landforms and combined processes in mountainous landscapes.

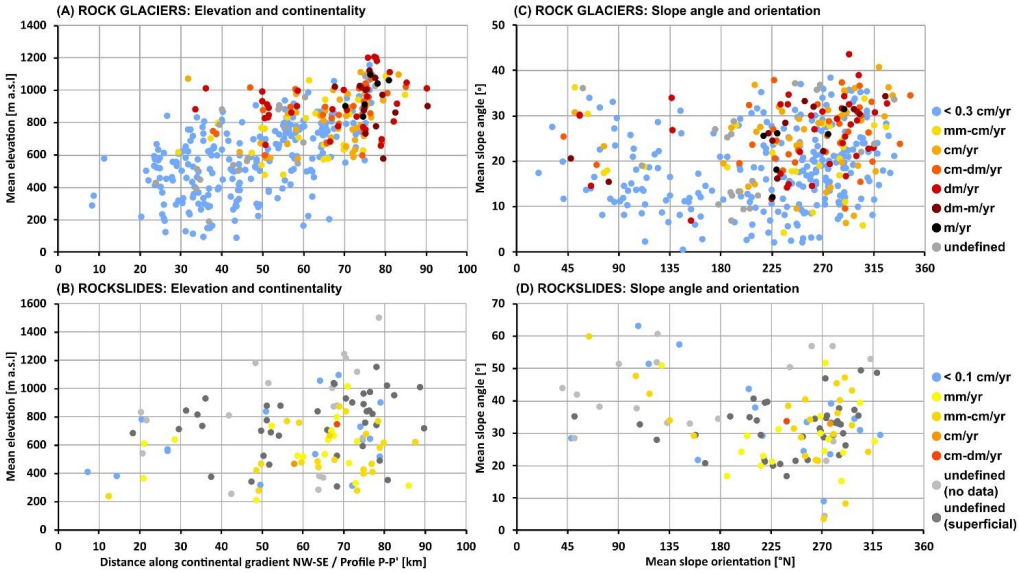

Figure 12. RG/RS distribution and topo-climatic factors. Left: Relation between kinematic attribute, mean elevation and continentality for the inventoried RG **(A)** and RS **(B)**. X-axis: Distance along NW–SE continental gradient (landforms projected along profile P-P', Figure 1). Right: Relation between kinematic attribute, slope angle and slope orientation for the inventoried RG **(C)** and RS **(D)**. Mean elevation, slope angle and orientation are based on a 10 m DEM (NMA, 2016).

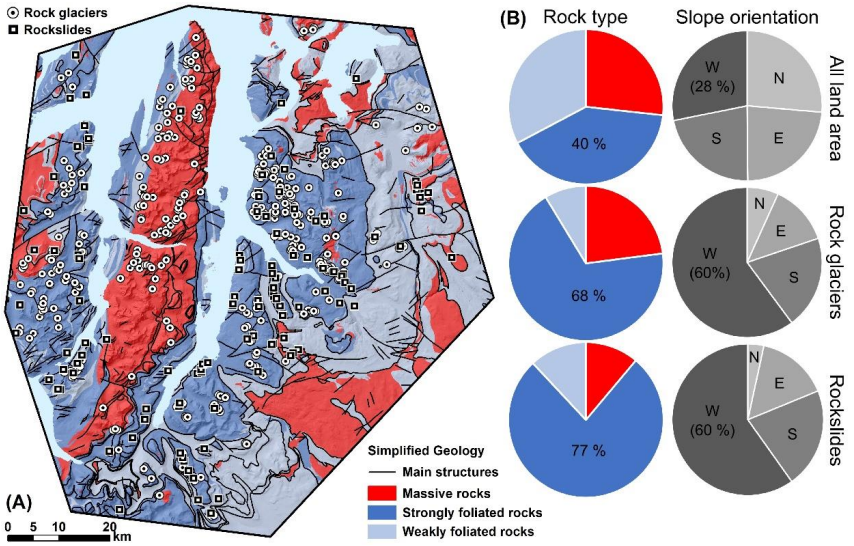

Figure 13. RG/RS distribution and geological factors. **(A)** Simplified geology map, classified into three main rock types (massive, strongly foliated and weakly foliated) and structural information (major faults, joints and shear zones) from a 1:250 000 geological map of the area (NGU, 2020a; Zwaan, 1988; Zwaan et al., 1998). **(B)** Pie charts comparing the fraction of rock type and slope orientation for all land areas and RG/RS landforms. Slope orientation is based on a 10 m DEM (NMA, 2016).

7 Conclusion

In this study, we developed semi-quantitative classified InSAR products to summarize kinematic information about slope movement and investigated periglacial processes in a mountainous area of Northern Norway. The methodology combines some of the strengths of commonly used InSAR techniques, to semi-automate the analysis, identify moving areas and cover a large range of ground velocities. Although the procedure takes benefit of a large set of satellite images, it summarizes several velocity maps into high order products easily exploitable by nonexperts. Complementing six velocity classes with three additional layers emphasizes the main typical InSAR limitations in mountainous environments and allows for differentiating the areas where there is no or little movement, areas with no data and those where the available information must be threated carefully. Based on the results, three main conclusions can be drawn:

1. Moving areas were identified and categorized by landform types (rock glaciers, rockslide, glaciers/moraines, talus/scree deposits, solifluction/cryoturbation and composite landforms). The InSAR kinematic inventory shows that the velocity ranges and spatial distribution of the different types of slope processes vary greatly within the study area.
2. InSAR products contributed to update the existing inventories of rock glaciers and rockslides. Delineations and units' division were refined, and newly detected landforms (54 rock glaciers and 20 rockslides) included in the databases. The updated inventories consist of 414 rock glacier units within 340 systems and 117 rockslides. A kinematic attribute documenting the magnitude order of the mean annual ground velocity was assigned to each inventoried landform.
3. Topo-climatic factors control the spatial distribution of the rock glaciers. Mean elevation of the rock glaciers increases towards the continental interior with a dominance of relict landforms in the NW and an increase of active landforms' occurrence towards the SE. Rock glaciers and rockslides are mostly located on W-facing slopes and in areas characterized by strongly foliated rocks. This distribution highlights the importance of geological preconditioning controls for both landform types.

Our study emphasizes the complementarity of kinematic and morphological approaches for the inventory of slope processes in complex periglacial environments. It shows the value of simplifying complex InSAR datasets for geoscientific applications. With the development of national to multi-national InSAR mapping services, the ability to identify moving areas over entire mountain ranges is dramatically increasing. However, relating the movements to their causes remains a challenging task at large scale, due to the variety of processes occurring in mountainous regions and the combination of landforms at similar locations, such as rock glaciers and scree deposits overlying or spatially connected to rockslides. Further research towards a more comprehensive use of InSAR to categorize the ground velocity and relate detected moving areas to specific landforms is needed to scale up the exploitation of InSAR for geomorphological studies, cryospheric science and geohazard management.

8 Conflict of Interest

The authors declare that the research was conducted in the absence of any commercial or financial relationships that could be construed as a potential conflict of interest.

9 Author Contributions

LR, LHB and TRL discussed and developed the original idea. LR processed the InSAR results, with contribution from YL. LR analysed the InSAR inventory and updated the inventories, with contributions from KL, MB and RD. RD leads the IPA Action Group 'Rock glacier inventories and kinematics', defining international recommendations towards standardized rock glacier inventories. KL and MB led the development of the initial inventories. MB compiled the dGNSS data. LR led the interpretation and manuscript writing. KL, RD and BE contributed to the discussion related to rock glaciers. MB, LV and LHB contributed to the discussion related to rockslides. YL and TRL contributed to the discussion of InSAR results. All co-authors have commented on the manuscript.

10 Funding

LR PhD study is funded by the Research Council of Norway (FrostInSAR project nr. 263005). The kinematic inventory and update of the rock glacier inventory has been supported by the ESA Climate Change Initiative (CCI) Permafrost CCN2 project (4000123681/18/I-NB) (https://climate.esa.int/en/projects/permafrost/). The development of the GSAR processing chain and previous research applying InSAR in periglacial environments have been supported by the Norwegian Space Centre, the Research Council of Norway (project nr. 212022) and the European Space Agency (project nr. 4000106830 and 4000119115).

11 Acknowledgments

We acknowledge the whole CCI Permafrost team for its work on delivering remotely sensed ECV products documenting permafrost state. We are grateful to the International Permafrost Association for its support to the Action Group 'Rock glacier inventories and kinematics', which is defining international recommendations towards standardized rock glacier inventories and time series of permafrost creep rate as climate change indicator (https://www3.unifr.ch/geo/geomorphology/en/research/ipa-action-group-rock-glacier/). Sentinel-1 scenes were provided by the EU Copernicus data service (2015–2019). We thank Henrik Sandbakken and the students of the SGG.00251 UNIFR course for commenting on an early version of the manuscript.

12 Data Availability Statement

The InSAR classified results, the InSAR kinematic inventory categorized by landform type, as well as the rock glacier and rockslide inventories are available in Pangaea: https://doi.pangaea.de/10.1594/PANGAEA.930856. Additional data sources used in this study are listed in the references, included in the figures and tables, or in the supporting information associated with the publication.

13 References

Andreassen, L. M., and Winsvold S. H. (2012). Inventory of Norwegian glaciers. *NVE Report 38*, 236 pp, Norges Vassdrags- og Energidirektorat. http://publikasjoner.nve.no/rapport/2012/rapport2012_38.pdf.

Augland, L. E., Andresen, A., Gasser, D., and Steltenpohl, M. G. (2014). Early Ordovician to Silurian evolution of exotic terranes in the Scandinavian Caledonides of the Ofoten–Troms area–terrane characterization and correlation based on new U–Pb zircon ages and Lu–Hf isotopic data. *Geological Society, London, Special Publications* 390(1), 655–678. https://doi.org/10.1144/SP390.19.

Ballantyne, C. K. (2002). A general model of paraglacial landscape response. *The Holocene* 12(3), 371–376. https://doi.org/10.1191/0959683602hl553fa.

Ballantyne, C. K. (2018). *Periglacial geomorphology*. John Wiley & Sons.

Baran, I., Stewart, M. P., Kampes, B. M., Perski, Z., and Lilly, P. (2003). A modification to the Goldstein radar interferogram filter. *IEEE T. Geosci. Remote* 41(9), 2114–2118. https://doi.org/10.1109/TGRS.2003.817212.

Barboux, C., Delaloye, R., and Lambiel, C. (2014). Inventorying slope movements in an Alpine environment using DInSAR. *Earth Surf. Process. Land.* 39(15), 2087–2099. https://doi.org/10.1002/esp.3603.

Barboux, C., Strozzi, T., Delaloye, R., Wegmüller, U., and Collet, C. (2015). Mapping slope movements in Alpine environments using TerraSAR-X interferometric methods. *ISPRS J. Photogramm.* 109, 178–192. https://doi.org/10.1016/j.isprsjprs.2015.09.010.

Berardino, P., Fornaro, G., Lanari, R., and Sansosti, E. (2002). A new algorithm for surface deformation monitoring based on small baseline differential SAR interferograms. *IEEE T. Geosci. Remote* 40(11), 2375–2383. https://doi.org/10.1109/TGRS.2002.803792.

Bergh, S. G., Eig, K., Kløvjan, O. S., Henningsen, T., Olesen, O., and Hansen, J. A. (2007). The Lofoten-Vesterålen continental margin: a multiphase Mesozoic-Palaeogene rifted shelf as shown by offshore-onshore brittle fault-fracture analysis. *Norw. J. Geol.* 87(1), 29–58.

Berthling, I. (2011). Beyond confusion: Rock glaciers as cryo-conditioned landforms. *Geomorphology* 131, 98–106. https://doi.org/10.1016/j.geomorph.2011.05.002.

Blikra, L. H., Longva, O., Braathen, A., Anda, E., Dehls, J. F., and Stalsberg, K. (2006). Rock slope failures in Norwegian Fjord areas: examples, spatial distribution and temporal pattern. *Landslides Massive Rock Slope Fail.* 475–496. https://doi.org/10.1007/978-1-4020-4037-5_26.

Blikra, L. H., Henderson, I., and Nordvik, T. (2009). Faren for fjellskred fra Nordnesfjellet i Lyngenfjorden, Troms [In Norwegian]. *NGU report 2009.026*. Geological Survey of Norway. https://hdl.handle.net/11250/2664691.

Blikra L. H., and Kristensen, L. (2013). "Monitoring concepts and requirements for large rockslides in Norway", in *Landslide Science and Practice* (Springer, Berlin, Heidelberg), 193–200. https://doi.org/10.1007/978-3-642-31445-2_25.

Blikra, L. H., and Christiansen, H. H. (2014). A field-based model of permafrost-controlled rockslide deformation in northern Norway. *Geomorphology* 208, 34–49. https://doi.org/10.1016/j.geomorph.2013.11.014.

Blikra, L. H., Christiansen, H. H., Kristensen, L., and Lovisolo, M. (2015). "Characterization, geometry, temporal evolution and controlling mechanisms of the Jettan Rock-Slide, Northern Norway", in *Engineering Geology for Society and Territory, Volume 2* (Springer, Cham), 273–278.

Bodin, X., Krysiecki, J. M., Schoeneich, P., Le Roux, O., Lorier, L., Echelard, T., Peyron, M., and Walpersdorf, A. (2017). The 2006 Collapse of the Bérard rock glacier (southern French Alps). *Permafrost Periglac.* 28(1), 209–223. https://doi.org/10.1002/ppp.1887.

Bouali, E.H., Oommen, T. and Escobar-Wolf, R. (2018). Mapping of slow landslides on the Palos Verdes Peninsula using the California landslide inventory and persistent scatterer interferometry. *Landslides* 15(3), 439–452. https://doi.org/10.1007/s10346-017-0882-z.

Braathen, A., Blikra, L. H., Berg, S. S., and Karlsen, F. (2004). Rock-slope failures in Norway; type, geometry, deformation mechanisms and stability. *Norw. J. Geol.* 84, 67–88.

Bunkholt H., Redfield T. F., Osmundsen, P. T., Oppikofer, T., Hermanns, R. L., and Dehls, J. F. (2012). "Landslide processes in hard rock in Troms, Norway", in *Landslides and Engineered slopes*, eds E. Eberhardt, C. Froese, K. Turner, K. (CRC, Canada), 855–861.

Böhme, M., Bunkholt, H., Dehls, J., Oppikofer, T., Hermanns, R., Dalsegg, E., Kristensen, L., Lauknes, T. R., and Eriksen, H. Ø. (2016). Geologisk modell og fare-og risikoklassifisering av det ustabile fjellpartiet Gamanjunni 3 i Manndalen, Troms [in Norwegian]. *NGU report 2016.031*. Geological Survey of Norway. https://hdl.handle.net/11250/2664288.

Böhme M., Hermanns, R. L., Gosse J., Hilger, P., Eiken, T., Lauknes, T. R., and Dehls, J. F. (2019). Comparison of monitoring data with paleo–slip rates: cosmogenic nuclide dating detects acceleration of a rockslide. *Geology* 47, 1–4. https://doi.org/10.1130/G45684.1/4655152/g45684.pdf.

Cavalié, O., Doin, M. P., Lasserre, C., and Briole, P. (2007). Ground motion measurement in the Lake Mead area, Nevada, by differential synthetic aperture radar interferometry time series analysis: Probing the lithosphere rheological structure. *J. Geophys. Res.-Sol. Ea.* 112(B3). https://doi.org/10.1029/2006JB004344.

Chen, C., and Zebker, H. A. (2002). Phase unwrapping for large SAR interferograms: Statistical segmentation and generalized network models. *IEEE T. Geosci. Remote* 40(8), 1709–1719. https://doi.org/10.1109/TGRS.2002.802453.

Christiansen, H. H., Etzelmüller, B., Isaksen, K., Juliussen, H., Farbrot, H., Humlum, O., et al. (2010). The thermal state of permafrost in the Nordic area during the International Polar Year 2007–2009. *Permafrost Periglac.* 21(2), 156–181. https://doi.org/10.1002/ppp.687.

Cicoira, A., Beutel, J., Faillettaz, J. and Vieli, A. (2019). Water controls the seasonal rhythm of rock glacier flow. *Earth and Planetary Science Letters* 528, 115844. https://doi.org/10.1016/j.epsl.2019.115844.

Colucci, R. R., Forte, E., Žebre, M., Maset, E., Zanettini, C., and Guglielmin, M. (2019). Is that a relict rock glacier? *Geomorphology* 330, 177–189. https://doi.org/10.1016/j.geomorph.2019.02.002.

Corner, G. D. (2005). "Scandes Mountains", in *The physical geography of Fennoscandia*, ed M. Seppälä (Oxford University Press), p. 468.

Crosta, G. B., Frattini, P., and Agliardi, F. (2013). Deep seated gravitational slope deformations in the European Alps. *Tectonophysics* 605, 13–33. https://doi.org/10.1016/j.tecto.2013.04.028.

Dehls, J. F., Larsen, Y., Marinkovic, P., Lauknes, T.R., Stødle, D., and Moldestad, D. A. (2019). "INSAR.No: A National Insar Deformation Mapping/Monitoring Service In Norway -- From Concept To Operations", in *Proceedings of IGARSS 2019*, IEEE International Geoscience and Remote Sensing Symposium, 5461–5464. https://doi.org/10.1109/IGARSS.2019.8898614.

Delaloye, R., Lambiel, C., Lugon, R., Raetzo, H., and Strozzi, T. (2007). "Typical ERS InSAR signature of slope movements in a periglacial mountain environment (Swiss Alps)", in *Proceedings Envisat Symposium 2007*, Montreux, Switzerland, 23–27 April 2007 (ESA SP-636, July 2007), 3P7.

Delaloye, R., Lambiel, C., and Gärtner-Roer, I. (2010). Overview of rock glacier kinematics research in the Swiss Alps. *Geographica Helvetica* 65(2), 135–145. https://doi.org/10.5194/gh-65-135-2010.

Delaloye, R., Morard, S., Barboux, C., Abbet, D., Gruber, V., Riedo, M., and Gachet, S. (2013). "Rapidly moving rock glaciers in Mattertal", in *Mattertal–ein Tal in Bewegung, Publikation zur Jahrestagung der Schweizerischen Geomorphologischen Gesellschaft*, ed C. Graf, 29, 21–31.

Delaloye, D., and Staub, B. (2016). "Seasonal variations of rock glacier creep: time series observations from the Western Swiss Alps", in *Proceedings of the XI. International Conference on Permafrost*, 20–24 June 2016, Potsdam, Germany.

Delaloye, D., Lambiel, C., Staub, B., Kummert, M., Morra di Cella, U., and Pogliotti, P. (2017). Accelerating versus decelerating rock glaciers in the context of ongoing climate warming, *Asian Conference on Permafrost*, 2–6 July 2017, Sapporo, Japan.

Dini, B., Daout, S., Manconi, A., and Loew, S. (2019). Classification of slope processes based on multitemporal DInSAR analyses in the Himalaya of NW Bhutan. *Remote Sens. Environ.* 233. 111408. https://doi.org/10.1016/j.rse.2019.111408.

Dini, B., Aaron, J., Manconi, A., De Palezieux, L., Leith, K., and Loew, S. (2020). Regional-Scale Investigation of Preconditioning Factors of Rock Slope Instabilities in NW Bhutan. *J. Geophys. Res.-Earth* 125(9), e2019JF005404. https://doi.org/10.1029/2019JF005404.

Eberhardt, E., Preisig, G., and Gischig, V. (2016). "Progressive failure in deep-seated rockslides due to seasonal fluctuations in pore pressures and rock mass fatigue", in *Landslides and Engineered Slopes. Experience, Theory and Practice*, Proceedings of the 12th International Symposium on Landslides, 121–136, 12–19 June 2016, Napoli, Italy.

Eckerstorfer, M., Eriksen, H. Ø., Rouyet, L., Christiansen, H. H., Lauknes, T. R., and Blikra, L. H. (2018). Comparison of geomorphological field mapping and 2D-InSAR mapping of periglacial landscape activity at Nordnesfjellet, northern Norway. *Earth Surf. Process. Land.* 43(10), 2147–2156. https://doi.org/10.1002/esp.4380.

Erener, A., and Düzgün, H. S. B. (2010). Improvement of statistical landslide susceptibility mapping by using spatial and global regression methods in the case of More and Romsdal (Norway). *Landslides* 7(1), 55–68. https://doi.org/10.1007/s10346-009-0188-x.

Eriksen, H. Ø., Lauknes, T. R., Larsen, Y., Corner, G. D., Bergh, S. G., Dehls, J., and Kierulf, H. P. (2017a). Visualizing and interpreting surface displacement patterns on unstable slopes using multi-geometry satellite SAR interferometry (2D InSAR). *Remote Sens. Environ.* 191, 297–312. https://doi.org/10.1016/j.rse.2016.12.024.

Eriksen, H. Ø., Bergh, S. G., Larsen, Y., Skrede, I., Kristensen, L., Lauknes, T. R., Blikra, L. H., and Kierulf, H. P. (2017b). Relating 3D surface displacement from satellite-and ground-based InSAR to structures and geomorphology of the Jettan rockslide, northern Norway. *Norw. J. Geol.* 97(4), 283–303. https://doi.org/10.17850/njg97-4-03.

Eriksen, H. Ø., Rouyet, L., Lauknes, T. R., Berthling, I., Isaksen, K., Hindberg, H., Larsen, Y. and Corner, G. D. (2018). Recent acceleration of a rock glacier complex, Ádjet, Norway, documented by 62 years of remote sensing observations. *Geophys. Res. Lett.* 45(16), 8314–8323. https://doi.org/10.1029/2018GL077605.

Etzelmüller, B., Patton, H., Schomacker, A., Czekirda, J., Girod, L., Hubbard, A., Lilleøren, K. S., and Westermann, S. (2020). Icelandic permafrost dynamics since the Last Glacial Maximum–model results and geomorphological implications. *Quaternary Science Reviews* 233, 106236. https://doi.org/10.1016/j.quascirev.2020.106236.

Falaschi, D., Castro, M., Masiokas, M., Tadono, T., and Ahumada, A. L. (2014): Rock glacier inventory of the Valles Calchaquíes region (~ 25 S), Salta, Argentina, derived from ALOS data. *Permafrost Periglac.* 25(1), 69–75. https://doi.org/10.1002/ppp.1801.

Farbrot, H., Isaksen, K., and Etzelmüller, B. (2008). "Present and past distribution of mountain permafrost in Gaissane Mountains, Northern Norway", in *Proceedings of the Ninth International Conference on Permafrost*, Vol. 1, 427–432, Fairbanks, U.S.A.

Farbrot, H., Isaksen, K., Etzelmüller, B., and Gisnås, K. (2013). Ground thermal regime and permafrost distribution under a changing climate in northern Norway. *Permafrost Periglac.* 24(1), 20–38. https://doi.org/10.1002/ppp.1763.

Ferretti, A., Prati, C., and Rocca, F. (2001). Permanent scatterers in SAR interferometry. *IEEE T. Geosci. Remote* 39(1), 8–20. https://doi.org/10.1109/36.898661.

French, H. M. (2007). *The Periglacial Environment, Third Edition*. John Wiley & Sons, Ltd. https://doi.org/10.1002/9781118684931.

Geertsema, M., Clague, J. J., Schwab, J. W., and Evans, S. G. (2006). An overview of recent large catastrophic landslides in northern British Columbia, Canada. *Eng. Geol.* 83(1-3), 120–143. https://doi.org/10.1016/j.enggeo.2005.06.028.

Gisnås, K., Etzelmüller, B., Farbrot, H., Schuler, T. V., and Westermann, S. (2013). CryoGRID 1.0: Permafrost distribution in Norway estimated by a spatial numerical model. *Permafrost Periglac.* 24(1), 2–19. https://doi.org/10.1002/ppp.1765.

Gisnås, K., Etzelmüller, B., Lussana, C., Hjort, J., Sannel, A. B. K., Isaksen, K., et al. (2017). Permafrost map for Norway, Sweden and Finland. *Permafrost Periglac.* 28(2), 359–378. https://doi.org/10.1002/ppp.1922.

Goldstein, R. M., and Werner, C. L. (1998). Radar interferogram filtering for geophysical applications. *Geophysical Res. Lett.* 25(21), 4035–4038. https://doi.org/10.1029/1998GL900033.

Gruber, S., and Haeberli, W. (2009). "Mountain permafrost", in *Permafrost soils* (Springer, Berlin, Heidelberg), 33–44. https://doi.org/10.1007/978-3-540-69371-0_3.

Gruber, S. (2020): Ground subsidence and heave over permafrost: hourly time series reveal interannual, seasonal and shorter-term movement caused by freezing, thawing and water movement. *The Cryosphere* 14(4). https://doi.org/10.5194/tc-14-1437-2020.

Harris, C., Kern-Luetschg, M., Murton, J., Font, M., Davies, M., and Smith, F. (2008). Solifluction processes on permafrost and non-permafrost slopes: results of a large-scale laboratory simulation. *Permafrost Periglac.* 19(4), 359–378. https://doi.org/10.1002/ppp.630.

Hermanns, R., Oppikofer, T., Anda, E., Blikra, L., Böhme, M., Bunkholt, H., et al. (2013). Hazard and risk classification for large unstable rock slopes in Norway. *Italian Journal of Engineering Geology and Environment, Book Series 6*, 245–254. http://dx.doi.org/10.4408/IJEGE.2013-06.B-22.

Hermanns, R. L., Oppikofer, T., Böhme, M., Dehls, J. F., Yugsi Molina, F. X., and Penna, I. M. (2016). "Rock slope instabilities in Norway: First systematic hazard and risk classification of 22 unstable rock slopes from northern, western and southern Norway", in *Landslides and Engineered Slopes. Experience, Theory and Practice–Proceedings of the 12th International Symposium on Landslides*, Vol. 12, p. 19.

Hilger, P., Hermanns, R. L., Czekirda, J., Myhra, K. S., Gosse, J. C., and Etzelmüller, B. (2021). Permafrost as a first order control on long-term rock-slope deformation in (Sub-) Arctic Norway, *Quat. Sci. Rev.* 251, 106718. https://doi.org/10.1016/j.quascirev.2020.106718.

Hjort, J., Ujanen, J., Parviainen, M., Tolgensbakk, J., and Etzelmüller, B. (2014). Transferability of geomorphological distribution models: Evaluation using solifluction features in subarctic and Arctic regions. *Geomorphology* 204, 165–176. https://doi.org/10.1016/j.geomorph.2013.08.002.

Ikeda, A., Matsuoka, N., and Kääb, A. (2008). Fast deformation of perennially frozen debris in a warm rock glacier in the Swiss Alps: An effect of liquid water. *J. Geophys. Res.-Earth* 113(F1). https://doi.org/10.1029/2007JF000859.

IPA (2020a). Towards standard guidelines for inventorying rock glaciers, Baseline concepts, Version 4.1. *IPA Action Group Rock glacier inventories and kinematics*. https://bigweb.unifr.ch/Science/Geosciences/Geomorphology/Pub/Website/IPA/CurrentVersion/Current_Baseline_Concepts_Inventorying_Rock_Glaciers.pdf.

IPA (2020b). Kinematics as an optional attribute of standardized rock glacier inventories, Version 2.1. *IPA Action Group Rock glacier inventories and kinematics*. https://bigweb.unifr.ch/Science/Geosciences/Geomorphology/Pub/Website/IPA/Guidelines/KinematicsAttribute/200429_KinematicsAttribute_V2.1.pdf.

Isaksen, K., Sollid, J. L., Holmlund, P., and Harris, C. (2007). Recent warming of mountain permafrost in Svalbard and Scandinavia. *J. Geophys. Res.-Earth* 112(F2). https://doi.org/10.1029/2006JF000522.

Isaksen, K., Farbrot, H., Blikra, L. H., Johansen, B., Sollid, J. L., and Eiken, T. (2008). "Five-year ground surface temperature measurements in Finnmark, Northern Norway", in *Proceedings of the Ninth International Conference on Permafrost*, Vol. 1, 789–794, Fairbanks, U.S.A.

Jaboyedoff, M., Penna, I., Pedrazzini, A., Baroň, I., and Crosta, G. B. (2013). An introductory review on gravitational-deformation induced structures, fabrics and modelling. *Tectonophysics* 605, 1–12. https://doi.org/10.1016/j.tecto.2013.06.027.

Johnson, B. G., Thackray, G. D., and Van Kirk, R. (2007). The effect of topography, latitude, and lithology on rock glacier distribution in the Lemhi Range, central Idaho, USA. *Geomorphology* 91(1-2). 38–50, https://doi.org/10.1016/j.geomorph.2007.01.023.

Kääb, A., Huggel, C., Fischer, L., Guex, S., Paul, F., Roer, I., Salzmann, N., S. Schlaefli, S., Schmutz, K., Schneider, D., Strozzi, T., and Weidmann, Y. (2005). Remote sensing of glacier-and permafrost-related hazards in high mountains: an overview. *Nat. Hazards and Earth Syst. Sci.* 5, 527–554. https://nhess.copernicus.org/articles/5/527/2005/nhess-5-527-2005.pdf.

Kääb, A., Frauenfelder, R., and Roer, I. (2007). On the response of rockglacier creep to surface temperature increase. *Global Planet. Change* 56(1-2), 172–187. https://doi.org/10.1016/j.gloplacha.2006.07.005.

Kääb, A., Strozzi, T., Bolch, T., Caduff, R., Trefall, H., Stoffel, M., and Kokarev, A. (2021). Inventory, motion and acceleration of rock glaciers in Ile Alatau and Kungöy Ala-Too, northern Tien Shan, since the 1950s. *The Cryosphere* 15, 927–949. https://doi.org/10.5194/tc-15-927-2021.

Karjalainen, O., Luoto, M., Aalto, J., Etzelmüller, B., Grosse, G., Jones, B. M., Lilleøren, K. S., and Hjort, J. (2020). High potential for loss of permafrost landforms in a changing climate. *Environ. Res. Lett.* 15, 104065. https://doi.org/10.1088/1748-9326/abafd5.

Kenner, R., Phillips, M., Beutel, J., Hiller, M., Limpach, P., Pointner, E., and Volken, M. (2017). Factors controlling velocity variations at short-term, seasonal and multiyear time scales, Ritigraben rock glacier, Western Swiss Alps. *Permafrost Periglac.* 28(4), 675– 684. https://doi.org/10.1002/ppp.1953.

Keuschnig, M., Hartmeyer, I., Höfer-Öllinger, G., Schober, A., Krautblatter, M., and Schrott, L. (2015). "Permafrost-related mass movements: Implications from a rock slide at the Kitzsteinhorn, Austria", in *Engineering Geology for Society and Territory-Volume 1*, (Springer, Cham), 255–259. https://doi.org/10.1007/978-3-319-09300-0_48.

Larsen, Y., Engen, G., Lauknes, T. R., Malnes, E., and Høgda, K. A. (2005). "A generic differential interferometric SAR processing system, with applications to land subsidence and snow-water equivalent retrieval", in *Proceedings of Fringe 2005 Workshop*, Vol. 61, Frascati, Italy, ESA SP-610.

Larsen, Y., Marinkovic, P., Dehls, J., Bredal, M., Bishop, C., Jøkulsson, G., et al. (2020). European Ground Motion Service: Service Implementation Plan and Product Specification Document. *EU-EEA Delegation Agreement Copernicus Land Monitoring Service*, pp. 166. https://land.copernicus.eu/pan-european/european-ground-motion-service.

Lauknes, T. R., Shanker, A. P., Dehls, J. F., Zebker, H. A., Henderson, I. H. C., and Larsen, Y. (2010). Detailed rockslide mapping in northern Norway with small baseline and persistent scatterer interferometric SAR time series methods. *Remote Sens. Environ.* 114(9), 2097–2109. https://doi.org/10.1016/j.rse.2010.04.015.

Lauknes, T. R. (2011a). *Rockslide mapping in Norway by means of interferometric SAR time series analysis* (Ph.D. thesis). The Arctic University of Norway (UiT), Tromsø, Norway.

Lauknes, T. R. (2011b). InSAR tropospheric stratification delays: Correction using a small baseline approach. *IEEE Geosci. Remote S.* 8(6), 1070–1074. https://doi.org/10.1109/LGRS.2011.2156381.

Lilleøren K. S., and Etzelmüller B. (2011). A regional inventory of rock glaciers and ice-cored moraines in Norway. *Geogr. Ann. A.* 93, 175–191. https://doi.org/10.1111/j.1468-0459.2011.00430.x.

Lilleøren, K. S., Etzelmüller, B., Schuler, T. V., Gisnås, K., and Humlum, O. (2012). The relative age of mountain permafrost—estimation of Holocene permafrost limits in Norway. *Global and Planetary Change* 92, 209–223. https://doi.org/10.1016/j.gloplacha.2012.05.016.

Lilleøren, K. S., Etzelmuller, B., Gartner-Roer, I., Kääb, A., Westermann, S., and Gudmundsson, A. (2013). The Distribution, Thermal Characteristics and Dynamics of Permafrost in Trollaskági, Northern Iceland, as Inferred from the Distribution of Rock Glaciers and Ice-Cored Moraines. *Permafrost and Periglacial Processes* 24, 322–335. https://doi.org/10.1002/ppp.1792.

Liu, L., Millar, C. I., Westfall, R. D., and Zebker, H. A. (2013). Surface motion of active rock glaciers in the Sierra Nevada, California, USA: inventory and a case study using InSAR. *The Cryosphere* 7, 1109–1119. https://doi.org/10.5194/tc-7-1109-2013.

Luckman, B. H. (2017). "Glacier landscapes in the Canadian Rockies" in *Landscapes and Landforms of Western Canada* (Springer, Cham), 241–255.

Lyons, S., and Sandwell, D. (2003). Fault creep along the southern San Andreas from interferometric synthetic aperture radar, permanent scatterers, and stacking. *J. Geophys. Res.-Sol. Ea.* 108(B1). https://doi.org/10.1029/2002JB001831.

Marcer, M., Bodin, X., Brenning, A., Schoeneich, P., Charvet, R., and Gottardi, F. (2017). Permafrost favorability index: spatial modeling in the French Alps using a rock glacier inventory. *Front. in Earth Sci.* 5, 105. https://doi.org/10.3389/feart.2017.00105.

Matsuoka, N. (2001). Solifluction rates, processes and landforms: a global review. *Earth-Sci. Rev.* 55(1-2), 107–134. https://doi.org/10.1016/S0012-8252(01)00057-5.

Müller, J., Vieli, A., and Gärtner-Roer, I. (2016). Rock glaciers on the run-understanding rock glacier landform evolution and recent changes from numerical flow modelling. *The Cryosphere* 10(6), 2865–2886. https://doi.org/10.5194/tc-10-2865-2016.

NCCS (2021). Observations and weather statistics, Stations Skibotn II, Tromsø–Langnes, Hekkingen Fyr and Botnhamn, 2010–2020 daily and yearly air temperature and precipitation. *Norwegian Centre for Climate Services (NCCS)*. https://seklima.met.no/observations/ (accessed 06/01/2021).

NGU (2020a). Bedrock maps, Berggrunn data N250. https://kartkatalog.geonorge.no/. Map viewer: https://geo.ngu.no/kart/berggrunn_mobil/. *Geological Survey of Norway*.

NGU (2020b): Unstable rock slope inventory map. Map viewer: https://geo.ngu.no/kart/ustabilefjellparti_mobil/?lang=eng. *Geological Survey of Norway*.

NGU (2020c). InSAR Norway. www.insar.no. Map viewer: https://insar.ngu.no/. *Geological Survey of Norway*.

NMA (2011). Aerial images 2006-07-28, 2006-08-20, 2006-08-24, 2011-08-16, 2011-08-17. https://www.norgeibilder.no/. *Norwegian Mapping Authority*.

NMA (2016). DTM 10 Terrengmodell (UTM33). https://kartkatalog.geonorge.no/. *Norwegian Mapping Authority*.

NMA (2020a). Toporaster 4 WMS, https://kartkatalog.geonorge.no/, *Norwegian Mapping Authority*.

NMA (2020b). Norge i bilder WMTS (Euref89 UTM33). Aerial images 2016-07-22, 2016-08-18, 2016-08-19, 2016-07-22, 2017-07-23. *Norwegian Mapping Authority*. https://www.norgeibilder.no/.

Obu, J., Westermann, S., Bartsch, A., Berdnikov, N., Christiansen, H. H., Dashtseren, A., et al. (2019). Northern Hemisphere permafrost map based on TTOP modelling for 2000–2016 at 1 km2 scale. *Earth-Science Reviews* 193, 299–316. https://doi.org/10.1016/j.earscirev.2019.04.023.

Onaca, A., Ardelean, F., Urdea, P., and Magori, B. (2017). Southern Carpathian rock glaciers: Inventory, distribution and environmental controlling factors. *Geomorphology* 293, 391–404. https://doi.org/10.1016/j.geomorph.2016.03.032.

Østrem, G. (1964). Ice-cored moraines in Scandinavia. *Geografiska Annaler* 46(3), 282–337. https://doi.org/10.1080/20014422.1964.11881043.

Oppikofer, T., Nordahl, B., Bunkholt, H., Nicolaisen, M., Jarna, A., Iversen, S., et al. (2015). Database and online map service on unstable rock slopes in Norway—From data perpetuation to public information. *Geomorphology* 249, 69–81. https://doi.org/10.1016/j.geomorph.2015.08.005.

Osmundsen, P. T., Henderson, I., Lauknes, T. R., Larsen, Y., Redfield, T. F., and Dehls, J. (2009). Active normal fault control on landscape and rock-slope failure in northern Norway. *Geology* 37(2), 135–138. https://doi.org/10.1130/G25208A.1.

Patton, A. I., Rathburn, S. L., and Capps, D. M. (2019). Landslide response to climate change in permafrost regions. *Geomorphology* 340, 116–128. https://doi.org/10.1016/j.geomorph.2019.04.029.

Pedrazzini, A., Humair, F., Jaboyedoff, M., and Tonini, M. (2016). Characterisation and spatial distribution of gravitational slope deformation in the upper Rhone catchment (western Swiss Alps). *Landslides* 13, 259–277. https://doi.org/10.1007/s10346-015-0562-9.

Roer, I., Haeberli, W., Avian, M., Kaufmann, V., Delaloye, R., Lambiel, C., and Kääb, A. (2008). "Observations and considerations on destabilizing active rock glaciers in the European Alps", in *Proceedings of the 9th International Conference on Permafrost*, Fairbanks, Alaska, 29 June – 3 July 2008, 1505–1510.

Rosi, A., Tofani, V., Tanteri, L., Stefanelli, C. T., Agostini, A., Catani, F., and Casagli, N. (2018). The new landslide inventory of Tuscany (Italy) updated with PS-InSAR: geomorphological features and landslide distribution. *Landslides* 15(1), 5–19. https://doi.org/10.1007/s10346-017-0861-4.

Rouyet, L., Lauknes, T. R., Christiansen, H. H., Strand, S. M., and Larsen, Y. (2019). Seasonal dynamics of a permafrost landscape, Adventdalen, Svalbard, investigated by InSAR. *Remote Sens. Environ.* 231, 111236. https://doi.org/10.1016/j.rse.2019.111236.

Sandwell, D. T. and Price, E. J. (1998). Phase gradient approach to stacking interferograms. *J. Geophys. Res.-Sol. Ea.* 103(B12), 30183–30204. https://doi.org/10.1029/1998JB900008.

Scotti, R., Brardinoni, F., Alberti, S., Frattini, P., and Crosta, G. B. (2013). A regional inventory of rock glaciers and protalus ramparts in the central Italian Alps. *Geomorphology* 186, 136–149. https://doi.org/10.1016/j.geomorph.2012.12.028.

Smith, D. J. (1987). Solifluction in the southern Canadian Rockies. *Canadian Geographer* 31(4), 309–318. https://doi.org/10.1111/j.1541-0064.1987.tb01656.x.

Sollid, J. L., and Sørbel, L. (1992). Rock glaciers in Svalbard and Norway. *Permafrost and Periglacial Processes* 3(3), 215–220. https://doi.org/10.1002/ppp.3430030307.

Sollid, J. L., and Torp, B. (1984). Glasialgeologisk kart over Norge, 1:1 000 000 [in Norwegian]. Nasjonalatlas for Norge. Geografisk Institutt, *Oslo Universitet*.

Stead, D., and Wolter, A. (2015). A critical review of rock slope failure mechanisms: the importance of structural geology. *J. Struct. Geol.* 74, 1–23. https://doi.org/10.1016/j.jsg.2015.02.002.

Stoffel, M., Tiranti, D., and Huggel, C. (2014). Climate change impacts on mass movements—case studies from the European Alps. *Science of the Total Environment* 493, 1255–1266. https://doi.org/10.1016/j.scitotenv.2014.02.102.

Strozzi, T., Caduff, R., Jones, N., Barboux, C., Delaloye, R., Bodin, X., Kääb, A., Mätzler, E., and Schrott, L. (2020). Monitoring Rock Glacier Kinematics with Satellite Synthetic Aperture Radar. *Remote Sensing* 12(3), 559. https://doi.org/10.3390/rs12030559.

Thompson, S., Benn, D. I., Mertes, J., and Luckman, A. (2016). Stagnation and mass loss on a Himalayan debris-covered glacier: processes, patterns and rates. *Journal of Glaciology* 62(233), 467–485. https://doi.org/10.1017/jog.2016.37.

Tolgensbakk, J. and Sollid, J. L. (1988). Kåfjord, kvartærgeologi og geomorfologi. 1:50-000 [in Norwegian]. 1634 ii. Geografisk Instiutt, *Universitetet i Oslo*.

Vick, L. M., Böhme, M., Rouyet, L., Bergh, S.G., Corner, G. D. and Lauknes, T. R. (2020). Structurally controlled rock slope deformation in northern Norway. *Landslides 17*, 1745–1776. https://doi.org/10.1007/s10346-020-01421-7.

Villarroel, C. D., Tamburini Beliveau, G., Forte, A. P., Monserrat, O., and Morvillo, M. (2018). DInSAR for a Regional inventory of active rock glaciers in the dry Andes mountains of Argentina and chile with sentinel-1 data. *Remote Sensing* 10(10), 1588. https://doi.org/10.3390/rs10101588.

Wang, X., Liu, L., Zhao, L., Wu, T., Li, Z., and Liu, G. (2017). Mapping and inventorying active rock glaciers in the northern Tien Shan of China using satellite SAR interferometry. *The Cryosphere* 11(2). https://doi.org/10.5194/tc-11-997-2017.

Wasowski, J., and Bovenga, F. (2014). Investigating landslides and unstable slopes with satellite Multi Temporal Interferometry: Current issues and future perspectives. *Engineering Geology* 174, 103–138. https://doi.org/10.1016/j.enggeo.2014.03.003.

Wilson, P. (2009). Rockfall talus slopes and associated talus-foot features in the glaciated uplands of Great Britain and Ireland: periglacial, paraglacial or composite landforms? *Geological Society, London, Special Publications* 320(1), 133–144. https://doi.org/10.1144/SP320.9.

Winsvold, S. H., Andreassen, L. M., and Kienholz. C. (2014). Glacier area and length changes in Norway from repeat inventories. *The Cryosphere* 8, 1885–1903. https://doi.org/10.5194/tc-8-1885-2014.

Zwaan, K. B. (1988). Bedrock geology map Nordreisa, M 1:250 000 [In Norwegian: Berggrunnsgeologisk kart]. *Geological Survey of Norway*.

Zwaan, K. B., Farseth, E., and Grogan P. (1998). Bedrock geology map Tromsø, M 1:250 000 [In Norwegian: Bergrunnsgeologisk kart]. *Geological Survey of Norway*.

Supplementary Material

Regional InSAR inventory of slope movement in Northern Norway

Line Rouyet, Karianne Staalesen Lilleøren, Martina Böhme, Louise Mary Vick, Reynald Delaloye, Bernd Etzelmüller, Tom Rune Lauknes, Yngvar Larsen, Lars Harald Blikra

Table S0. Statistics of the classified InSAR results based on multi temporal baseline InSAR stacking. Rows 1–2 summarize the results for the land area. Rows 3–4 focus on the E-W facing slopes (22.5–257.5°/202.5–227.5°). Details about classes are in Table 2 (main manuscript).

	Class 0 <0.3 cm/yr	Class 1 0.3–1 cm/yr	Class 2 1–3 cm/yr	Class 3 3–10 cm/yr	Class 4 10–30 cm/yr	Class 5 >30 cm/yr	Decorrelated	Layover/Shadow
Land area (km^2) (all) *	4527	92	43	10	6	1	1525	57
Fraction of land (%) (all) *	72.3	1.5	0.7	0.2	0.1	0.0	24.4	0.9
Land area (km^2) (E-W slopes)	3407	81	36	8	5	1	1292	56
Fraction of land (%) (E-W slopes)	69.7	1.7	0.7	0.2	0.1	0.0	26.4	1.2

* Note that the velocity may be underestimated on N-S facing slopes due the LOS measurements.

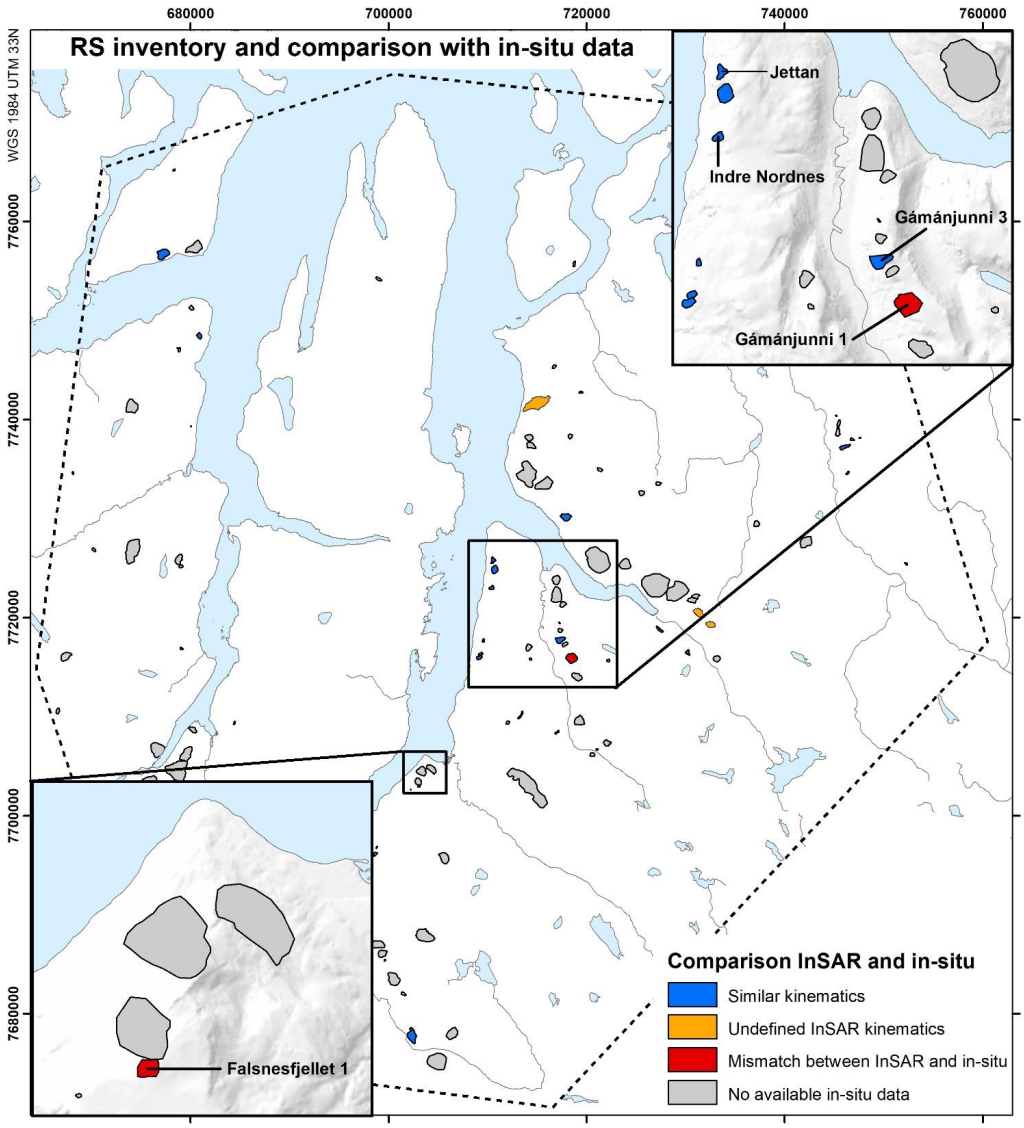

Figure S1. Rockslide inventory and distribution of the 20 landforms for which InSAR results have been compared to in-situ measurements. Gámánjunni 3, Jettan and Indre Nordnes are permanently monitored. The 17 other sites are periodically measured with dGNSS. Sea, lakes and rivers from NMA (2020a).

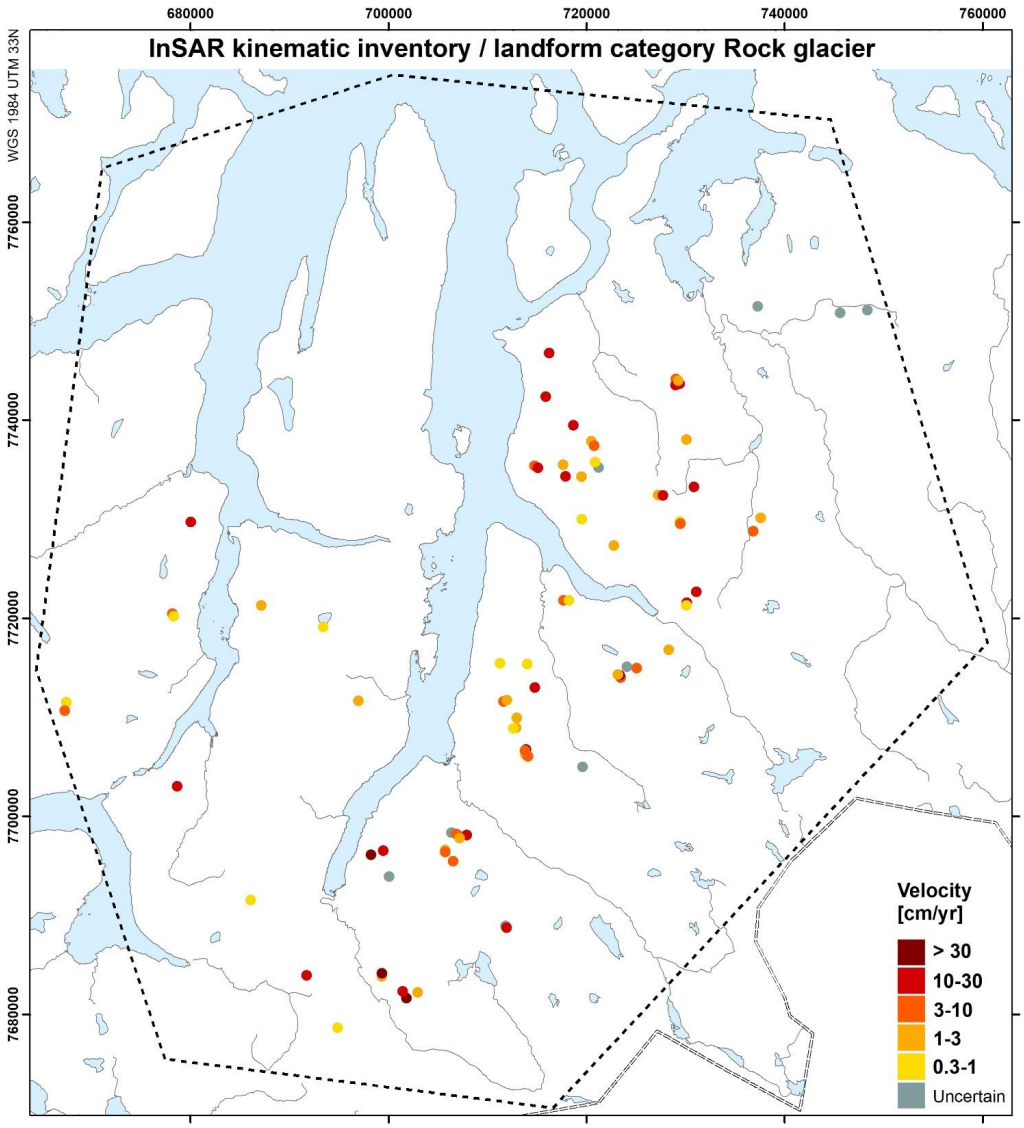

Figure S2. InSAR kinematics for the rock glacier (RG) category. Grey symbols correspond to areas where slope movement has been detected and the landform type categorized, but the velocity is uncertain due to location on N-S slopes. Sea, lakes, rivers and border from NMA (2020a).

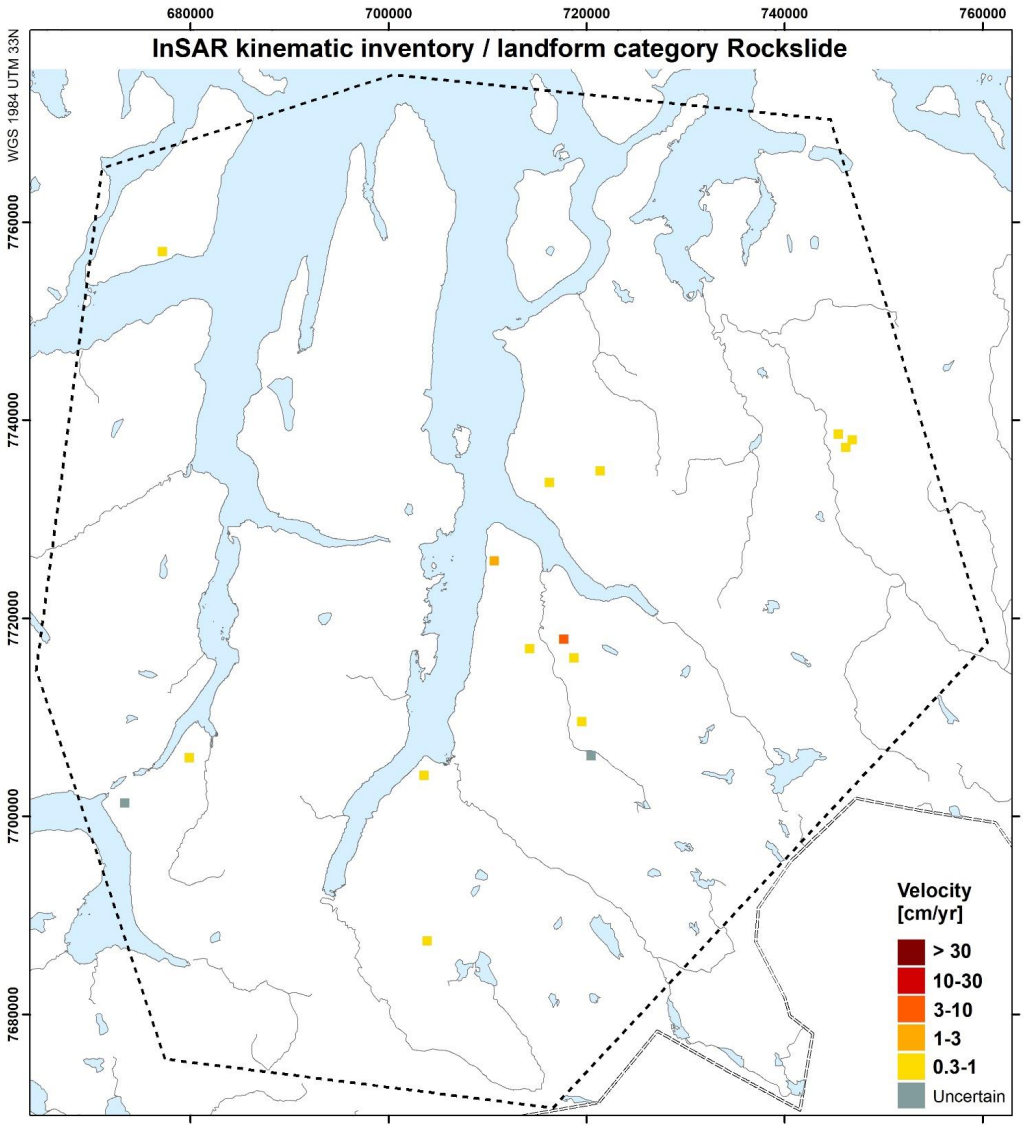

Figure S3. InSAR kinematics for the rockslide (RS) category. Grey symbols correspond to areas where slope movement has been detected and the landform type categorized, but the velocity is uncertain due to location on N-S slopes. Sea, lakes, rivers and border from NMA (2020a).

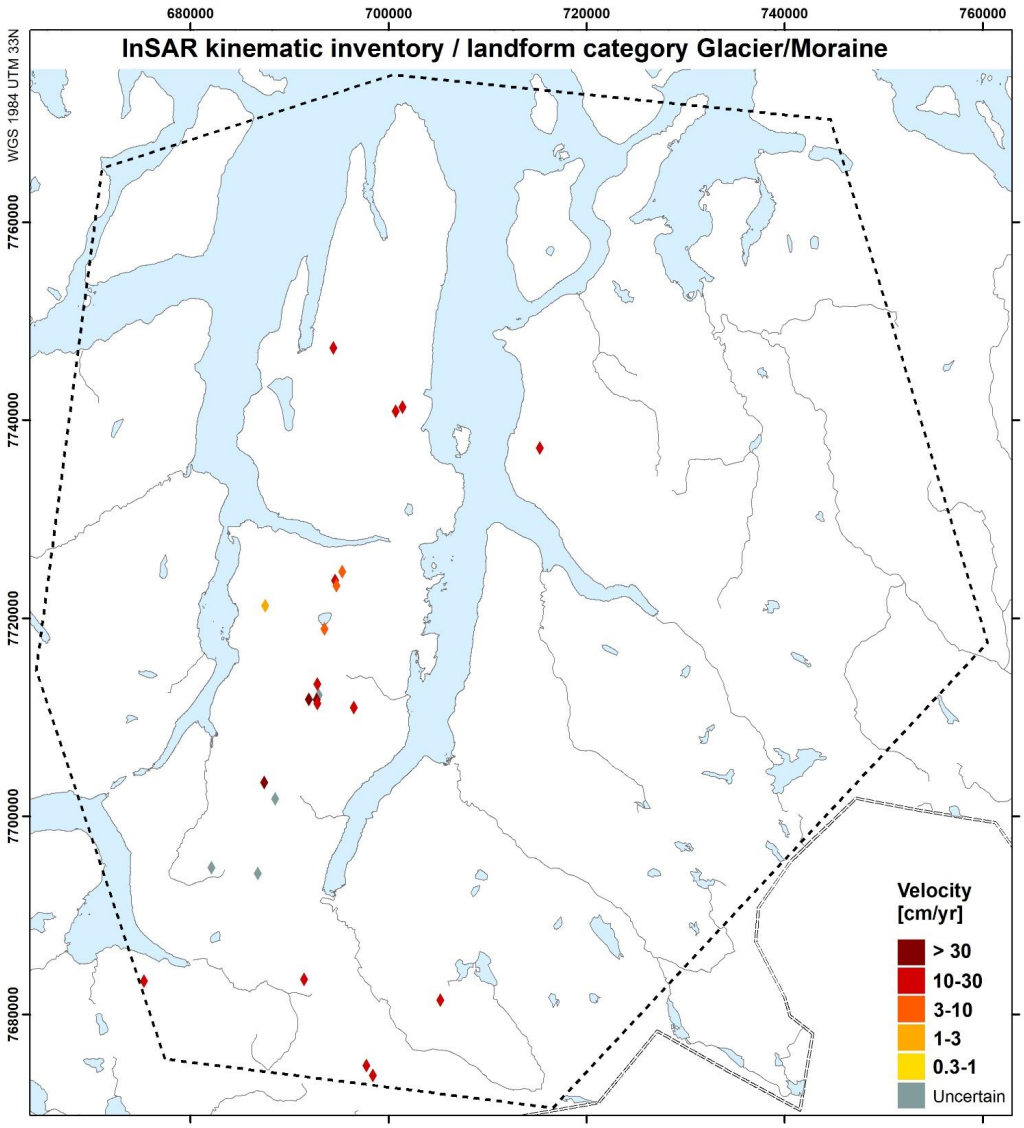

Figure S4. InSAR kinematics for the glacier/moraine (GM) category. Grey symbols correspond to areas where slope movement has been detected and the landform type categorized, but the velocity is uncertain due to location on N-S slopes. Sea, lakes, rivers and border from NMA (2020a).

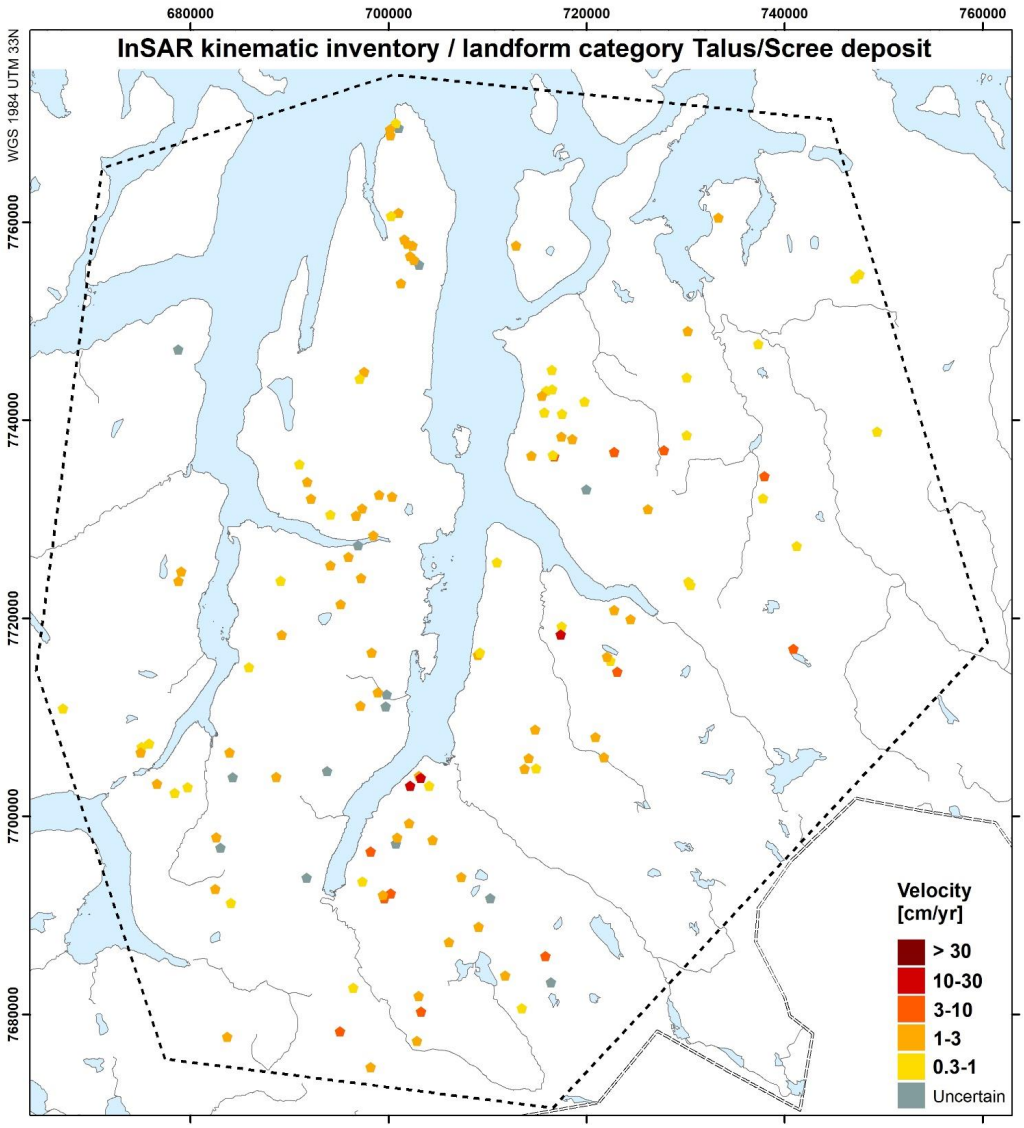

Figure S5. InSAR kinematics for the talus/scree deposit (TS) category. Grey symbols correspond to areas where slope movement has been detected and the landform type categorized, but the velocity is uncertain due to location on N-S slopes. Sea, lakes, rivers and border from NMA (2020a).

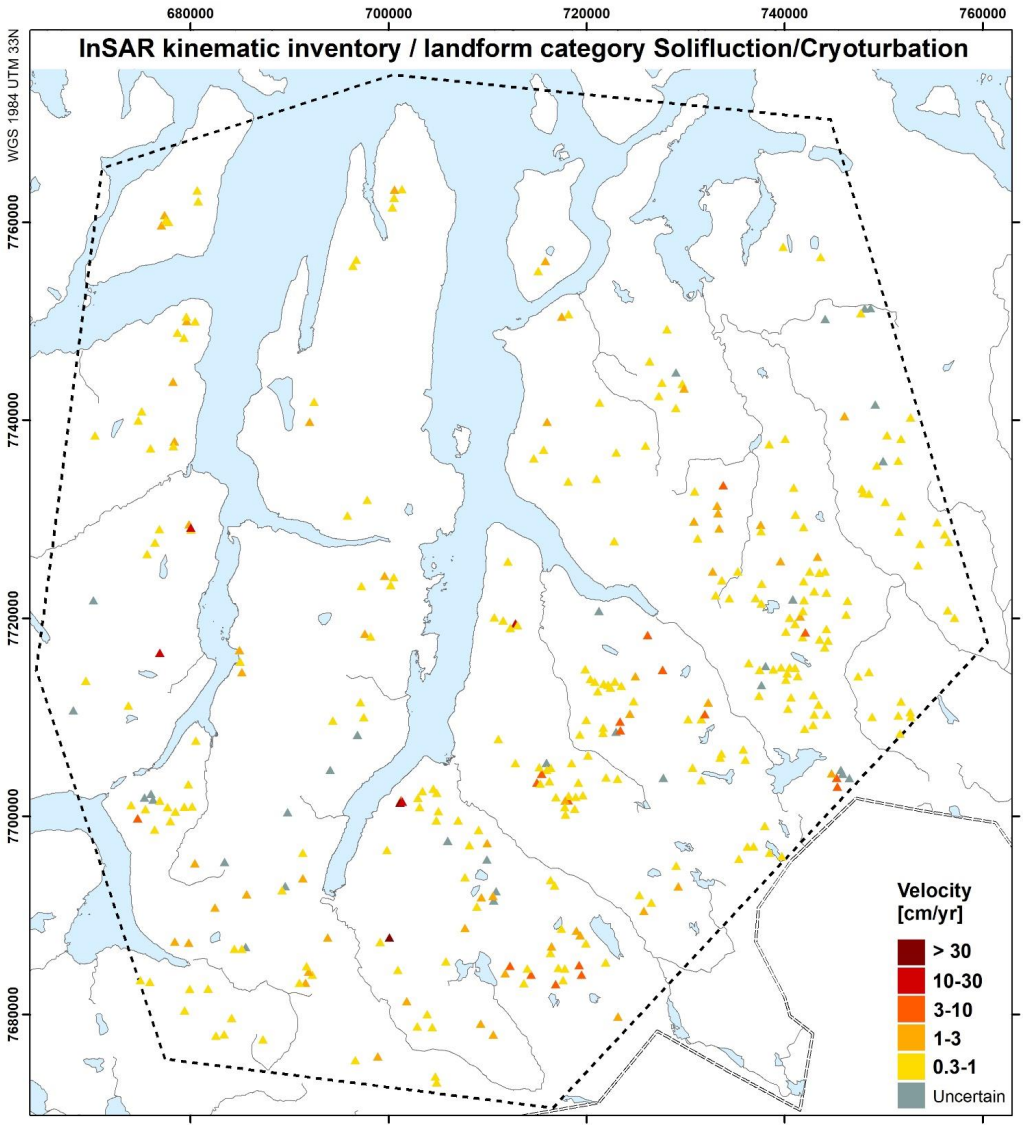

Figure S6. InSAR kinematics for the solifluction/cryoturbation (SC) category. Grey symbols correspond to areas where slope movement has been detected and the landform type categorized, but the velocity is uncertain due to location on N-S slopes. Sea, lakes, rivers and border from NMA (2020a).

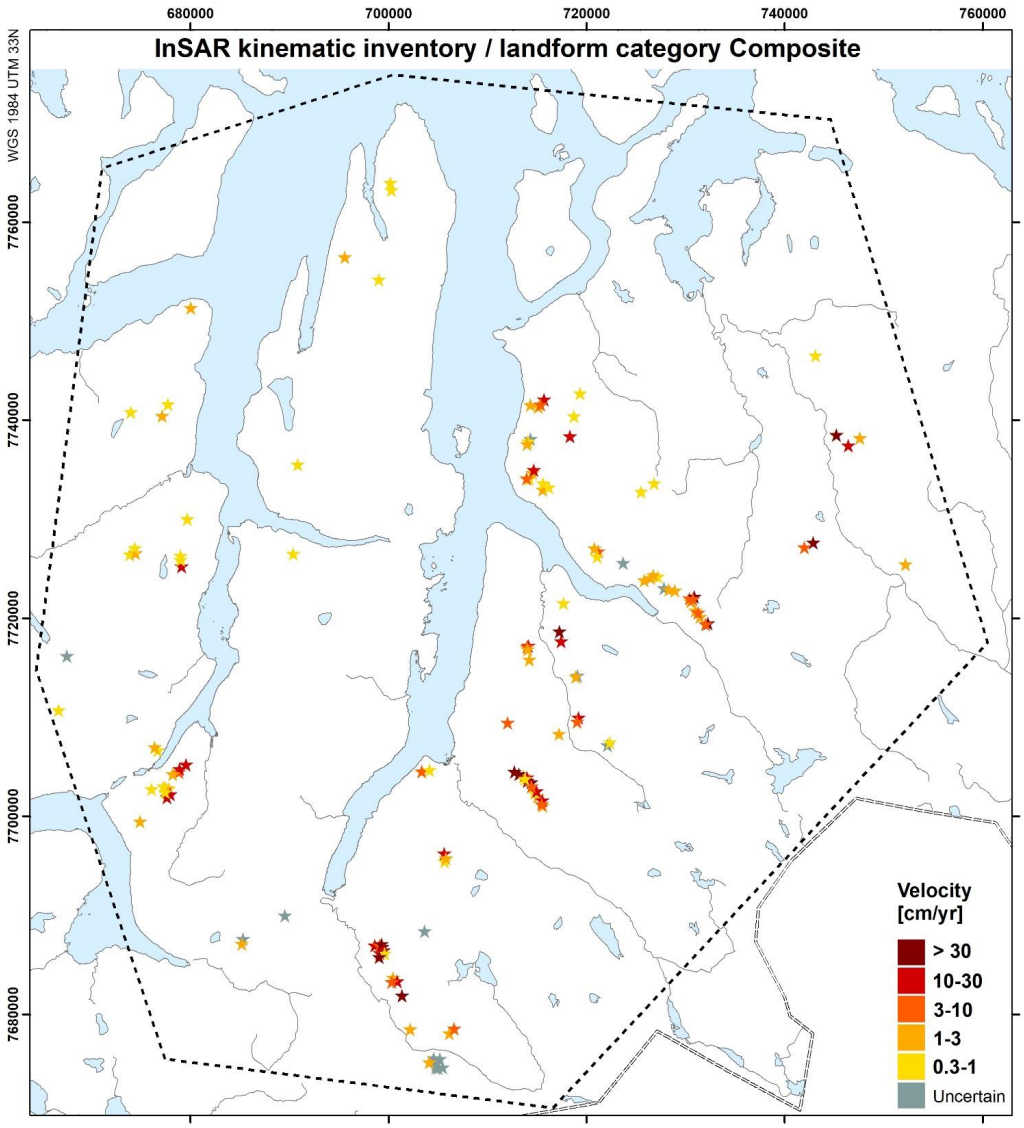

Figure S7. InSAR kinematics for the composite (CO) category. Grey symbols correspond to areas where slope movement has been detected and the landform type categorized, but the velocity is uncertain due to location on N-S slopes. Sea, lakes, rivers and border from NMA (2020a).

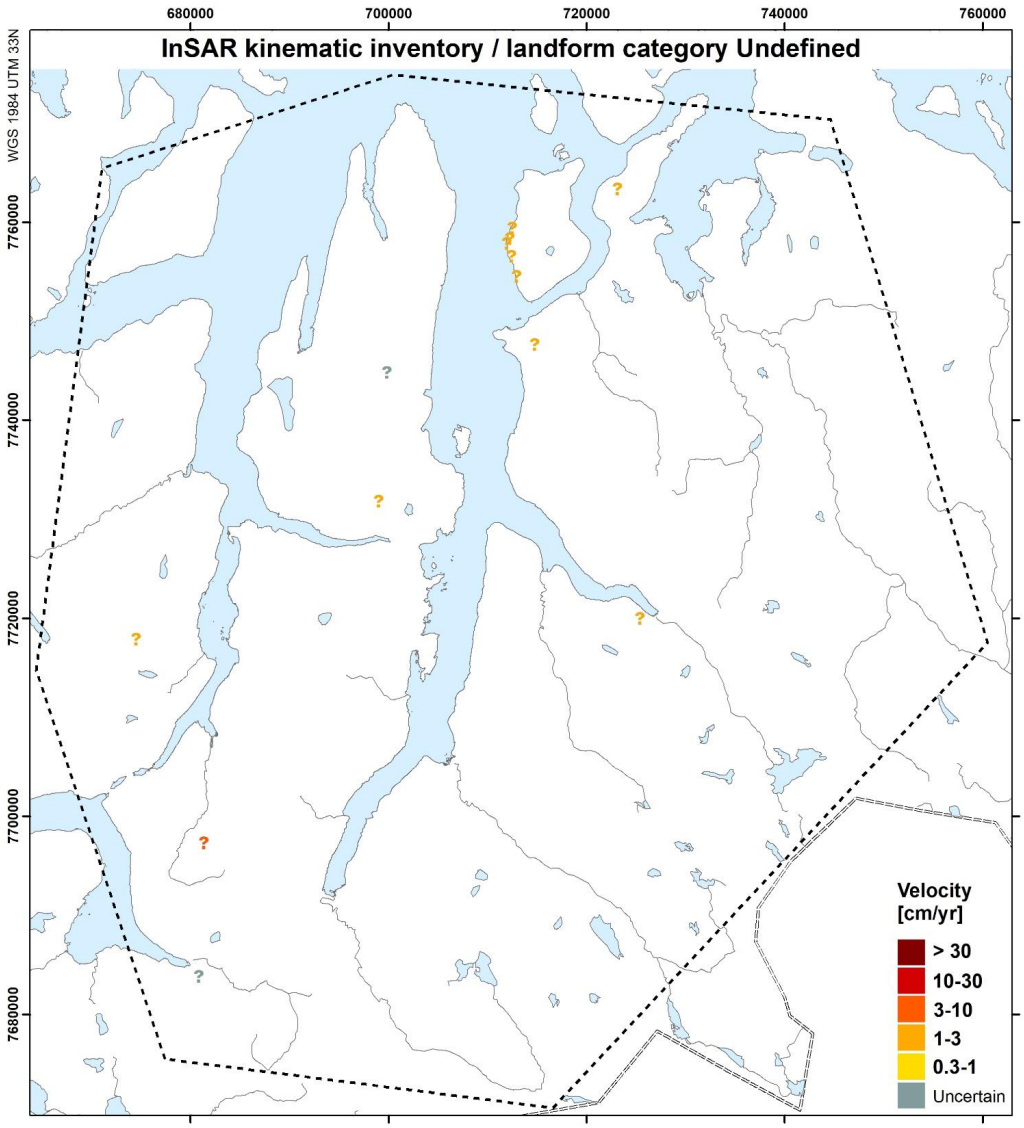

Figure S8. InSAR kinematics for the undefined (UD) category. Grey symbols correspond to areas where slope movement has been detected and the landform type categorized, but the velocity is uncertain due to location on N-S slopes. Sea, lakes, rivers and border from NMA (2020a).

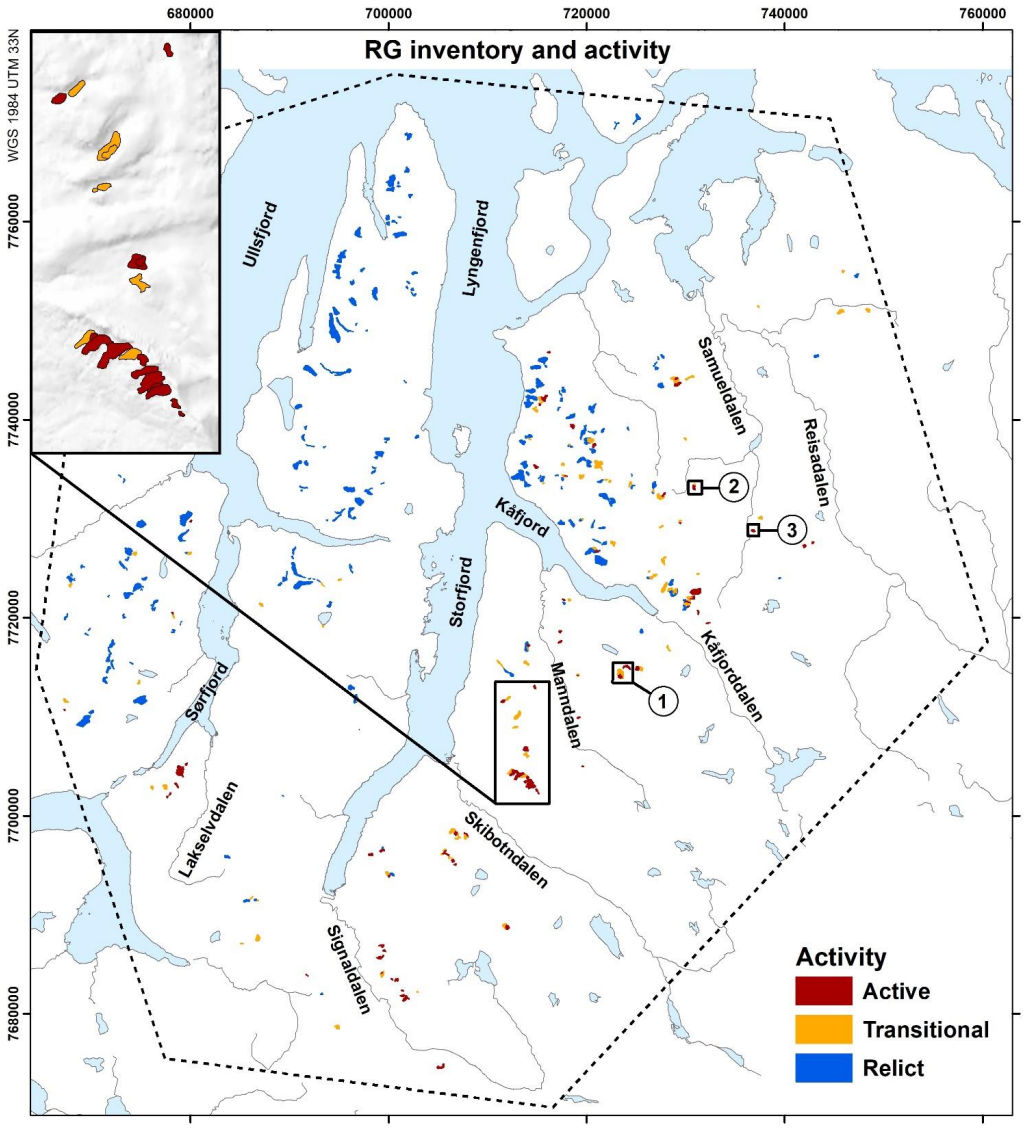

Figure S9. Rock glacier inventory and attribute 'Activity' according to the new activity categories recommended by IPA (2020a). Sea, lakes, rivers and reference names from NMA (2020a).

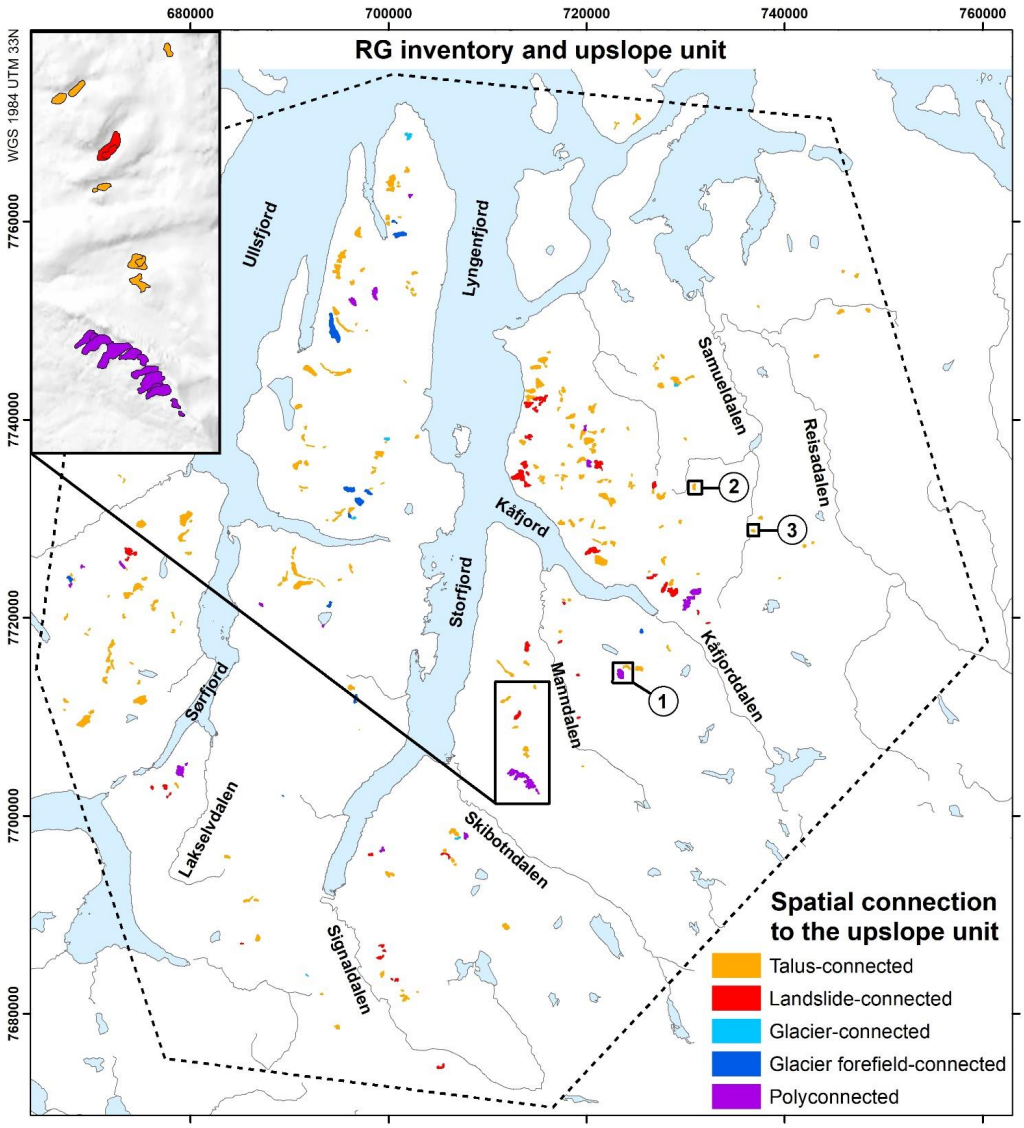

Figure S10. Rock glacier inventory and attribute 'Spatial connection to the upslope unit' according to the new activity categories recommended by IPA (2020a). Sea, lakes, rivers and reference names from NMA (2020a).

Paper IV: Recent acceleration of a rock glacier complex, Ádjet, Norway, documented by 62 Years of remote sensing observations

Eriksen, H. Ø., Rouyet, L., Lauknes, T. R., Berthling, I., Isaksen, K., Hindberg, H., Larsen, Y., Corner, G. D.

Published in *Geophysical Research Letters*, *45*(16), 8314–8323, 2018.

Article and Supplements:
https://doi.org/10.1029/2018GL077605

AGU100 ADVANCING EARTH AND SPACE SCIENCE

Geophysical Research Letters

RESEARCH LETTER
10.1029/2018GL077605

Key Points:
- Sixty-two years (1954–2016) of aerial photography and radar data document recent acceleration of a rock glacier complex in northern Norway
- Results show spatial and temporal variations as extension and compression, uplift, and subsidence in a permafrost landform
- Simultaneous increase of temperature and precipitation suggests that the landform is affected by permafrost warming

Supporting Information:
- Supporting Information S1
- Figure S1
- Figure S2
- Figure S3
- Figure S4
- Figure S5
- Figure S6
- Figure S7
- Figure S8
- Figure S9
- Figure S10
- Figure S11
- Figure S12
- Figure S13
- Figure S14
- Figure S15
- Data Set S1
- Data Set S2
- Movie S1
- Movie S2
- Movie S3
- Movie S4

Correspondence to:
H. Ø. Eriksen,
haraldoverlieriksen@gmail.com

Citation:
Eriksen, H. Ø., Rouyet, L., Lauknes, T. R., Berthling, I., Isaksen, K., Hindberg, H., et al. (2018). Recent acceleration of a rock glacier complex, Adjet, Norway, documented by 62 years of remote sensing observations. *Geophysical Research Letters*, *45*, 8314–8323. https://doi.org/10.1029/2018GL077605

Received 7 MAR 2018
Accepted 27 JUL 2018
Accepted article online 3 AUG 2018
Published online 23 AUG 2018

Recent Acceleration of a Rock Glacier Complex, Ádjet, Norway, Documented by 62 Years of Remote Sensing Observations

H. Ø. Eriksen[1,2], L. Rouyet[1], T. R. Lauknes[1], I. Berthling[3], K. Isaksen[4], H. Hindberg[1], Y. Larsen[1], and G. D. Corner[2]

[1]Norut, Tromsø, Norway, [2]Department of Geosciences, UiT-The Arctic University of Norway, Tromsø, Norway, [3]Department of Geography, Norwegian University of Science and Technology, Trondheim, Norway, [4]Norwegian Meteorological Institute, Research and Development Department, Oslo, Norway

Abstract Recent acceleration of rock glaciers is well recognized in the European Alps, but similar behavior is hardly documented elsewhere. Also, the controlling factors are not fully understood. Here we provide evidence for acceleration of a rock glacier complex in northern Norway, from 62 years of remote sensing data. Average annual horizontal velocity measured by aerial feature tracking increased from ~0.5 myr^{-1} (1954–1977) to ~3.6 myr^{-1} (2006–2014). Measured by satellite synthetic aperture radar offset-tracking, averages increased from ~4.9 to ~9.8 myr^{-1} (2009–2016) and maximum velocities from ~12 to ~69 myr^{-1}. Kinematic analysis reveals different spatial-temporal trends in the upper and the lower parts of the rock glacier complex, suggesting progressive detachment of the faster front. We suggest that permafrost warming, topographic controls, and increased water access to deeper permafrost layers and internal shear zones can explain the kinematic behavior.

Plain Language Summary Using remote sensing data we document unusual high surface displacement and accelerations on a rock glacier complex in a mountain hillside in northern Norway. Increasing creep rates have been reported from the European Alps, but an acceleration of this order has not been documented in Scandinavia before. Rock glaciers are permafrost landforms consisting of a mix of ice and debris. Using aerial photos, we document an acceleration from ~0.5 m per year (1954–1977) to ~3.6 m per year (2006–2014) for the lower parts of the rock glacier complex. For the same area, we observe an increase from ~4.9 to ~9.8 m per year, measured by satellite-based radar between 2009 and 2016. Maximum velocities increased from ~12 to ~69 m per year. Results suggest that the fast lower part is detaching from the slower upper part. Radar data delineate areas with subsidence and uplift, compression, and extension. Increase in temperature and precipitation during the 62-year period indicates possible permafrost degradation. Our work demonstrates the value of combining remote sensing data sources in documenting permafrost landforms in the Arctic. Important work still remains to document and understand their evolution and the effects of climate change.

1. Introduction

Rock glaciers are striking landforms developed from deformation of ice/debris mixtures under permafrost conditions (Barsch, 1996; Berthling, 2011; Gorbunov et al., 1992; Haeberli et al., 2006). They form a common but not ubiquitous part of high alpine and polar slope systems. Ground temperature influences the rheology of such ice/debris mixtures in a nonlinear manner (Kääb et al., 2007; Moore, 2014), but rock glaciers also respond dynamically to changes in sediment input (Müller et al., 2016) and rain or snow-meltwater infiltration (Ikeda et al., 2008). For more than a decade, a significant acceleration, and in some cases even collapse, of rock glaciers has been documented in the European Alps (Avian et al., 2005; Bodin et al., 2016; Delaloye et al., 2008; Ikeda et al., 2008; Kääb et al., 2007; Kellerer-Pirklbauer & Kaufmann, 2018; Müller et al., 2016; Noetzli et al., 2016; Roer et al., 2008). This development has been attributed to higher permafrost temperatures (Kääb et al., 2007; Kellerer-Pirklbauer & Kaufmann, 2012; Roer et al., 2005) combined with increasing liquid water content (Ikeda et al., 2008; Kenner et al., 2017) and local overloading by debris (Delaloye et al., 2013). The factors controlling acceleration and complex velocity variations are not known in detail (Haeberli et al., 2010; Müller et al., 2016). Importantly, similar behaviors are still poorly documented outside the European Alps, except for work by Darrow et al. (2016, 2017), making the present work an important contribution to obtaining a global overview of accelerating permafrost landforms in the context of climate

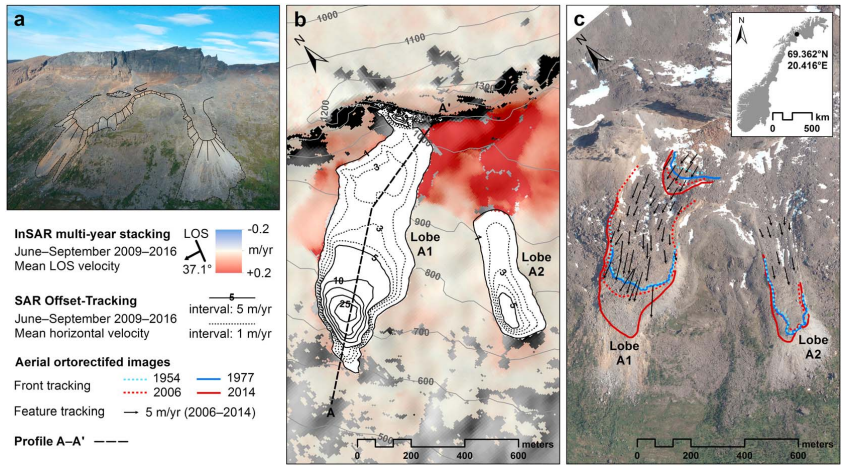

Figure 1. Spatial distribution of ground displacements in the rock glacier complex at the Ádjet mountain. (a) Aerial photo close-up of the two most active rock glacier lobes (NGU, 14 August 2011). (b) Mean annual ground velocities along the line-of-sight measured by InSAR multiyear stacking (2009–2016, minus 2015). The red areas indicate active slope processes with displacements away from the satellite (downward and westward). The contours on lobes, A1 and A2, indicate projected horizontal mean annual velocities (myr^{-1}) detected using SAR offset-tracking (2009–2016, minus 2015). Background: shaded relief from 10-m resolution digital elevation model (Norwegian Mapping Authority, 2013). (c) Results from aerial feature- and front tracking in 1954, 1977, 2006, and 2014. Background: orthorectified image from 31 August 2014. Inset: location of the study area in northern Norway.

change. Over the last few decades, developing remote sensing techniques have complemented traditional in situ investigation and monitoring methods. Optical and radar sensors mounted on satellite, airborne, and ground-based platforms have proven especially suitable for measurement of deformation on rock glaciers (Kääb et al., 1997; Liu et al., 2013; Rignot et al., 2002; Wang et al., 2017).

The objective of this paper is to document and analyze spatiotemporal trends and changes of displacement rates over a fast-moving rock glacier complex in northern Norway by exploiting optical and radar remote sensing data sets spanning 62 years (1954–2016).

2. Ádjet Rock Glacier Complex, Northern Norway

Our study area is located in Troms County, northern Norway (Figure 1c inset), which has a high density of rockslides (Bunkholt et al., 2013; Corner, 2005; Lauknes et al., 2010; Osmundsen et al., 2009), and the highest density of rock glaciers in Norway (Lilleøren & Etzelmüller, 2011). We focus on a prominent rock glacier complex, composed of two lobes (A1 and A2), located below a summit reaching up to 1,300 m above sea level (asl), on the southwest-facing slope of Ádjet mountain in the Skibotn valley (Figure 1 and Figures S1 and S9 and Text S1 in the supporting information). Lobe A1 ranges in elevation from ~690 to 1,080 m asl (Figures 1, S1, S2, S9, S10, and S12), close to the regional altitudinal limit of mountain permafrost (600–800 m asl) according to borehole temperature data and modeling (Farbrot et al., 2013; Kellerer-Pirklbauer & Kaufmann, 2018). Scree aprons on the steep front of lobe A1 reach down to 580 m asl (Figures 1, S1, S2, and S10 and File S1 in the supporting information). The rock glaciers have developed from debris from rockslides and rockfalls accumulated below a ~200-m high, subvertical, and highly fractured headwall consisting of quartz-rich schist and garnet-mica-schist (Bakkhaug, 2015; Nopper, 2015). The lobes have longitudinal and transverse furrows, some with snow and perennial ice in the bottom. The deepest depression is ~16 m deep, located on the gently sloping middle part of lobe A1 (~880 m asl). On lobe A2, we observed during the summers 2015–2017, a thermokarst lake with bottom ice between large boulders (File S1).

3. Data and Methods

3.1. Data

The study is based on four remote sensing data sets comprising (1) four orthorectified aerial images from 1954, 1977, 2006, and 2014; (2) 63 snow-free TerraSAR-X (TSX) satellite images, StripMap (SM) mode, in ascending geometry; (3) 75 snow-free TSX images, SM mode, in descending geometry; and (4) Gamma Portable Radar Interferometer images acquired during two campaigns in August 2014 and May–June 2015.

Remote sensing data sets are complemented with climatic data comprising (1) modeled air temperature, precipitation, and snow cover data from SeNorge.no portal, 2012 and (2) in situ air, ground surface, and ground temperature from iButton loggers (Eriksen, 2018).

Characteristics of remote sensing, modeled, and in situ data are summarized in Table S1 in the supporting information.

3.2. Methods

The remote sensing techniques applied are (1) aerial feature- and front tracking based on the orthorectified aerial images; (2) SAR interferometry (InSAR) multiyear stacking based on TSX images in descending geometry; (3) SAR offset-tracking (OT) technique based on TSX images in ascending and descending geometries; and (4) Terrestrial InSAR (TRI) based on Gamma Portable Radar Interferometer images. As summarized in Table S2, the combination of these remote sensing methods is necessary to span over the whole time period (62 years from 1954 to 2014), detect ground displacements on both slow and fast moving areas, and document both long-term trend and seasonal variations. More information about each method is available in Texts S2a–S2d).

Offset-tracking and TRI results are projected using an assumption of displacements parallel to the surface and analyzed along a profile A-A′ (Figures 1 and S2). Velocities from aerial feature- and front tracking, OT and TRI are compared by computing the mean annual horizontal velocity for a common area in the middle of lobe A1 (Figures S1 and S2). InSAR documents displacement rates in surrounding areas. TRI documents seasonal variations of rates by comparing results from summer 2014 and spring 2015. The kinematic analysis includes the calculation of the strain rate (extension/compression) and variations of uplift/subsidence trends, based on TRI and OT results (Text S2e).

The modeled climatic data are used to compute mean annual air temperature (MAAT), mean annual precipitation, and maximum annual snow depth (MASP). This provides a long temporal coverage (1957–2016) to investigate climate change in the region. For comparison with modeled data, we calculated MAAT based on in situ air temperature data. To characterize the ground thermal regime at local scale, mean annual ground surface and ground temperature are calculated. Using the Bottom Temperature of Snow (BTS) method (Haeberli, 1973; Hoelzle, 1992), stable temperatures during snow cover provide an indication of permafrost presence/absence at different locations. More information about climatic analysis is available in Text S2f.

4. Results

The results from the four complementary remote sensing methods document high velocities on the rock glacier complex, with fastest velocities located on lobe A1 (Figures 1b and 1c). Aerial feature- and front tracking shows that the lobe front of A1 advanced by ~180 m and one upper internal lobe front advanced by ~100 m between 1954 and 2014 (Figures 1c, S3, and S4). The front of lobe A2 advanced ~35 m during the same time span. Mean annual velocities from InSAR multiyear stacking show velocities up to 0.15 myr^{-1} along the LOS in the source area under the headwall supplying the rock glacier complex (Figures 1c and S1). Because of large displacements on lobes A1 and A2, InSAR fails to provide correct measurements (Text S2b). However, SAR offset-tracking is able to follow the displacement and documents 2009–2016 (minus 2015) mean annual velocities up to ~27 myr^{-1} on lobe A1 and up to ~6 myr^{-1} on lobe A2 (Text S2c), including a clear acceleration between 2009 and 2016 (Figures S6 and S7).

4.1. Long-Term Trends

To compare the results, the surface-parallel flow approximation was used to project OT and TRI velocities in the downslope direction, using a profile along the fastest lobe A1 (Figures 1 and S2). Figure 2a shows velocities from each year separately along the profile A-A′. OT results for 2016 show a maximum surface-

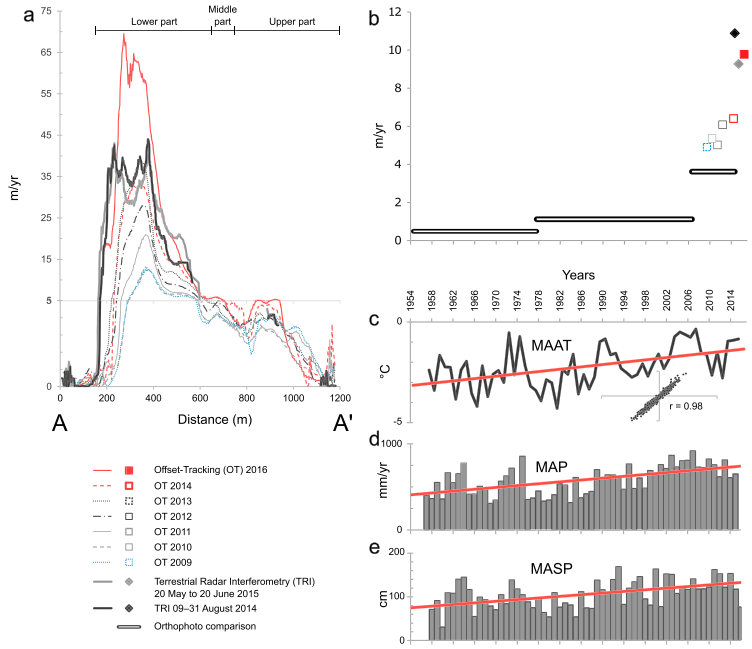

Figure 2. Spatial and temporal variations of displacement rates compared to modeled local climatic data for lobe A1 at Ádjet. (a) Surface-parallel annual velocity in profile A-A′ from offset-tracking (OT; 2009–2016, minus 2015) and Terrestrial InSAR (TRI; August 2014 and May–June 2015). Note the break in the vertical scale at 5 myr^{-1}. (b) Comparison of mean annual horizontal velocity in the direction of profile A-A′ for a common area in the middle part of lobe A1 (Figure S2) from aerial feature tracking, OT, and TRI. (c) Mean annual air temperature (1954–2014). Inset shows gridded daily temperature compared to in situ logger ALT 1 (Text S2f). (d) Mean annual precipitation. (e) Maximum annual snow depth. The red lines show linear trend of climatic data from 1957 to 2016. Modeled climatic data from SeNorge.no.

parallel flow of ~69 myr^{-1} in the lower part and ~5 myr^{-1} in the upper part (for a visual impression see Movie S2 in the supporting information). This is an increase of 575% in the lower part and 128% in the upper, compared to velocities measured in 2009.

Surface-parallel annual velocities in profile A-A′ show detailed interannual variations separating the upper part in two: (1) above and (2) below 950 m (Figure 2a). Area (1) shows general deceleration, and area (2) shows general acceleration. The middle and lower part show acceleration after a period with stable velocities in 2009 and 2010 (Figures 2a, S6, and S7). Notably, after the stable period, acceleration is delayed in the middle part (starting in 2013) with respect to the lower part.

We compare decadal displacement rates from aerial feature tracking, with single year rates from OT results and seasonal rates from TRI results, by computing the mean annual horizontal velocity in the direction of profile A-A′ for a common area (Figure S2) on the lower part of lobe A1 (Figure 2b). Velocities increase at a decadal scale from ~0.5 to ~3.6 myr^{-1} from 1954 to 2014, with a recent acceleration from ~4.9 to ~9.8 myr^{-1} from 2009 to 2016. A comparison between TRI and OT confirms the recent very high velocities but highlights also that the rock glacier complex is affected by seasonal fluctuations normal for rock glaciers (Kenner et al., 2017; Figure 2b).

4.2. Seasonal Trends

TRI results indicate seasonal variability of displacement rates, with higher velocities in August 2014 than in May–June 2015 (Figures 2a and 2b and S8). The accumulated LOS displacements are up to ~3.5 m in

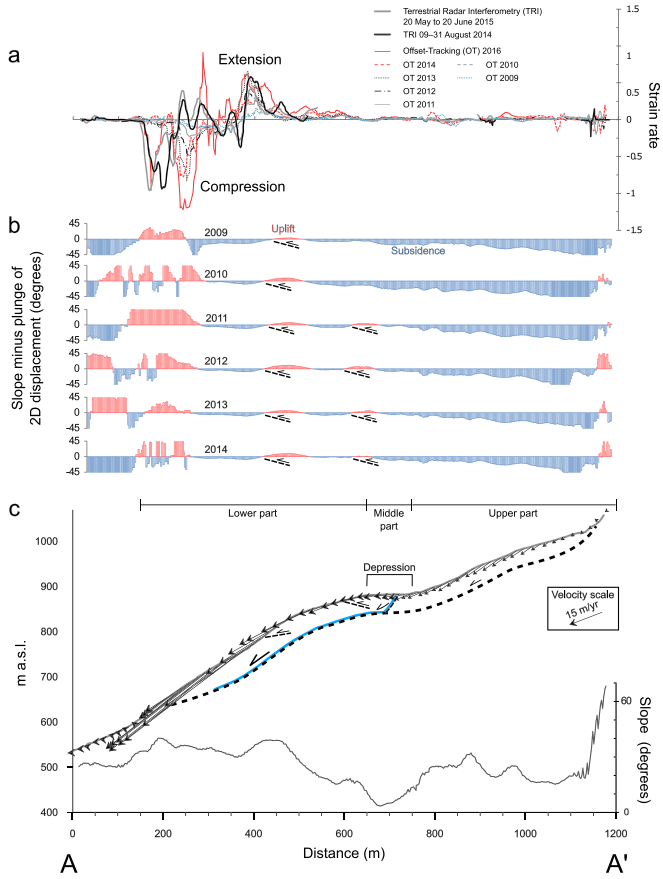

Figure 3. Kinematic analysis along profile A-A′ in lobe A1, from offset-tracking (OT) and Terrestrial InSAR (TRI) results. (a) Spatial and temporal variations in strain rate from individual years based on surface-parallel annual velocities from OT (2009–2014) and TRI data (2014 and 2015). (b) Annual variations in uplift and subsidence calculated by subtracting slope from averaged plunge of 2-D OT surface displacement vectors. (c) Model of proposed internal structure with inferred deformation pattern, terrain surface, and slope. The vectors indicate average surface velocity and plunge from 2-D OT (2009–2014). A central depression and possible zone of elevated pore pressures (blue line) due to infiltration of water are marked. Bedrock position (dashed line) interpreted from surrounding outcrops.

23 days in August 2014 and up to ~2.7 m in 32 days in May–June 2015 (Figure S8, File S2, and Movie S1), corresponding to extrapolated mean annual velocities along the LOS of up to ~55 myr^{-1} in August 2015 and ~30 myr^{-1} in May–June 2015.

4.3. Kinematic Analysis

Based on an analysis of the strain rate along profile A-A′ (Text S2e), the most noticeable kinematic signal is the pulse from extension to compression within the lower part of the rock glacier (at ~300 m from the start of profile A-A′, Figure 3a). The extension increased from 2009 to 2014 in the area where the rock glacier moves over convex terrain. Further toward the front, compression has been steadily increasing from 2009 to 2014 (Figure 3a). In the low-velocity upper part, there are small-scale variations in strain rate related to slope

gradient, especially across transverse ridges and internal lobe fronts (at ~800 and ~1,050 m from the start of profile A-A′; Figure 3).

To study spatial and temporal variations, and identify the plunge of displacements, we computed 2-D vectors identified from OT results (Text S2c; Eriksen et al., 2017). Two-dimensional vectors were compared to the slope to give plunge into the ground (subsidence) and out of the ground (uplift) along profile A-A′ (Figures 3b and 3c). We observe a general trend of subsidence in the upper part and alternation between uplift and subsidence in the middle and lower parts. This spatial pattern is relatively constant over time, but a new zone of uplift appears in 2011 at ~650 m from the start of the profile (Figure 3b). This uplift zone has a convex topography (slope in Figure 3c), suggesting that it is an internal lobe front. In addition, it is in an area of compression (Figure 3a), and this may therefore be the surface signal of a lobe moving over material at its front.

4.4. Climatic Analysis

In situ temperature measurements (Text S2f and Figure S14) indicate permafrost conditions in the coarse blocky layer of the rock glacier lobes. Temperature measurements (362 days from August 2015 to August 2016) in fractures and cavities of the active layer at lobe A2 provided an average of −0.74 °C (logger GTL 2_2015 at ~2.9 m depth) and an average of −1.92 °C at lobe A1 (logger GTL 3_2015 at ~4 m depth; Figure S2 and File S3). Stable temperatures beneath snow (BTS) indicate that permafrost probably occurs in both lobes. The BTS value at logger GTL 4 (lobe A2) was −3.9 °C in February–April 2016 and −3.25 °C in February–May 2017. At logger GTL 3_2015 (lobe A1) BTS values were more varying in 2016, ending at −5.2 °C in April, and at −3.75 °C in April 2017 (File S3). An average temperature of 2.43 °C in ground surface temperatures based on 341 days (2016–2017, missing days in September) shows permafrost-free terrain in the area between the rock glacier lobes (logger GST 1), compared to an average of 0.05 °C on lobe A2 (missing days in August; logger GST 1; Figure S2 and File S3).

Modeled temperature, precipitation, and snow cover data (Text S2f) indicate that climate has changed during the 62-year time span covered by the remote sensing data. Data show an increase in MAAT of 1.8 °C during this period and an annual precipitation increase of 330 mm (55%). Moreover, the MASP increased by 58 cm (56%; Figures 2c–2e). If we compare the first 30 years (1957–1986) with the last 29 years (1986–2015), the MAAT has increased by 0.91 °C, from −2.62 °C (σ: 0.9 °C) to −1.71 °C (σ: 0.83 °C). The mean annual precipitation increased with 177 mm, from 497 to 674 mm/yr from the first to the last period (σ: 142 and 126 mm, respectively). Finally, the MASP increased with 33 mm, from 90 to 123 mm (σ: 33 mm). MAAT from modeled data were compared with MAAT from in situ logger ATL 1 (Text S2f and Figures S2 and S14) and show a correlation of 0.98 (Figure 2c inset).

5. Discussion

The results provide information about the displacement of a rock glacier complex having rates that are comparable to advances of frozen debris lobes in Alaska (Darrow et al., 2016) and destabilized rock glaciers in the Swiss and Central Italian Alps (Delaloye et al., 2013; Scotti et al., 2016). The long time series and complementarity of methods document the temporal fluctuations of displacement rates. TRI results highlight that seasonal variations have to be considered. Seasonal variations of rock glaciers are well documented (Barsch, 1996; Haeberli, 1985; Kenner et al., 2017; Liu et al., 2013; Wirz et al., 2016). In some cases, the seasonal amplitude of the displacement is very high as, for example, in the extremely rapid Grabengufer rock glacier, which has a ratio of 1:9 between winter and summer velocities (Delaloye & Staub, 2016). Therefore, we expect that our annual displacement rates based on OT observations are overestimated. Nevertheless, the comparison of annual displacement rates from individual snow-free seasons is not affected by seasonal variations and shows a clear increasing trend.

Spatial variations in the displacement rates on the two lobes studied are well documented. The acceleration and deceleration phases in the upper part (Figure 2a) may be a consequence of irregular overloading due to rockfall and landslide activity from the highly fractured headwall, as suggested for the Grabengufer rock glacier (Delaloye et al., 2013). The results of the strain rate calculation indicate pulses from extension to compression within the lower part of the landform (Figure 3a). The increase in extension from 2009 to 2014 suggests that the rock glacier behavior is controlled by the topography and that the high velocity lower part is becoming increasingly detached from the slower upper part, as also shown for the Hinteres Langtalkar

rock glacier by Kaufmann and Ladstädter (2003) and Kaufmann and Ladstädter (2004). The reaction of the middle part is delayed compared to the fast lower part (Figure 3a). Our hypothesis is that the displacements may be taking place along internal shear zones, retrogressively propagating higher up on the rock glacier (as seen in Movie S3). Similar dynamics is described by Gorbunov et al. (1992) for the Burkutty rock glacier and by Hartl et al. (2016) for the Outer Hochebenkar rock glacier.

Velocities recorded in the lower part of the Ádjet rock glacier exceed the empirical model considered by Kääb et al. (2007) by an order of magnitude. Internal deformation of the rock glacier can be estimated using Glens' flow law of ice. The surface velocity from internal deformation is calculated using $U_s = 2A(\rho g \sin\alpha)^3 H^4/4$, where A is a rate factor depending especially on temperature, ρ is the density of the deforming material, g is the acceleration due to gravity, H is the total thickness of the deforming material, and α is the surface slope averaged over ~10 H (e.g., Kääb et al., 2007). Following their approach further, using a maximum rock glacier thickness of 35 m, an overall density of ~2,000 kg/m^3 (~40% ice of density 910 kg/m^3, ~60% debris of density 2,700 kg/m^3), a spatially averaged surface slope of 30° and an A value for temperate ice (2.1×10^{-16} Pa^{-3}a^{-1}), provides a surface velocity estimate of ~147 myr^{-1} based on Glen's flow law. For reference, a more conservative A value of 7×10^{-17} Pa^{-3} yr^{-1} (adapted from Huhh1 rock glacier; Müller et al., 2016) gives a surface velocity of 50 myr^{-1}. Our recorded velocities could thus potentially stem from internal deformation alone, but it is likely that other factors contribute. In particular, the nonlinear temporal changes in velocities require other explanations. Increased displacements along shear zones may be due to meltwater percolation and increasing pore pressures (Buchli, 2016). Our calculated strain rates are above critical strain rates for crevasse formation in frozen debris (Haeberli et al., 1979) and in an isothermal ice body, water could easily percolate into the rock glacier through such structures. Similarly to destabilized rock glaciers in Mattertal (Delaloye et al., 2013), the Ádjet rock glacier moves over bedrock causing a convex break of slope. Such topography can be a controlling factor for the observed spatial pattern of extension and compression. The depression at ~700 m might be related to an underlying shear zone extending toward the surface, as documented by Merz et al. (2016) from the Furggwanghorn rock glacier.

The analysis of climatic data shows a significant increase of temperature and precipitation during the 62-year period (Figures 2c–2e). From the literature, regional observed trends in permafrost temperatures in northern Scandinavia show accelerating warming since 2000 (Isaksen et al., 2007) with a change in mean annual ground temperature of between +0.1 and +0.4 °C/decade (Romanovsky et al., 2016). In addition, permafrost degradation has been observed in an instrumented borehole ~30 km east of Ádjet (Farbrot et al., 2013). Based on in situ measurements, climate data (since 1958), and modeling, Frauenfelder et al. (2018) found it likely that long general warming, an extreme warm summer the year before, resulted in degrading permafrost that contributed to trigger a rock avalanche in the nearby Signaldalen 26 June 2008. Combined, these results suggest increasing permafrost temperatures within the rock glacier body. Permafrost degradation may have started a positive feedback process where infiltrating water has accessed the rock glacier interior through taliks, causing energy input and hydrologic connectivity between surface and internal shear zones (Wirz et al., 2016). The increased flow velocities resulted in stretching of the permafrost body, introduced new shear zones/fractures, and enhanced percolation of water. Precipitation or melting events may then rapidly elevate pore water pressures and reduce effective stress along water-bearing shear zones (Kenner et al., 2017). Such factors might explain the observation that the lower part of the rock glacier increasingly tends to detach from the upper part. Notably, variability in seasonal displacements of the TRI results (Figures 2b and S8) and a downslope progression of TRI peak displacement from summer 2014 to spring 2015 (~400–550 m in profile A-A′ Figure 2a) could be a surface signal of a progression of water pressure through such a water-bearing shear zone, as observed by Darrow et al. (2017) for frozen debris lobes in the Brooks Range of Alaska.

We have no data directly describing subsurface conditions and thermal properties for the Ádjet rock glacier complex. Nevertheless, our detailed remote sensing analysis of surface displacements gives information about areas of extension and compression possibly related to active shear zones and areas with uplift or subsidence (Figure 3). Such kinematic information provides additional details to the surface-parallel shear zone described for many alpine rock glaciers (Arenson et al., 2002; Haeberli et al., 2006) and curving shear zones found in recent results combining geophysical surveys and borehole inclinometer measurements (Merz et al., 2015).

One hypothesis is that large-scale failures due to stress release, glacio-isostatic uplift, and climate change after deglaciation ~9,100 14C yr B.P. (ca. 10,200 cal yr B.P.; Corner, 1980; Nopper, 2015) helped form the rock glaciers. Nopper documented multiple inactive (relict) lobes between lobes A1 and A2 (Figure S18), which suggest that today's advance is not unique, but possibly part of a repeated pattern of advances controlled by variations in climatic and sediment input. Depending on the reaction to future climate forcing, variations in sediment input, and the topographic setting, failure of destabilized rock glaciers may occur (Barsch, 1996). This could have severe consequences for infrastructure and settlements in mountainous regions having a high density of creeping permafrost bodies, such as rock glaciers (Harris, 2005; Kääb, 2008; Krainer et al., 2012). As permafrost landforms often are located in inaccessible, rough terrain, our remote sensing approach in conjunction with increasing availability of satellite radar data, for example, from the EU Copernicus Sentinel-1 mission, could help fulfill an urgent need to monitor the consequences of climate change (Haeberli et al., 2010). The ability to investigate large areas and to upscale site-specific geophysical and geotechnical investigations (Merz et al., 2016; Springman et al., 2012) could pave the way for an improved understanding, a more detailed characterization, and better monitoring of changes in periglacial environments.

6. Conclusions

Our work demonstrates the value of combining multiple remote sensing for documenting displacement of permafrost landforms. For the Ádjet rock glacier in northern Norway, we measured higher velocities and accelerations than documented in Scandinavia before. Our observations of surface displacement reveal interesting spatial and temporal kinematic patterns. In particular, two different patterns are observed, one suggesting irregular overloading in the upper part, and one possibly caused by the fast lower part progressively detaching from the slower upper part due to decreasing flow resistance. Moreover, data indicate internal kinematics as zones of compression and extension and variations in the plunge of displacement. The analysis of climatic data shows an increase of temperature and precipitation during the 62-year period, suggesting that permafrost warming with increased amounts of available water having access to internal shear zones have triggered the destabilization of the landform, but with topography as an additional control. This research is relevant for understanding the kinematics of destabilizing permafrost landforms in mountainous environments, and for improving forecasting and mitigation of future geohazards.

Acknowledgments
TerraSAR-X satellite data were provided by DLR (projects GEO0565, GEO0764, and GEO2497). Additional data can be downloaded from https://doi.org/10.6084/m9.figshare.5955460. Funding for H.Ø.E. was provided by a grant (project 217720, grant RDA12/165) from Troms County Council. Development of the Norut InSAR processing chain was supported by the Norwegian Space Centre, the Research Council of Norway, and by the European Space Agency. The authors acknowledge support from Bjørn Barstad (Terratec) for preparing the orthophotos from 1954 and 1977. We are grateful to Wilfried Haeberli, Andreas Kellerer-Pirklbauer, and one anonymous reviewer whose comments clearly improved the manuscript. In addition we thank Reynald Delaloye and two anonymous reviewers for their comments on an earlier version of the manuscript. We thank Patrick Larsen, Markus Eckerstorfer, and Aleksander Amundsen for the helping during field campaigns. We are grateful to the Geological Survey of Norway for help regarding logistics, to Iselin Bakkhaug and Hannah Nopper for installing temperature loggers, and to Stein Rune Karlsen (Norut) for supplying us with tripods. We acknowledge Øyvind Ørnebakk who cleared the forest in Skibotn during the terrestrial-based radar campaigns and Tromsø Astronomy Association for letting us stay in their Skibotn Observatory during fieldwork.

References

Arenson, L., Hoelzle, M., & Springman, S. (2002). Borehole deformation measurements and internal structure of some rock glaciers in Switzerland. *Permafrost and Periglacial Processes*, *13*(2), 117–135. https://doi.org/10.1002/ppp.414

Avian, M., Kaufmann, V., & Lieb, G. K. (2005). Recent and Holocene dynamics of a rock glacier system: The example of Langtalkar (Central Alps, Austria). *Norsk Geografisk Tidsskrift*, *59*(2), 149–156. https://doi.org/10.1080/00291950510020637

Bakkhaug, I. (2015). Undersøkelse av ustabilt fjellparti ved Adjet, Storfjord, Troms. Betydningen av ulike kategorier av glideplan i berggrunnen og mekanismer for utglidning, Storfjord, Troms, Master Thesis, (in Norwegian). UiT-The Arctic University of Norway, pp. 126.

Barsch, D. (1996). *Rockglaciers. Indicators for the present and former geoecology in High Mountain Environments*. Heidelberg: Springer Verlag.

Berthling, I. (2011). Beyond confusion: Rock glaciers as cryo-conditioned landforms. *Geomorphology*, *131*(3–4), 98–106. https://doi.org/10.1016/j.geomorph.2011.05.002

Bodin, X., Krysiecki, J.-M., Schoeneich, P., Le Roux, O., Lorier, L., Echelard, T., et al. (2016). The 2006 collapse of the Bérard rock glacier (Southern French Alps). *Permafrost and Periglacial Processes*, *28*(1), 209–223. https://doi.org/10.1002/ppp.1887

Buchli, T. (2016). Instabilities in Alpine permafrost: Characterisation, monitoring and modelling of active rock glaciers, (PhD thesis). ETH Zürich.

Bunkholt, H., Redfield, T., Osmundsen, P. T., Oppikofer, T., Hermanns, R. L., & Dehls, J. (2013). The role of inherited structures in deep seated slope failures in Kåfjorden, Norway. In C. Margottini, P. Canuti, & K. Sassa (Eds.), *Landslide science and practice* (pp. 265–271). Berlin: Springer.

Corner, G. D. (1980). Preboreal deglaciation chronology and marine limits of the Lyngen-Storfjord area, Troms, North Norway. *Boreas*, *9*(4), 239–249. https://doi.org/10.1111/j.1502-3885.1980.tb00700.x

Corner, G. D. (2005). Ch. 13. Scandes Mountains. In M. Seppälä (Ed.), *The physical geography of Fennoscandia*, *Oxford Regional Environments Series*. Oxford University Press.

Darrow, M. M., Daanen, R. P., & Gong, W. (2017). Predicting movement using internal deformation dynamics of a landslide in permafrost. *Cold Regions Science and Technology*, *143*(Supplement C), 93–104. https://doi.org/10.1016/j.coldregions.2017.09.002

Darrow, M. M., Gyswyt, N. L., Simpson, J. M., Daanen, R. P., & Hubbard, T. D. (2016). Frozen debris lobe morphology and movement: An overview of eight dynamic features, southern Brooks Range, Alaska. *The Cryosphere*, *10*(3), 977–993. https://doi.org/10.5194/tc-10-977-2016

Delaloye, R., Morard, S., Barboux, C., Abbet, D., Gruber, V., Riedo, M., & Gachet, S. (2013). Rapidly moving rock glaciers in Mattertal. In C. Graf (Ed.), *Jahrestagung der Schweizerischen Geomorphologischen Gesellschaft* (pp. 21–31).

Delaloye, R., Perruchoud, E., Avian, M., Kaufmann, V., Bodin, X., Hausmann, H., et al. (2008). Recent interannual variations of rock glacier creep in the European Alps. Proceeding of the Ninth International Conference on Permafrost, (June), 343–348. https://doi.org/10.5167/uzh-7031

Delaloye, R., & Staub, B. (2016). Seasonal variations of rock glacier creep: Time series observations from the Western Swiss Alps. Paper presented at the International Conference on Permafrost June 20–24, 2016, Potsdam, Germany.
Eriksen, H. Ø. (2018). Instrumentation and temperature data (2014–2017) for the Ádjet mountain in Skibotn, Troms. Norut report 18/2018. Norut Research Institute. http://norut.no/nb/node/6968
Eriksen, H. Ø., Lauknes, T. R., Larsen, Y., Corner, G. D., Bergh, S. G., Dehls, J., & Kierulf, H. P. (2017). Visualizing and interpreting surface displacement patterns on unstable slopes using multi-geometry satellite SAR interferometry (2D InSAR). *Remote Sensing of Environment*, *191*, 297–312. https://doi.org/10.1016/j.rse.2016.12.024
Farbrot, H., Isaksen, K., Etzelmüller, B., & Gisnas, K. (2013). Ground thermal regime and permafrost distribution under a changing climate in northern Norway. *Permafrost and Periglacial Processes*, *24*(1), 20–38. https://doi.org/10.1002/ppp.1763
Frauenfelder, R., Isaksen, K., Lato, M. J., & Noetzli, J. (2018). Ground thermal and geomechanical conditions in a permafrost-affected high-latitude rock avalanche site (Polvartinden, northern Norway), *The Cryosphere*, *12*, 1531–1550. https://doi.org/10.5194/tc-12-1531-2018
Gorbunov, A. P., Titkov, S. N., & Polyakov, V. G. (1992). Dynamics of rock glaciers of the Northern Tien Shan and the Djungar Ala Tau, Kazakhstan. *Permafrost and Periglacial Processes*, *3*(1), 29–39. https://doi.org/10.1002/ppp.3430030105
Haeberli, W. (1973). Die Basis Temperatur der winterlichen Schneedecke als möglicher Indikator für die Verbreitung von Permafrost. *Zeitschrift für Gletscherkunde und Glazialgeologie*, *9*(1–2), 221–227.
Haeberli, W. (1985). Creep of mountain permafrost: Internal structure and flow of Alpine rock glaciers. Mitteilung VAW/ETHZ, 74.
Haeberli, W., Hallet, B., Arenson, L., Elconin, R., Humlum, O., Kääb, A., et al. (2006). Permafrost creep and rock glacier dynamics. *Permafrost and Periglacial Processes*, *17*(3), 189–214. https://doi.org/10.1002/ppp.561
Haeberli, W., King, L., & Flotron, A. (1979). Surface movement and lichen cover studies at the active rock glacier near the Grubengletscher, Wallis, Swiss Alps. *Arctic and Alpine Research*, *11*(4), 421–441. https://doi.org/10.2307/1550561
Haeberli, W., Noetzli, J., Arenson, L., Delaloye, R., Gärtner-Roer, I., Gruber, S., et al. (2010). Mountain permafrost: Development and challenges of a young research field. *Journal of Glaciology*, *56*(200), 1043–1058. https://doi.org/10.3189/002214311796406121
Harris, C. (2005). Climate change, mountain permafrost degradation and geotechnical hazard. In U. M. Huber, H. K. M. Bugmann, & M. A. Reasoner (Eds.), *Global change and mountain regions: An overview of current knowledge* (pp. 215–224). Dordrecht: Springer Netherlands. https://doi.org/10.1007/1-4020-3508-X_22
Hartl, L. E. A., Fischer, A., Stocker-Waldhuber, M., & Abermann, J. (2016). Recent speed-up of an alpine rock glacier: An updated chronology of the kinematics of outer Hochebenkar rock glacier based on geodetic measurements. *Geografiska Annaler: Series A, Physical Geography*, *98*(2), 129–141. https://doi.org/10.1111/geoa.12127
Hoelzle, M. (1992). Permafrost occurrence from BTS measurements and climatic parameters in the eastern Swiss Alps. *Permafrost and Periglacial Processes*, *3*(2), 143–147.
Ikeda, A., Matsuoka, N., & Kääb, A. (2008). Fast deformation of perennially frozen debris in a warm rock glacier in the Swiss Alps: An effect of liquid water. *Journal of Geophysical Research*, *113*, F01021. https://doi.org/10.1029/2007JF000859
Isaksen, K., Sollid, J. L., Holmlund, P., & Harris, C. (2007). Recent warming of mountain permafrost in Svalbard and Scandinavia. *Journal of Geophysical Research*, *112*, F02S04. https://doi.org/10.1029/2006JF000522
Kääb, A. (2008). Remote sensing of permafrost-related problems and hazards. *Permafrost and Periglacial Processes*, *19*(2), 107–136. https://doi.org/10.1002/ppp.619
Kääb, A., Frauenfelder, R., & Roer, I. (2007). On the response of rockglacier creep to surface temperature increase. *Global and Planetary Change*, *56*(1–2), 172–187. https://doi.org/10.1016/j.gloplacha.2006.07.005
Kääb, A., Haeberli, W., & Gudmundsson, G. H. (1997). Analysing the creep of mountain permafrost using high precision aerial photogrammetry: 25 years of monitoring Gruben rock glacier, Swiss Alps. *Permafrost and Periglacial Processes*, *8*(4), 409–426. https://doi.org/10.1002/(SICI)1099-1530(199710/12)8:4<409::AID-PPP267>3.0.CO;2-C
Kaufmann, V., & Ladstädter, R. (2003). Quantitative analysis of rock glacier creep by means of digital photogrammetry using multi-temporal aerial photographs: Two case studies in the Austrian Alps. In 8th International Conference on Permafrost. (pp. 525–530). Zurich, Switzerland.
Kaufmann, V., & Ladstädter, R. (2004). Documentation of the movement of the Hinteres Langtalkar rock glacier abstract. In Proceedings of the 20th ISPRS Congress (6 pp.).
Kellerer-Pirklbauer, A., & Kaufmann, V. (2012). About the relationship between rock glacier velocity and climate parameters in central Austria. *Austrian Journal of Earth Sciences*, *105*(2), 94–112.
Kellerer-Pirklbauer, A., & Kaufmann, V. (2018). Deglaciation and its impact on permafrost and rock glacier evolution: New insight from two adjacent cirques in Austria. *Science of the Total Environment*, *621*, 1397–1414. https://doi.org/10.1016/j.scitotenv.2017.10.087
Kenner, R., Phillips, M., Beutel, J., Hiller, M., Limpach, P., Pointner, E., & Volken, M. (2017). Factors controlling velocity variations at short-term, seasonal and multiyear time scales, Ritigraben rock glacier, Western Swiss Alps. *Permafrost and Periglacial Processes*, *28*(4), 675–684. https://doi.org/10.1002/ppp.1953
Krainer, K., Mussner, L., Behm, M., & Hausmann, H. (2012). Multi-disciplinary investigation of an active rock glacier in the Sella group (dolomites; northern Italy). *Austrian Journal of Earth Sciences*, *105*(2), 48–62.
Lauknes, T. R., Shanker, A. P., Dehls, J. F., Zebker, H. A., Henderson, I. H. C., & Larsen, Y. (2010). Detailed rockslide mapping in northern Norway with small baseline and persistent scatterer interferometric SAR time series methods. *Remote Sensing of Environment*, *114*(9), 2097–2109. https://doi.org/10.1016/j.rse.2010.04.015
Lilleøren, K. S., & Etzelmüller, B. (2011). A regional inventory of rock glaciers and ice-cored moraines in Norway. *Geografiska Annaler*, *93*(3), 175–191. https://doi.org/10.1111/j.1468-0459.2011.00430.x
Liu, L., Millar, C. I., Westfall, R. D., & Zebker, H. A. (2013). Surface motion of active rock glaciers in the Sierra Nevada, California, USA: Inventory and a case study using InSAR. *The Cryosphere*, *7*(4), 1109–1119. https://doi.org/10.5194/tc-7-1109-2013
Merz, K., Green, A. G., Buchli, T., Springman, S. M., & Maurer, H. (2015). A new 3-D thin-skinned rock glacier model based on helicopter GPR results from the Swiss Alps. *Geophysical Research Letters*, *42*, 4464–4472. https://doi.org/10.1002/2015GL063951
Merz, K., Maurer, H., Rabenstein, L., Buchli, T., Springman, S. M., & Zweifel, M. (2016). Multidisciplinary geophysical investigations over an alpine rock glacier. *Geophysics*, *81*(1), WA147–WA157. https://doi.org/10.1190/geo2015-0157.1
Moore, P. L. (2014). Deformation of debris-ice mixtures. *Reviews of Geophysics*, *52*(3), 435–467. https://doi.org/10.1002/2014RG000453
Müller, J., Vieli, A., & Gärtner-Roer, I. (2016). Rock glaciers on the run—Understanding rock glacier landform evolution and recent changes from numerical flow modeling. *The Cryosphere*, *10*(6), 2865–2886. https://doi.org/10.5194/tc-10-2865-2016
Noetzli, J., Luethi, R., & Staub, B. (2016). PERMOS 2016. Permafrost in Switzerland 2010/2011 to 2013/2014. Glaciological Report (Permafrost) No. 12-15 of the Cryospheric Commission of the Swiss Academy of Sciences, 85.
Nopper, H. (2015). Geomorphological study of the rock-slope failure at Adjet, Storfjord, Troms, (Master thesis). (123 pp.) UiT-The Arctic University of Norway, Tromsø, Norway.

Osmundsen, P. T., Henderson, I. H. C., Lauknes, T. R., Larsen, Y., Redfield, T. F., & Dehls, J. (2009). Active normal fault control on landscape and rock-slope failure in northern Norway. *Geology*, *37*(2), 135–138. https://doi.org/10.1130/G25208A.1

Rignot, E., Hallet, B., & Fountain, A. (2002). Rock glacier surface motion in Beacon Valley, Antarctica, from synthetic-aperture radar interferometry. *Geophysical Research Letters*, *29*(12), 1607. https://doi.org/10.1029/2001GL013494

Roer, I., Haeberli, W., Avian, M., Kaufmann, V., Delaloye, R., Lambiel, C., & Kääb, A. (2008). Observations and considerations on destabilizing active rock glaciers in the European Alps. Ninth International Conference on Permafrost, 2, 1505–1510.

Roer, I., Kääb, A., & Dikau, R. (2005). Rockglacier acceleration in the Turtmann valley (Swiss Alps): Probable controls. *Norsk Geografisk Tidsskrift - Norwegian Journal of Geography*, *59*(2), 157–163. https://doi.org/10.1080/00291950510020655

Romanovsky, V. E., Smith, S. L., Isaksen, K., Shiklomanov, N. I., Streletskiy, D. A., Kholodov, A. L., et al. (2016). Terrestrial permafrost [in "State of the Climate in 2015"]. *American Meteorological Society*, *97*(8), 149–152.

Scotti, R., Crosta, G. B., & Villa, A. (2016). Destabilisation of creeping permafrost: The Plator rock glacier case study (Central Italian Alps). *Permafrost and Periglacial Processes.*, *28*(1), 224–236. https://doi.org/10.1002/ppp.1917

Springman, S. M., Arenson, L. U., Yamamoto, Y., Maurer, H., Kos, A., Buchli, T., & Derungs, G. (2012). Multidisciplinary investigations on three rock glaciers in the Swiss Alps: Legacies and future perspectives. *Geografiska Annaler: Series A, Physical Geography*, *94*(2), 215–243. https://doi.org/10.1111/j.1468-0459.2012.00464.x

Wang, X., Liu, L., Zhao, L., Wu, T., Li, Z., & Liu, G. (2017). Mapping and inventorying active rock glaciers in the northern Tien Shan of China using satellite SAR interferometry. *The Cryosphere*, *11*(2), 997–1014. https://doi.org/10.5194/tc-11-997-2017

Wirz, V., Gruber, S., Purves, R. S., Beutel, J., Gärtner-Roer, I., Gubler, S., & Vieli, A. (2016). Short-term velocity variations at three rock glaciers and their relationship with meteorological conditions. *Earth Surface Dynamics*, *4*(1), 103–123. https://doi.org/10.5194/esurf-4-103-2016

Paper V: Environmental controls of InSAR-based periglacial ground dynamics in a Sub-Arctic landscape

Rouyet, L., Karjalainen, O., Niittynen, P., Aalto, J., Luoto, M., Lauknes, T. R., Larsen, Y., Hjort, J.

Under review in *Journal of Geophysical Research: Earth Surface*

Dataset: `http://doi.org/10.5281/zenodo.4173256`

Environmental Controls of InSAR-based Periglacial Ground Dynamics in a Sub-Arctic Landscape

Line Rouyet[1,2,3], Olli Karjalainen[4], Pekka Niittynen[5], Juha Aalto[5,6], Miska Luoto[5], Tom Rune Lauknes[1,2], Yngvar Larsen[1], Jan Hjort[4]

[1] NORCE Norwegian Research Centre AS, Tromsø, Norway
[2] Department of Geosciences, The Arctic University of Norway (UiT), Tromsø, Norway
[3] Arctic Geology Department, The University Centre in Svalbard (UNIS), Longyearbyen, Norway
[4] Geography Research Unit, University of Oulu, Oulu, Finland
[5] Department of Geosciences and Geography, University of Helsinki, Helsinki, Finland
[6] Weather and Climate Change Impact Research, Finnish Meteorological Institute, Helsinki, Finland

Key Points

- Multi-geometry Synthetic Aperture Radar Interferometry documents the distribution of the ground velocity in a periglacial environment.
- Coupling remote sensing and statistical modelling provides insights on the environmental controls of the velocity at the landscape scale.
- Topo-climatic variables are the key factors explaining the ground dynamics associated with cryoturbation and solifluction processes.

Abstract

Periglacial environments are characterized by highly dynamic landscapes. Freezing and thawing lead to ground movement, associated with cryoturbation and solifluction. These processes are sensitive to climate change and variably distributed depending on multiple environmental factors. In this study, we used multi-geometry Sentinel-1 Synthetic Aperture Radar Interferometry (InSAR) to investigate the spatial distribution of the mean annual ground velocity in a mountainous landscape in Northern Norway. Statistical modelling was employed to examine how periglacial ground velocity is related to environmental variables characterizing the diverse climatic, geomorphic, hydrological and ecological conditions within a 148 km^2 study area.

Two-dimensional (2D) InSAR results document mean annual ground velocity up to 15 mm/yr. Vertical and horizontal velocity components in the East–West plane show variable spatial distribution, which can be explained by the characteristics of cryoturbation and solifluction operating differently over flat and sloping terrain. Statistical modelling shows that slope angle and mean annual air temperature variables are the most important environmental factors explaining the distribution of the horizontal and vertical components, respectively. Vegetation and snow cover also have a local influence, interpreted as indicators of the ground material and moisture conditions. The results show contrasted model performance depending on the velocity component used as a response variable. In general, our study highlights the potential of integrating radar remote sensing and statistical modelling to investigate mountainous regions and better understand the relations between environmental factors, periglacial processes and ground dynamics.

Plain Language Summary

In cold regions, freeze and thaw cycles lead to movement in the upper part of the ground. The landscape distribution of these movements depends on several environmental conditions, such as the local climate, topography, vegetation, material type and soil moisture. Here we mapped millimetre to centimetre mean annual ground velocities using a measurement technique based on satellite radar images. We analysed how the environmental conditions are related to the distribution of the ground velocity at the landscape scale. Statistical models were applied to relate the ground velocity to environmental conditions at similar locations and showed that the spatial variability of the air temperature and the slope inclination are the two main controlling factors. Vegetation and snow cover have also an indirect effect due to their link with the ground material and moisture conditions. In general, the study contributes to the development of approaches integrating remote sensing and modelling techniques to cover large and hard-to-access mountainous regions and provide new insights on the processes shaping the landscape in cold environments.

1 Introduction

Cold polar and mountainous regions encompass a broad range of frost-driven processes that shape the landscape. Characterized by seasonally or perennially frozen ground (permafrost), these so-called periglacial environments are highly dynamic (French, 2007) and especially sensitive to climate change (Aalto et al., 2017; Biskaborn et al., 2019; Hjort et al., 2018). Seasonal ground freezing and thawing in the upper part of the ground cause heave and subsidence due to water-to-ice phase change (Bonnaventure & Lamoureux, 2013; Thomas et al., 2009). On periglacial slopes, mass wasting processes driven by gravity induce downslope movement (Harris et al., 2008a; Matsuoka, 2001). When considering slow deformation of unconsolidated material over flat areas and slopes, periglacial processes are respectively referred to as cryoturbation and solifluction (French, 2007). On flat areas covered by thin fine-grained unconsolidated deposits and low ice content, the ground typically heaves and subsidies with a millimetric to centimetric seasonal amplitude (Gruber, 2020; Matsuoka, 2003; Smith, 1987). On slopes, millimetric to centimetric solifluction annual rates (net downslope velocities) have been measured in subarctic areas and mid-latitude mountainous regions with seasonal frost or warm permafrost conditions (Ballantyne, 2013; Harris et al., 2008b; Matsuoka et al., 1997; Ridefelt et al., 2009). At local to regional scales, a large set of climatic (temperature, precipitation), geomorphic (topography, substrate type), ecological (vegetation type) and hydrological factors (soil moisture/water content) have an influence on the spatio-temporal dynamics of the ground (Etzelmüller et al., 2001; Guglielmin et al., 2008; Harris et al., 2003; Hinzman et al., 1991). Changing environmental conditions modify the periglacial ground dynamics, which can impact infrastructure and ecosystems (Harris et al., 2009; Hjort et al., 2018; Jorgenson et al., 2001; Nelson et al., 2002). However, the complexity of the relations between the environmental conditions (controlling factors), the periglacial processes (causes), the ground dynamics and the induced landforms (effects), makes the future impacts challenging to assess (Knight & Harrison, 2013).

Traditionally, geomorphological studies and monitoring of periglacial processes are conducted by in-situ field mapping and measurements (Harris et al., 2009; Romanovsky et al., 2010; Shiklomanov et al., 2012). These observations are often difficult to perform and usually provide sparse and unevenly distributed measurement data. Over the last decades, satellite remote sensing has become a valuable tool to map and monitor periglacial landforms, especially in remote and hard-to-access mountainous areas and Arctic regions (Kääb et al., 2005; Westermann et al., 2015). Repeat-pass satellite Synthetic Aperture Radar Interferometry (InSAR) enables the quantification of ground displacements over large areas. InSAR allows for measuring submillimetre to centimetre sensor-to-ground distance changes derived from the phase differences detected between Synthetic Aperture Radar (SAR) images acquired

at different times (Massonnet & Feigl, 1998). InSAR measurements are along the radar line-of-sight (LOS) and thus intrinsically one-dimensional. The Sentinel-1 SAR mission of the European Commission Copernicus Programme follows a sunsynchronous polar orbit, and observes at an oblique incidence angle towards East (ascending passes) or West (descending passes). Thus, the radar is nearly blind to horizontal North–South displacements, but by combining InSAR results from the two satellite geometries, 2D information in the vertical E–W plane can be estimated (Eriksen et al., 2017). InSAR has been intensively used to map moving landforms in mountainous regions (Barboux et al., 2014, 2015; Dini et al., 2019). Several studies have also analysed InSAR-detected periglacial ground displacements against environmental variables. They demonstrated that the spatio-temporal variability of InSAR results can be related to the air and ground temperature (Bartsch et al., 2019; Strozzi et al., 2019), the thickness of the active layer (Liu et al., 2012; Wang et al., 2018), the water/ice content (Chen et al., 2020; Daout et al., 2017) and the surficial geology (Rouyet et al., 2019; Rudy et al., 2018). The findings show that InSAR has not only a value to identify moving landforms, but also the potential to indirectly document the spatio-temporal patterns of environmental variables controlling periglacial processes (Rouyet et al., 2019). However, the strong spatial heterogeneities characterizing mountainous areas lead to a large variability and combination of processes over short distances (Haeberli et al., 2010). Relating detected moving areas to actual geomorphological processes and their drivers can therefore be a challenging task.

To exploit remotely sensed information for the interpretation of environmental controls of ground dynamics, modern empirical techniques are required to analyse large datasets at regional to global scales. This has been made possible by the development of advanced statistical methods. Several studies have shown the potential of statistical modelling to estimate permafrost distribution (Aalto et al., 2018a; Boeckli et al., 2012; Etzelmüller et al., 2001; Gruber & Hoelzle, 2001) and to capture the multivariate nature of periglacial processes at landscape-scale by documenting how their distribution and dynamics are influenced by environmental factors (Hjort & Luoto, 2011, 2013; Hjort et al., 2014; Karjalainen et al., 2019; Rudy et al., 2017). By statistically identifying the variables influencing the ground thermal regime and periglacial processes, it becomes possible to better explain their current distribution and predict their future evolution based on climate change scenarios (Aalto et al., 2017; Blois et al., 2013; Hjort et al., 2018; Karjalainen et al., 2020). However, previous research has been primarily based on in-situ measurements (e.g. ground temperature from boreholes) or mapped landforms (e.g. inventory of solifluction lobes and palsas) and few studies have integrated advanced remote sensing data documenting periglacial activity, such as InSAR-based ground velocity.

Here we examine the environmental controls associated with the spatial variability of mean annual ground velocities derived from Sentinel-1 InSAR measurements in a sub-arctic landscape. We use statistical multivariate modelling to relate the response variables (horizontal, vertical and combined 2D velocities) to seven environmental factors represented with geospatial data. To our knowledge, this is the first study to analyse InSAR results using spatially explicit statistical modelling. Specifically, we aim to 1) document the distribution of ground velocity associated with cryoturbation and solifluction in a mountainous environment in Northern Norway, 2) examine the relative importance and effects of the environmental factors on the periglacial ground dynamics, and 3) discuss the limitations and implications of our findings in the context of periglacial research.

2 Study area

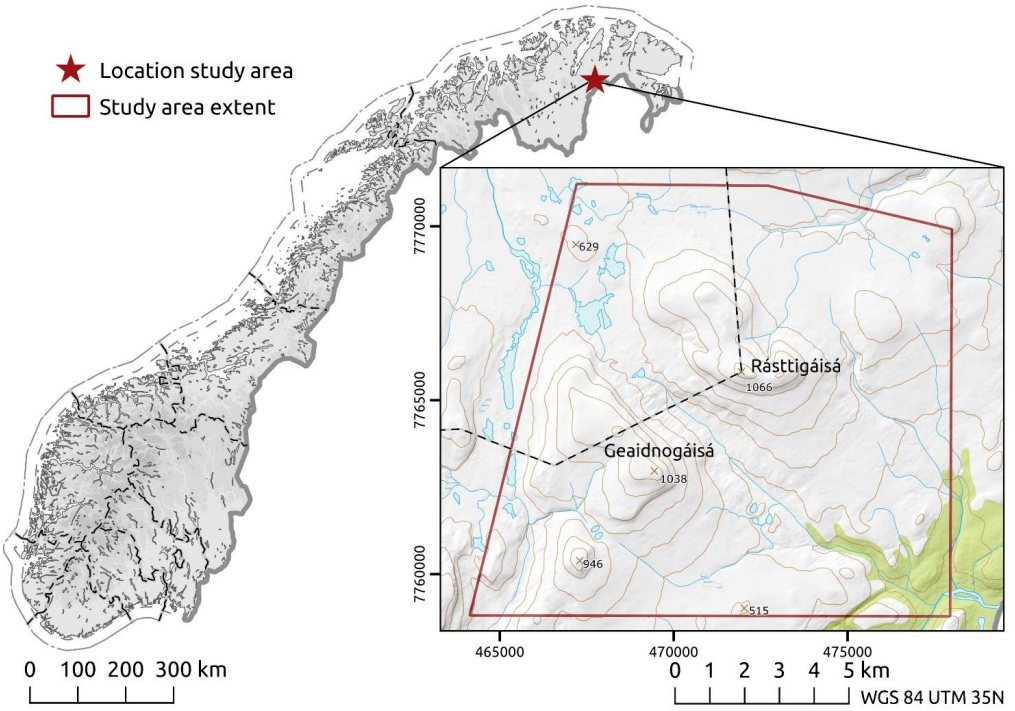

Figure 1. Study area location in Troms and Finnmark county (Northern Norway) centred around two mountains: Geaidnogáisá and Rásttigáisá. Background: topographical map of the Norwegian territory (NMA, 2020a). Brown lines: 100 m elevation contour lines. Grey-black lines: administrative borders (dashed lines in inset: border between Tana and Lebesby municipalities).

The study area is located in the Gaissane mountain massif in the county of Troms and Finnmark, Northern Norway (70°00'N, 26°14'E). The region is part of the subarctic zone, characterized by long cold winters and short cool summers (NCCS, 2021). Northern Norway is affected by a large climatic gradient between the temperate and humid coasts and the cold and dry continental interior. The permafrost follows a similar distribution. The limit of the discontinuous zone, where permafrost is underlying 50–90% of the landscape, is around 1000 m a.s.l in the North-West and decreases below 400 m a.s.l. towards South-East (Farbrot et al., 2013; Gisnås et al., 2017). Both direct observations and physical models indicate that permafrost in Northern Norway is mainly warm (temperature above -3°C), and variably distributed depending on the vegetation and snow cover (Farbrot et al., 2008; Isaksen et al., 2008). In-situ measurements indicate that the permafrost has warmed and degraded (Christiansen et al., 2010; Isaksen et al., 2007), and models project that this trend is likely to continue for the next decades (Gisnås et al., 2013; Farbrot et al., 2013).

The study area consists of ca. 148 km^2 (Figure 1). The topography is characterised by two mountain massifs (Rásttigáisá at 1,066 m a.s.l and Geaidnogáisá at 1,038 m a.s.l) separated by a 2-km wide and 0.5-km deep NW-SE valley. The area has a large altitudinal gradient between 122 m a.s.l and 1,066 m a.s.l. The bedrock is composed of Precambrian crystalline rocks and layers of shales (Hyolithus zone), covered by peat, fluvial sediments, glacial till and boulder fields (Niittynen & Luoto, 2018). The study

area has a mean annual air temperature below zero (-0.3 to -5.7°C; 1981–2010) and a mean annual precipitation sum between 457 and 669 mm (Aalto et al., 2017). The altitudinal gradient leads to a large spatial variability of the mean annual air temperature within the area (Aalto et al., 2017). Due to the complex local topography, the snow accumulates unevenly, and the snow persistence pattern is highly variable (Niittynen et al., 2018). Rásttigáisá-Geaidnogáisá area is part of the circumpolar arctic vegetation zone (Olson et al., 2001; Virtanen et al., 2016), at the transition between different main biomes of the northern high-latitude environment. The mountain birch forest line is at 250–350 m a.s.l., and thus, trees are only present in the lowest valleys.

According to the circum-arctic map of permafrost and ground-ice conditions (Brown et al., 2002), the study area is at the interface between the sporadic permafrost zone with medium ground ice content (10–20 %) and thick overburden (lowlands, highlands, and intra- and intermontane depressions), and the discontinuous permafrost zone with low ground ice content (0–10 %), thin overburden and exposed bedrock (mountains, highlands ridges, and plateaus). Kilometric products based on thermal remote sensing and physical modelling also show a large variability of the ground temperature, permafrost probability and active layer thickness (typically between 1 and 3 m) (Gisnås et al., 2017; Obu et al., 2019; 2020). Freeze and thaw processes lead to the development of a large range of periglacial landforms, such as patterned ground, peat plateaus, earth hummocks and solifluction lobes (Martin et al., 2019; Seppälä, 2011).

3 Data and methods

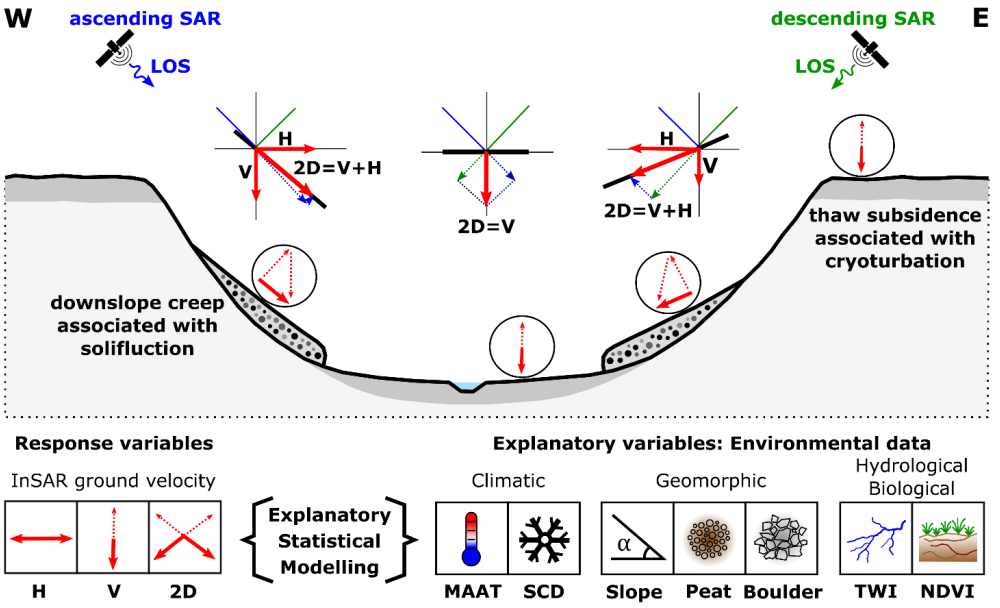

Figure 2: Conceptual scheme of the contribution of explanatory statistical modelling to relate ground dynamics documented by multi-geometry InSAR to environmental factors and provide new insights on the controls and effects of periglacial processes in mountainous landscapes. Dotted arrows show the expected components of the ground velocity associated with cryoturbation and solifluction. Solid bold arrows show the components that are measured using multi-annual 2D InSAR. The acronyms refer to Synthetic Aperture Radar (SAR), line-of-sight (LOS), vertical (V), horizontal (H), two-dimensional (2D), mean annual air temperature (MAAT), snow cover duration (SCD), topographic wetness index (TWI) and normalized difference vegetation index (NDVI).

The study presents an analysis of InSAR-based 2D mean annual ground velocity maps using multivariate statistical modelling. 2D InSAR results (response variables, Section 3.1) document the ground dynamics associated with periglacial processes identified in the study area (field observations, Section 3.2). The response variables are related to seven explanatory variables describing the environmental conditions (Sections 3.3) using statistical models (Section 3.4). This provides new insights about the factors controlling the horizontal, vertical and combined 2D ground velocities associated with cryoturbation and solifluction (Figure 2).

3.1 InSAR products as response variables

InSAR results are based on SAR images from the Sentinel-1 mission of the European Commission Copernicus Programme. The selected Interferometric Wide swath Mode scenes were acquired between 2015 and 2018 (Table 1). A total of 72 scenes were used in ascending geometry (track 14), and 67 in descending geometry (track 124). The sensor looks obliquely downward (~30° between the normal to the Earth's surface and the beam; see LOS incidence angles in Table 1), towards ENE for ascending acquisitions and towards WNW for descending acquisitions (~74°N and ~286°N of compass directions, see LOS orientations in Table 1). The observation period lasts 1,236 days (03.06.2015–21.10.2018) but the dataset includes gaps in winter, as only scenes with little snow cover have been selected (June to October).

Table 1: Properties of the Sentinel-1 SAR images used for InSAR processing. Acronyms refer to Interferometric Wide (IW) swath mode and line-of-sight (LOS).

SAR sensor	Frequency band (wavelength)	Time intervals for interferogram generation	SAR mode, track number and geometry	Number of selected scenes	Observation period (first-last selected scenes)	LOS orientation and incidence angle
Sentinel-1	C (5.55 cm)	6 to 360 days	IW, 14, ascending	72	03.06.2015 – 21.10.2018 (June–October)	74.2° 30.4°
			IW, 124, descending	67	11.06.2015 – 05.10.2018 (June–October)	286.3° 30.4°

We applied an InSAR technique employing spatial averaging (multi-looking) to reduce noise from scattering mechanisms in nonurban areas (Berardino et al., 2002). InSAR results were processed using the NORCE GSAR software (Larsen et al., 2005). Single Look Complex (SLC) images were co-registered and multi-looked using a range/azimuth factor of 8x2, providing a ground resolution of ca. 40 m. We chose this multi-looking factor as a trade-off for preserving the highest resolution as possible, while avoiding reducing the reliability of the coherence estimate that decreases with low factors (Bamler & Hartl, 1998). Interferometric image pairs (interferograms) were generated with a maximal temporal baseline of 360 days, accounting for expected low velocities in the study area (mm–cm/year). The pairwise distance between the satellite positions at the acquisition times used for generating each interferogram, the so called spatial baseline, has not been restricted. The effective maximal values (210 m for the ascending stack, 136 m for the descending stack) are clearly under the limit, for which there is no remaining spatial coherence (critical baseline, approximately 5 km for Sentinel-1). The small spatial baselines lead to small topographical component, which was estimated and removed using a 10 m DEM (NMA, 2016). The noise-level was reduced in all interferograms by applying a spatially adaptive coherence-dependent Goldstein filter (Goldstein & Werner, 1998; Baran et al., 2003). The datasets consist of 592 selected interferograms (SAR pairs) in ascending geometry and 471 in descending geometry (baseline plots in Supplement S1 and S2). Strongly decorrelated interferograms

(mean coherence under 0.45) were removed, and pixels affected by layover were masked out. Pixels affected by low signal stability due to snow (e.g. perennial patches), water (e.g. lakes, rivers) or dense vegetation (e.g. forested areas) in most of the pairs were removed by applying a coherence-based filter (above 0.45 in at least 50% of the interferograms) (Berardino et al., 2002). If snow cover dominated in one acquisition, the coherence drops and the interferograms based on that image were discarded. Similarly, if snow at one specific location was affecting too many interferograms in the stack (perennial patches), the pixel was discarded. Despite the relatively conservative thresholds, the effect of scattering mechanisms in coherent areas must be considered, as the differential propagation of the electromagnetic wave due to changing dielectric properties of the ground surface may lead to biased phase estimates. In high-latitude environments, one main limitation for InSAR is the snow (Zwieback et al., 2016). If the coherence dropped for isolated pixels in a limited amount of image pairs (e.g. early or late summer), wrong estimates may have been included in the results. As for snow, phase bias can occur due to volume scattering from ground moisture and biomass (De Zan et al., 2014; Zwieback et al., 2015; Zwieback & Hajnsek, 2014). However, the large stack and long temporal baseline used in the current study is expected to mitigate these effects (Ansari et al., 2020).

The conversion from cyclic to continuous phase differences, so called unwrapping, is performed using the SNAPHU algorithm (Chen & Zebker, 2002). Due to the low velocity and good coherence in the study area, no major unwrapping errors have been identified in the processed interferograms. InSAR is a spatially relative technique, meaning that it must be calibrated to a reference location. The calibration is ideally performed using a point with a known velocity (Eriksen et al., 2017b). In a remote environment where in-situ measurements are not available or not comparable to the resolution of the InSAR measurements, this is unfortunately often not feasible (Antonova et al., 2018). Different reference points were tested and a common reference for both datasets was chosen in an area assumed to be stable. It is located in the valley between Rásttigáisá and Geaidnogáisá (70°00’15.1’’N 26°11’57.1’’E, mapped in Figures 5–6), in flat terrain (< 2° slope angle) with visible rock crop and little soil cover, leading to high InSAR coherence (> 0.7 for both geometries). All InSAR results are spatially relative to this location. We estimated ground displacements using the Small Baseline Subset (SBAS) method (Berardino et al., 2002). The focus is placed on spatial distribution, and all results are based on averaged values. The phase inversion was performed using a linear deformation model. We solved for the mean annual ground velocity based on a L1-norm-based cost function, which is more robust than L2-norm with respect to unwrapping errors (Lauknes et al., 2011b). For the atmospheric filtering, we used a spatial filter of 2000 m spatial filter and a temporal filter of 120 days. The contribution from the stratified atmosphere was mitigated by a data-driven approach where we study the relation between residual phase and topography (Cavalié et al., 2007) using a Digital Elevation Model (DEM) at 10 m resolution (NMA, 2016). Based on a redundant set of interferograms, we further solved for the stratified delay per scene using a network-based approach (Lauknes, 2011a). The initial InSAR ground velocity maps from both ascending and descending geometries were compared with results from the freely available InSAR Norway ground motion mapping service (Dehls et al., 2019; NGU, 2020). The processing is also based on Sentinel-1 images, but applies a Persistent Scatterer Interferometry (PSI) algorithm (Ferretti et al., 2001) that allows for preserving the full resolution of the images (5 x 20 m in range x azimuth). PSI results are based on different reference points and document another scattering mechanism than SBAS. They are used to qualitatively assess the general consistency of our results.

InSAR measurements from ascending and descending geometries correspond to one-dimensional (1D) sensor-to-ground distance change along the LOS. By combining both geometries, it is possible to estimate the 2D velocity in the vertical plane spanned by the ascending and descending LOS orientations, which approximately is E–W (Eriksen et al., 2017). The results were also decomposed into vertical (Up–Down, U–D) and horizontal (East–West, E–W) components (Figure 2). It should be noted that the radar is still blind to displacements orthogonal to the LOS plane, which leads to an

underestimation of the measurements in case of a large North–South (N–S) horizontal component. To avoid misinterpretation when analysing gravity-driven processes such as solifluction, we masked out pixels in areas where a significant horizontal component towards N or S is expected (Rouyet et al., 2019). As reported by Matsuoka (2001), the slope angles of documented solifluction landforms can range from 2 to 41°. Based on this information, we masked out areas with slope angles over 2° and slope orientations ± 22.5° around 360° (N) and 180° (S) (compass directions 337.5–22.5°N and 157.5–202.5°N) (grey areas in Figure 3). All areas with slope angles below 2° were included assuming that they are mainly affected by a vertical component. All E–W slopes are included, assuming that they do not include a significant N–S component.

InSAR processing leads to the development of three products, further used as response variables: 1) the horizontal velocity, 2) the vertical velocity, 3) the 2D velocity consisting in the combination of the two previous components. Considering the long total observation period (3 years) and the relatively small extent of the study area (approx. 12x12 km), we estimate that the accuracy is well below 1 mm/yr (Supplement S3), assuming that atmosphere is the dominant noise source (Emardson et al., 2003). The closer to the reference point, the higher the accuracy. The results document mean velocities in mm/yr that are mostly designed for gradual multi-annual processes, such as the net downslope component of the solifluction. However, as no winter scenes are included, the InSAR results are mostly representative of the thawing periods, which emphasize the downward component of the cryoturbation. Prior to statistical modelling, all results are converted to absolute values to focus on the magnitude of the vertical, horizontal and combined 2D velocities, instead of their direction. The number of pixels where ground displacement is documented is 69,035, corresponding to ca. 74% of the study area (110 km^2). They were geocoded using a DEM at 10 m resolution (NMA, 2016). The final products have a 40 m ground resolution, documenting the averaged contribution of scatterers within the pixels. Although very fine-scale processes may not be captured by these medium resolution products, the results are assumed to be appropriate to assess the relative spatial variability of the ground dynamics in the study area and discuss their relations with environmental variables.

3.2 Field observations of cryoturbation and solifluction

The cover of cryoturbation and solifluction (m^2) activity within 100 m^2 grids was mapped at 674 randomly selected field sites across the study area during the 2015–2016 summer seasons. The activity was visually estimated using indicators, such as vegetation density, lichen cover and frost disturbance, following the methodology presented in Hjort & Luoto (2009). Based on the field observations, the activity was then classified as negligible (< 20 m^2), low (20–40 m^2), medium (40–60 m^2) and high (> 60 m^2) for both processes. Solifluction is the dominant process in the area (Figure 3A). At 429 locations, the InSAR results overlap with field sites (at maximum one per pixel, Figure 3A) and the activity rating has been compared with the response variables to assess the relevance of the spatial variability of InSAR-detected ground velocity. A quantitative comparison is not feasible due to the differences of measure and spatial resolution between the remotely sensed (ground velocity within 40x40 m pixels) and field information (qualitative documentation of activity within 10x10 m grids). The field observations are however valuable to assess the overall consistency of the InSAR spatial patterns at the landscape scale. Additional visual interpretation has been performed using 0.25–0.5 m resolution orthophotos from summer 2010, 2016 and 2018 (NMA, 2020b).

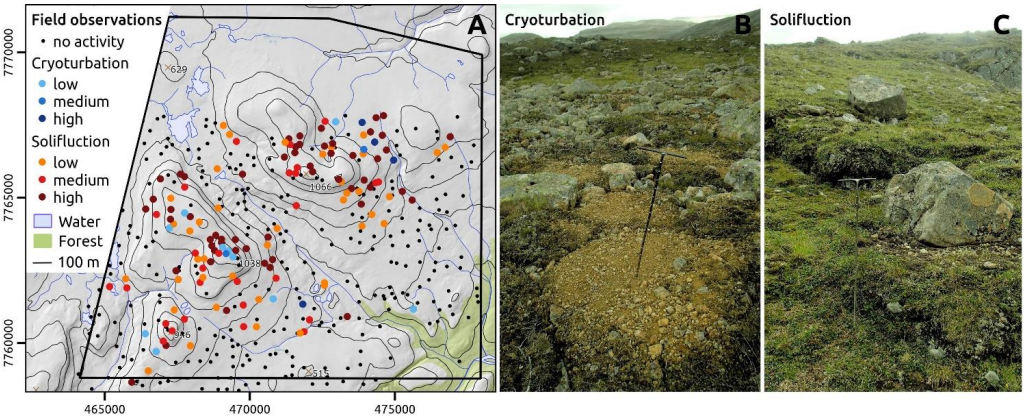

Figure 3: Field observation of cryoturbation and solifluction activity. A) The field observation sites (dots) and locations where cryoturbation (blue dots) and solifluction (red dots) activity has been qualitatively rated as negligeable, low, medium or high. Topographical data from NMA (2020a). B) An example of field site with high cryoturbation activity. C) An example of field site with high solifluction activity.

3.3 Environmental data as explanatory variables

Seven environmental datasets, used as explanatory variables, were related to the InSAR products (response variables). The explanatory variables represent the climatic, geomorphic, hydrological and biological conditions in the study area (Table 2).

Climatic variables include the mean annual air temperature (MAAT) based on air temperature modelled from 942 climate stations in Scandinavia between 1981–2010 (Aalto et al., 2017) (Figure 4A) and snow cover duration (SCD) using 1984–2016 Landsat-5, -7 and -8 imagery (Niittynen et al., 2018; Niittynen & Luoto, 2018). InSAR does not document the winter period and the pixels persistently covered by snow. However, variable duration of seasonal snow cover prior to InSAR measurements leads to variable meltwater input and impacts the thermal transfer between the atmosphere and the ground.

Geomorphic variables include the slope angle based on the ArcticDEM (Porter et al., 2018) and the Norwegian DEM (NMA, 2016) (Figure 4B) and surface geology variables. The Norwegian DEM (original resolution 10 m) was used to fill missing data in the ArcticDEM mosaic (~5% of the study area) by bilinearly interpolating the Norwegian DEM to match with the ArcticDEM original resolution (1.857 m) and aggregating the merged product by a factor of six resulting in a final ~11 m DEM (Niittynen et al., 2020). Surface geology variables are extracted from a 2 m resolution land cover map based on field surveys and optical images (resolution 0.5–1.4 m) (Niittynen & Luoto, 2018), documenting the distribution of 6 classes: water bodies, fluvial deposits, moraines, bedrock, boulder fields and peat material (Supplement S4). The binary dataset has been transformed to continuous by calculating the number of 2 m pixels inside 40 m pixels. The resulting values represent the percent (0–100%) of the material covering the pixel surface. In order to reduce model complexity and overfitting potential, we included only two surface geology variables, hereafter referred to as Peat and Boulder (Table 2). The selection was based on the decrease in explained deviance by the models when each variable was omitted in their turn from a model containing all variables. Based on averaged deviance reductions over 10 permutations for each modelling technique (see Section 3.4) and the three InSAR responses, Peat and Boulder had the highest statistical contributions.

Hydrological and biological variables include the topographic wetness index (TWI) computed in SAGA GIS (System for Automated Geoscientific Analyses, Conrad et al., 2015) and the pixel-wise

95% quantile of the normalized difference vegetation index (NDVI) computed from 97 mostly cloud-free Sentinel-2 images from June–September 2016–2019. Pixels with adverse conditions (deep shadows, snow, water or clouds) were masked out prior to calculating the quantiles. The 95% quantile was selected over the pixel-wise maximum to further limit the possible effects of erroneous pixel values.

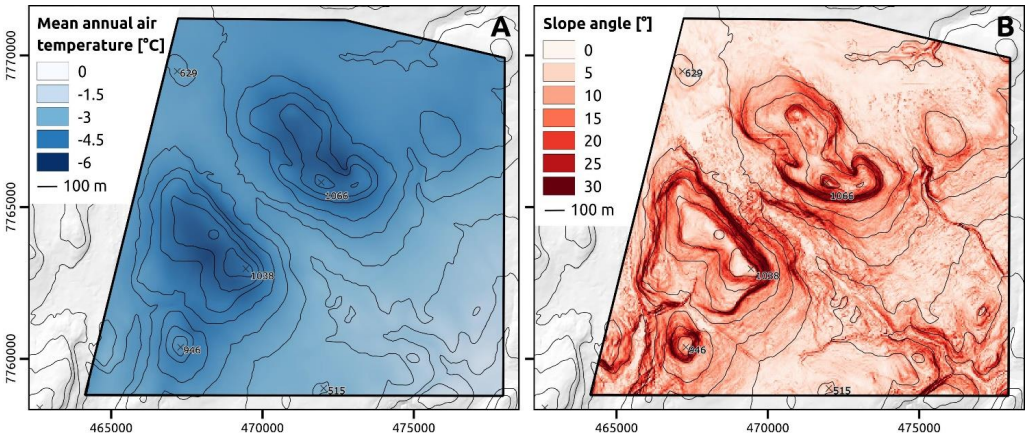

Figure 4: Spatial distribution of two explanatory variables. A. Mean annual air temperature (MAAT) (Aalto et al., 2017). B. Slope angle (Porter et al., 2018; NMA, 2016). Similar maps for the five other selected variables (Table 2) are shown in Supplement (S4).

Table 2: List of explanatory variables and properties of the initial datasets. Acronyms refer to mean annual air temperature (MAAT), snow cover duration (SCD), topographic wetness index (TWI) and normalized difference vegetation index (NDVI). *unit after binary to continuous transformation.

Name	Description	Unit	Data source	Native resolution [m]	References
MAAT	Mean Annual Air Temperature	°C	Weather stations and topo-climatic modelling	10 m	*Aalto et al., 2017*
SCD	Snow Cover Duration	days	Landsat-5, -7 and -8	30 m	*Niittynen et al., 2018* *Niittynen & Luoto, 2018*
Slope	Slope angle	degrees	ArcticDEM and Norwegian Mapping authority	11.142 m	*Porter et al., 2018* *NMA, 2016*
Peat	Surface geology class "Peat"	unitless (%*)	Pleiades imagery	2 m	*Niittynen & Luoto, 2018*
Boulder	Surface geology class "Boulder"	unitless (%*)	Pleiades imagery	2 m	*Niittynen & Luoto, 2018*
TWI	Topographic wetness index	unitless	ArcticDEM and Norwegian Mapping authority	11.142 m	*Böhner et al., 2002* *Conrad et al., 2015* *NMA, 2016*
NDVI	95% quantile of Normalized Difference Vegetation Index	unitless	Sentinel-2	10 m	*Rouse et al., 1974*

All the variables (Table 2) were resampled to 40 m pixel resolution using Resample function in ArcGIS 10.7.1 (ESRI, 2019) with bilinear sampling to spatially match with InSAR results. After removing pixels with no data, there were 68,590 pixels documented both by the InSAR products (response variables) and the environmental data (explanatory variables). Maps showing the spatial distribution of SCD, NDVI Peat, Boulder, TWI are in Supplement (S4). The distributions of all variable values are shown in Supplement (S5).

3.4 Explanatory statistical modelling

We used statistical modelling to examine the importance and effect of the selected environmental factors on InSAR mean annual ground velocities. The model inputs and outputs are floating velocity values expressed in mm/yr. The modelling was conducted with the R Statistical Software (R-version 3.6.3). Prior to modelling, we explored bivariate Spearman correlations in the modelling dataset (Supplement S6). Only the correlation between MAAT and NDVI (0.70) reached the usually applied |0.70| threshold for multicollinearity (Dormann et al., 2013). We additionally applied variance inflation factor (VIF) analysis to test whether multicollinearity between the explanatory variables was confounding the modelling. VIF values for each variable were < 6, which is under the critical threshold value of 10 (Dormann et al., 2013). This suggests that strong multicollinearity is not present in the dataset. The three InSAR products (see Section 3.1) are examined separately as response variables: 1) the horizontal velocity, 2) the vertical velocity, and 3) the combined 2D velocity.

In order to account for the potential uncertainties related to single models, we used four techniques. The generalized boosting method (GBM, R package dismo; Elith et al., 2008) is the main method used to discuss the findings, while three others are applied to assess the results' consistency (Supplement S0). GBM was run with a learning rate of 0.001, a bag fraction of 0.75, and a tree complexity of 5 (Elith et al., 2008). A slow learning rate was chosen to ensure that single trees would not have an overly high contribution to the final model. We also made sure that 1000 trees at minimum and 3000 trees at maximum were fitted and used the gbm.step function (Elith et al., 2008) to determine the optimal number of trees in order to minimize holdout deviance.

The models were fitted using all the selected seven environmental variables (see Section 3.3) in order to allow comparisons between variable contributions for each response. The procedure follows the workflow illustrated in Figure 5. In total, the InSAR mapping yielded 69,035 pixels across the study area. The high density of measurements can lead to a problem of spatial autocorrelation, i.e. nearby observations are likely to be more similar with each other than those further away (Legendre, 1993). Spatial autocorrelation can affect modelling by overfitting some random spatial patterns in variables and underestimating prediction errors. It may produce unrealistic responses and increase Type I errors in statistical testing, i.e. a variable is selected to the model even if it should not be (false positive) (Dormann et al., 2007). To ensure that the spatial autocorrelation is not causing bias to model estimates, we first selected 500 random samples of 1,000 InSAR pixels and fitted exponential variograms to average semi-variances calculated from the prediction residuals of a generalized additive model based on the entire dataset (Supplements S0 and S7). Among the three responses, the average distance at which spatial autocorrelation dissipated was 289 meters. We then used this distance to select 200 random samples, i.e. modelling datasets, from all InSAR measurements using the "Create random points" tool in ArcMap (ESRI, 2019). Thereby, on average 1,110 pixels were selected in each dataset with distributions similar to that of all InSAR measurements (Supplement S8).

Model evaluation was performed by using 90% of the spatially independent InSAR pixel values in each modelling dataset to calibrate the models and the remaining 10% to evaluate their performance. A high calibration proportion was used to maximise the representativeness of the calibration datasets of all InSAR observations. Based on the 200 runs, we computed means and confidence intervals of

coefficient of determination (R^2, i.e. the proportion of explained variance), root mean square error (RMSE, in mm) and mean absolute error (MAE, in mm).

The relative importance of each environmental variable in the models was estimated by calculating a measure of variable importance (Thuiller et al., 2009). The variable importance value is the inverse Pearson's correlation between predictions that are produced with the previously calibrated models for two distinct datasets; one with intact seven variables, and another where one variable is randomized:

$$\text{Variable importance} = 1 - r(\text{Prediction}_{\text{intact variables}}, \text{Prediction}_{\text{one variable randomized}}) \quad (1)$$

Where r is the Pearson product-moment correlation. The closer the variable importance is to 1, the higher its individual contribution to predicted velocity. Each modelling technique was run using the 200 modelling datasets for each response with each variable randomized separately.

Lastly, we plotted response curves based on GBM results averaged over the 200 runs. We used the calibrated 200 models to predict the InSAR velocities for the 68,590 common pixels, in which each explanatory variable in turn was kept intact while the others were fixed to their mean. This way, we obtained 200 values depicting the response of the velocity components to each realized value of an explanatory variable over the entire range of the InSAR velocities. We then computed the average and standard deviation of these 200 values to plot response curves for each variable across their range in the entire dataset.

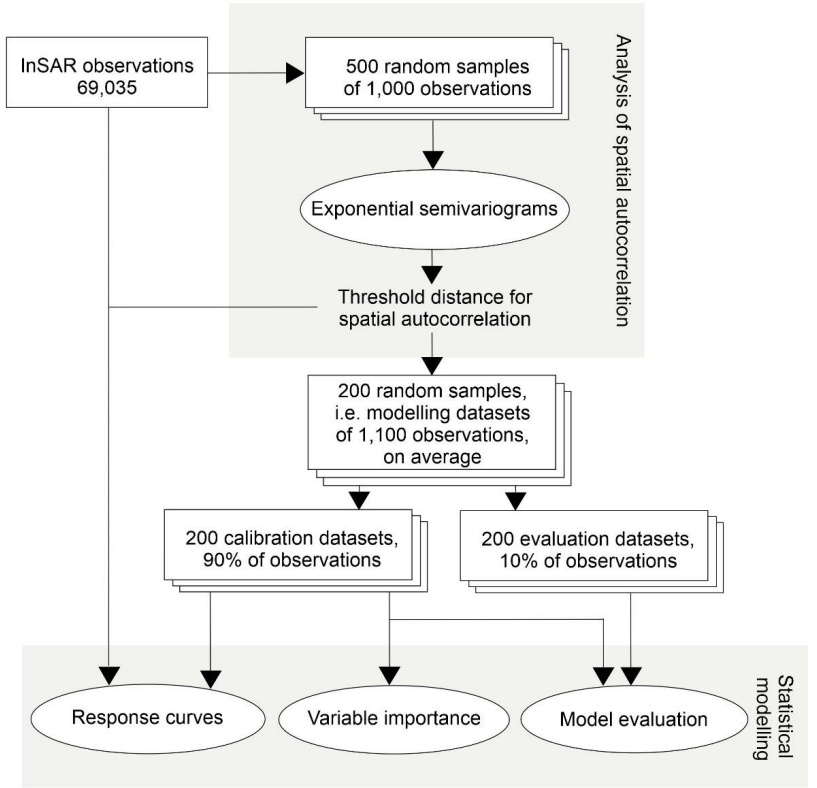

Figure 5: Schematic illustration of the statistical modelling workflow.

4 Results

4.1 InSAR results

The initial InSAR results along LOS from both the ascending and descending geometries show expected velocities towards the sensor on slopes facing the radar, and away from the sensor on back-facing slopes (Figure 6, A–B). Pixels with no data correspond to areas with radar layover or shadow due to steep topography, forested areas in the south-eastern part, lakes/ponds or persistent snow (InSAR coherence under the chosen threshold, see Section 3.1). Ascending and descending SBAS results are compared to the PSI maps from the InSAR Norway mapping service (see Section 3.1). Similar velocity ranges (mm/yr to cm/yr) and spatial distribution are found (Supplement S9), which can be considered as an indicator of the results' validity.

After 2D InSAR calculation and decomposition, the results show that the vertical and horizontal components of the velocity are differently distributed. On slopes, mass wasting processes lead to a combination of horizontal and vertical velocities, while the flat areas are affected by vertical velocities, especially on mountain tops (Figure 6, C–D). Before conversion to absolute values, we analyse the relevance of the directional patterns for both the horizontal and vertical components. The average velocity at the InSAR reference point (black star in Figures 5–6) is -0.23, 0.20 and 0.30 mm/yr for the horizontal, vertical and 2D velocity, respectively. As expected, westwards horizontal velocities (negative values) are located on west-facing slopes, while eastwards (positive values) are on east-facing slopes (Figure 6C). Horizontal velocity has a mean of 0.44 mm/yr with a higher number of positive pixels (eastwards). This may indicate a minor shift of the velocity values due to a westward velocity at the InSAR reference point, but also represent the natural higher proportion of east-facing slopes in the area. The vertical values are mostly positive (> 80%) (Figure 6D), corresponding to a subsidence, which is expected when using mean velocity measurements based on observations during the thawing periods. Among the pixels with negative (upwards) trend, over 75 % are between 0 and -0.5 mm/yr and less than 1% are under -1 mm/yr. These values are part of the overall dataset variability. They are likely due to phase bias (sources introduced in Section 3.1 and further discussed in 5.3), but may also represent a natural trend.

For the exploratory statistical modelling, absolute values are considered, to focus on the movement magnitude instead of its direction. InSAR detects velocity up to 11 mm/year eastwards and westwards (horizontal component), up to 14 mm/yr vertically and up to 15 mm/yr when combining both components into a 2D information (Figure 7). The distribution is right-skewed, with clearly a higher proportion of low values (Figure 7D). Despite the low velocity in average, the results show a clear spatial pattern, with higher velocities on slopes and mountain tops (Figure 6 and Supplement S10). At the 429 locations where InSAR results overlapped with field observations (see Section 3.2), the activity rate is overall higher in areas where InSAR detected high velocities, i.e. on slopes and mountain tops (Figures 7–8). The InSAR 2D velocity from locations rated with high activity is overall higher than those with negligible, low and medium activity (Supplement S11). Detailed maps show highly active areas where patterned ground (Figure 8, a, d, f) and solifluction lobes (Figure 8, b, c, e, g, h) can be seen on aerial imagery.

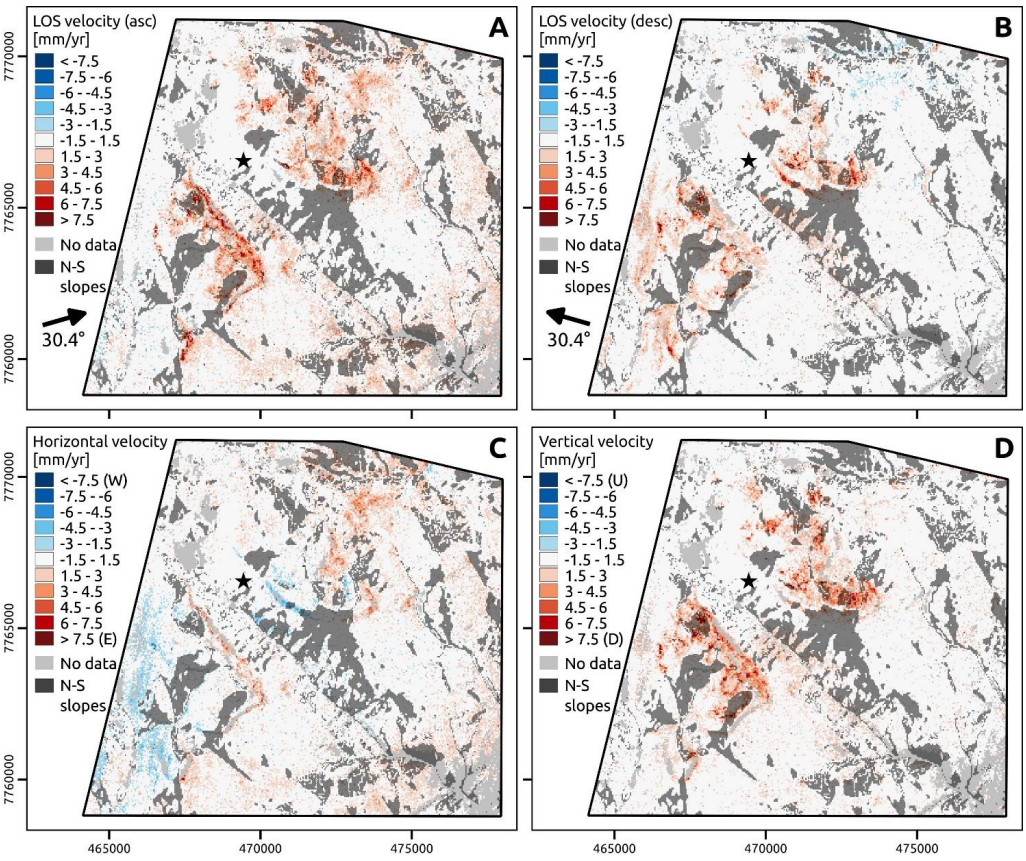

Figure 6: Initial InSAR datasets. A–B) Mean annual ground velocity maps along the line-of-sight (LOS). Black arrow shows the LOS orientation (the label indicates the incidence angle). Negative values indicate a decrease of the sensor-to-ground distance, positive values an increase of the sensor-to-ground distance. A) Velocity [mm/yr] along the ascending (asc) LOS. B) Velocity [mm/yr] along the descending (desc) LOS. C–D) Directional velocity after 2D decomposition. C) Horizontal East–West velocity. Negative values: towards West (W). Positive values: towards East (E). D) Vertical Up–Down velocity. Negative values: upwards (U). Positive values: downwards (D). Black star: InSAR reference point. Semi-opaque dark grey layer: areas masked out in further analysis (North-/South-facing slopes, see Section 3.1).

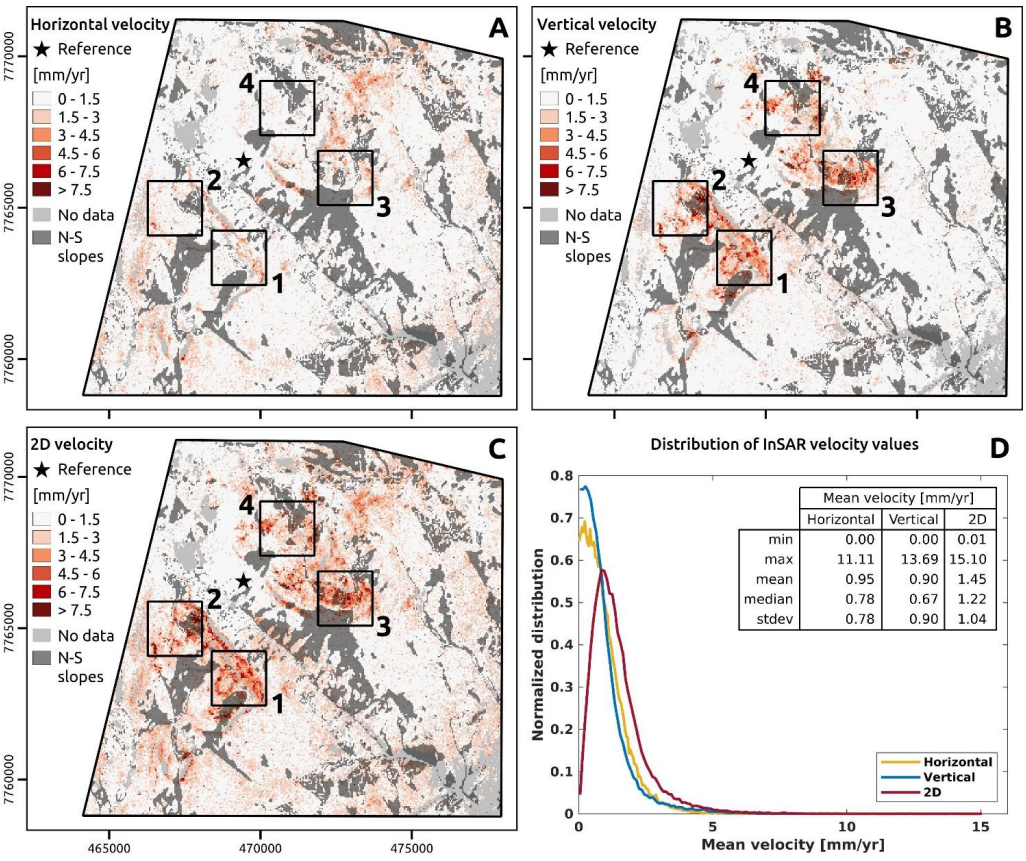

Figure 7: Absolute 2D InSAR mean annual ground velocity results used as response variables. A) Horizontal component of the velocity [mm/yr]. B) Vertical component of the velocity [mm/year]. C. 2D combined velocity [mm/year]. A–C) Black star: InSAR reference point. Semi-opaque dark grey layer: areas masked out in further analysis (North-/South-facing slopes, see Section 3.1). Black squares: detailed areas shown in Figure 8. D) Distribution (kernel densities) and statistics of the response variables: horizontal, vertical and 2D combined velocity for the 69,035 available InSAR pixels.

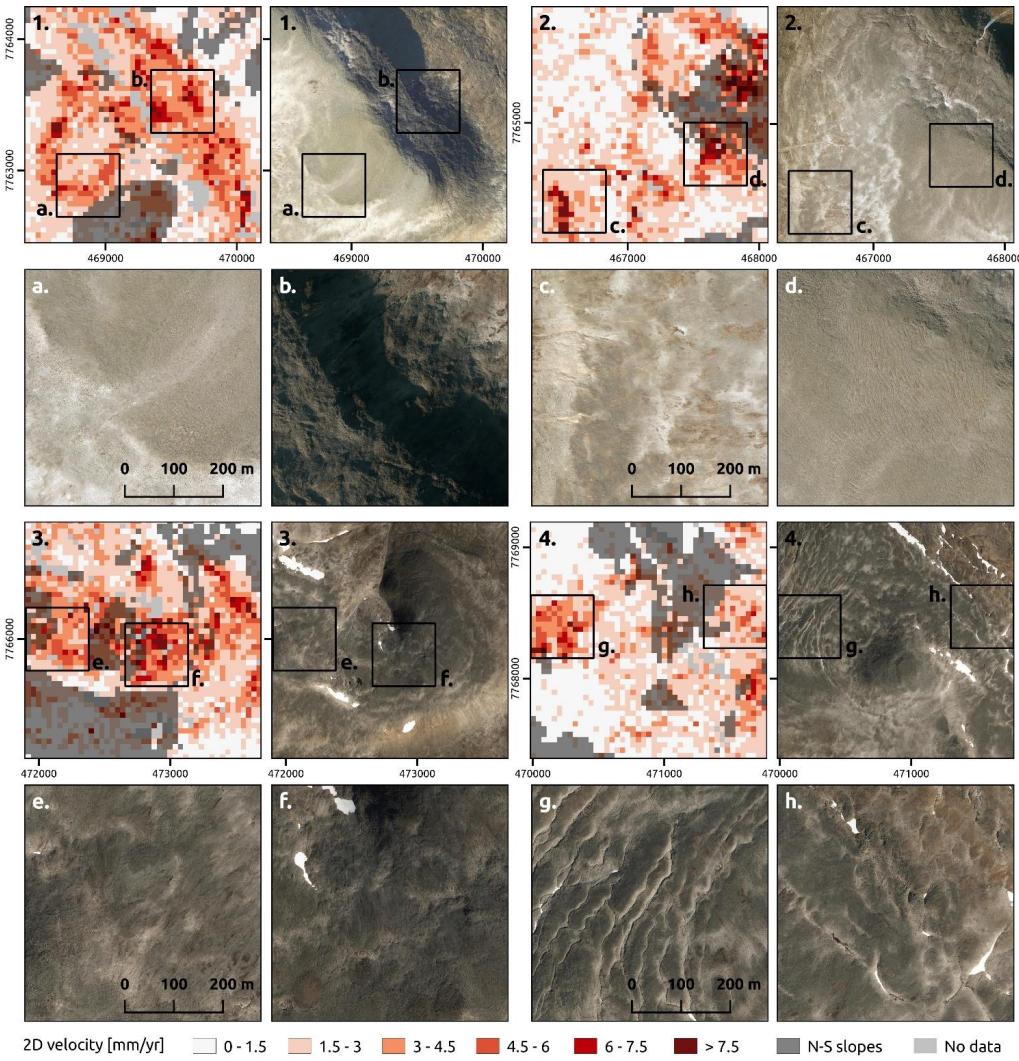

Figure 8: Detailed areas comparing 2D InSAR mean annual ground velocity (see locations 1–4 in Figure 7) and aerial orthoimagery (NMA, 2020b). a–h: Orthophoto view at a smaller extent with visual expression of cryoturbation (a, d, f) and solifluction (b, c, e, g, h) features (patterned ground and solifluction lobes) associated with the detected velocities.

4.2 Statistical modelling

GBM results highlight contrasted model performance (Table 3). The model performed better based on the vertical component (47% of the explained variance), compared to the horizontal component (24% of the explained variance). Prediction errors for each velocity component were slightly higher for evaluation datasets and the variations explained by the models decrease sharply when predicted over independent evaluation datasets. The modelling datasets have similar distributions compared to the 69,035 InSAR measurements shown in Figure 7D (Supplement S8).

Table 3. GBM modelling performance in terms of coefficient of determination (R^2), root mean square error (RMSE) and mean absolute error (MAE) and for each response variable. The values (averages +/- one standard deviation) are based on 200 resampling rounds for calibration (90% of observations in each sample) and evaluation datasets (10%). Evaluation results for the three complementary models are listed in Supplement S12.

	R^2		**RMSE**		**MAE**	
	Calibration	Evaluation	Calibration	Evaluation	Calibration	Evaluation
Horizontal	0.24 ± 0.04	0.08 ± 0.08	0.68 ± 0.03	0.74 ± 0.10	0.52 ± 0.02	0.56 ± 0.05
Vertical	0.47 ± 0.04	0.28 ± 0.13	0.66 ± 0.03	0.75 ± 0.13	0.47 ± 0.02	0.51 ± 0.05
2D	0.38 ± 0.04	0.21 ± 0.10	0.82 ± 0.04	0.90 ± 0.13	0.60 ± 0.02	0.65 ± 0.06

On average, Slope and MAAT (Figure 4) are the most important variables contributing to the variation of InSAR velocity (Figure 9A). Clear differences between the responses are visible. Horizontal velocity depends foremostly on slope angle, while MAAT exerts the highest influence on vertical velocity. NDVI and SCD have also notable importance, but dissimilar effects on the horizontal and vertical components. Horizontal velocity is more affected by SCD than vertical velocity, which is more influenced by NDVI. Considering the 2D velocity, which combines the horizontal and vertical components, MAAT, Slope and NDVI can be retained for their importance. Despite its importance for the horizontal component, SCD has lower relative significance for the combined 2D velocity. The importance of the remaining variables (Peat, TWI and Boulder) is low (< 0.1) for all responses, albeit all three variables present a higher influence on the horizontal component. The three complementary modelling methods (Supplementary S0) yield similar relative importance values among the variables (Supplement S13).

The response curve for the slope angle (Figure 9B) shows that it has a positive influence on the velocity, with a clear increase when slope angle exceeds 10°. Despite the difference of importance (higher for the horizontal component), the shape of the curve is similar for the three responses. The relationship between MAAT and the mean velocity is also nonlinear but more ambiguous: the vertical velocity tends to decrease with higher MAAT values, while the horizontal velocity is highest where MAAT is around -2°C. The response curve for the 2D velocity highlights the combined effect of the two previous elements, influencing differently the horizontal and vertical components. NDVI has a U-shaped response with the vertical and 2D components; the velocity tends to increase where NDVI is either lowest (< 0.2) or highest (> 0.6). SCD response curve shows the clearest trend for the horizontal component, with a positive impact of snow coverage duration on the velocity.

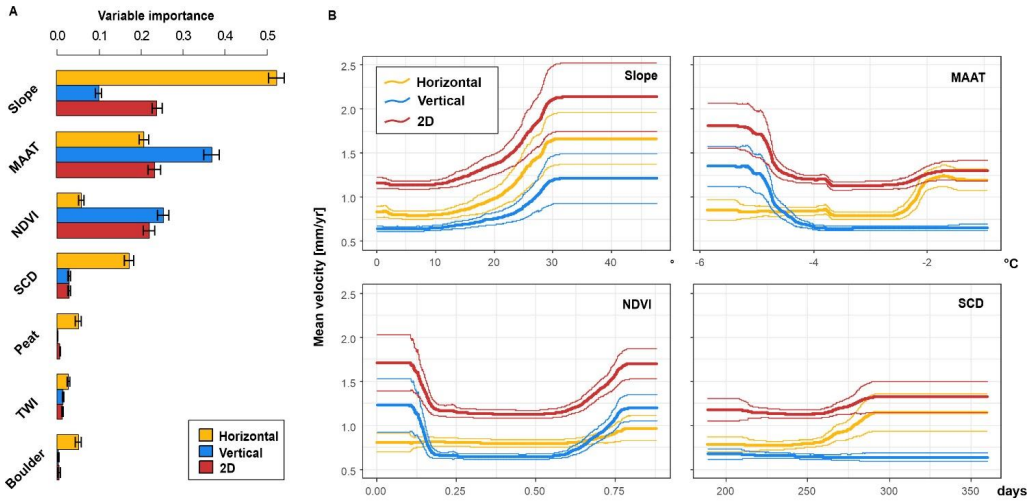

Figure 9: Variable importance and response curves based on generalized boosting method (GBM). A) The bars represent the mean relative importance of the seven environmental variables over 200 resampling rounds and the whiskers depict 95% confidence intervals. Variables are ordered based on their average importance for the three velocity components. B) Response curves depict the predicted mean annual ground velocity (Y-axis) across the range of variables values in their original scale (X-axis). Thin curves represent one standard deviation from average response over 200 permutations. Response curves for the three least important variables are presented in Supplement S14. The acronyms refer to mean annual air temperature (MAAT), normalized difference vegetation index (NDVI), snow cover days (SCD), and topographic wetness index (TWI).

5 Discussion

5.1 Ground dynamics in Rásttigáisá-Geaidnogáisá area

The combined 2D InSAR product indicates values up to 15 mm/year. Ground dynamics in the study area is spatially variable, with higher velocities on slopes and mountain tops. The detected ground velocity is assumed to be primarily associated with cryoturbation and solifluction processes considering the periglacial context, the field and orthophoto observations (Figures 3 and 8), the low velocities (Figures 6 and 7) and the sloping but gentle topography (predominantly < 30 degrees slope angle, Figures 1 and 4B). The presence of rockslides and deep-seated gravitational slope deformation has to our knowledge not been documented in the area but can nevertheless not be excluded. Surface run-off, erosion and transport of weathered material by meltwater on steep slopes may also have a local significance.

Ground ice formation and melting associated with active layer freeze and thaw leads to frost heave and thaw subsidence (Morgenstern & Nixon, 1971; Rempel, 2007). The cryoturbation activity is typically associated with differential movement due to the variability of the frost-susceptibility and the ground water content (Peterson & Krantz, 2008; Van Vliet-Lanoë, 1991; Wilson & Sellier, 1995). Although complex mixing and convection are known to have a significant impact on the dynamics of cryoturbated ground and the redistribution of organic material (Bockheim, 2007; Van Vliet-Lanoë, 1991), these subsurface mechanisms are expected to have a negligible effect in this study due to the surface measurements. Small magnitude and heterogenous deformation over small surfaces are in addition likely to remain undetected when documenting ground velocities with 40 m resolution InSAR pixels. The InSAR results emphasize the downward component of the cryoturbation due to the use of

SAR images during the thawing seasons. Millimetric to centimetric seasonal amplitude is in the expected range in mountainous and subarctic areas, characterized by discontinuous permafrost, thin fine-grained unconsolidated deposits and low ice content (Gruber, 2020; Matsuoka, 2003; Smith, 1987). In this study however, the seasonal component is underestimated due to the use of mean annual products.

Solifluction is the dominant process (Figure 3) due to the sloping terrain of the study area (Figures 1 and 4B). Solifluction combines the effect of the needle ice and frost creep (heave normal to the inclined surface followed by vertical settlement) and the gelifluction (shear deformation associated with water content from the seasonal thawing of ground containing excess ice) (Harris, 1997; Harris & Davies, 2000, Harris et al., 2008a; Matsuoka, 2001). The net movement is downslope, which explains why 2D InSAR detects a combination of horizontal and vertical components in these areas. Millimetric to centimetric solifluction annual rate (net downslope velocities) is in the range of subarctic areas and mid-latitude mountainous regions with seasonal frost or warm permafrost conditions (Ballantyne, 2013; Harris et al., 2008b; Matsuoka et al., 1997; Ridefelt et al., 2009). Decimetric to metric annual rates have also been reported but are generally associated with high frequency freeze-thaw cycles or deep freeze-thaw penetration in fine frost-susceptible material (Matsuoka, 2001).

At the regional scale, the results show that InSAR is valuable in studying the distribution of the ground velocity over large areas and locating the most active parts of the landscape, at a scale and resolution hard to achieve by other techniques. However, as also discussed by other studies (Daout et al., 2017; Eckerstorfer et al., 2018, Eriksen, et al., 2017; Reinosch et al., 2020; Rouyet et al., 2019), relating these measurements to actual processes to further interpret their controls is the major scientific challenge of the exploitation of InSAR technology in periglacial environments. The ground type (grain size influencing the frost susceptibility), the ground moisture, the topography and the snow/vegetation distribution have an impact on the local variability of movement magnitude but the respective influence of each factor is still not fully understood. This is why the combination of InSAR and statistical modelling can positively contribute to further understand the links between ground dynamics and environmental conditions.

5.2 Factors controlling InSAR ground velocity

The Slope and MAAT variables (Figure 4) are the key factors contributing to the spatial variability of the ground velocity, but they have different importance and effects on both components of the 2D mean velocity (Figure 9). The high importance of slope angle for the horizontal component matches the theoretical expectation that the solifluction rate increases with the slope inclination (Harris, 1997; Matsuoka, 2001). However, the response curves indicate that there is an upper limit for the effect, as just under 30° the curves begin to flatten. This suggests that steeper slopes are less favourable for solifluction occurrence (Matsuoka, 2001). Too steep slopes do not allow for thick layer of soil to hold, and may lead to high water drainage and little snow accumulation, detrimental for solifluction to occur (Matsuoka, 2001). A similar levelling off effect has been found by Hjort & Luoto (2011) and Hjort et al. (2014) who showed good concordance with hypothetical response curves. It should be noted, however, that the flat curves after ~32° are also affected by the relatively small amount of observations in the randomly sampled modelling datasets, as suggested by the distribution of the values in all available InSAR pixels (Supplement S5). The air temperature is the second most important factor, controlling primarily the vertical component of the ground velocity (Figure 9A). Interestingly, the response curves show that MAAT has a two-sided effect, impacting the two velocity components differently (Figure 9B). For the vertical component, the negative relationship suggests that low temperatures in the high-altitude parts of the study area promoting frost action, which concurs with conclusions from Hjort (2014). For the horizontal component, the relationship is nonlinear and positive. This seems reasonable as well-developed soils including fine sediments promote solifluction at low

altitudes characterized by relatively high MAAT. Frost-susceptible silt-rich soils are typically expected to be more favourable to frost creep (Harris et al., 1995). Longer thawing seasons and warmer ground conditions also tend to increase the amount of liquid water into the ground and promote the gelifluction component of the solifluction. Low temperatures may delay and decrease the length of the thawing season, thus decreasing the solifluction activity. It concurs with other studies showing that solifluction rates increase with higher MAAT (Matsuoka, 2001; Ridefelt et al., 2009).

Despite their more ambiguous importance and effects, NDVI and SCD have notable contributions in the models. NDVI mostly influences the vertical component (Figure 9A). The response curve shows a nonlinear and complex relationship (Figure 9B), indicating that sparsely vegetated surfaces (typically rocky terrain at high-altitude) tend to be associated with high velocities recorded at the tops and upper slopes of the mountains in the areas affected by subsidence. Solifluction lobes at the mountain footslopes are covered by low vegetation to a varying degree. Near the mountain tops, only lichen is found on rocky surfaces while the underlying finer material is sparsely or not vegetated. The effect of the vegetation on the velocity is in line with the MAAT and partly related to their high mutual correlation. Both variables reflect the prominent altitudinal gradient in the study area (> 900 m), which strongly controls the preconditions for frost activity. However, NDVI also allows for examining additional indirect factors affecting ground movement. High NDVI can indeed be associated with high velocity, a positive effect visible both on the response curves for the vertical and horizontal components. The two-sided and apparently contradictory relationship between vegetation cover and periglacial processes have also been discussed in previous studies related to cryoturbation and solifluction activity. Peterson et al. (2003) show that vegetation cover may have a constraining effect on cryoturbation, especially in the presence of insulative plant communities. The biogeomorphic model on solifluction lobes from Eichel et al. (2017) also highlights that dense vegetation acts to stabilize the ground. On the other hand, high NDVI coincides with areas where the soil is well-developed allowing for cryoturbation and solifluction to occur due to water accumulation and fine-grained frost-susceptible sediments. Earth or turf hummocks showing strong frost action can for example be covered by abundant low-stature vegetation (Grab, 2005; Kojima, 1994). On solifluction lobes, Eichel et al. (2017) showed that vegetation growing in wet areas can be associated with high amplitude of cryotic deformation. Positive relationship between NDVI and solifluction are similarly found in Ridefelt et al. (2009; 2010) and Hjort et al. (2014). The presence of vegetation may also influence the snow distribution, leading to variable water content and thus promoting differential frost heave (Daanen et al., 2008; Nicolsky et al., 2008). In general, as discussed by Hjort (2014) and Hjort & Luoto (2009), the vegetation is mostly an indirect factor for periglacial activity and encompasses a variety of species with different habits, which can have contrasting impacts on ground stability. This complexity may explain the ambiguous relationship with the response variables. It should also be noted that the positive effect of high NDVI to the vertical component can also correspond to an artefact. Even in areas where the InSAR coherence is over the chosen threshold, scattering mechanisms related to herbaceous vegetation may still affect the results (Ansari et al., 2020). Birefringence through the plant elements, phenological and interannual variations in plant height may lead to biased displacement estimates (Zwieback & Hajnsek, 2014). SCD positively influences the horizontal component (Figure 9). This concurs with conclusions from several studies, showing that uneven distribution of snow leads to differential ground movement and melting of prolonged snow patches raises the ground moisture content of the thawed layer, which promotes gelifluction (Jaesche et al., 2003; Matsuoka, 2001). Early and deep snow patches can also prevent ground freezing in nivation hollows and provide entry points for groundwater seepage further downslope (Harris et al., 2008).

Considering the conclusions of other studies about the controls of cryoturbation and solifluction processes, the low contributions of the surface geology (Peat, Boulder) and hydrological (TWI) factors may seem surprising. In this study, we hypothesize that the low importance of these variables is related

to the thin and/or coarse sediment cover, little frost-susceptibility and low–medium ice content (see Sections 2 and 3.2) that lead to the low detected velocities in the area. It is also likely due to the characteristics of the products/indexes used for documenting the spatial variability of the two factors. The ground type, in terms of grain size and frost susceptibility, is expected to have an impact on the movement amplitude (Konrad, 1999; Van Vliet-Lanoë, 1991). However, the variables Peat and Boulder are based on relatively coarse products (Figure S4) that do not fully allow for documenting the frost susceptibility at the resolution of the analysis. Similarly, water availability is expected to contribute to the differential distribution of frost-related ground movement (Harris et al., 1995; Hjort, 2014; Jaesche et al., 2003). The fact that TWI has a negligible importance may indicate that this index is not the most adapted at the considered resolution despite its documented potential in explaining measured fine-scale (1 m^2) variability of soil moisture in a similar sub-arctic environment (Kemppinen et al., 2018). In the context of ground dynamics, this could be because TWI is a purely topographically-based surface water distribution index that does not consider soil properties, influencing infiltration or runoff conditions, as well as ground ice formation. These elements show the challenge of studying ground freeze-thaw processes due to the highly variable water content, ice and sediment distribution at very fine-scale; an issue that has been further discussed in several other studies (Cable, et al., 2018; Gruber, 2020; Schuh, et al., 2017; Shiklomanov et al., 2010). It highlights the need for including alternative data in future studies and considering the properties of the ground material to document the effective significance of soil moisture on ground movement.

In general, the limitation of a potential scale discrepancy must be considered when considering any geoscientific study based on remote sensing. Low to medium resolution satellite products have the advantage to document large areas with near-continuous coverage, but the drawback of averaging information at a scale that is not fully representative. The conclusions about the relative spatial variability of the measurements and their relations with environmental variables at similar resolution are valid, but inferred links between remotely sensed measurements and ground processes must always be treated carefully.

5.3 InSAR and statistical modelling: potential and limitations

We acknowledge that due to the low magnitude of the InSAR velocities and the right-skewed distribution of the values, the results are sensitive to small bias of displacement estimates. The main InSAR error sources are 1) the uncorrected atmospheric effects (Zebker et al., 1997); 2) the bias due to changes of surface properties and their effects on scattering mechanisms, in relation with snow, moisture and vegetation (De Zan et al., 2014; Zwieback et al., 2015; 2016; Zwieback & Hajnsek, 2014); and 3) a potential shift of the velocity due a wrong assumption of stability at the location of the reference point (Antonova et al., 2018). The procedure to mitigate these three elements have been presented in Section 3.1 and we estimated that the accuracy is below 1 mm/yr (Supplement S3). It should however be noted that the impact of the scattering mechanisms on SBAS results are not fully understood yet and thus difficult to assess quantitatively. Understanding the physical sources of the potential bias and modelling the complex effects of the moisture, snow and biomass changes is a dedicated on-going research topic (Ansari et al., 2020). It should also be reminded that this study focuses on the relative spatial distribution of the ground velocities and that the use of a multi-annual averaging and a linear deformation model does not allow for documenting the seasonality of the processes. Comprehensive time series analyses should be considered in future studies combining InSAR and statistical modelling. Due to the unavailability of complementary displacement measurements in the area, this study does not provide a quantitative validation of the InSAR results. However, several qualitative indicators have been used to assess the results' validity (see Section 4.1). First, the amplitude and distribution of the results are generally consistent with the PSI results from the InSAR Norway ground motion mapping service. Second, the spatial variability of the velocity follows

expected patterns eastwards/westwards horizontal velocities on respectively east- and west-facing slopes, and with higher velocities on slopes and mountain tops. This is overall consistent with field observations of the cryoturbation and solifluction activity. Third, results from 2D InSAR calculation do not show any major shift of the velocity indicating that the choice of the InSAR reference point was adapted.

The relatively low model performance (Table 3) in this study can be explained by 1) the overall low magnitude of ground movement across the area; 2) the complex and indirect relation between environmental variables and the ground velocities, as well as the scale discrepancy between measurements and processes; and 3) the relatively small number of observations in the calibration sets (on average 1,100) may not cover the entire gradient of environmental conditions in the study area. Contrary to the previous studies applying modelling based on field-mapped processes and landforms (Hjort et al., 2007; Hjort & Luoto, 2009; Hjort, 2014), the responses here represent ground velocity regardless of the underlying processes. The unexplained variation by the models is arguably attributed to the frost susceptibility of ground material, fine-scale soil moisture, and microclimatic conditions (e.g., solar radiation, wind processes) (Aalto et al., 2018b), which could not be accounted for at optimal thematic or spatial resolution. A central aspect that may have affected our ability to accurately predict the mean velocity is the scale mismatch between the InSAR resolution (40 m) and the assumed ground processes (Walsh et al, 1998; Luoto & Hjort, 2006). We argue that examination of frost-related ground movement would benefit from a higher spatial resolution in both InSAR and geospatial data on environmental conditions. Our results show a notably higher amount of explained variation for the vertical component compared to the horizontal velocity. We suggest that it is more complicated to explain the horizontal component because eastwards/westwards movement can less directly be related to a specific process. A slope affected by solifluction typically includes both a vertical and a horizontal component, and flat areas are dominated by vertical patterns. While the vertical downward trend documented by the InSAR averaged measurements can be related to the melting of the ice in the seasonally thawing layer of the ground, the horizontal component is a more complex interaction of the frost action (needle ice and frost creep) and the gelifluction (shear deformation).

Despite the discussed challenges, the results of the statistical modelling of 2D InSAR measurements in Rásttigáisá-Geaidnogáisá area provide interesting insights on the environmental controls of periglacial ground dynamics. This study is a first contribution towards integrating InSAR and statistical modelling in periglacial research. Other strategies based on similar techniques could be investigated in the future. Better model performance may be reached by focusing on one previously inventoried landform type and clearer response curves may be found by selecting areas where movement magnitude is expected to be higher. The exploitation of time series can be considered to analyse the seasonal progression of the displacement. InSAR maps could also be used as a variable among others to explain the distribution of specific landforms.

6 Conclusion

We mapped mean annual ground velocity in a mountainous landscape in Northern Norway using Sentinel-1 Synthetic Aperture Radar Interferometry (InSAR). The 2D InSAR products were used as response variables in statistical modelling based on a set of seven climatic, geomorphic, hydrological and biological variables.

Based on the results, four main conclusions can be drawn:

1) The study area is affected by mm/yr to cm/yr mean annual ground velocities, with values up to 15 mm/yr. The horizontal and vertical components of the 2D velocity are distributed differently over flat areas and slopes and highlight the areas affected by active cryoturbation and solifluction.
2) The statistical models showed contrasted performance depending on the velocity component (R^2 between 0.24 and 0.47). The unexplained variance may be attributed to the low velocities, the

discrepancy between the spatial resolution of the remote sensing products and the studied processes, as well as the complex relationships between environmental variables, periglacial processes and documented responses (ground velocities).

3) The slope angle and the mean annual air temperature are the key factors contributing to the spatial variability of the ground velocity in the study area. The amount of vegetation and the snow cover duration have also notable contributions in the models and are interpreted as indirect proxies of ground material and moisture conditions.
4) The relative importance of the environmental factors on both components of the 2D velocity vary significantly. The vertical velocity is mostly influenced by the air temperature and the vegetation, while the main variable controlling the variability of the horizontal component is the slope angle, followed by the air temperature and the snow coverage. These results are attributed to the different characteristics of cryoturbation and solifluction processes, operating differently over flat areas and slopes.

As a first attempt of coupling InSAR and explanatory statistical modelling in periglacial landscapes, our study highlights the potential to integrate both techniques for a better understanding of the environmental factors controlling ground dynamics and suggest novel ways to characterize extensive and hard-to-access cold environments.

Acknowledgments

LR's Ph.D. project is funded by the Research Council of Norway (grant 263005). OK and JH are funded by the Academy of Finland (grant 315519). JA acknowledges the funding by the Academy of Finland (grants 307761 and 337552). The development of the GSAR processing chain and previous research applying InSAR in periglacial environments have been supported by the Norwegian Space Centre, the Research Council of Norway (grant 212022) and the European Space Agency (grants 4000106830 and 4000119115). Sentinel-1 scenes were provided by the EU Copernicus data service (2015–2018). We thank Olli-Matti Kärnä, Mikko Kivelä and Ville Savilampi who assisted on the field. We acknowledge the extensive work performed by Ann Chen and two anonymous reviewers, who commented on the previous version of the manuscript.

Author contributions

LR and JH developed the original idea. LR processed InSAR results, with contributions from TRL and YL. PN and ML led the compilation of the environmental data, with contributions from JA, OK and JH. OK and LR uniformized the datasets for further analysis. OK performed the statistical modelling, with contributions from PN, JA, JH and LR. LR led the work on interpretation and wrote the manuscript, with contributions from all the authors.

Open Research

Model inputs (response and environmental variables) and outputs (calibration/evaluation model performance and predictions) are available in Zenodo (http://doi.org/10.5281/zenodo.4173256). Additional data sources used in this study are listed in the references, included in the figures and tables, or in the supporting information associated with this publication.

References

Aalto, J., Harrison, S., & Luoto, M. (2017). Statistical modelling predicts almost complete loss of major periglacial processes in Northern Europe. *Nature Communications, 8*, 515. https://doi.org/10.1038/s41467-017-00669-3.

Aalto, J., Karjalainen, O., Hjort, J., & Luoto, M. (2018). Statistical forecasting of current and future circum-Arctic ground temperatures and active layer thickness. *Geophysical Research Letters, 45*(10), 4889–4898. https://doi.org/10.1029/2018GL078007.

Aalto, J., Scherrer, D., Lenoir, J., Guisan, A., & Luoto, M. (2018). Biogeophysical controls on soil-atmosphere thermal differences: implications on warming Arctic ecosystems. *Environmental Research Letters, 13*(7). 074003. https://doi.org/10.1088/1748-9326/aac83e.

Ansari, H., De Zan, F., & Parizzi, A. (2020). Study of Systematic Bias in Measuring Surface Deformation With SAR Interferometry. *IEEE Transactions on Geoscience and Remote Sensing*. https://doi.org/10.1109/TGRS.2020.3003421.

Antonova, S., Sudhaus, H., Strozzi, T., Zwieback, S., Kääb, A., Heim, B., Langer, M., Bornemann, N., & Boike, J. (2018). Thaw Subsidence of a Yedoma Landscape in Northern Siberia, Measured In Situ and Estimated from TerraSAR-X Interferometry. *Remote Sensing of Environment*, *10*(4), 494, https://doi.org/10.3390/rs10040494.

Ballantyne, C. K. (2013). A 35-year record of solifluction in a maritime periglacial environment. *Permafrost and Periglacial Processes*, *24*(1), 56–66. https://doi.org/10.1002/ppp.1761.

Bamler, R., & Hartl, P. (1998). Synthetic aperture radar interferometry. *Inverse Problems*, *14*(4), R1. https://doi.org/10.1088/0266-5611/14/4/001.

Baran, I., Stewart, M. P., Kampes, B. M., Perski, Z., & Lilly, P. (2003). A modification to the Goldstein radar interferogram filter. *IEEE Transactions on Geoscience and Remote Sensing*, *41*(9), 2114–2118. https://doi.org/10.1109/TGRS.2003.817212.

Barboux, C., Delaloye, R., & Lambiel, C. (2014). Inventorying slope movements in an Alpine environment using DInSAR. *Earth Surface Processes and Landforms*, *39*(15), 2087–2099. https://doi.org/10.1002/esp.3603.

Barboux, C., Strozzi, T., Delaloye, R., Wegmüller, U., & Collet, C. (2015). Mapping slope movements in Alpine environments using TerraSAR-X interferometric methods. *ISPRS Journal of Photogrammetry and Remote Sensing*, *109*, 178–192. https://doi.org/10.1016/j.isprsjprs.2015.09.010.

Bartsch, A., Leibman, M., Strozzi, T., Khomutov, A., Widhalm, B., Babkina, E., et al. (2019). Seasonal progression of ground displacement identified with satellite radar interferometry and the impact of unusually warm conditions on permafrost at the Yamal Peninsula in 2016. *Remote Sensing*, *11*(16), 1865. https://doi.org/10.3390/rs11161865.

Berardino, P., Fornaro, G., Lanari, R., & Sansosti, E. (2002). A new algorithm for surface deformation monitoring based on small baseline differential SAR interferograms. *IEEE Transactions on Geoscience and Remote Sensing*, *40*(11), 2375–2383. https://doi.org/10.1109/TGRS.2002.803792.

Biskaborn, B. K., Smith, S. L., Noetzli, J., Matthes, H., Vieira, G., Streletskiy, D. A., et al. (2019). Permafrost is warming at a global scale. *Nature Communications*, 10(1), 1–11. https://doi.org/10.1038/s41467-018-08240-4.

Blois, J. L., Williams, J. W., Fitzpatrick, M. C., Jackson, S. T., & Ferrier, S. (2013). Space can substitute for time in predicting climate-change effects on biodiversity. In *Proceedings of the National Academy of Sciences* (Vol. 110(23), pp. 9374–9379). https://doi.org/10.1073/pnas.1220228110.

Bockheim, J. G. (2007). Importance of cryoturbation in redistributing organic carbon in permafrost-affected soils. *Soil Science Society of America Journal*, *71*(4), 1335–1342. https://doi.org/10.2136/sssaj2006.0414N.

Boeckli, L., Brenning, A., Gruber, S., & Noetzli, J. (2012). Permafrost distribution in the European Alps: calculation and evaluation of an index map and summary statistics. *The Cryosphere*, *6*(4), 807–820. https://doi.org/10.5194/tc-6-807-2012.

Bonnaventure, P. P., & Lamoureux, S. F. (2013). The active layer: a conceptual review of monitoring, modelling techniques and changes in a warming climate. *Progress in Physical Geography*, *37*(3), 352–376. https://doi.org/10.1177/0309133313478314.

Böhner, J., Köthe, R., Conrad, O.,Gross, J., Ringeler, A., & Selige, T. (2002). Soil Regionalisation by Means of Terrain Analysis and Process Parameterisation. In E. Micheli, E., F. Nachtergaele, L. Montanarella (Eds.), *Soil Classification 2001* (213–222). European Soil Bureau, Research Report No. 7, EUR 20398 EN, Luxembourg. 213–222.

Cable, S., Elberling, B., & Kroon, A. (2018). Holocene permafrost history and cryostratigraphy in the High-Arctic Adventdalen Valley, central Svalbard. *Boreas*, *47*(2), 423–442. http://doi.org/10.1111/bor.12286.

Chen, C., & Zebker, H. A. (2002). Phase unwrapping for large SAR interferograms: Statistical segmentation and generalized network models. *IEEE Transactions on Geoscience and Remote Sensing*, *40*(8), 1709–1719. https://doi.org/10.1109/TGRS.2002.802453.

Chen, J., Wu, Y., O'Connor, M., Cardenas, M. B., Schaefer, K., Michaelides, R., & Kling, G. (2020). Active layer freeze-thaw and water storage dynamics in permafrost environments inferred from InSAR. *Remote Sensing of Environment*, *248*, 112007. https://doi.org/10.1016/j.rse.2020.112007.

Christiansen, H. H., Etzelmüller, B., Isaksen, K., Juliussen, H., Farbrot, H., Humlum, O., et al. (2010). The thermal state of permafrost in the nordic area during the international polar year 2007–2009. *Permafrost and Periglacial Processes*, *21*(2), 156–181. https://doi.org/10.1002/ppp.687.

Conrad, O., Bechtel, B., Bock, M., Dietrich, H., Fischer, E., Gerlitz, L., et al. (2015). System for Automated Geoscientific Analyses (SAGA) v. 2.1.4. *Geoscientific Model Development*, *8*, 1991–2007. https://doi.org/10.5194/gmdd-8-2271-2015.

Daanen, R. P., Misra, D., Epstein, H., Walker, D., & Romanovsky, V. (2008). Simulating nonsorted circle development in arctic tundra ecosystems. *Journal of Geophysical Research: Biogeosciences*, *113*(G3). https://doi.org/10.1029/2008JG000682.

Daout, S., Doin, M.P., Peltzer, G., Socquet, A., & Lasserre, C. (2017). Large-scale InSAR monitoring of permafrost freeze-thaw cycles on the Tibetan Plateau. *Geophysical Research Letters*, *44*(2), 901–909. https://doi.org/10.1002/2016GL070781.

Dehls, J. F., Larsen, Y., Marinkovic, P., Lauknes, T.R., Stødle, D., & Moldestad, D. A. (2019). INSAR.No: A National Insar Deformation Mapping/Monitoring Service In Norway -- From Concept To Operations. In *Proceedings of IGARSS 2019 - IEEE International Geoscience and Remote Sensing Symposium* (pp. 5461–5464). https://doi.org/10.1109/IGARSS.2019.8898614.

De Zan, F., Parizzi, P., Prats-Iraola, P., & López-Bekker, P. (2014). A SAR interferometric model for soil moisture. *IEEE Transactions on Geoscience and Remote Sensing*, *52*(1), 418–425. https://doi.org/10.1109/TGRS.2013.2241069.

Dini, B., Daout, S., Manconi, A., & Loew, S. (2019). Classification of slope processes based on multitemporal DInSAR analyses in the Himalaya of NW Bhutan. *Remote Sensing of Environment*, *233*, 111408. https://doi.org/10.1016/j.rse.2019.111408.

Dormann, C. F., McPherson, J. M., Araújo, M.B., Bivand, R., Bolliger, J., Carl, G., et al. (2007). Methods to account for spatial autocorrelation in the analysis of species distributional data: a review. *Ecography*, *30*(5), 609–628. https://doi.org/10.1111/j.2007.0906-7590.05171.x.

Dormann, C. F., Elith, J., Bacher, S., Buchmann, C., Gudrun, C., Carré, G., et al. (2013). Collinearity: a review of methods to deal with it and a simulation study evaluating their performance. *Ecography*, *36*, 27–46. https://doi.org/10.1111/j.1600-0587.2012.07348.x.

Eckerstorfer, M., Eriksen, H. Ø., Rouyet, L., Christiansen, H. H., Lauknes, T. R., & Blikra, L. H. (2018). Comparison of geomorphological field mapping and 2D-InSAR mapping of periglacial landscape activity at Nordnesfjellet, northern Norway. *Earth Surface Processes and Landforms*, *43*(10), 2147–2156. https://doi.org/10.1002/esp.4380.

Eichel, J., Draebing, D., Klingbeil, L., Wieland, M., Eling, C., Schmidtlein, S., Kuhlmann, H., & Dikau, R. (2017). Solifluction meets vegetation: the role of biogeomorphic feedbacks for turf-banked solifluction lobe development. *Earth Surface Processes and Landforms*, *42*(11), 1623–1635. https://doi.org/10.1002/esp.4102.

Elith, J., Leathwick, J. R., & Hastie, T. (2008). A working guide to boosted regression trees. *Journal of Animal Ecology*, *77*(4), 802–813. https://doi.org/10.1111/j.1365-2656.2008.01390.x.

Emardson, T. R., Simons, M., & Webb, F. H. (2003). Neutral atmospheric delay in interferometric synthetic aperture radar applications: Statistical description and mitigation. *Journal of Geophysical Research: Solid Earth*, *108*(B5). https://doi.org/10.1029/2002JB001781.

Eriksen, H. Ø., Lauknes, T. R., Larsen, Y., Corner, G.D., Bergh, S. G., Dehls, J., & Kierulf, H. P. (2017a). Visualizing and interpreting surface displacement patterns on unstable slopes using multi-geometry satellite SAR interferometry (2D InSAR). *Remote Sensing of Environment*, *191*, 297–312. https://doi.org/10.1016/j.rse.2016.12.024.

Eriksen, H. Ø., Bergh, S. G., Larsen, Y., Skrede, I., Kristensen, L., Lauknes, T. R., Blikra, L. H., & Kierulf, H. P. (2017b). Relating 3D surface displacement from satellite-and ground-based InSAR to structures and geomorphology of the Jettan rockslide, northern Norway. *Norwegian Journal of Geology*, *97*(4), 283–303. https://doi.org/10.17850/njg97-4-03.

Environmental Systems Research Institute (ESRI). (2019). *ArcGIS Release 10.7.1*. Redlands, CA.

Etzelmüller, B., Hoelzle, M., Flo Heggem, E.S., Isaksen, K., Mittaz, C., Mühll, D. V., et al. (2001). Mapping and modelling the occurrence and distribution of mountain permafrost. *Norwegian Journal of Geography*, *55*(4), 186–194. https://doi.org/10.1080/00291950152746513.

Farbrot, H., Isaksen, K., & Etzelmüller, B. (2008). Present and past distribution of mountain permafrost in Gaissane Mountains, Northern Norway. In *Proceedings of the Ninth International Conference on Permafrost* (Vol. 1, 427–432), Fairbanks, U.S.A.

Farbrot, H., Isaksen, K., Etzelmüller, B., & Gisnås, K. (2013). Ground thermal regime and permafrost distribution under a changing climate in northern Norway. *Permafrost and Periglacial Processes*, *24*(1), 20–38. https://doi.org/10.1002/ppp.1763.

Ferretti, A., Prati, C., & Rocca, F. (2001). Permanent scatterers in SAR interferometry. *IEEE Transactions on geoscience and remote sensing*, *39*(1), 8–20. https://doi.org/10.1109/36.898661

French, H. M. (2017). *The Periglacial Environment*. Third Edition. John Wiley & Sons, Chichester, England.

Gisnås, K., Etzelmüller, B., Farbrot, H., Schuler, T. V., & Westermann, S. (2013). CryoGRID 1.0: Permafrost distribution in Norway estimated by a spatial numerical model. *Permafrost and Periglacial Processes*, *24*(1), 2–19. https://doi.org/10.1002/ppp.1765.

Gisnås, K., Etzelmüller, B., Lussana, C., Hjort, J., Sannel, A. B. K., Isaksen, K., et al. (2017). Permafrost map for Norway, Sweden and Finland. *Permafrost and Periglacial Processes*, *28*(2), 359–378. https://doi.org/10.1002/ppp.1922.

Guglielmin, M., Evans, C. J. E., & Cannone, N. (2008). Active layer thermal regime under different vegetation conditions in permafrost areas. A case study at Signy Island (Maritime Antarctica). *Geoderma*, *144*(1-2), 73–85. https://doi.org/10.1016/j.geoderma.2007.10.010.

Goldstein, R. M., & Werner, C. L. (1998). Radar interferogram filtering for geophysical applications. *Geophysical Research Letters*, *25*(21), 4035–4038. https://doi.org/10.1029/1998GL900033.

Grab, S. (2005). Aspects of the geomorphology, genesis and environmental significance of earth hummocks (thufur, pounus): miniature cryogenic mounds. *Progress in Physical Geography, 29*(2), 139–155. https://doi.org/10.1191/0309133305pp440ra.

Gruber, S., & Hoelzle, M. (2001). Statistical modelling of mountain permafrost distribution: local calibration and incorporation of remotely sensed data. *Permafrost and Periglacial Processes, 12*(1), 69–77. https://doi.org/10.1002/ppp.374.

Gruber, S. (2020). Ground subsidence and heave over permafrost: hourly time series reveal interannual, seasonal and shorter-term movement caused by freezing, thawing and water movement. *The Cryosphere, 14*(4), 1437–1447. https://doi.org/10.5194/tc-14-1437-2020.

Haeberli, W., Noetzli, J., Arenson, L., Delaloye, R., Gärtner-Roer, I., Gruber, S., et al. (2010). Mountain permafrost: development and challenges of a young research field. *Journal of Glaciology, 56*(200), 1043–1058. https://doi.org/10.3189/002214311796406121.

Harris, C., Davies, M. C., & Coutard, J. P. (1995). Laboratory simulation of periglacial solifluction: significance of porewater pressures, moisture contents and undrained shear strengths during soil thawing. *Permafrost and Periglacial Processes, 6*(4), 293–311. https://doi.org/10.1002/ppp.3430060403.

Harris, C., Davies, M. C., & Coutard, J. P. (1997). Rates and processes of periglacial solifluction: an experimental approach. *Earth Surface Processes and Landforms, 22*(9), 849–868. https://doi.org/10.1002/(SICI)1096-9837(199709)22:9<849::AID-ESP784>3.0.CO;2-U, 1997.

Harris, C., & Davies, M. C. (2000). Gelifluction: Observations from large-scale laboratory simulations. *Arctic, Antarctic and Alpine Research, 32*(2), 202–207. https://doi.org/10.1080/15230430.2000.12003356.

Harris, C., Mühll, D. V., Isaksen, K., Haeberli, W., Sollid, J. L., King, L., et al. (2003). Warming permafrost in European mountains. *Global and Planetary Change, 39*(3-4), 215–225. https://doi.org/10.1016/j.gloplacha.2003.04.001.

Harris, C., Kern-Luetschg, M., Murton, J., Font, M., Davies, M., & Smith, F. (2008a). Solifluction processes on permafrost and non-permafrost slopes: results of a large-scale laboratory simulation. *Permafrost and Periglacial Processes, 19*(4), 359–378. https://doi.org/10.1002/ppp.630.

Harris, C., Kern-Luetschg, M., Smith, F., & Isaksen, K. (2008b). Solifluction processes in an area of seasonal ground freezing, Dovrefjell, Norway. *Permafrost and Periglacial Processes, 19*, 31–47. https://doi.org/10.1002/ppp.609.

Harris, C., Arenson, L. U., Christiansen, H. H., Etzelmüller, B., Frauenfelder, R., Gruber, S., et al. (2009). Permafrost and climate in Europe: Monitoring and modelling thermal, geomorphological and geotechnical responses. *Earth-Science Reviews, 92*(3-4), 117–171. https://doi.org/10.1016/j.earscirev.2008.12.002.

Hinzman, L. D., Kane, D. L., Gieck, R. E., & Everett, K. R. (1991). Hydrologic and thermal properties of the active layer in the Alaskan Arctic. *Cold Regions Science and Technology, 19*(2), 95–110. https://doi.org/10.1016/0165-232X(91)90001-W.

Hjort, J., Luoto, M., & Seppälä, M. (2007). Landscape scale determinants of periglacial features in subarctic Finland: a grid-based modelling approach. *Permafrost and Periglacial Processes, 18*(2), 115–127.

Hjort, J., & Luoto, M. (2009). Interaction of geomorphic and ecologic features across altitudinal zones in a subarctic landscape. *Geomorphology, 112*(3-4), 324–333. https://doi.org/10.1016/j.geomorph.2009.06.019.

Hjort, J., Etzelmüller, B., & Tolgensbakk, J. (2010). Effects of scale and data source in periglacial distribution modelling in a high arctic environment, western Svalbard. *Permafrost and Periglacial Processes, 21*(4), 345–354. https://doi.org/10.1002/ppp.705.

Hjort, J., & Luoto, M. (2011). Novel theoretical insights into geomorphic process–environment relationships using simulated response curves. *Earth Surface Processes and Landforms, 36*(3), 363–371. https://doi.org/10.1002/esp.2048.

Hjort, J., & Luoto, M. (2013). Statistical methods for geomorphic distribution modeling. In J. Schroder, A. C. W. Baas (Eds), *Treatise on Geomorphology* (Vol.2. Quantitative modeling of geomorphology, pp. 59–73). Academic Press, San Diego. https://doi.org/10.1016/B978-0-12-374739-6.00028-2.

Hjort, J. (2014). Which environmental factors determine recent cryoturbation and solifluction activity in a subarctic landscape? A comparison between active and inactive features. *Permafrost and Periglacial Processes, 25*(2), 136–143. https://doi.org/10.1002/ppp.1808.

Hjort, J., Ujanen, J., Parviainen, M., Tolgensbakk, J., & Etzelmüller, B. (2014). Transferability of geomorphological distribution models: Evaluation using solifluction features in subarctic and Arctic regions. *Geomorphology, 204*, 165–176. https://doi.org/10.1016/j.geomorph.2013.08.002.

Hjort J., Karjalainen, O., Aalto, J., Westermann, S., Romanovsky, V. E., Nelson F. E., Etzelmüller, B., & Luoto, M. (2018). Degrading permafrost put Arctic infrastructure at risk by midcentury. *Nature Communications, 9*, 5147. https://doi.org/10.1038/s41467-018-07557-4.

Isaksen, K., Sollid, J. L., Holmlund, P., & Harris, C. (2007). Recent warming of mountain permafrost in Svalbard and Scandinavia. *Journal of Geophysical Research: Earth Surface, 112*(F2). https://doi.org/10.1029/2006JF000522.

Isaksen, K., Farbrot, H., Blikra, L. H., Johansen, B., Sollid, J. L., & Eiken, T. (2008). Five year ground surface temperature measurements in Finnmark, Northern Norway. In *Proceedings of the Ninth International Conference on Permafrost* (Vol. 1, 789–794), Fairbanks, U.S.A.

Jaesche, P., Veit, H., & Huwe, B. (2003). Snow cover and soil moisture controls on solifluction in an area of seasonal frost, eastern Alps. *Permafrost and Periglacial Processes, 14*(4), 399–410. https://doi.org/10.1002/ppp.471.

Jorgenson, M. T., Racine, C. H., Walters, J. C., & Osterkamp, T. E. (2001). Permafrost degradation and ecological changes associated with a warming climate in central Alaska. *Climatic Change, 48*(4), 551–579. https://doi.org/10.1023/A:1005667424292.

Kääb, A., Huggel, C., Fischer, L., Guex, S., Paul, F., Roer, I., et al. (2005). Remote sensing of glacier-and permafrost-related hazards in high mountains: an overview. *Natural Hazards and Earth System Sciences, 5*(4), 527–554. https://doi.org/10.5194/nhess-5-527-2005.

Karjalainen, O., Aalto, J., Luoto, M., Westermann, S., Romanovsky, V. E., Nelson, F. E., Etzelmüller, B., & Hjort, J. (2019). Circumpolar permafrost maps and geohazard indices for near-future infrastructure risk assessments. *Scientific Data, 6*, 190037. https://doi.org/10.1038/sdata.2019.37.

Karjalainen, O., Luoto, M., Aalto, J., Etzelmuller, B., Grosse, G., Jones, B. M., Lilleøren, K. S., & Hjort, J. (2020). High potential for loss of permafrost landforms in a changing climate. *Environmental Research Letters, 15*(10), 104065. https://doi.org/10.1088/1748-9326/abafd5.

Kemppinen, J., Niittynen, P., Riihimäki, H., & Luoto, M. (2018). Modelling soil moisture in a high-latitude landscape using LiDAR and soil data. *Earth Surface Processes and Landforms, 43*(5), 1019–1031. https://doi.org/10.1002/esp.4301.

Knight, J., & Harrison, S. (2013). The impacts of climate change on terrestrial Earth surface systems. *Nature Climate Change, 3*(1), 24–29. https://doi.org/10.1038/nclimate1660.

Kojima, S. (1994). Relationships of vegetation, earth hummocks and topography in the high Arctic environment of Canada. In *Proceedings of NIPR Symposium on Polar Biology* (Vol. 7, pp. 256–269).

Konrad, J. M. (1999). Frost susceptibility related to soil index properties. *Canadian Geotechnical Journal, 36*(3), 403–417. https://doi.org/10.1139/t99-008.

Larsen, Y., Engen, G., Lauknes, T. R., Malnes, E., & Høgda, K. A. (2005). A generic differential interferometric SAR processing system, with applications to land subsidence and snow-water equivalent retrieval. In *Proceedings of Fringe 2005 Workshop* (Vol. 61), Frascati, Italy. ESA SP-610.

Lauknes, T. R. (2011). InSAR tropospheric stratification delays: Correction using a small baseline approach. *IEEE Transactions on Geoscience and Remote Sensing, 8*(6), 1070–1074. https://doi.org/10.1109/LGRS.2011.2156381.

Lauknes, T. R., Zebker, H. A., & Larsen, Y. (2011).InSAR deformation time series using an L1-norm small-baseline approach. *IEEE Transactions on Geoscience and Remote Sensing, 49*(1), 536–546. https://doi.org/10.1109/TGRS.2010.2051951.

Legendre, P. (1993). Spatial autocorrelation: trouble or new paradigm? *Ecology, 74*(6), 1659–1673. https://doi.org/10.2307/1939924.

Liu, L., Schaefer, K., Zhang, T., & Wahr, J. (2012). Estimating 1992–2000 average active layer thickness on the Alaskan North Slope from remotely sensed surface subsidence. *Journal of Geophysical Research: Earth Surface, 117*(F1). https://doi.org/10.1029/2011JF002041.

Luoto, M., & Hjort, J. (2006). Scale matters–a multi-resolution study of the determinants of patterned ground activity in subarctic Finland. *Geomorphology, 80*(3-4), 282–294. https://doi.org/10.1016/j.geomorph.2006.03.001.

Martin, L. C. P., Nitzbon, J., Aas, K. S., Etzelmüller, B., Kristiansen, H., & Westermann, S. (2019). Stability conditions of peat plateaus and palsas in northern Norway. *Journal of Geophysical Research: Earth Surface, 124*(3), 705–719. https://doi.org/10.1029/2018JF004945.

Massonnet, D., & Feigl, K. L. (1998). Radar interferometry and its application to changes in the Earth's surface. *Reviews of Geophysics, 36*(4), 441–500. https://doi.org/10.1029/97RG03139.

Matsuoka, N., Hirakawa, K., Watanabe, T., & Moriwaki, K. (1997). Monitoring of periglacial slope processes in the Swiss Alps: the first two years of frost shattering, heave and creep. *Permafrost and Periglacial Processes, 8*, 155–177. https://doi.org/10.1002/(SICI)1099-1530(199732)8:2<155::AID-PPP248>3.0.CO;2-N.

Matsuoka, N. (2001). Solifluction rates, processes and landforms: a global review. *Earth-Science Reviews, 55*(1-2), 107–134. https://doi.org/10.1016/S0012-8252(01)00057-5.

Matsuoka, N., Abe, M., & Ijiri, M. (2003). Differential frost heave and sorted patterned ground: field measurements and a laboratory experiment. *Geomorphology, 52*(1-2), 73–85. https://doi.org/10.1016/S0169-555X(02)00249-0.

Morgenstern, N. R., & Nixon, J. F. (1971). One-dimensional consolidation of thawing soils. *Canadian Geotechnical Journal, 8*, 558–565. https://doi.org/10.1139/t71-057.

Nelson, F. E., Anisimov, O. A., & Shiklomanov, N. I. (2002). Climate change and hazard zonation in the circum-Arctic permafrost regions. *Natural Hazards, 26*(3), 203–225. https://doi.org/10.1023/A:1015612918401.

Nicolsky, D. J., Romanovsky, V. E., Tipenko, G. S., & Walker, D. A. (2008). Modeling biogeophysical interactions in nonsorted circles in the Low Arctic. *Journal of Geophysical Research: Biogeosciences., 113*(G3). https://doi.org/10.1029/2007JG000565.

Niittynen, P., & Luoto, M. (2018). The importance of snow in species distribution models of arctic vegetation. *Ecography, 41*(6), 1024–1037. https://doi.org/10.1111/ecog.03348.

Niittynen, P., Heikkinen, R. K., & Luoto, M. (2018). Snow cover is a neglected driver of Arctic biodiversity loss. *Nature Climate Change, 8*(11), 997–1001. https://doi.org/10.1038/s41558-018-0311-x.

Niittynen, P., Heikkinen, R. K., & Luoto, M. (2020). Decreasing snow cover alters functional composition and diversity of Arctic tundra. In *Proceedings of the National Academy of Sciences* (Vol. 117(35), pp. 21480–21487). https://doi.org/10.1073/pnas.2001254117.

NCCS (2021). Observations and weather statics. Norwegian Centre for Climate Services (NCCS), https://seklima.met.no/observations/.

NGU (2020). InSAR Norway, www.insar.no. Map viewer: https://insar.ngu.no/.

NMA. (2016). *DTM 10 Terrengmodell (UTM33)*. Norwegian Mapping Authority. https://kartkatalog.geonorge.no/.

NMA. (2020a). *Toporaster 4 WMS*. Norwegian Mapping Authority. https://kartkatalog.geonorge.no/.

NMA. (2020b). *Norge i bilder WMTS (Euref89 UTM33)*. Images 115 (Finnmark 2011-08-15), 217 (2016-08-18) and 118 (Finnmark 2018-07-19). Norwegian Mapping Authority. https://www.norgeibilder.no/.

Obu, J., Westermann, S., Bartsch, A., Berdnikov, N., Christiansen, H. H., Dashtseren, A., et al. (2019). Northern Hemisphere permafrost map based on TTOP modelling for 2000–2016 at 1 km2 scale. *Earth-Science Reviews, 193*, 299–316. https://doi.org/10.1016/j.earscirev.2019.04.023.

Obu, J., Westermann, S., Barboux, C., Bartsch, A., Delaloye, R.; Grosse, G., & Wiesmann, A. (2020). ESA Permafrost Climate Change Initiative (Permafrost_cci): Permafrost active layer thickness for the Northern Hemisphere, v2.0. Centre for Environmental Data Analysis, *02 November 2020*. http://dx.doi.org/10.5285/29c4af5986ba4b9c8a3cfc33ca8d7c85.

Olson, D. M., Dinerstein, E., Wikramanayake, E. D., Burgess, N. D., Powell, G.V., Underwood, E. C., et al. (2001). Terrestrial Ecoregions of the World: A New Map of Life on EarthA new global map of terrestrial ecoregions provides an innovative tool for conserving biodiversity. *BioScience, 51*(11), 933–938. https://doi.org/10.1641/0006-3568(2001)051[0933:TEOTWA]2.0.CO;2.

Peel, M. C., Finlayson, B. L., & McMahon, T. A. (2007). Updated world map of the Köppen-Geiger climate classification. *Hydrology and Earth System Sciences, 11*, 1633–1644. https://doi.org/10.5194/hess-11-1633-2007.

Peterson, R. A., Walker, D. A., Romanovsky, V. E., Knudson, J. A., Raynolds, M. K., & Krantz, W. B. (2003). A differential frost heave model: cryoturbation-vegetation interactions. In *Proceedings of the Eighth International Conference on Permafrost* (Vol. 2, pp. 885–890), Lisse, Zürich, Switzerland. AA Balkema.

Peterson, R. A., & Krantz, W. B. (2008). Differential frost heave model for patterned ground formation: Corroboration with observations along a North American arctic transect. *Journal of Geophysical Research: Biogeosciences, 113*(G3). https://doi.org/10.1029/2007JG000559.

Porter, C., Morin, P., Howat, I., Noh, M. J., Bates, B., Peterman, K., et al. (2018). *ArcticDEM*. Harvard Dataverse, 1.

Reinosch, E., Buckel, J., Dong, J., Gerke, M., Baade, J., & Riedel, B. (2020). InSAR time series analysis of seasonal surface displacement dynamics on the Tibetan Plateau. *The Cryosphere, 14*(5), 1633–1633. https://doi.org/10.5194/tc-14-1633-2020.

Rempel, A. W. (2007). Formation of ice lenses and frost heave. *Journal of Geophysical Research: Earth Surface, 112*(F2). https://doi.org/10.1029/2006JF000525.

Ridefelt, H., Etzelmüller, B., & Boelhouwers, J. (2010). Spatial analysis of solifluction landforms and process rates in the Abisko Mountains, northern Sweden. *Permafrost and Periglacial Processes, 21*(3), 241–255. https://doi.org/10.1002/ppp.681.

Ridefelt, H., Åkerman, J., Beylich, A. A., Boelhouwers, J., Kolstrup, E., & Nyberg, R. (2009). 56 years of solifluction measurements in the abisko mountains, northern sweden–analysis of temporal and spatial variations of slow soil surface movement. *Geografiska Annaler, Series A: Physical Geography, 91*(3), 215–232. https://doi.org/10.1111/j.1468-0459.2009.00365.x.

Romanovsky, V. E., Smith, S. L., & Christiansen, H. H. (2010). Permafrost thermal state in the polar Northern Hemisphere during the international polar year 2007–2009: a synthesis. *Permafrost and Periglacial Processes, 21*(2), 106–116. https://doi.org/10.1002/ppp.689.

Rouse, J. W., Haas, R. H., Schell, J. A., & Deering, D. W. (1974). Monitoring vegetation systems in the Great Plains with ERTS. In *Proceedings of the Third Earth Resources Technology Satellite-1 Symposium* (pp. 309–317). NASA, Washington, D.C.

Rouyet, L., Lauknes, T. R., Christiansen, H. H., Strand, S. M., & Larsen, Y. (2019). Seasonal dynamics of a permafrost landscape, Adventdalen, Svalbard, investigated by InSAR. *Remote Sensing of Environment*, 231, 111236. https://doi.org/10.1016/j.rse.2019.111236.

Rudy, A. C. A, Lamoureux, S. F., Treitz, P., Ewijk, K. V., Bonnaventure, P. P., & Budkewitsch, P. (2017). Terrain controls and landscape-scale susceptibility modelling of active-layer detachments, Sabine Peninsula, Melville Island, Nunavut. *Permafrost and Periglacial Processes, 28*, 79–91. https://doi.org/10.1002/ppp.1900.

Rudy, A. C., Lamoureux, S. F., Treitz, P., Short, N., & Brisco, B. (2018). Seasonal and multi-year surface displacements measured by DInSAR in a High Arctic permafrost environment. *International Journal of Applied Earth Observation and Geoinformation, 64*, 51–61. https://doi.org/10.1016/j.jag.2017.09.002.

Sandwell, D. T., & Price, E. J. (1998). Phase gradient approach to stacking interferograms. *Journal of Geophysical Research: Solid Earth, 103*(B12), 30183–30204. https://doi.org/10.1029/1998JB900008.

Schuh, C., Frampton, A., & Christiansen, H. H. (2017). Soil moisture redistribution and its effect on inter-annual active layer temperature and thickness variations in a dry loess terrace in Adventdalen, Svalbard. *The Cryosphere, 11*(1), 635. https://doi.org/10.5194/tc-11-635-2017.

Seppälä, M. (2011). Chapter 3. Periglacial phenomena of northern Fennoscandia. In J. Boardman (Eds.), *Periglacial processes and landforms in Britain and Ireland* (pp. 45–55). Cambridge University Press.

Shiklomanov, N I., Streletskiy, D. A., Nelson, F. E., Hollister, R. D., Romanovsky, V. E., Tweedie, C. E., et al. (2010). Decadal variations of active-layer thickness in moisture-controlled landscapes, Barrow, Alaska. *Journal of Geophysical Research: Biogeosciences, 115*(G4). https://doi.org/10.1029/2009JG001248.

Shiklomanov, N. I., Streletskiy, D. A., & Nelson, F. E. (2012). Northern hemisphere component of the global circumpolar active layer monitoring (CALM) program. In *Proceedings of the 10th International Conference on Permafrost* (Vol. 1, pp. 377–382), Salekhard, Russia.

Smith, D. J. (1987) Frost-heave activity in the Mount Rae area, Canadian Rocky Mountains. *Arctic and Alpine. Research, 19*(2), 155–166. https://doi.org/10.1080/00040851.1987.12002589.

Strozzi, T., Antonova, S., Günther, F., Mätzler, E., Vieira, G., Wegmüller, U., Westermann, S., & Bartsch, A. (2018). Sentinel-1 SAR interferometry for surface deformation monitoring in low-land permafrost areas. *Remote Sensing, 10*(9), 1360. https://doi.org/10.3390/rs10091360.

Thomas, H. R., Cleall, P., Li, Y. C., Harris, C., & Kern-Luetschg, M. (2009). Modelling of cryogenic processes in permafrost and seasonally frozen soils. *Géotechnique, 59*(3), 173–184. https://doi.org/10.1680/geot.2009.59.3.173.

Thuiller, W., Lafourcade, B., Engler, R., & Araujo, M. B. (2009). BIOMOD—a platform for ensemble forecasting of species distributions. *Ecography, 32*, 369–373. https://doi.org/10.1111/j.1600-0587.2008.05742.x.Van Vliet-Lanoë, B. (1991). Differential frost heave, load casting and convection: converging mechanisms; a discussion of the origin of cryoturbations. *Permafrost and Periglacial Processes*, 2(2), 123–139. https://doi.org/10.1002/ppp.3430020207.

Virtanen, R., Oksanen, L., Oksanen, T., Cohen, J., Forbes, B. C., Johansen, B., et al. (2016). Where do the treeless tundra areas of northern highlands fit in the global biome system: toward an ecologically natural subdivision of the tundra biome. *Ecology and Evolution, 6*(1), 143–158. https://doi.org/10.1002/ece3.1837.

Walsh, S. J., Butler, D. R., & Malanson, G. P. (1998). An overview of scale, pattern, process relationships in geomorphology: a remote sensing and GIS perspective. *Geomorphology, 21*(3-4), 183–205. https://doi.org/10.1016/S0169-555X(97)00057-3.

Wang, C., Zhang, Z., Zhang, H., Zhang, B., Tang, Y., & Wu, Q. (2018). Active layer thickness retrieval of Qinghai–Tibet permafrost using the TerraSAR-X InSAR technique. *IEEE Journal of Selected Topics in Applied Earth Observations and Remote Sensing, 11*(11), 4403–4413. https://doi.org/10.1109/JSTARS.2018.2873219.

Westermann, S., Duguay, C. R., Grosse, G., & Kääb, A. (2015). Chapter 13. Remote sensing of permafrost and frozen ground. In: Tedesco, M. (eds), *Remote Sensing of the Cryosphere*, First Edition. John Wiley & Sons.

Wilson, P., & Sellier, D. (1995). Active patterned ground and cryoturbation on Muckish mountain, Co. Donegal, Ireland. *Permafrost and Periglacial Processes, 6*(1), 15–25. https://doi.org/10.1002/ppp.3430060104.

Zebker, H. A., Rosen, P. A., & Hensley, S. (1997). Atmospheric effects in interferometric synthetic aperture radar surface deformation and topographic maps. *Journal of Geophysical Research: Solid Earth, 102*(B4), 7547–7563. https://doi.org/10.1029/96JB03804.

Zwieback, S., & Hajnsek, I. (2014). The impact of vegetation growth on DInSAR coherence regions and estimated deformations. In *Proceedings of IEEE Geoscience and Remote Sensing Symposium* (pp. 966–969).

Zwieback, S., Hensley, S., & Hajnsek, I. (2015). Assessment of soil moisture effects on L-band radar interferometry. *Remote Sensing of Environment, 164*, 77–89. https://doi.org/10.1016/j.rse.2015.04.012.

Zwieback, S., Liu, X., Antonova, S., Heim, B., Bartsch, A., Boike, J., & Hajnsek, I. (2016). A statistical test of phase closure to detect influences on DInSAR deformation estimates besides displacements and decorrelation noise: Two case studies in high-latitude regions. *IEEE Transactions on Geoscience and Remote Sensing, 54*(9), 5588–5601. https://doi.org /10.1109/TGRS.2016.2569435.

Supplement Material

Environmental Controls of InSAR-based Periglacial Ground Dynamics in a Sub-Arctic Landscape

Line Rouyet, Olli Karjalainen, Pekka Niittynen, Juha Aalto, Miska Luoto, Tom Rune Lauknes, Yngvar Larsen, Jan Hjort

Text S0: Model parameterization (complement to Section 3.4):

In addition to the Generalized boosting method (GBM) used as primary modelling technique in the study (see Section 3.4), we applied three complementary methods to assess the consistency of the results:

- Generalized linear model (GLM; R base function *glm*; Nelder & Wedderburn, 1972): GLM was calibrated using linear and quadratic functions. Owing to the skewed distribution of velocity values (Figure 7D), we used a gaussian log link function.
- Generalized additive model (GAM, R package *mgcv*; Hastie & Tibshirani, 1990): Responses are related to explanatory variables using a smoothing spline, which are controlled with a pre-defined maximum degree of freedom, here four at maximum. As for GLM, we applied a gaussian log link function.
- Random forest (RF, R package *randomForest*; Breiman, 2001): 200 trees were fitted with a minimum of five observations per terminal node and mtry was set to 2 to allow two randomly selected environmental variables to be used in splitting each node in a tree. The sufficient number of trees fitted was determined by assessing how many trees were needed to minimize the internally estimated prediction error of the model.

References:

Breiman, L. (2001). Random forests. *Maching Learning*, *45*(1), 5–32.
Hastie, T. J., & Tibshirani, R. J. (1990). *Generalized additive models* (Vol. 43). CRC press.
Nelder, J. A., & Wedderburn, R. W. (1972). Generalized linear models. *Journal of the Royal Statistical Society: Series A (General)*, *135*(3), 370–384. https://doi.org/10.2307/2344614.

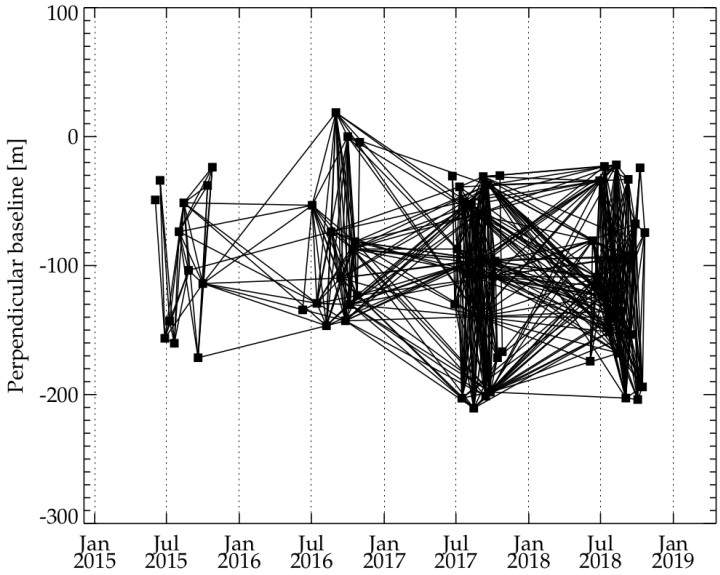

Figure S1. Baseline plot of the interferometric pairs used for the ascending Sentinel-1 dataset (black squares: SAR acquisitions, black lines: interferograms)

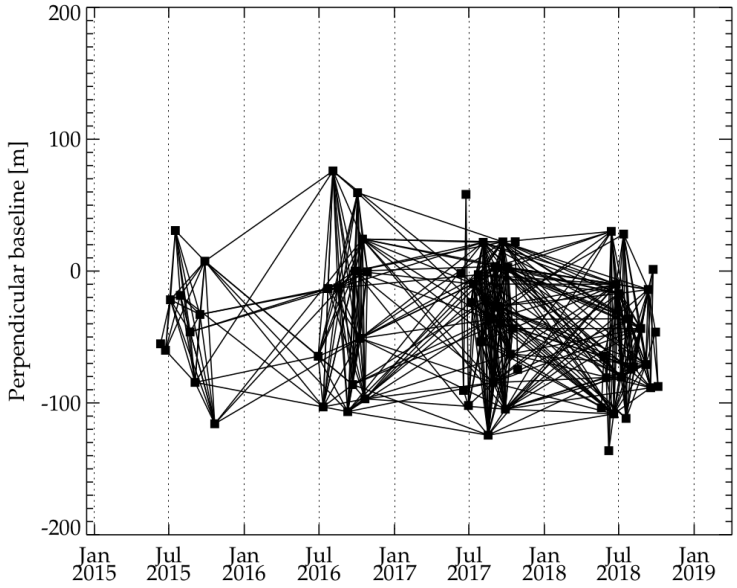

Figure S2. Baseline plot of the interferometric pairs used for the descending Sentinel-1 dataset (black squares: SAR acquisitions, black lines: interferograms)

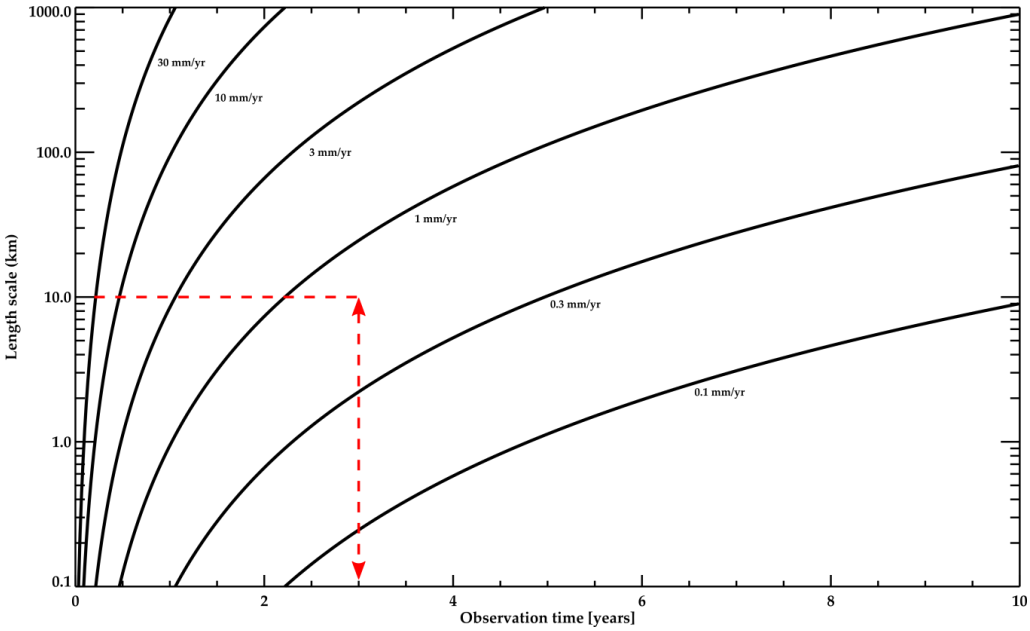

Figure S3. InSAR minimum detectable velocity, v_{min}, as a function of observation time and length scale as calculated from the equation 19 in Emardson et al. (2003). Contour labels are $\log_{10} v_{min}$, with v_{min} in units of mm/yr. T_{orb} (repeat-pass) is 6 days, and noise is assumed to come only from the neutral atmosphere; v_{min} is based on viewing geometry of 38° off zenith (Sentinel-1 midswath incidence angle). Red arrows show the range of applicable values for the current study considering the observation period and size of the area.

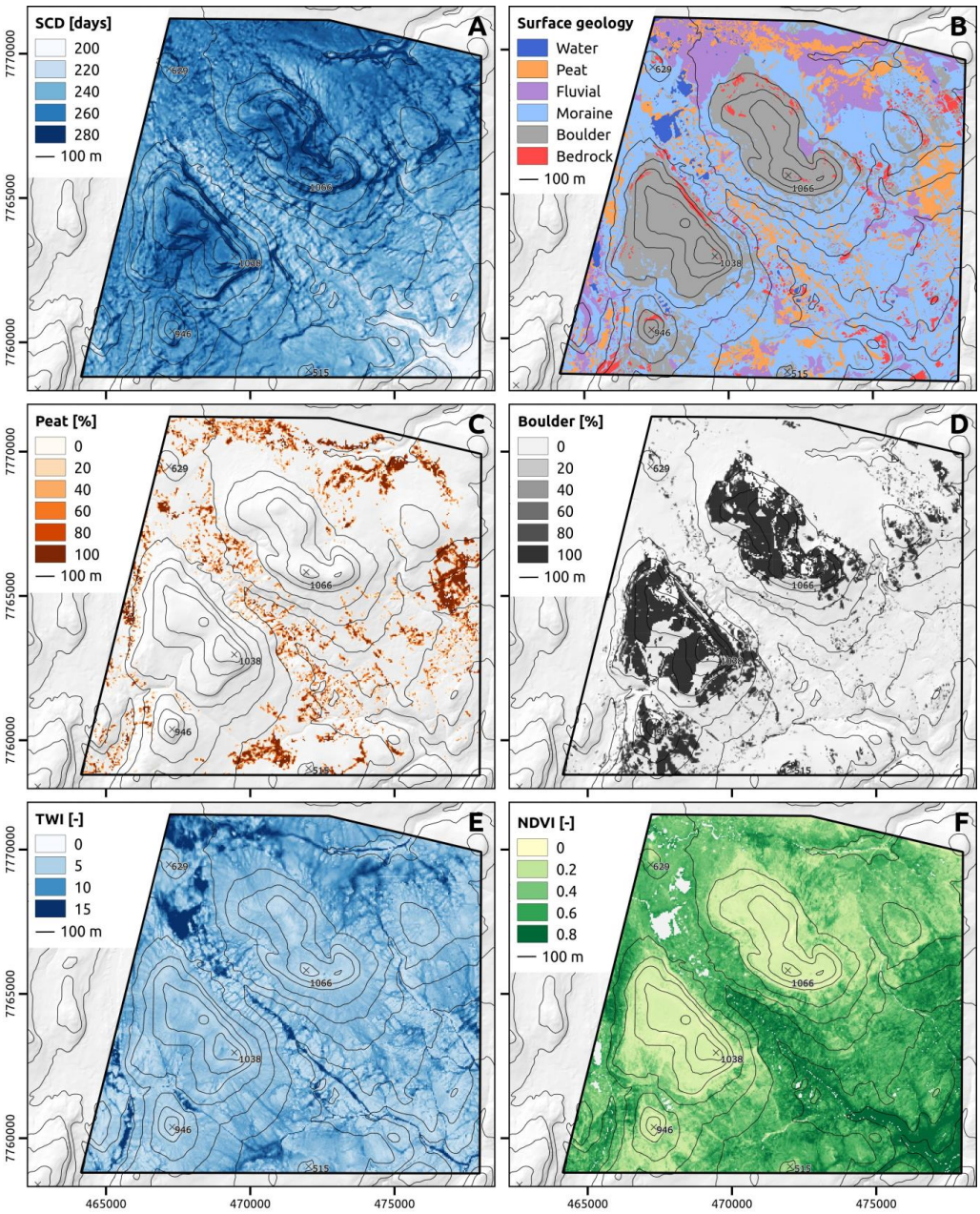

Figure S4. Spatial distribution of the explanatory variables. A. Snow cover duration (SCD); B. Initial simplified 6-classes surface geology map; C. Peat deposits, extracted from B and converted to continuous variable [%]; D. Boulder fields, extracted from B and converted to continuous variables [%]. E. Topographic wetness index (TWI); F. Normalized difference vegetation index (NDVI). The mean annual air temperature (MAAT) and slope angle (Slope) are shown in the main manuscript (Figure 4).

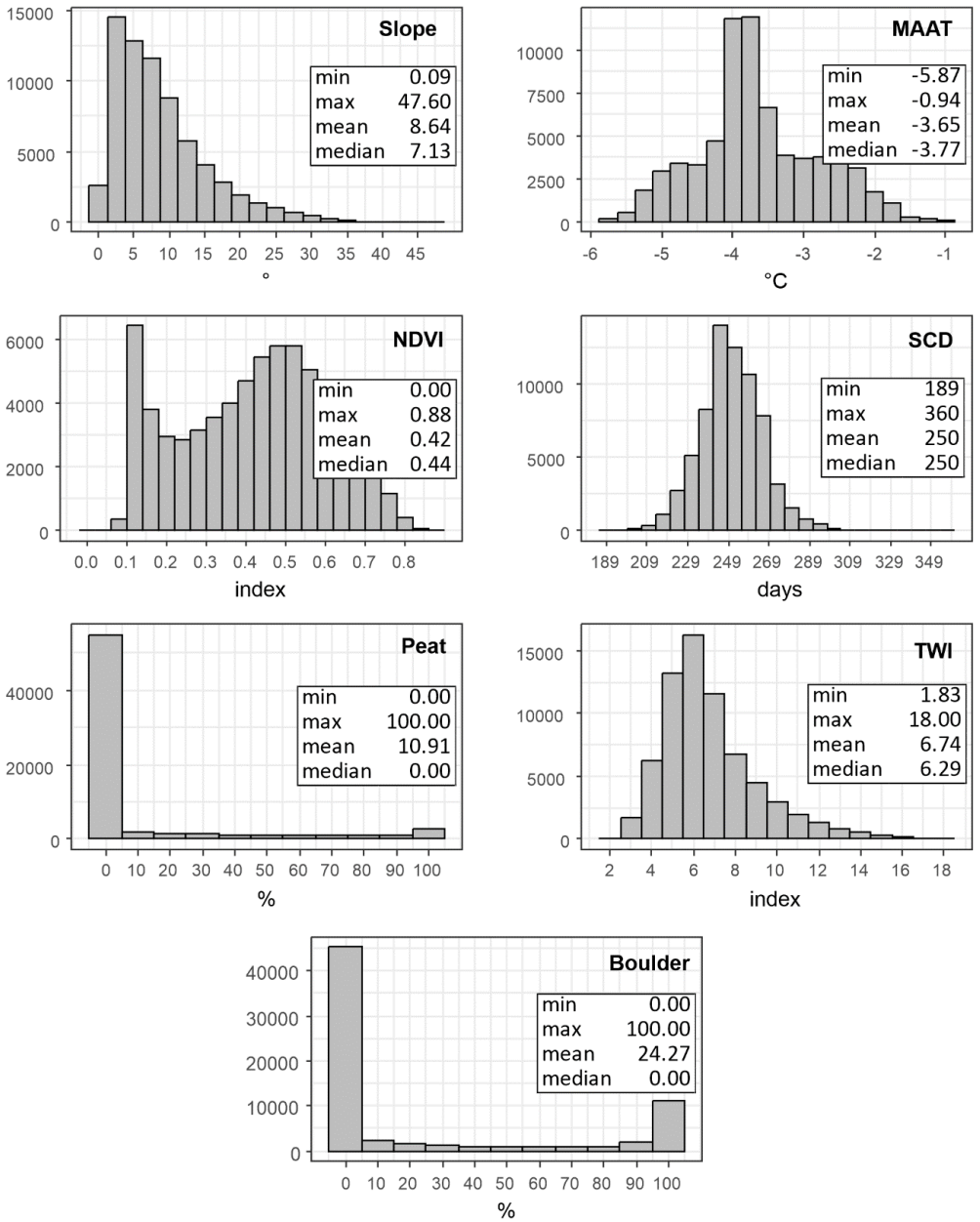

Figure S5. Histograms of the distribution for the seven explanatory variables at the locations of the InSAR pixels. The acronyms refer to mean annual air temperature (MAAT), normalized difference vegetation index (NDVI), snow cover duration (SCD), and topographic wetness index (TWI).

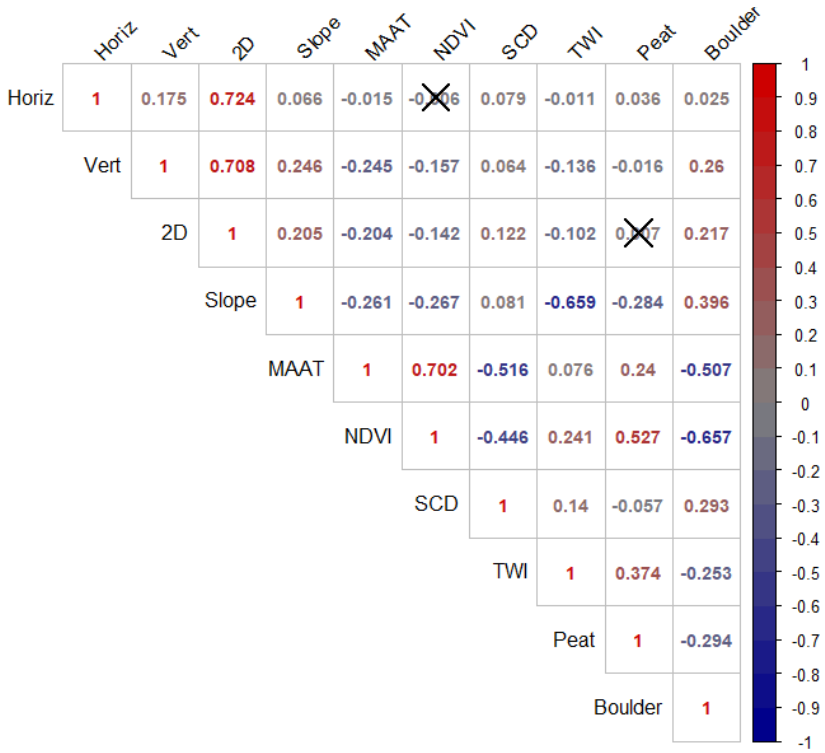

Figure S6. Spearman rank-order correlations between the response and explanatory variables. Non-significant correlations ($p > 0.01$) are marked with an X symbol. The acronyms refer to mean annual air temperature (MAAT), normalized difference vegetation index (NDVI), snow cover duration (SCD), and topographic wetness index (TWI).

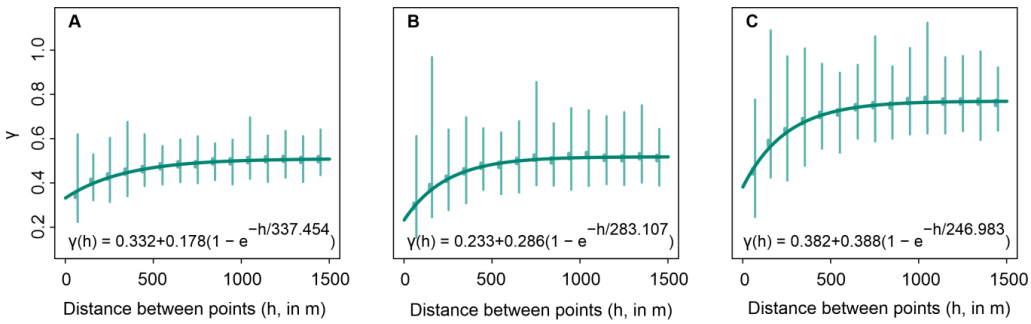

Figure S7. Fitted exponential variograms for the estimation of the distance at which spatial autocorrelation dissipates for the three response variables. A. Horizontal mean velocity. B. Vertical mean velocity C. 2D mean velocity.

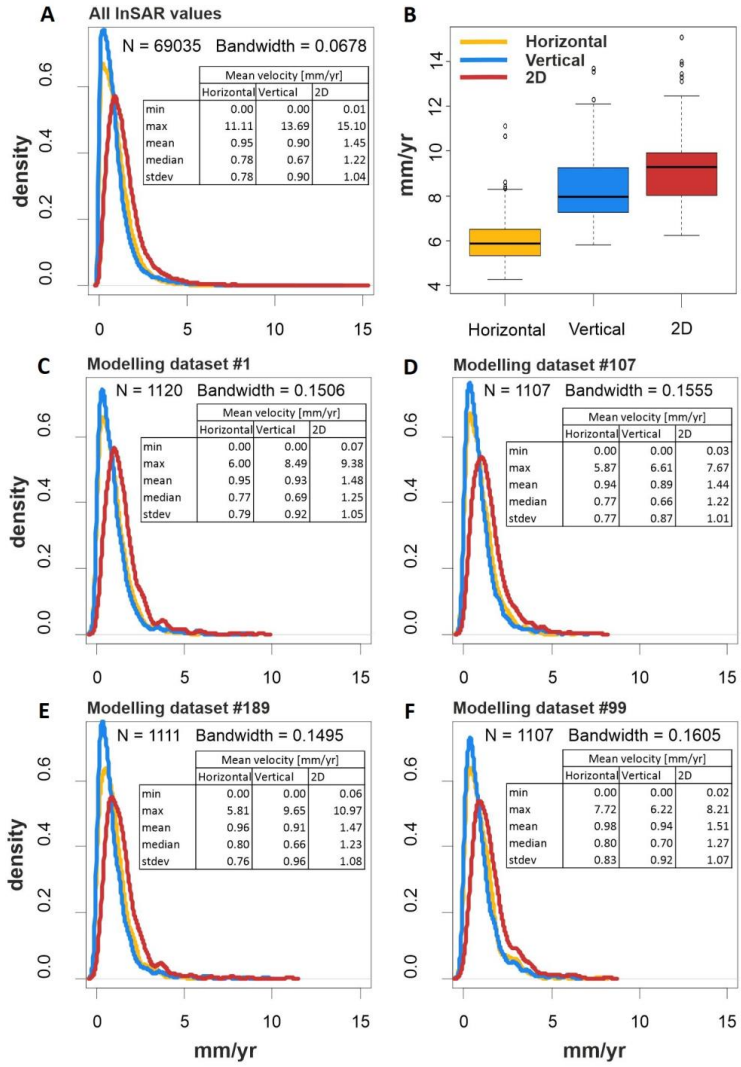

Figure S8. Distribution and statistics of InSAR-based ground velocities in all obtained InSAR pixels (A), and four randomly selected modelling datasets (C–F). The graphs display Kernel densities. Panel B summarizes the distributions of the 200 maximum values based on the 200 modelling datasets. The black line in the box represents the median, and the lower and upper borders of the box are 25th and 75th percentiles, respectively. Circle symbols represent outliers, i.e. values outside 1.5 times the interquartile range.

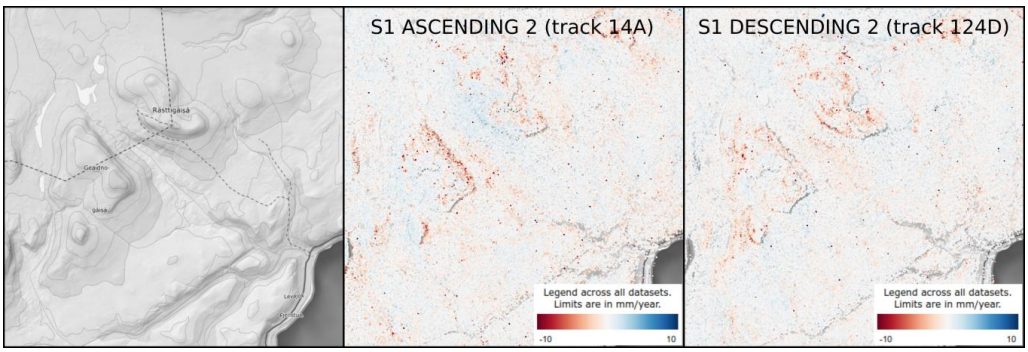

Figure S9. Overviews of the ascending and descending Persistent Scatterer Interferometry (PSI) results from the freely available on InSAR Norway ground motion mapping service. Interactive view and 3D mode publicly available on insar.ngu.no. Explanations on https://www.ngu.no/en/topic/insar-norway. Link to the area: https://insar.ngu.no/#llh=26.23111673,69.98276632,17175.26740577&look=-0.15129546,-0.9395897,-0.30705191&right=0.89701846,0,-0.44199308&up=-0.41529228,0.34230195,-0.84282958&layers=nma-topo-gray

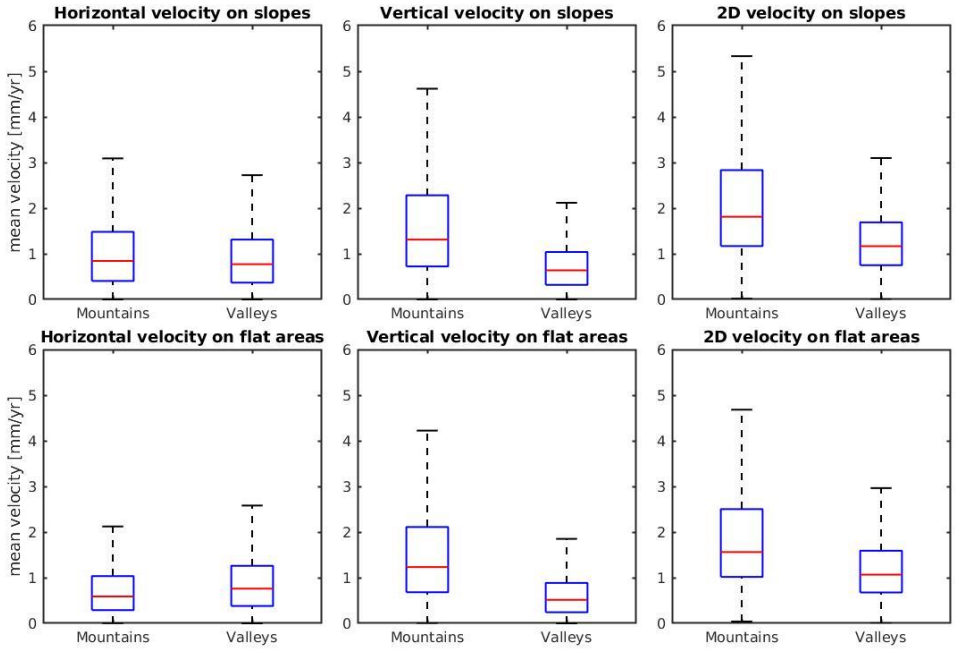

Figure S10. Comparison of the InSAR values for the horizontal, vertical and 2D velocity for four geographical groups within the study area. Group "Slopes" correspond to pixels with slope angles > 5°. Group "Flat areas" correspond to pixels with slope angles ≤ 5°. Group "Mountains" corresponds to elevations > 700 m asl. Group "Valleys" corresponds to elevations ≤ 700 m asl. Note that the outliers (by default value over 1.5 times the interquartile range away from the box limits) are here not displayed.

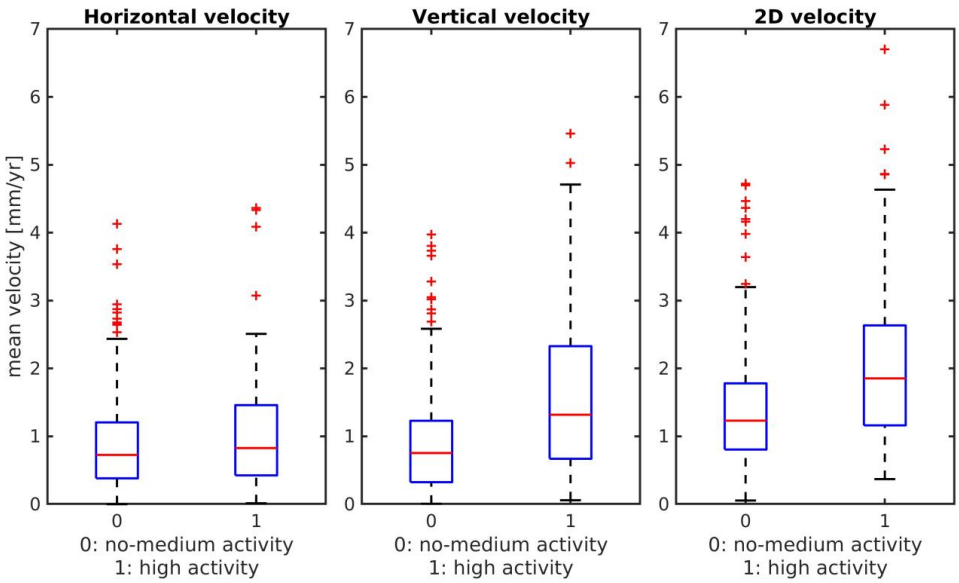

Figure S11. Comparison between qualitatively rated field activity at 429 stations (10 m grids) and InSAR mean velocity in mm/yr at similar locations (40 m pixels). 0: negligible, low and medium activity. 1: high activity.

Table S12. Model performance based on the amount of explained variation in the modelling data (coefficient of determination, R^2) and prediction errors in mm: root mean square error (RMSE) and mean absolute error (MAE). All the statistics are computed for calibration (90% of observations) and evaluation datasets (10%) to allow assessments of model stability. The acronyms refer to generalized linear model (GLM), generalized additive model (GAM), generalized boosting method (GBM) and random forest (RF).

Horizontal velocity

	R^2		RMSE		MAE	
	Calibration	Evaluation	Calibration	Evaluation	Calibration	Evaluation
GLM	0.093	0.013	0.743	0.760	0.561	0.571
GAM	0.126	0.037	0.729	0.752	0.550	0.565
GBM	0.235	0.077	0.682	0.737	0.518	0.555
RF	0.796	0.054	0.352	0.745	0.259	0.562

Vertical velocity

	R^2		RMSE		MAE	
	Calibration	Evaluation	Calibration	Evaluation	Calibration	Evaluation
GLM	0.339	0.252	0.739	0.757	0.504	0.514
GAM	0.362	0.265	0.726	0.752	0.496	0.511
GBM	0.472	0.280	0.661	0.746	0.465	0.509
RF	0.835	0.271	0.369	0.749	0.240	0.512

2D velocity

	R^2		RMSE		MAE	
	Calibration	Evaluation	Calibration	Evaluation	Calibration	Evaluation
GLM	0.253	0.188	0.900	0.913	0.642	0.657
GAM	0.270	0.196	0.889	0.909	0.635	0.655
GBM	0.382	0.209	0.818	0.904	0.595	0.653
RF	0.820	0.200	0.441	0.908	0.304	0.655

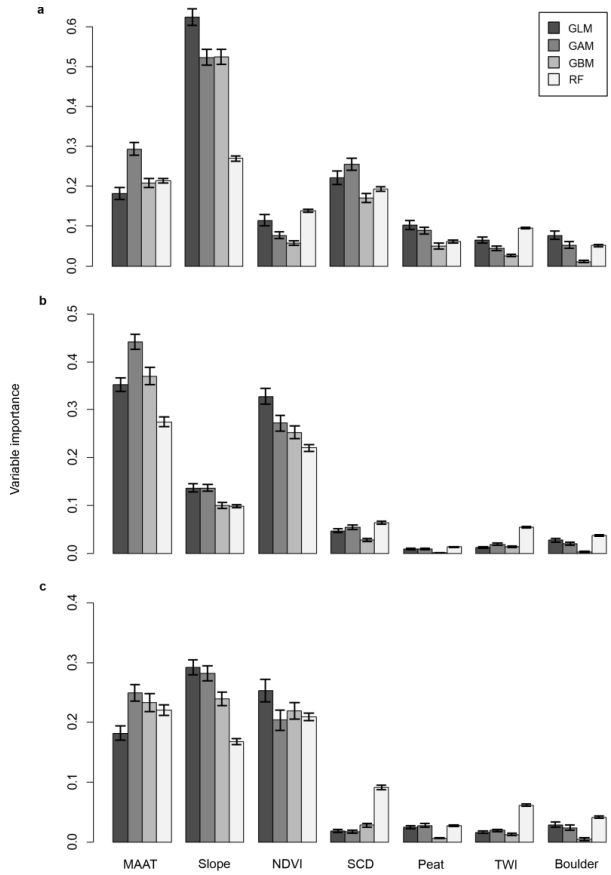

Figure S13. Variable importance for horizontal (a), vertical (b) and 2D velocities (c) based on the four applied modelling methods. Error bars show 95% confidence intervals. The acronyms refer to mean annual air temperature (MAAT), normalized difference vegetation index (NDVI), snow cover duration (SCD) and topographic wetness index (TWI).

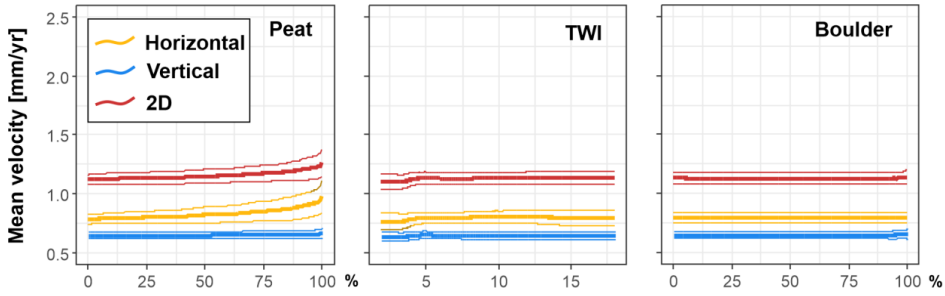

Figure S14. Response curves depicting the modelled mean velocity (Y-axis) across the range of variables´ values in their original scale (X-axis). Hatched curves represent one standard deviation from average response over 200 permutations with generalized boosting method (GBM). The acronym TWI refers to Topographic Wetness Index.